
Measurement of top quark pair production in association with charm quarks at $\sqrt{s} = 13$ TeV with the ATLAS detector

Dissertation

for the award of the degree
“Doctor of Philosophy” (Ph.D.)
Division of Mathematics and Natural Sciences
of the Georg-August-Universität Göttingen

within the Physics doctoral program
of the Georg-August University School of Science (GAUSS)

submitted by

Matthew Kingston

from Belfast

Göttingen, 2025



Thesis Committee

Prof. Dr. Arnulf Quadt

II. Physikalisches Institut, Georg-August-Universität Göttingen

Prof. Dr. Steffen Schumann

Institut für Theoretische Physik, Georg-August-Universität Göttingen

Prof. Dr. Stan Lai

II. Physikalisches Institut, Georg-August-Universität Göttingen

Members of the Examination Board:

Reviewer: Prof. Dr. Arnulf Quadt
II. Physikalisches Institut, Georg-August-Universität Göttingen

Second Reviewer: Prof. Dr. Andrew Mehta
Department of Physics, University of Liverpool

Further members of the Examination Board:

Prof. Dr. Steffen Schumann

II. Physikalisches Institut, Georg-August-Universität Göttingen

Prof. Dr. Laura Covi

II. Physikalisches Institut, Georg-August-Universität Göttingen

Prof. Dr. Sami Solanki

Max-Planck-Institut für Sonnensystemforschung, Göttingen

Prof. Dr. Laurent Gizon

Max-Planck-Institut für Sonnensystemforschung, Göttingen

Date of the oral examination: 20/03/2025

Referenz: II.Physik-UniGö-Diss-2025/01

Measurement of top quark pair production in association with charm quarks at $\sqrt{s} = 13$ TeV with the ATLAS detector

Abstract

The Large Hadron Collider at CERN has produced a uniquely large set of proton-proton collision data at never-before-seen energies since the beginning of its operation in 2010.

Using data collected by the ATLAS detector at a centre-of-mass energy of 13 TeV between 2015 and 2018, corresponding to an integrated luminosity of 140 fb^{-1} , this thesis presents the results of the first dedicated ATLAS measurement of the production cross-section of top quark pairs in association with charm quarks. This measurement tests and provides information for future improvements of the modelling in quantum chromodynamics of systems which act at multiple distinct energy scales. This process is also an important background to measurements of other, much rarer, top quark processes such as $t\bar{t}H(H \rightarrow b\bar{b})$ and $t\bar{t}t\bar{t}$.

A key challenge of this measurement is the simultaneous identification of b - and c -jets, for which a custom heavy-flavour tagging algorithm is employed. A profile likelihood fit is used to extract the cross-sections for top quark pairs in association with two or more c -jets ($t\bar{t} + \geq 2c$) and with one c -jet ($t\bar{t} + 1c$). This measurement is performed both in a fiducial phase space designed to mimic the acceptance of the ATLAS detector, and in a more inclusive phase space. In the fiducial phase space this measures cross-sections of $1.28^{+0.27}_{-0.24} \text{ pb}$ and $6.4^{+1.0}_{-0.9} \text{ pb}$ for $t\bar{t} + \geq 2c$ and $t\bar{t} + 1c$ production, respectively. An additional fit extracts the ratios of $t\bar{t} + \geq 2c$ and $t\bar{t} + 1c$ cross-sections to that of total $t\bar{t} + \text{jets}$ production. The measured values tend to exceed predictions from simulation, but nonetheless are consistent with them within 0.5 to 2 standard deviations. Sensitivity is ultimately limited by uncertainties in the modelling of the $t\bar{t}$ system, as well as in the calibration of the heavy-flavour tagging algorithm and by limited data statistics. A focus is placed in this thesis on the work done to validate and understand the fit model.

Contents

1. Introduction	1
2. Standard Model	3
2.1. Overview of the Standard Model	3
2.2. Electroweak interaction and symmetry breaking	6
2.3. Quantum chromodynamics	9
2.4. The top quark	12
2.5. Top quarks in association with heavy flavour quarks	17
2.6. Limitations of the Standard Model	19
3. Experimental Setup	21
3.1. The Large Hadron Collider	21
3.2. The ATLAS detector	25
3.3. Monitoring of Pixel Detector tuning	27
4. Modelling of Signal and Background	37
4.1. $t\bar{t}$ events	37
4.2. Background processes	39
5. Physics Object Identification and Reconstruction	41
5.1. Electrons	41
5.2. Muons	43
5.3. Jets	44
5.4. Heavy flavour tagging	46
5.5. b/c -tagger	48
5.6. Missing transverse momentum	51
5.7. Overlap removal	51

6. Event Selection	53
6.1. Event pre-selection	53
6.2. Estimation of backgrounds	55
6.3. Classification of simulated events	56
6.4. Definition of regions	57
7. Analysis Strategy	63
7.1. Fitting strategy	63
7.2. Fiducial phase space definition	66
7.3. Fitting parameterisations	66
7.4. Comparison of strategy with the CMS analysis	67
8. Systematic Uncertainties	69
8.1. Handling of systematic templates	69
8.2. Experimental uncertainties	71
8.3. Theoretical uncertainties	73
9. Fit Studies	81
9.1. Control plots of kinematic variables	82
9.2. Individual pull/constraint studies	82
9.3. Studies of region and observable changes	83
9.4. MPI/FSR studies	86
10. Results	91
10.1. Fiducial phase space measurement	91
10.2. Inclusive phase space measurement	104
10.3. Comparison of uncertainties and results to the CMS analysis	106
11. Summary and Conclusions	109
Bibliography	111
Appendices	131
A. CMS Analysis Results	133
B. Expected Number of Events in Analysis Regions	135
C. Pruning of Systematic Uncertainties	139
D. Kinematics Control Plots	161
D.1. Pre-fit plots - lepton + jets channel	161
D.2. Pre-fit plots - dilepton channel	174
D.3. Post-fit plots - lepton + jets channel	185
D.4. Post-fit plots - dilepton channel	198

E. Additional Figures - Results	209
E.1. Fiducial phase space fit to data	209
E.2. Inclusive phase space fit to data	214

Acknowledgements

A PhD like this can't be done alone, and I would like to acknowledge some of those who made it all possible. I would like to take this opportunity to thank Arnulf Quadt, without whom I wouldn't be at this point (in several ways). When I first came to Göttingen from Cambridge for a summer project over seven years ago, I couldn't have imagined how major a part this place would play in my life. Thank you for giving me the opportunity to begin this PhD, and for all of the support and assistance along the way. I would also like to thank Steffen Schumann and Stan Lai for acting as members of my Thesis Advisory Committee, and the examination committee members who have agreed to play their part in the final stages of this process.

My Qualification Task would have been impossible without the regular input and motivation from Marcello Bindi and Tobias Bisanz, to whom I am very grateful. I am, of course, also deeply indebted to the entire $t\bar{t}$ + charm analysis team. In particular I want to thank Luisa Carvalho, who led me by the hand through the initial stages of understanding and starting work on this analysis; Knut Zoch, for all of his assistance, expertise and understanding throughout; and Elizaveta Shabalina, for bringing to bear her seemingly boundless experience and guiding the work.

A massive thank you to the other members of the II. Institute past and present. The coffees, game nights and pub quizzes have in many ways been the heart of this PhD experience. Thanks to those who have helped me through in both the professional and personal sphere: I hope you know who you are.

Last, but certainly not least, I would like to thank my other friends and family. Fabi and Stephi, you've been such a huge part of my life in Göttingen - thank you for all the dinners shared. Phil - we seem to have a habit of always living in different countries, but I value your constant friendship so deeply. Andy, Cath and Leo, I hope I will shortly be assuming the full title of "Dr. Uncle Matt": congratulations if you make it this far into reading this thesis. Mum and Dad, you have never wavered once in your love, support and belief in me: I could never thank you enough.

Contributions by the Author

All publications by the ATLAS Collaboration are credited to almost 3000 authors, reflecting the fact that no ATLAS scientific results belong to one person, or even any small group. The work discussed in this thesis relies on decades of development and work: from the development and operation of the LHC and ATLAS detector, to methods in modelling of physics processes, to tools to interpret and manage data.

The focus of this thesis is the author's contribution to the first dedicated ATLAS measurement of top quark pairs in association with charm quarks [1]. In order to fully contextualise this, the work of others will also be discussed, and this preface provides a non-exhaustive overview of the author's personal contributions.

At the time of the author joining the analysis team, provisional analysis strategies consisting of data and events from Monte Carlo simulation, systematics models and fitting strategies were in place for both dilepton and lepton + jets channels. The main analysers for these channels were Luisa Carvalho and Lukas Ehrke, respectively, with additional work from Johnny Raine and Jelena Jovicevic amongst others. The calibration of the b/c -tagger was performed by Lukas Ehrke. The author carried out investigations of problematic pulls and constraints in the dilepton channel and the combined fit, as well as a number of other studies of the fit model, some of which are presented in Chapter 9. The pseudo-data tests briefly described in that chapter were performed by Luisa Carvalho and Knut Zoch. The production of pre-fit and post-fit kinematic distributions was also done by the author, as was a re-production of the dilepton channel $t\bar{t}$ samples with an updated matching procedure for jets and hadrons. Following unblinding, the final production of results across the range of fit setups was done by the author alongside Knut Zoch, who also performed the calculation of cross-section values.

In addition to the work on the main thesis topic, over the course of the PhD study period the author contributed to the running of the ATLAS detector through the Qualification Project described in Section 3.3, as well as through working in the ATLAS Control Room. Finally, the author also undertook roles in teaching and within the ATLAS top quark physics working group.

CHAPTER 1

Introduction

A quote from Albert Michelson of the famous Michelson-Morley experiment [2], the sentiment of which is often misattributed to the (Belfast-born) Lord Kelvin, itself quotes another unnamed scientist: “An eminent physicist remarked that the future truths of physical science are to be looked for in the sixth place of decimals.”

This idea, to whomever it is attributed or in whichever form, is often taken as an example of the arrogance of physicists of the era. It supposes a belief in the practice of physics as simply an exercise in neatening up the edges of the existing fabric of ideas. The modern era of particle physics may be viewed as, in some ways, having reached a similar stage. The greatest breakthroughs of the last decades arguably have more represented confirmations of pre-existing ideas than revolutions. Certain constants of the Standard Model have indeed been measured with precision far beyond the sixth decimal place.

The most obvious objection to such a characterisation is that many fundamental parameters of nature have yet to be precisely measured in the first place. Furthermore there are many obvious incomplete holes in the current best theories of fundamental physics.

However the sentiment of these words need not necessarily be viewed in simply a dismissive light. It is quite possible that at such a sixth decimal place, when it is found, a new chink in the armour of current understandings may be opened. It may be through such a surprising digit that a new understanding will ultimately be motivated into existence. The project that the author feels they have played a small part in, alongside thousands of others, may be viewed as a search for such inconsistencies and surprises.

This thesis presents a measurement of the production cross-section of top quark pairs in association with charm quarks. Chapter 2 provides an overview of the Standard Model of particle physics, which is the theoretical basis for the thesis topic. Chapter 3 then describes the experimental setup needed to obtain the data used: the LHC and

1. Introduction

the ATLAS detector, alongside a brief overview of the work the author performed to contribute to its future operation. The Monte Carlo (MC) simulations used to model the signal and background processes are the topic of Chapter 4. Chapter 5 summarises the relevant set of procedures used to identify and reconstruct particles from detector information. Of particular importance is the identification of jets containing b and c hadrons. Chapter 6 then outlines how the full dataset is narrowed down to only those of interest, and split into several analysis regions. More information is given on background estimation, focusing on the data-driven procedures used for non-prompt leptons. It furthermore details the way top quark pairs produced in association with additional jets are categorised, and the observables used in signal regions to better separate the different contributions. The topic of Chapter 7 is the procedure used to fit the expected number of events to those observed, and the steps to extract the final cross-section measurements. A description of the systematic uncertainties considered, both experimental and theoretical, is given in Chapter 8. Chapter 9 aims to highlight some of the work done in studying and validating the fit model. In Chapter 10 several complementary sets of results are presented corresponding to the different procedures described. These are compared both to predictions from simulation, and previous measurements. Chapter 11 finally gives a summary and conclusions. Additional material is contained in Appendices A to E.

CHAPTER 2

Standard Model

The Standard Model (SM) [3–15] is our current best understanding of fundamental physics, built up over the course of the 20th century. Of the four fundamental forces of nature: gravity, electromagnetism, and the strong and weak interactions, it provides a description for the latter three that has remained almost entirely robust to decades to experiment. It also comes with a description of fundamental particles, all of which have now been experimentally observed. Section 2.1 gives a summary of the underlying theory of the SM, then in Section 2.2 the unified electroweak interaction is described, combining the theories of the weak and electromagnetic interactions, in addition to the mechanism of spontaneous symmetry breaking responsible for particle masses. Section 2.3 describes the strong interaction, which is particularly relevant to the measurement performed in this thesis. In Section 2.4 the physics of top quarks in association with heavy flavour quarks, like the charm quark, is examined in detail. As already indicated, the SM is not a complete theory of nature - these limitations are discussed in Section 2.6.

2.1. Overview of the Standard Model

Mathematically, the SM is a renormalisable quantum field theory based on a local $SU(3) \otimes SU(2) \otimes U(1)$ gauge symmetry.

Two categories of particle exist in the SM: *fermions*, which have half-integer spin, and *bosons*, which have integer spin. In reality all of the elementary fermions have spin equal to $\frac{1}{2}$. Three types of interaction are described by this model, with each being mediated by bosons. The strong interaction, governed by the theory known as *quantum chromodynamics* (QCD) is experienced by the quarks and mediated by the massless gluon (g). The electromagnetic interaction, with its coupling of electric charge, is mediated by the photon (γ) - the massless boson familiarly known as light. Finally

2. Standard Model

the weak interaction is participated in by all fermions, and has three associated bosons: the W^+ , W^- and the neutral Z . These are massive, and the W bosons carry an electric charge.

The fermions are divided into the categories of *quarks* and *leptons*, with 6 of each type (as well as associated *anti-particles*). They are arranged into three *generations*, with increasing mass. The quarks, the up and down flavours of which are familiar in everyday life as the constituents of atomic nuclei, are characterised by having *colour charge*, the quantum number associated with the strong interaction. They participate in all interactions, having both weak and electric charges in addition. In each generation there is one *up*-type quark with charge $+\frac{2}{3}$ and one *down*-type with charge $-\frac{1}{3}$, forming an isospin doublet (see Section 2.2). The up-type quarks are the up (u), charm (c) and top (t) quarks, and the down-type are the down (d), strange (s) and bottom (b) in generational order. All leptons have weak charges, however they are further divided into two groups: the *charged leptons*, which have electric charge, and the massless *neutrinos*, which do not. Charged leptons and neutrinos also form weak isospin doublets in each generation. The charged leptons are the electron (e), muon (μ) and tau (τ), with the neutrino in each generation named for these.

The final particle to complete the SM is the Higgs boson - the only *scalar boson*, having spin 0, while the others are *vector bosons*, with spin 1. The Higgs field is responsible for particle masses, via coupling to particles following *spontaneous symmetry breaking* of the electroweak interaction. Figure 2.1 summarises the particle content of the SM.

Gauge theory

Any quantum field theory can be described by a *Lagrangian density*¹, which prescribes its equations of motion. This Lagrangian must reflect the underlying *symmetries* of the system, which by Noether's theorem also correspond to conserved quantities. Gauge theories are core to the SM, originating in the theory of *quantum electrodynamics* (QED), and extended by Yang and Mills [17]. They are field theories which are invariant under gauge transformations, the symmetries of which can be described by *symmetry groups*. Of relevance for particle physics are the special unitary groups $SU(2)$ and $SU(3)$, and the unitary group $U(1)$.

The QFT Lagrangian for a free spin- $\frac{1}{2}$ particle (fermion) is:

$$\mathcal{L} = \bar{\Psi}(i\not{\partial} - m)\Psi \quad (2.1)$$

where $\not{\partial}$ denotes $\gamma^\mu \partial_\mu$, Ψ is a bi-spinor, m is a mass term and γ^μ are the four *gamma matrices*. Now it is imposed that \mathcal{L} remains gauge invariant under the transformation $\Psi \rightarrow U\Psi$, with U a member of the symmetry group being considered, which is a *Lie group*. The group is defined by a set of *generators* T^a , satisfying the relation $[T_a, T_b] = T_a T_b - T_b T_a = if_{abc} T_c$. The terms f_{abc} are anti-symmetric, and called the *structure*

¹Shortened hereafter to Lagrangian

2.1. Overview of the Standard Model

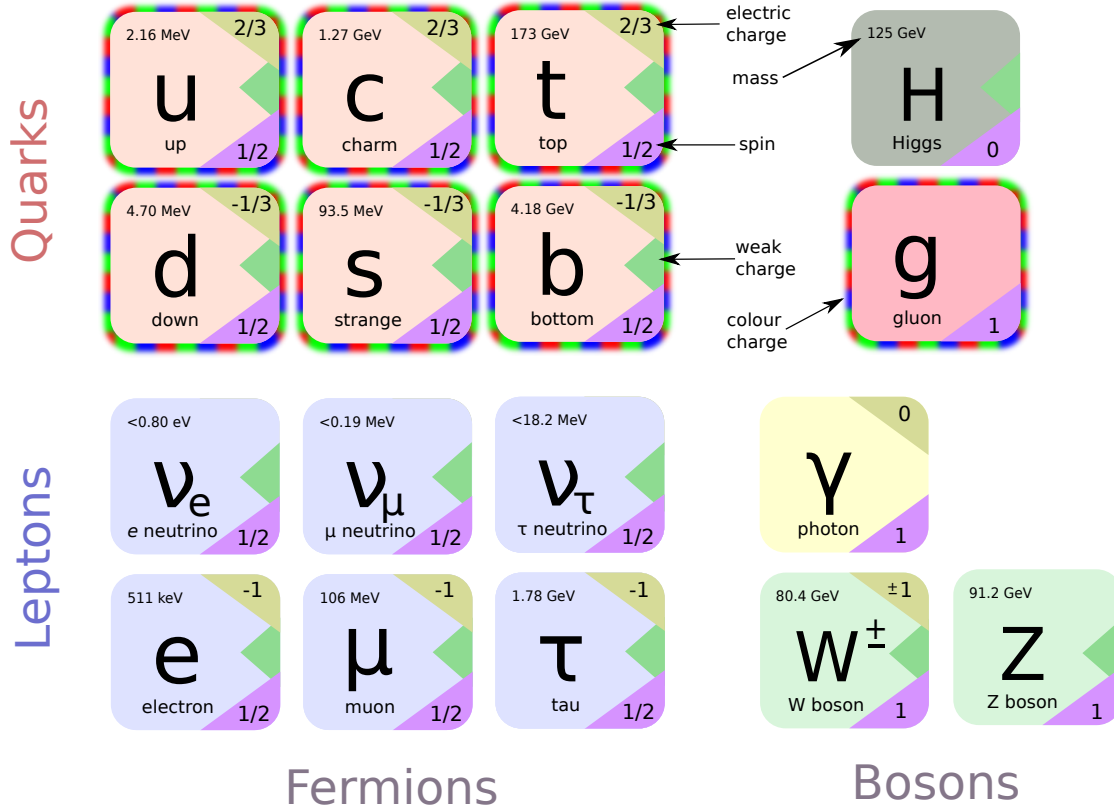


Figure 2.1.: Depiction of the particles in the Standard Model and selected properties. Each of the fermions additionally has an anti-particle partner with opposite charge, and the W^+ and W^- bosons are shown together. Coloured additions indicate which interactions particles participate in: yellow for the electromagnetic interaction, green for the weak interaction, and a multi-coloured border for the strong interaction. Masses are taken from Ref. [16], and are not necessarily given to full known precision.

2. Standard Model

constants. For an Abelian group like $U(1)$ these structure constants are evidently zero. The Lagrangian can be modified in the following way to maintain gauge invariance:

$$\mathcal{L}_{YM} = \bar{\Psi}(i\mathcal{D} - m)\Psi - \frac{1}{4}F_{\mu\nu}^a F^{a\mu\nu} \quad (2.2)$$

where the covariant derivative has been replaced $\mathcal{D} \rightarrow \mathcal{D}$ and the new term \mathcal{L}_{gauge} in $F_{\mu\nu}$ is introduced with definitions:

$$\begin{aligned} D_\mu &= \partial_\mu + igA_\mu^a T_a \\ F_{\mu\nu}^a &= \partial_\mu A_\nu^a - \partial_\nu A_\mu^a - gf^{abc} A_\mu^b A_\nu^c \end{aligned} \quad (2.3)$$

A new set of fields A_μ^a has been introduced - the same number as the number of generators of the underlying symmetry group. Physically, these describe the bosons for the given interaction. g is termed the *coupling constant*. The new F^2 term in the Lagrangian contains third- and fourth-power terms in these fields, corresponding to self-interactions of the field. However given that the structure constants are all 0 for an Abelian group like $U(1)$, no self-interaction is present for them. This has the consequence that for the $U(1)$ electromagnetic interaction, photons do not directly couple to each other.

The gauge theories used to build the SM also have the property of *renormalisability* [7, 8]. This will be discussed again in Section 2.3.

2.2. Electroweak interaction and symmetry breaking

Historically, the electromagnetic and weak interactions were physically modelled separately, described by quantum electrodynamics and flavourdynamics respectively. Glashow, Weinberg and Salam developed an *electroweak* theory combining these [3–5]. This used both the groups underlying the existing theories, resulting in a $SU(2) \otimes U(1)$ symmetry group. As per the discussion above, this results in a total of four new gauge fields: $W_\mu^{i=1,2,3}$ for $SU(2)$, and B_μ associated with $U(1)$, with associated quantities termed the *weak isospin*, $I^{i=1,2,3}$, and *weak hypercharge*, Y_W . Naively one would associate these directly with the three weak bosons W^\pm and Z , and the photon respectively. However as shown below this is not the case.

One key experimental observation preceding this theoretical leap was that the weak interaction is *parity violating* [18], and it is in fact maximally parity violating. Following conventional notation, this means that *left-handed* chiral components ψ_L act as doublets in $SU(2)$, while the right-handed components ψ_R are singlets. The doublets, known as *weak isospin doublets* are:

$$\begin{pmatrix} u_L \\ d'_L \end{pmatrix}, \begin{pmatrix} c_L \\ s'_L \end{pmatrix}, \begin{pmatrix} t_L \\ b'_L \end{pmatrix}, \begin{pmatrix} \nu_{e,L} \\ e_L \end{pmatrix}, \begin{pmatrix} \nu_{\mu,L} \\ \mu_L \end{pmatrix}, \begin{pmatrix} \nu_{\tau,L} \\ \tau_L \end{pmatrix} \quad (2.4)$$

2.2. Electroweak interaction and symmetry breaking

defined by the eigenvalue of the third component of weak isospin $I^3 = \begin{pmatrix} +\frac{1}{2} \\ -\frac{1}{2} \end{pmatrix}$. Additionally considering the right-handed singlets, it is notable that in the SM right-handed neutrinos do not exist.

The dashes on the down-type quarks are indicative of the fact that these are the weak eigenstates, and are a linear combination of the down-type quark mass eigenstates. This mixture is described by the Cabibbo–Kobayashi–Maskawa (CKM) matrix [19, 20]:

$$\begin{pmatrix} d' \\ s' \\ b' \end{pmatrix} = \begin{pmatrix} V_{ud} & V_{us} & V_{ub} \\ V_{cd} & V_{cs} & V_{cb} \\ V_{td} & V_{ts} & V_{tb} \end{pmatrix} \begin{pmatrix} d \\ s \\ b \end{pmatrix} \quad (2.5)$$

The diagonal elements of this matrix are experimentally determined to be the largest, with magnitudes close to 1.

Using the above fields in the previously described gauge-theoretical lens yields a co-variant derivative:

$$D_\mu = \partial_\mu + i\frac{g}{2}\sigma^i W_\mu^i + i\frac{g'}{2}B_\mu \quad (2.6)$$

with σ_i the Pauli matrices, the generators of the $SU(2)$ symmetry group, and terms of $\frac{1}{2}$ introduced by convention.

Considering the new corresponding Lagrangian for (as an example) the lepton field $(\nu_{e,L})$ and multiplying out the Pauli matrices yields terms in W^1 and W^2 of the form:

$$\bar{e}_L(W^1 + iW^2)\nu_{e,L} \quad \bar{\nu}_{e,L}(W^1 - iW^2)e_L \quad (2.7)$$

so the flavour-changing field can be more neatly rewritten:

$$W^\pm = \frac{1}{\sqrt{2}}(W^1 \mp iW^2) \quad (2.8)$$

corresponding to the previously-seen W bosons.

If the B_μ field is to describe electromagnetism, there is an issue whereby it would interact with the uncharged neutrinos. This can be resolved by making the remaining weak gauge field Z_μ and the electromagnetic field A_μ an orthogonal combination of W_μ^3 and B_μ :

$$\begin{aligned} Z_\mu &= -B_\mu \sin(\theta_W) + W_\mu^3 \cos(\theta_W) \\ A_\mu &= B_\mu \cos(\theta_W) + W_\mu^3 \sin(\theta_W) \end{aligned} \quad (2.9)$$

In keeping with this, the electric charge must be expressed in terms of I^3 and Y_W , written in the form $Q = I^3 + \frac{Y_W}{2}$. The QED coupling strength e can also be expressed in terms of the previously defined coupling constants as $e = g \sin(\theta_W) = g' \cos(\theta_W)$. θ_W is termed the *weak mixing angle*². This mixing allows the fact that while W bosons couple solely to left-handed fermions, the Z boson couples to left and right handed bosons, albeit not equally.

²Also known as the *Weinberg angle*.

2. Standard Model

Brout–Englert–Higgs mechanism

One aspect that has been left unaddressed in the preceding description is how particles gain mass in the SM. This was resolved by the theoretical framework put forward by Brout, Englert and Higgs among others³ [14, 15]. This adds an additional $SU(2)$ complex doublet $\phi = \begin{pmatrix} \phi_1 + i\phi_2 \\ \phi_1 - i\phi_2 \end{pmatrix}$ with an associated potential $V(\phi)$ as shown in its associated Lagrangian:

$$\mathcal{L}_{\text{Higgs field}} = (D_\mu \phi)^\dagger (D^\mu \phi) - V(\phi) = (D_\mu \phi)(D^\mu \phi)^* - (-\mu^2 \phi^\dagger \phi + \lambda(\phi^\dagger \phi)^2) \quad \mu^2 > 0 \quad (2.10)$$

If the condition for μ is met the potential no longer has a minimum at 0, but an infinite number of minima at $\phi^\dagger \phi = \frac{v^2}{2}$, where v is termed the *vacuum expectation value*. The choice can then be arbitrarily made, given the resulting freedom to choose a gauge, thus rewriting the field in the form:

$$\phi = \frac{1}{\sqrt{2}} \begin{pmatrix} 0 \\ v + h(x) \end{pmatrix} \quad (2.11)$$

where h is the physical Higgs field. This choice is known as the *unitary gauge*, and ultimately these degrees of freedom correspond to the longitudinal degrees of freedom of the W and Z bosons. Expanding the covariant derivative and considering the previously defined W^\pm and Z field definitions, it can be seen that *mass* (quadratic in the field) terms appear, dependent on the coupling constants and v :

$$\begin{aligned} M_W &= \frac{gv}{2} \\ M_Z &= \frac{gv}{2 \cos(\theta_W)} \end{aligned} \quad (2.12)$$

As well as the mass of the Higgs boson itself:

$$M_H = \sqrt{2\lambda}v \quad (2.13)$$

Only the W and Z bosons gain mass through this symmetry breaking - the photon remains massless.

To explain the fermion masses requires postulating the *Yukawa coupling* terms of the Lagrangian, of form $\bar{\psi}\phi\psi$. This acts on up and down-type fermions, coupling states of opposite helicity. Each fermion f has a coupling strength y_f , and in the unitary gauge the vacuum expectation term yields quadratics in the fermion fields, with masses:

$$m_f = \frac{y_f v}{\sqrt{2}} \quad (2.14)$$

³Higgs himself reportedly suggested the hyper-inclusive name of ‘ABEGHHK’tH mechanism’.

Additional terms in h describe couplings between the Higgs boson and the fermions, as well as trilinear and quartic self-interaction terms.

The discovery of the Higgs boson at the LHC in 2012 [21, 22] confirmed the existence of a Higgs mechanism and completed the observations of the particles of the SM. Brout, Englert and Higgs were subsequently awarded the Nobel Prize for Physics.

2.3. Quantum chromodynamics

Quantum chromodynamics is the theory of the strong interaction - its name coming from the *colour charge* carried by the quarks and gluons which participate. This name is chosen to analogise real-life colour theory, with the three colours red, green and blue (r, g, b) combining to make a colourless state [10–13]. It is a gauge theory with $SU(3)$ symmetry, with eight generators $\frac{1}{2}\lambda_c$, with $\lambda_{c=1,2,3\dots 8}$ the 3×3 Gell-Mann matrices as the canonical representation. This means there are a total of eight gluons, the gauge bosons of the strong interaction, each carrying colour⁴. They are massless, have spin 1, and couple to each other. The QCD Lagrangian can be written, with gauge covariant derivative expanded and without fermion mass terms, as:

$$\mathcal{L}_{\text{QCD}} = \sum_q i\bar{\psi}_{q,a}\not{D}\psi_{q,a} - g_s\bar{\psi}_{q,a}\gamma^\mu(\lambda_c)_{ab}G_\mu^c\psi_{q,b} - \frac{1}{4}G_{\mu\nu}^c G^{c\mu\nu} \quad (2.15)$$

where sums are implied over $a, b = 1, 2, 3$ for the three colours in quarks, and $c = 1, 2, 3\dots 8$ for the gluon fields and corresponding Gell-Mann matrices. q runs over all quark flavours. $G_{\mu\nu}^c$ is defined:

$$G_{\mu\nu}^c = \partial_\mu G_\nu^c - \partial_\nu G_\mu^c - g_s f^{cde} G_\mu^d G_\nu^e \quad (2.16)$$

One can see from the Lagrangian all possible strong interaction vertices: $q\bar{q}g$, ggg and $gggg$. Rather than g_s , the coupling strength $\alpha_s = \frac{g_s^2}{4\pi}$ is usually used to describe the effect of the strong interaction.

Non-physical infinite predictions arise when this theory is applied straightforwardly, considering loop effects and self-interactions - hence *renormalisation* must be used to be able to make perturbative calculations. This requires the choice of a *renormalisation scale* μ_R , normally chosen to be close to the energy scale of the interaction being considered. Furthermore the value of α_s depends on the momentum transfer Q^2 , which can also be thought of as the energy scale involved. Expanding perturbatively, the dependence on μ_R is to leading order (corresponding to considering one-loop effects):

$$\mu_R^2 \frac{\partial \alpha_s(\mu_R^2)}{\partial \mu_R^2} = -\frac{11n_C - 2n_f}{12\pi} \alpha_s^2 + O(\alpha_s^3) \quad (2.17)$$

where $n_{c/f}$ is the number of colours and flavours of quarks, respectively. While naturally $n_c = 3$, the number of flavours depends on the energy scale, where the formalism

⁴There is no colourless gluon state due to the $SU(3)$ group structure. If the strong interaction were based on $U(3)$ this would exist, and would in many ways behave like a photon.

2. Standard Model

used is valid only for quarks with masses $m_q \ll \mu_R$. With such assumptions, α_S can be written:

$$\alpha_S(Q^2) = \frac{\alpha_S(\mu_R^2)}{1 + \left(\frac{11n_c - 2n_f}{12\pi}\right)\alpha_S(\mu_R^2)\ln\left(\frac{Q^2}{\mu_R^2}\right)} \quad (2.18)$$

showing that for increasing Q^2 , $\alpha_S \rightarrow 0$. This property is known as *asymptotic freedom* [23, 24]. The changing value of α_S is termed *running*, with the decreasing value at higher energies meaning that at this scale, which is prevalent at the LHC, perturbative calculations can be performed. Numerous measurements have been made of the running of α_S , as depicted in Figure 2.2. α_S can also be expressed in terms of Λ_{QCD} , the *QCD scale*, which is the energy scale where the perturbative approach breaks down entirely.

The rapid growth of α_S at low energies hints towards a key property of the QCD sector: *confinement*, whereby single quarks or gluons do not exist as unbound stable particles, but must combine to form colourless states: the *hadrons*. These may take the form of mesons ($q\bar{q}$), baryons such as the proton and neutron ($qqq/\bar{q}\bar{q}\bar{q}$), or even rare states such as tetraquarks [25, 26] and pentaquarks [27]. This phenomenon is often modelled with a potential that grows linearly. It has also been shown in models of lattice QCD, which provides a way to perform QCD modelling at low energy scales [28].

QED features a similar running of the coupling $\alpha = \frac{e^2}{4\pi} \approx \frac{1}{137}$. Due to lack of photon self-interaction, this actually increases with increasing energy scale.

2.3.1. QCD at the LHC

The LHC does not collide elementary particles, but rather protons: hadrons with nominal quark composition of uud . These are the *valence quarks*. However these are not simply lone, static constituents of the proton - there are also *sea quarks* (and anti-quarks) and gluons being produced, interacting and annihilating in numbers which diverge at lower energies $Q^2 \ll \Lambda_{QCD}$. When protons collide, it may be any of the range of constituents which undergoes the *hard interaction*, carrying a fraction, x , of the proton's total momentum. The constituents are known as *partons*. This superficially simple description of a complex system assumes that the probability of finding a particular flavour of parton at a particular momentum fraction is independent of the subsequent interaction process. These probabilities are called *parton distribution functions* (PDFs), written in the form $f_{a,h}(x, \mu_F^2)$ for parton a in hadron h . The *factorisation scale*, μ_F sets the energy scale separating the long-distance interactions inside the hadron from the high-energy hard interaction which can once more be described perturbatively. The relation to μ_F is described by the Dokshitzer–Gribov–Lipatov–Altarelli–Parisi (DGLAP) evolution equations [44–46].

PDFs are key to the *factorisation theorem* [47] for cross-sections in proton-proton collisions, here for a process $p + p \rightarrow X$ for a given final state X (not necessarily a single

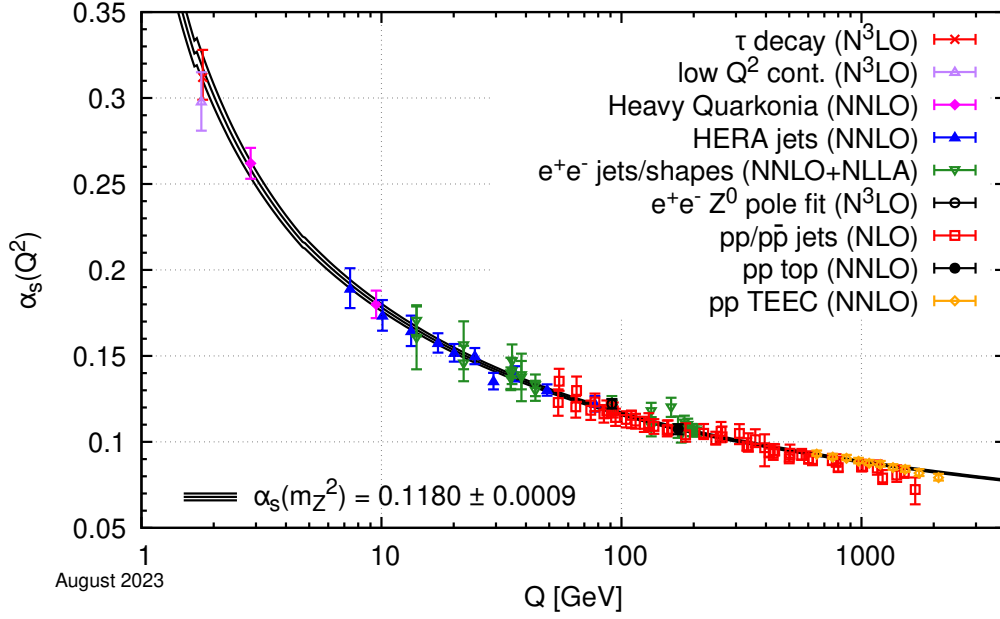


Figure 2.2.: Summary plot of different measurements of α_s , compared to a theoretical prediction computed at the five-loop level, taking as input the world average value for $\alpha_s(m_Z^2)$. Taken from Ref. [16], with data from Refs. [29–43].

particle):

$$\sigma_{p+p \rightarrow X} = \sum_{a,b} \int_0^1 dx_a \int_0^1 dx_b f_{a,p}(x_a, \mu_F^2) f_{b,p}(x_b, \mu_F^2) \hat{\sigma}_{a+b \rightarrow X}(\hat{s}, \mu_F^2, \mu_R^2) \quad (2.19)$$

with a, b running over all possible partons and $\hat{\sigma}$ the *parton-level cross-section*, which can be calculated using perturbative QCD. This is the ‘factorisation’ - separating the non-perturbative regime described by PDFs from the hard-scattering cross-section. \hat{s} is the effective squared centre-of-mass energy for the partons, related to the overall proton-proton centre of mass energy s by $\hat{s} = x_a x_b s$. $\hat{\sigma}$ naturally depends on \hat{s} , as well as the chosen scales and the particular final state X .

The determination of PDFs is a complex task, relying on a wide range of data from several collider experiments. This is combined with calculations such as using the DGLAP equations to extrapolate to new energy scales, and has been performed by groups including ABM [48], CTEQ [49], MSTW [50] and NNPDF [51].

Another consequence of the proton’s extended nature is *multi-parton interaction* (MPI). This describes the phenomenon where at least one additional parton from each proton interacts, contributing additional scatterings to the overall collision final state. Most of these additional interactions are at low energy, however that may also occur at large transverse momentum. Like many complex QCD effects this cannot be modelled rigor-

2. Standard Model

ously from first principles, but through a combination of phenomenology and theoretical considerations [52].

2.3.2. b/c jets

As previously stated, all coloured objects are subject to confinement, meaning that when produced all quarks (with the notable exception of the top quark, see Section 2.4) will undergo hadronisation. The resultant collimated spray of mesons and baryons is termed a *jet*. However the relatively large mass of b and c quarks mean that the b/c -hadrons they form are able to undergo weak decay, producing a wide range of possible final states including leptons and other hadrons, depending on the hadron initially formed. Crucially, these hadrons have sufficient lifetime to fly macroscopic distances before decay. As one example, the B^\pm mesons, with a quark content of $u\bar{b}/\bar{u}b$, have a mean lifetime of $\tau_{B^\pm} = 1.6$ ps [16], meaning the distance travelled $l = \beta\gamma c\tau_{B^\pm}$ may be on the order of several millimetres at the LHC. In the case of b -hadrons, it is also possible to decay to states containing c quarks. Typical lifetimes for c -hadrons are shorter, but have a similar displaced decay. This decay separated from the primary interaction point produces a *secondary vertex*, which can be experimentally reconstructed. Furthermore the subsequent fragmentation behaviour of b/c -hadrons have distinctive topologies, typically producing clusters within the jet. These behaviours enable *heavy flavour tagging*: the identification of jets originating from b and c hadrons [53]. This technique is of particular importance to the measurement in this thesis, and its experimental details are discussed in more detail in Section 5.4.

2.4. The top quark

The existence of the top quark was first postulated by Kobayashi and Maskawa in 1973, with the CKM mechanism [19], with its name credited to Harari [54]. A third generation of quarks provided a way to account for observed CP violation in the decay of neutral K mesons [55]. This theory was lent support by the discovery of the τ lepton in 1975 [56], with the b quark joining the observed third generation of fermions in 1977 [57].

It took until 1995, following many developments in accelerator and detector technology, for the top quark itself to be observed at the TEVATRON collider by the CDF [58] and DØ [59] collaborations. This completed the quark sector in the SM.

The most striking property of the top quark is its mass, with a current world average of 172.57 ± 0.29 GeV⁵ [16], coming from electroweak precision measurements and a combination of direct measurements made at the LHC [60]. It is thus the most massive particle in the SM. The Yukawa coupling of the top quark and Higgs is order unity, with the values of these particles' masses being key to understanding electroweak symmetry breaking. One question of note is *vacuum stability* [61, 62], determining the nature of the minima of the Higgs potential. The top quark mass is a principal uncertainty in determining whether the current vacuum is only a local minimum, and in a meta-stable

⁵This figure is specifically the 'pole mass'

state. Its Yukawa coupling and large mass also mean that, through loop corrections, the top quark is an important parameter in electroweak measurements, such as that of the mass of the W boson. Therefore measurements of its properties are an important way to test the consistency of the SM.

Like all up-type quarks, the top quark has a charge of $+\frac{2}{3}$ and a predicted, but unmeasured, third component of weak isospin $+\frac{1}{2}$. Another characteristic property is its lifetime τ_t (equivalent to the decay width Γ_t), which is discussed in more detail in Section 2.4.2.

2.4.1. Top quark production

Top quark pair production

The LHC performs pp collisions at a high centre-of-mass energy: $\sqrt{s} = 13$ TeV for the data used in this analysis (see Chapter 3 for more detail). This produces a large number of top quarks, such that the LHC has been called a ‘top factory’. Top quark production mainly occurs in $t\bar{t}$ pairs, modelled as either gluon-gluon fusion or quark-anti-quark annihilation, both via the strong interaction. Leading-order Feynman diagrams for these are shown in Figure 2.3. At the TEVATRON, a proton-anti-proton collider, quark-anti-quark annihilation was the dominant production mechanism. This was due to having both valence quarks and anti-quarks in the collision, and due to the fact that the (compared to the LHC) relatively low centre-of-mass energy of $\sqrt{s} = 1.96$ TeV meant a high momentum fraction x was necessitated in each parton to reach the threshold production energy. However at the LHC (at $\sqrt{s} = 13$ TeV) gluon-gluon fusion is responsible for about 90% of $t\bar{t}$ production, due to the higher density of gluons with sufficient energy. Figure 2.4 compares measurements of the top quark production cross-section from the TEVATRON and LHC with theory predictions at NNLO in QCD, with NNLL resummation of soft gluons and an assumed top quark mass of 172.5 GeV. For the LHC at $\sqrt{s} = 13$ TeV this yields a prediction of $\sigma_{t\bar{t}} = 833.9^{+20.5+21.0}_{-30.0-21.0}$ pb, with the first uncertainty due to scale dependence and the second from parton distribution functions and α_S [63]. The predictions show good agreement across the whole range of centre-of-mass energies, and for both collider types.

Single top production

The other way top quarks can be made is singly, known as *single top* production. This occurs via the weak interaction, specifically through the exchange or decay of a W boson in association with a b quark. Leading order Feynman diagrams for this are shown in Figure 2.5, consisting of t -channel and s -channel W boson exchange, as well as the production with a W boson in the final state, termed tW production. When discussing uncertainties in theoretical predictions for single top cross-sections in the following, the first uncertainty is from scale dependence and the second (if given) is from parton distribution functions and α_S . All of the values given are for the LHC at $\sqrt{s} = 13$ TeV. NNLO predictions for the t -channel production cross section yield a value

2. Standard Model

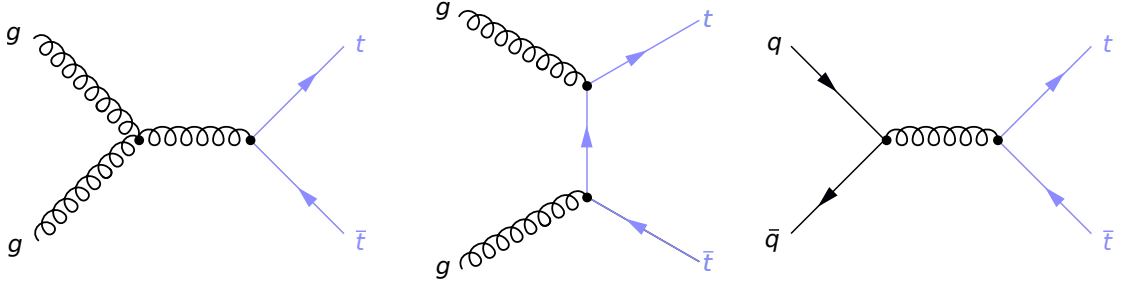


Figure 2.3.: Leading order Feynman diagrams for production of top quark-anti-top quark pairs, shown in blue. Left: s -channel gluon-gluon fusion. Centre: t -channel gluon-gluon fusion (u -channel production is also possible). Right: quark-anti-quark annihilation.

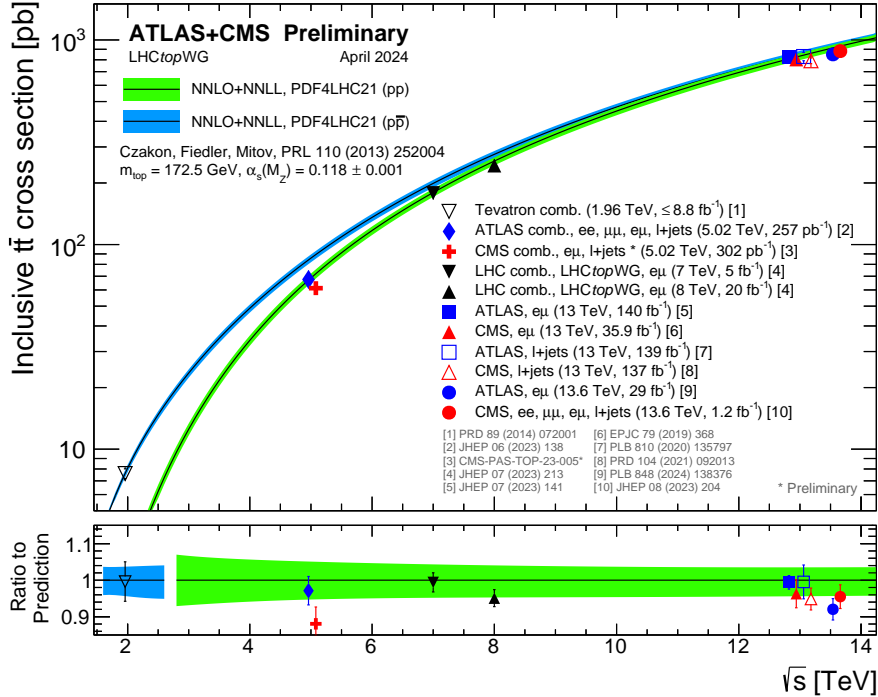


Figure 2.4.: Summary of measurements of the top quark pair production cross-section at a range of centre-of-mass energies \sqrt{s} at the TEVATRON and LHC colliders [64–73]. They are compared to NNLO QCD theoretical predictions with NNLL resummation for pp and $p\bar{p}$ colliders [63]. Figure is taken from Ref. [74].

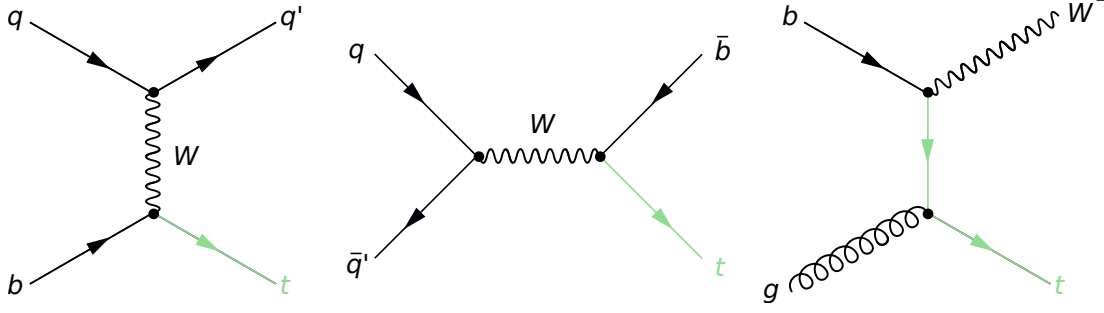


Figure 2.5.: Representative leading order Feynman diagrams for production of single top quarks, shown in green. Left: t -channel production. Centre: s -channel production. Right: Wt production.

of $\sigma_{t, t\text{-channel}} = 214.2^{+2.4+3.3}_{-1.7-2.0}$ pb [75, 76]. There is also a predicted asymmetry between top and anti-top production due to the underlying matter-anti-matter imbalance in the colliding protons, with top quarks expected to make up around 63%. Approximated NNLO calculations for s -channel productions predict $\sigma_{t, s\text{-channel}} = 6.84^{+0.06}_{-0.03}$ pb [77], while for Wt associated production NNLO + NLL predictions yield $\sigma_{t, Wt} = 79.3^{+1.9+2.2}_{-1.8-2.2}$ pb [78]. These values are significantly less than those for $t\bar{t}$ pair production, and the final states produced are not as easily separated from similar backgrounds.

Wt production poses a challenge for studies, as at NLO there is interference between some of its associated diagrams and those for $t\bar{t}$ production [79]. Thus strictly speaking this process cannot be calculated truly separately. Strategies used to mitigate this are discussed in Section 8.3.2 in the context of systematic uncertainties.

2.4.2. Top quark decay

The top quark has decay characteristics unlike any quark. Its large mass means that it is able to decay via an on-shell W boson, greatly increasing its rate of weak decay compared to lighter quarks. Furthermore the fact that the CKM matrix element $|V_{tb}|$ is close to unity [80], and much larger than $|V_{ts}|$ and $|V_{td}|$, means that it decays almost exclusively by $t \rightarrow W^+ b$ (and the equivalent for \bar{t}). The theoretical decay width of the top quark has been calculated up to NNLO in perturbative QCD as $\Gamma_t = 1.331$ GeV at $m_t = 172.69$ GeV, with an uncertainty of below 1% [81]. Experimentally, CMS performed an indirect measurement of Γ_t by combining measurements of the ratio $R = \frac{\mathcal{B}(t \rightarrow Wb)}{\mathcal{B}(t \rightarrow Wq)}$, where \mathcal{B} is a branching ratio and q may be any down-type quark, with a measurement of the partial decay width $\Gamma(t \rightarrow Wb)$ from t -channel single top production, yielding a value of $\Gamma_t = 1.36 \pm 0.02(\text{stat.})^{+0.14}_{-0.11}(\text{syst})$ GeV [82, 83].

This corresponds to an average lifetime of $\tau_t \approx 5 \times 10^{-25}$ s, which is shorter than the typical time-scale of hadronisation: $O(\Lambda_{QCD}^{-1}) \approx 10^{-23}$ s. This means it decays before t -containing hadrons or stable $t\bar{t}$ toponium bound states can form [84]. However, CMS

2. Standard Model

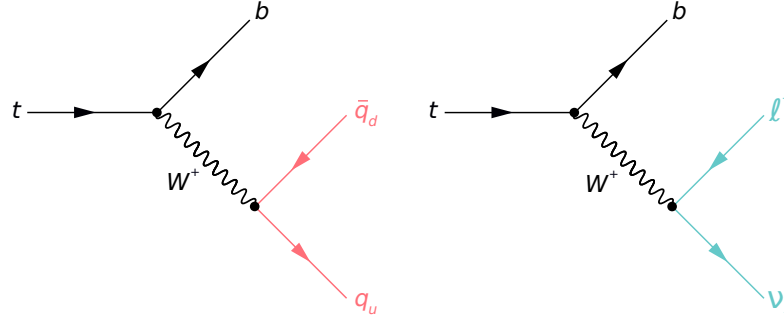


Figure 2.6.: Feynman diagrams illustrating the two decay modes for a W produced from top decay. Left: hadronic decay to a quark and anti-quark, one up-type and one down-type (red). Right: leptonic decay producing a charged lepton and neutrino (green).

has recently seen evidence of a pseudo-bound state η_t near the $t\bar{t}$ production threshold with cross-section $\sigma_{\eta_t} = 7.1 \pm 0.8$ [85]. This agrees with non-relativistic QCD predictions. Nevertheless, the top quark thus uniquely allows the study of what is effectively a free, or *bare* quark. Consequently the spin properties of the top quarks are passed onto their decay products approximately undisturbed, recently enabling the first ever observation of quantum entanglement in quarks, made first by ATLAS [86], then CMS [87].

The W produced may decay in two ways: either *hadronically*, producing a quark and anti-quark from the same isospin doublet which will then produce jets of hadrons; or *leptonically*, producing a charged lepton and its corresponding neutrino. Diagrams for these modes are shown in Figure 2.6. Considering the decay of top quark pairs, this produces a total of three decay channels, describing the products which are produced alongside two b quarks:

- The *all-hadronic* channel ($\sim 45.7\%$), where both W bosons decay hadronically. This decay has the largest branching fraction, but the decay products, consisting only of jets, are relatively difficult to distinguish from a large range of other processes and QCD background. Additionally, jets are more difficult to accurately reconstruct in detectors than the charged leptons seen in the other decay channels.
- The *dileptonic* (2ℓ) channel ($\sim 10.5\%$), in which both W bosons decay leptonically, producing a total of two charged leptons and two neutrinos, one of each being an anti-particle. The charged leptons provide a clear event signature, particularly in the case where one is an electron and one is a muon, having few background processes with which it can be confused. Precise reconstruction is aided by having only two jets, and electrons and muons can be measured relatively well in detectors. However, the two neutrinos, neither of which interact measurably with detectors, leave only a signature of missing energy/momentum. This leaves the overall kinematics of the system underconstrained, though techniques have been

2.5. Top quarks in association with heavy flavour quarks

developed to address this problem [88–91]. In the past analyses were also limited by poor statistical uncertainties when using this channel given the small branching fraction.

- The *lepton + jets* (1ℓ) channel ($\sim 43.8\%$) features one hadronic and one leptonic W boson decay. Historically this was the most useful channel for analysis, as it combined large numbers of events with improved reconstruction and background rates due to the presence of the lepton. Furthermore having only one neutrino means that (at least in principle) its transverse kinematics can be calculated simply by considering momentum conservation.

In leptonic decays, any τ leptons themselves decay before they are detected, with a lifetime of 2.9×10^{-17} s and with a branching fraction to hadrons of 64.79%, otherwise decaying to an electron or muon alongside neutrinos [16]. Thus in analyses such as the one presented here, when considering ‘leptons’ in final states, unless otherwise specified this will hereafter refer to electrons and muons alone, which may in some cases come from τ decays.

2.5. Top quarks in association with heavy flavour quarks

A feature of QCD calculations, as shown earlier in this chapter, is that when performing perturbative calculations it is necessary to define a renormalisation scale μ_R and factorisation scale μ_F . While there are conventions for this, picking values close to the energy scale of the process being examined, ultimately there is no exact prescription and the choice of scale remains a significant source of uncertainty in many QCD predictions. This becomes a particular challenge when attempting to model the production of so-called *heavy flavour* (HF) quarks⁶ in association with $t\bar{t}$ pair production. Due to the significant mass differences between the top and HF quarks, their production occurs at very different energy scales. This is particularly true as the HF quarks are predicted to be mainly produced via gluon splitting: eg. $g \rightarrow b\bar{b}$ [92], and there is no longer a natural single choice for μ_R and μ_F . Thus the measurement of this process provides a test for multi-scale QCD modelling.

Of the HF production modes, the one with bottom quarks ($t\bar{t}b\bar{b}$)⁷ has received more attention from the experimental particle physics community, with several studies performed modelling it at next-to-leading-order in QCD matched to parton showering algorithms (NLOPS) [92–96]. Furthermore numerous dedicated measurements have been made of the $t\bar{t}b\bar{b}$ production cross-section in different $t\bar{t}$ decay channels at the LHC, at $\sqrt{s} = 7$ TeV [97], $\sqrt{s} = 8$ TeV [98–100] and $\sqrt{s} = 13$ TeV [101–103]. Comparisons between experiment and theory at $\sqrt{s} = 13$ TeV show that modelling predictions consistently under-estimate the measured cross-section values, but still agree at the level

⁶This term is used hereafter to refer to only b and c quarks, excluding the top quark.

⁷Here the terminology $t\bar{t}b\bar{b}$ and $t\bar{t}c\bar{c}$ is used to describe these processes, in keeping with common terminology. However when discussing events used for analysis, the more precise form $t\bar{t} + 1b$, $t\bar{t} + \geq 2c$ etc will be used.

2. Standard Model

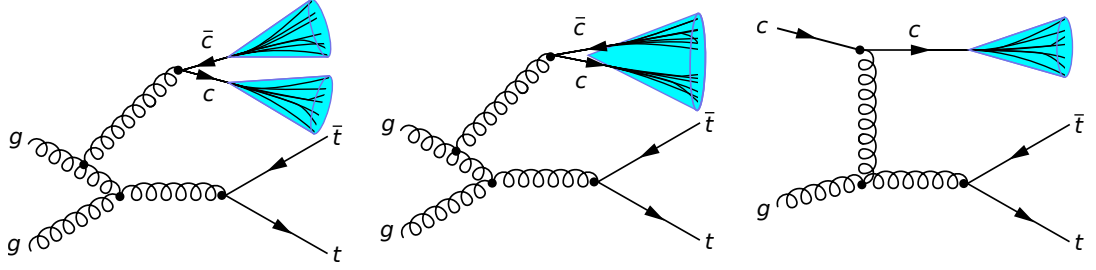


Figure 2.7.: Illustrative Feynman diagrams for the production of c quarks alongside $t\bar{t}$. Left: $c\bar{c}$ pair produced by splitting of a gluon radiated from the initial state, producing two separate jets. Centre: The same process, but with the $c\bar{c}$ pair forming a single jet. Right: Production of a single c quark from the initial state.

of one to two standard deviations. This highlights the previously discussed modelling challenges.

The equivalent process with c quarks, $t\bar{t}c\bar{c}$, meanwhile, has received less attention, providing motivation to perform the measurement in the analysis presented here. The only dedicated measurement of its cross-section prior to this analysis was performed by CMS [104] at $\sqrt{s} = 13$ TeV in dileptonic $t\bar{t}$ decays. Its results and methods are discussed in more detail below.

Similar to b quarks, c quarks are expected to be mainly produced through strong interactions via emission of a gluon which splits into a $c\bar{c}$ pair. The gluon may be emitted by any of the particles in the initial or final state (which participate in the strong interaction). The jets produced following hadronisation may be reconstructed separately, producing two c -jets. However they may also be sufficiently collinear so as to be reconstructed as a single jet, termed a C -jet. For the remainder of this analysis, no distinction is made between c - and C -jets. It is also possible for a single c quark to be present in the initial state from the sea quarks of the proton. These modes are exemplified in Figure 2.7.

A secondary motivation for measuring this process is its status as a major background to measurements of other, rarer processes. These include $t\bar{t}H(H \rightarrow b\bar{b})$, where a top quark pair is produced alongside a Higgs boson which decays to $b\bar{b}$, and the production of four top quarks: $t\bar{t}t\bar{t}$. In fact $t\bar{t}c\bar{c}$, as well as $t\bar{t}b\bar{b}$, are *irreducible* backgrounds to these, which both have final states with $t\bar{t}$ decay products and additional jets. Therefore better measurement and understanding of $t\bar{t}c\bar{c}$ has the potential to improve the precision of such measurements, which are sensitive to parameters such as the top-Higgs Yukawa coupling, and potential new effects beyond the SM.

2.5.1. Previous measurements of top quarks in association with charm quarks

The one existing dedicated measurement of $t\bar{t}$ in association with charm quarks was published by the CMS Collaboration in 2020 [104]. It targeted dileptonic $t\bar{t}$ final states in $\sqrt{s} = 13$ TeV data with an integrated luminosity of 41.5 fb^{-1} . The principal results were cross-sections of $t\bar{t}c\bar{c}$, $t\bar{t}b\bar{b}$ and $t\bar{t}LL$, corresponding to events containing at least two additional c , b or light-flavour jets, respectively. Two phase spaces were considered: a *fiducial* phase space designed to match the acceptance of the detector, and a *full* phase space without fiducial cuts applied. In each of these phase spaces, a template fit was performed to extract either the cross-sections ($\sigma_{t\bar{t}c\bar{c}}$, $\sigma_{t\bar{t}b\bar{b}}$ and $\sigma_{t\bar{t}LL}$) directly, or the ratio of $t\bar{t}c\bar{c}$ and $t\bar{t}b\bar{b}$ events to the total number of $t\bar{t}$ + jets events ($R_{c/b} = \frac{\sigma_{t\bar{t}c\bar{c}}/\sigma_{t\bar{t}b\bar{b}}}{\sigma_{t\bar{t}} + \text{jets}}$). This gives a total of four sets of measurements which are compared to predicted values from the POWHEG BOXV2 [105–109] and MADGRAPH5_aMC@NLO v2.4.2 [110] generators simulating QCD at NLO. The values found from both measurement and prediction are given in Appendix A. The measured cross-sections and ratios for $t\bar{t}c\bar{c}$ and $t\bar{t}b\bar{b}$ exceed the predictions, but nevertheless agree within uncertainties at the level of one to two standard deviations. A more detailed discussion of the analysis methods is given in comparison to those used here in Section 7.4.

Previous measurements targeting $t\bar{t}b\bar{b}$, $t\bar{t}H(bb)$ and $t\bar{t}t\bar{t}$ have necessarily included $t\bar{t}c\bar{c}$ as a background, and have thereby often included its normalisation as a free parameter of fitting. Recent examples of this include ATLAS $t\bar{t}Hbb$ [111] and $t\bar{t}b\bar{b}$ [112] measurements at $\sqrt{s} = 13$ TeV. Their *in-situ* measurements were of events containing at least one c -jet⁸ and no b -jets, and found a value larger than that predicted in MC simulation.

2.6. Limitations of the Standard Model

Despite its remarkable success in producing accurate experimental predictions across fundamental physics, the SM as presented has been known since its inception not to be a complete description of reality.

Perhaps the most obvious example of this is gravity: quantum mechanics, the basis of the SM, is generally considered to be inconsistent with general relativity, the theory which best describes gravity and the large-scale structure of the universe. The proposal of adding a *graviton* as a gauge boson and quantising gravity in a similar manner to the other forces suffer from a lack of renormalisability [113].

Remaining in the domain of cosmology, observations of the rotations of galaxies provided the first strong evidence for the existence of *dark matter* [114]. Its exact nature remains a mystery, as it is only known to interact gravitationally, yet it is key to a wide range of astrophysical and cosmological theories and observations, currently being believed to make up 84.4% of the mass in the universe [16]. Current dark matter models agree with observations at high accuracy [115]. The SM contains no particles which are

⁸ c -jets are defined for these purposes as jets associated at the particle level with at least one c -quark and not associated with any b quarks.

2. Standard Model

suitable candidates to act as dark matter, with one of the goals of high-energy particle colliders being the observation of such a new dark matter candidate. Further questions are provoked by *dark energy*, which in current models makes up around 69% of the universe’s energy, and is also unaddressed in the SM.

There are obvious contradictions to the SM even in the domain of its particle content, in the form of neutrino masses. Observations of *neutrino oscillations* [116, 117] prove that they cannot be massless as predicted, although the values of their masses are as yet not known. Instead constraints have only been placed on the differences between them.

Another issue with the SM could be considered less concrete: the large number (19) of seemingly arbitrary free parameters without motivation. Some argue that there appear to be aspects of fine-tuning in certain parameters, for example the seemingly near-perfect cancellation between the Higgs boson bare mass and its quantum loop corrections. Even the presence of three generations of fermions is *a priori* unmotivated. Numerous alternative models have been suggested to resolve these and other issues. One of the most popular class of theories is termed *supersymmetry*, in which each SM particle has a corresponding superpartner, which may have large masses and be dark matter candidates. The most prominent supersymmetric theory is the Minimal Supersymmetric Standard Model [118].

One prominent way in which searches for new physics have been performed is using Standard Model Effective Field Theory (SMEFT) [119–121]. This provides a framework to parameterise deviations from the SM, with minimal assumptions about the nature of such deviations. In SMEFT additional terms are added to the SM Lagrangian, and the extent of deviations is parameterised in terms of *Wilson coefficients*. A number of these are highly sensitive to top quark measurements, making top quark physics potentially key to the next revolution in fundamental physics.

The Large Hadron Collider (LHC) [122] is the world’s largest and most powerful particle accelerator, as well as being considered by many to be the world’s largest machine of any kind. It is a synchrotron accelerator designed to collide protons and/or lead nuclei at high energies and collision rates. The data used for the work in this thesis was collected from pp collisions with the ATLAS detector, one of a number of experimental apparatuses which measure the products of these collisions. The structure and operation of both the LHC and ATLAS are described in this chapter, followed by an overview of the work done by the author in developing a tool for the monitoring of the ATLAS Pixel Detector.

3.1. The Large Hadron Collider

The plan for the LHC was approved in 1994, with construction lasting from 1998-2008. It is housed in the tunnel previously occupied by the LEP (**L**arge **E**lectron-**P**ositron) collider. This has a ring shape with a circumference of 27 km and is located at an average of 100 m under the ground at CERN, spanning the Franco-Swiss border beside Lake Geneva. The purpose of the LHC is to accelerate and steer bunches of charged particles (protons or lead nuclei) travelling in opposite directions around the ring. Bunches travelling in opposite directions are brought into collision at one of four *interaction points* (IPs). In the case of protons, it is designed to be able to accelerate them to each have an energy of 7 TeV, for a centre-of-mass energy of $\sqrt{s} = 14$ TeV. However the data used in the work in this thesis is collected at $\sqrt{s} = 13$ TeV from 2015 – 2018, with the energy for current operation being $\sqrt{s} = 13.6$ TeV.

The LHC is the largest of an interlinked series of accelerators: the CERN accelerator complex, a schematic of which is shown in Figure 3.1. In Run 2, the data from which is used in this thesis, hydrogen atoms had their electrons stripped to make protons, which

3. Experimental Setup

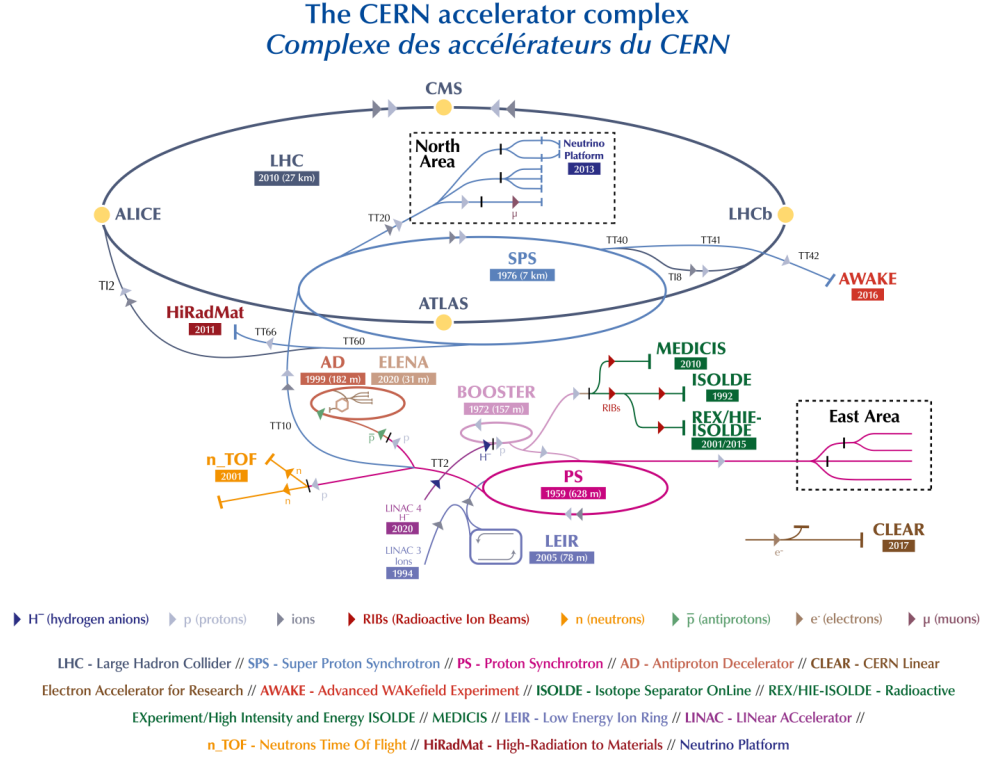


Figure 3.1.: The CERN accelerator complex, including the LHC and the pre-accelerators which feed into it. For current operation these are, in order of increasing energy: LINAC 4; the PS BOOSTER ring; the PS; the SPS, and finally the LHC itself. Additionally the four largest LHC detectors are shown at the four interaction points where the beams collide [123]. © CERN

were accelerated by the LINAC 2 linear accelerator¹ using radio-frequency (RF) cavities to an energy of 50 MeV. The Proton Synchrotron BOOSTER ring is itself made up of four synchrotron rings, raising the energy of protons to 1.4 GeV before they enter the Proton Synchrotron (PS) itself. This was CERN's first synchrotron accelerator, with a circumference of 628 m, and further accelerates protons to an energy of 26 GeV. The Super Proton Synchrotron raises this further to the energy of 450 GeV, from which they are injected into the LHC. It has a circumference of around 7 km, being the second-largest accelerator at CERN, and uses over 1317 room temperature electromagnets to bend and focus its beam.

The LHC ring has a total of eight straight sections and eight curved ones, at which the paths of particle beams are bent. This steering, as well as the focusing of beams,

¹From 2020 onwards LINAC 4 has been used instead, accelerating H^- ions.

3.1. The Large Hadron Collider

is performed by Nb-Ti superconducting magnets kept at a temperature of 1.9 K by liquid helium. The steering is done principally by 1232 dipole magnets which produce a field of ≈ 8.3 T. Additional quadrupole, sextupole and octupole magnets act to focus the counter-rotating beams. Acceleration is performed by RF cavities operating at a frequency of 400 MHz. This system utilises one klystron in each cavity to raise the energy of hadrons from the insertion energy of 450 GeV up to of 6.5 TeV. In the LHC, the ‘beam’ is in fact composed of up to 2808 *bunches* of around 10^{11} protons each. These are separated in time by 25 ns (≈ 7.5 m in space).

Several experiments are located at each of the four IPs where particle bunches collide. The four largest of these are the ATLAS (**A** Toroidal LHC Apparatu**S**) [124], CMS (Compact Muon Solenoid) [125], ALICE (**A** Large Ion Collider Experiment) [126] and LHCb (**LHC** beauty) [127] experiments. ATLAS and CMS are both general-purpose detectors with near-complete angular coverage. ALICE is specialised for the measurement of heavy-ion collisions, while LHCb covers a single arm, and is specialised to investigate the physics of the b quark via the decay and interactions of b -hadrons.

Operation of the LHC began in 2008, but was shortly followed by a lengthy shutdown after an accident involving the magnet systems. Following the restarting of operation in 2010, a total of 5.5 fb^{-1} [128] of integrated luminosity was delivered to the ATLAS detector at $\sqrt{s} = 7$ TeV by the end of 2011. 2012 saw a further 22.7 fb^{-1} [129] delivered at $\sqrt{s} = 8$ TeV. This period is referred to as ‘Run 1’, and was followed by a shutdown of operations until 2015. In this period numerous repairs and upgrades were made to the ATLAS detector, as well as the accelerator infrastructure. Run 2, lasting 2015–2018, saw an increase in energy to $\sqrt{s} = 13$ TeV, nearer the maximum design energy for LHC operation. The integrated luminosity delivered to the ATLAS detector during this period reached 156 fb^{-1} [130], of which 140 fb^{-1} passed data quality checks and was judged usable for physics analysis. Over the course of Run 2, the peak luminosity increased from $5 \times 10^{33} \text{ cm}^{-2}\text{s}^{-1}$ in 2015 to $19 \times 10^{33} \text{ cm}^{-2}\text{s}^{-1}$ in 2018. This saw a corresponding increase in the average number of inelastic pp interactions per bunch crossing $\langle\mu\rangle$, rising from a peak value of ≈ 16 to ≈ 55 from 2015–2018.

Following another shutdown for repairs and upgrades, Run 3 has at time of writing been ongoing since 2022 at an increased energy of $\sqrt{s} = 13.6$ TeV. It has seen a record quantity of delivered luminosity, with a preliminary total of around 195 fb^{-1} delivered as of the end of 2024. The cumulative integrated luminosities for each year of data-taking is shown in Figure 3.2.

Run 3 is planned to finish data-taking in 2026. Following this, an extended period of upgrades and repair will precede the scheduled beginning of Run 4 in 2030. This marks the beginning of the *High Luminosity LHC* (HL-LHC) era, in which up to 200 proton-proton interactions per bunch crossing are expected. This presents numerous challenges to data-taking, but the increased quantity of data also presents a great opportunity for future analysis.

3. Experimental Setup

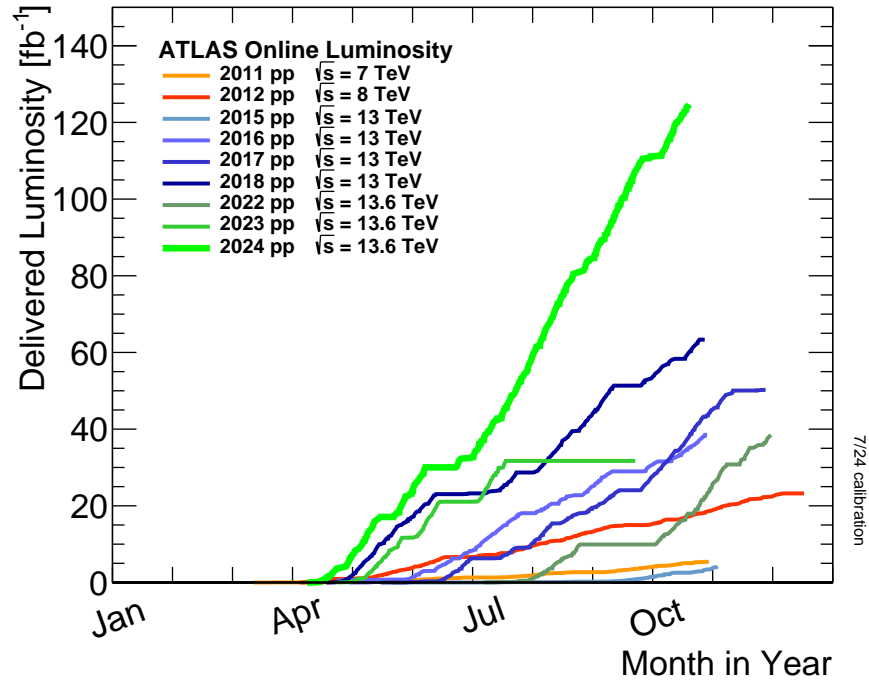


Figure 3.2.: Cumulative integrated luminosity delivered to the ATLAS detector in each year of LHC operation, 2011-2024. Taken from Ref. [131].

3.2. The ATLAS detector

The co-ordinate system of the ATLAS detector has the z -axis lying along the beam axis through the centre of the detector. The detector's side-A is in the $+z$ direction, with side-C in the $-z$ direction. In the Cartesian system, the x -axis is then defined pointing to the centre of the LHC ring, with the y -axis pointing vertically upwards. The centre of the co-ordinate system is placed at the *interaction point*, the nominal location where protons are collided.

To better reflect the detector's symmetry, the system more conventionally used is based on z , the azimuthal angle ϕ , and the polar angle to the $+z$ axis θ . Combining this with the *transverse* component of a kinematic vector, eg. transverse momentum p_T , allows a full description. Given that collision products may be boosted along the beam axis, it is convenient to define polar angles using *rapidity* y , defined for a particle of energy E and momentum component p_z along the z -axis as:

$$y = \frac{1}{2} \ln \left(\frac{E + p_z}{E - p_z} \right) \quad (3.1)$$

This has the property that the rapidity difference between objects Δy is Lorentz-invariant under boosts along z . Since this relies on a measurement of the kinematics, instead the *pseudorapidity* η is used:

$$\eta = -\ln \tan \left(\frac{\theta}{2} \right) \quad (3.2)$$

The rapidity and pseudorapidity are equal in the highly relativistic limit $E \gg m$ for a particle of mass m . Figure 3.3 contains a schematic summarising this co-ordinate system. Angular separation between two objects is defined in terms of the quantity ΔR , with:

$$\Delta R = \sqrt{(\Delta\phi)^2 + (\Delta\eta)^2} \quad (3.3)$$

3.2.1. Inner Detector

The ATLAS inner detector (ID) [132, 133] is, as indicated by its name, the innermost layer surrounding the interaction point. Its purpose is to precisely measure the tracks of charged particles produced in collisions, over a pseudorapidity range of $|\eta| < 2.5$. This in turn facilitates the location of vertices and measurement of particles' momenta. The latter is possible as the ID is surrounded by a 2T axial magnetic field, curving the paths of charged particles. The magnetic field is generated by the central solenoid [134], with a diameter of 2.3 m and a length of 5.3 m. It is designed to be as transparent as possible to particles passing through it to reach the calorimeters outside. Being closest to the interaction point, the ID must be particularly hard to radiation. It consists of three sub-detectors arranged in increasing distance from the interaction point: the

3. Experimental Setup

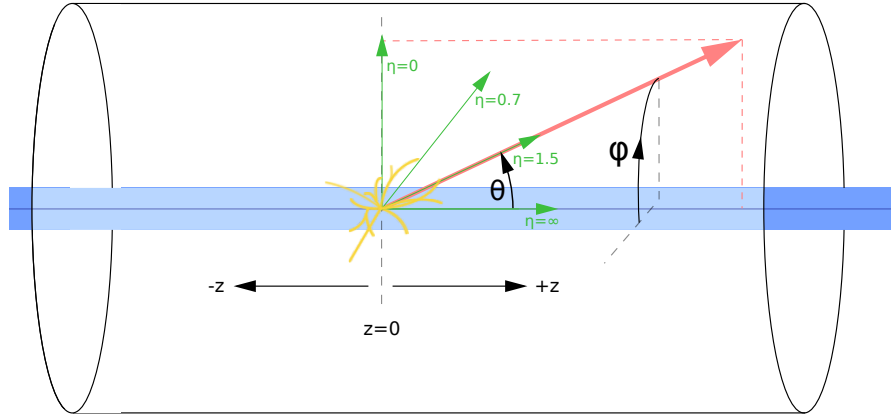


Figure 3.3.: Schematic showing the co-ordinate system used to describe objects in the ATLAS detector. The beam axis indicated by the blue band. The system is centred at the interaction point. The z -axis, azimuthal angle ϕ , polar angle θ , and example values of pseudorapidity $\eta = -\ln \tan(\theta/2)$ are shown.

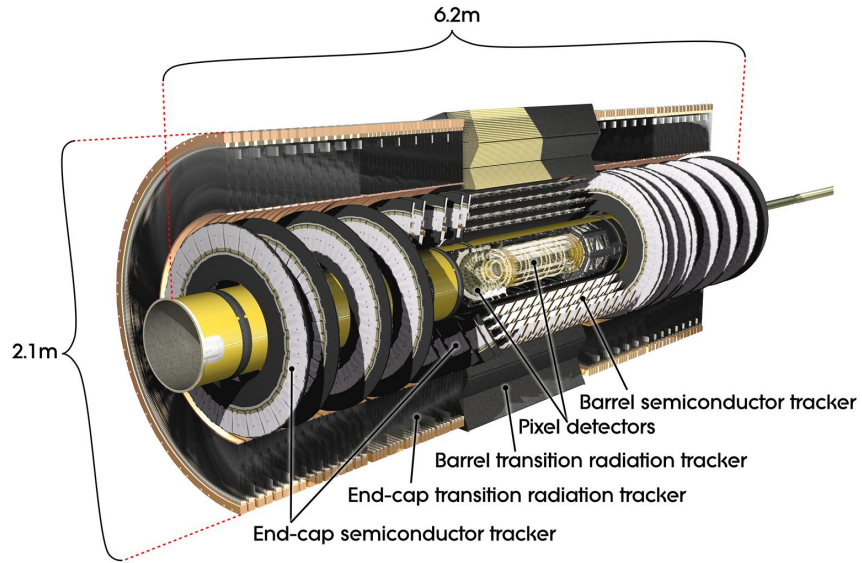


Figure 3.4.: Cut-away diagram showing the structure of the ATLAS inner detector. The Insertable B-Layer is not shown. Taken from Ref. [124].

3.3. Monitoring of Pixel Detector tuning

Pixel Detector, the Semiconductor Tracker (SCT) and the Transition Radiation Tracker (TRT). An overview of its structure is shown in Figure 3.4.

The Pixel Detector [135] is composed of four barrel layers, at average radii $r = 33, 50.5, 88.5,$ and 122.5 mm, and three end-cap disks on each side at $|z| = 495, 580,$ and 650 mm. The innermost barrel layer is the *Insertable B-Layer* (IBL) [136–138], which was installed in May 2014 to maintain tracking performance, despite the effects of radiation damage.

The Pixel Detector employs a total of 92 million silicon pixels of size $50 \times 250 \mu\text{m}^2$ in the IBL and $50 \times 400 \mu\text{m}^2$ elsewhere. These are bump-bonded onto front end chips (FEs), arranged into modules on staves (for barrel layers) or sectors (for end-cap disks).

The SCT [139] uses single-sided, p -in- n silicon microstrips, arranged in stereo pairs, rather than pixels. These are arranged into four cylindrical barrel layers, with a total of 8848 sensors, and nine disk layers on each end-cap with a total of 6944 sensors. The average radii of the barrel layers run from $299 - 524$ mm. The arrangement of the structures is designed to provide four spatial hit points per particle in the covered pseudorapidity range. Each strip has a width of $80 \mu\text{m}$ and a length of $6 - 12$ cm.

The TRT, the outermost ID sub-detector, is a straw-tube tracker, using gas-filled proportional drift tubes with a radius of 4 mm [140]. Layers of these are interleaved with transition radiation material, and arranged into barrel and end-cap sections. Their placement is such that each particle passing should leave $35 - 40$ hit points, albeit in a smaller pseudorapidity range of $|\eta| < 2$. The barrel is located in the radius range $554 \text{ mm} < r < 1082 \text{ mm}$. The TRT is particularly useful for the identification of electrons, as the signal produced in each straw tube is proportional to the Lorentz γ -factor of the traversing particle. This means it is especially sensitive to detecting light particles, which is important since electrons have on average lost $20 - 50\%$ of their energy by the time they exit the SCT.

Before running of the HL-LHC begins, the entire ID will be removed and replaced by the new, all-silicon *Inner Tracker* (ITk) detector [141, 142]. It will consist of an inner pixel detector, surrounded by a strip detector. It is designed to have improved granularity for tracking, improved radiation hardness and increased pseudorapidity coverage up to $|\eta| < 4$.

3.3. Monitoring of Pixel Detector tuning

In this section a brief overview is given of the author’s work developing a tool to visualise the tuning status of the Pixel Detector and IBL² at a given time, as well as to see historical trends. It was completed as part of a Qualification Project in order to become an ATLAS author, and the final results were presented in the ATLAS Pixel General Meeting. Full technical details of the detector and software are not described, rather a general overview of the tool’s functions and uses are given. Plots are illustrative examples, and not intended to convey information about detector function. This part of

²For the purposes of this section, ‘Pixel Detector’ refers to the outer layers only, excluding the IBL.

3. Experimental Setup

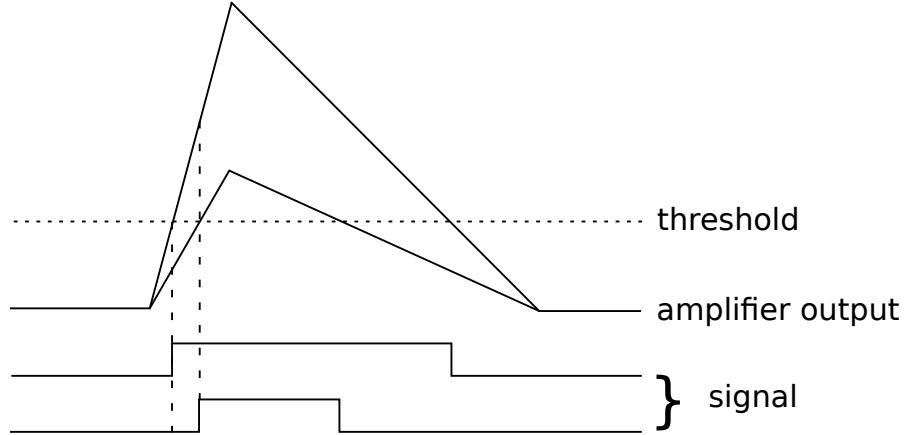


Figure 3.5.: Schematic displaying the principles of threshold and time over threshold, as tuned in the ATLAS Pixel Detector.

the detector is key to identifying jets containing b - and c -hadrons, which is an essential part of the analysis presented here. The methods for performing that task are described in Section 5.4.

Tuning and tool overview

In order to perform accurate and consistent measurements, each of the over 90 million silicon pixels must undergo a *tuning* procedure [143, 144]. Additional tuning parameters are applied at the level of each FE, containing many pixels. Different FE technologies are used in the Pixel Detector and IBL with different technical details, but the principles are consistent. Two key parameters to be tuned are the *threshold* to register a hit, and the total *time over threshold* (ToT), displayed schematically in Figure 3.5. The ToT gives a proxy for the total charge deposited.

Once a particular tuning is set, the corresponding tuning parameters are saved to a *configuration file* with an associated series of *configuration tags*. This also contains key information regarding which detector components are enabled or disabled, from the level of individual pixels to entire modules, consisting of groups of FEs.

The purpose of the tool developed is to enable experts to easily retrieve and examine historical detector configurations, as well as look for trends in the detector tuning over time. These trends may allow an assessment of the impact of radiation damage, as well as provide guidance as to when re-tuning must be performed. It is integrated into the existing ATLAS DAQ software repository as a stand-alone application. Users can pass a range of parameters to pick a particular detector configuration and get a wide range of information about its state in a flexible way. The inputs available to users include the relevant configuration tags, the time or times at which the configuration is to be retrieved, and lists of detector objects and variables to be examined.

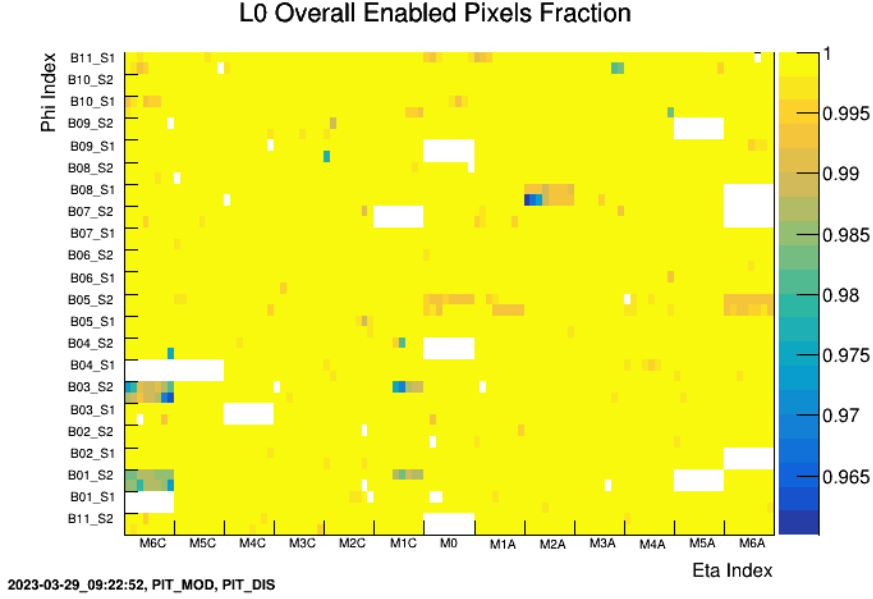


Figure 3.6.: Example 2D plot showing the fraction of enabled pixels in the L0 barrel layer of the Pixel Detector, with the time and tags used shown in the bottom left corner. The system used to label position in η and ϕ is standard for relevant experts. Entirely disabled FEs are shown as white.

Features implemented

The most detailed information made available is a set of 2D plots, plotted by average value per FE, for each Pixel/IBL region, and for each variable considered. Figure 3.6 shows an example, displaying the fraction of enabled pixels in the L0 barrel layer. The necessary position information, as well as other information on the connectivity of objects, is taken from a separate database. All variables need to account for which detector regions are disabled, so these key variables are hard coded into the framework. In addition to that in the configuration files, information on disabled objects is also given in a separate set of files, with an additional tag.

For a more detailed understanding of detector behaviour, 2D plots are also split out by the different pixel types present: normal, long, (long) ganged and (long) inter-ganged. These types are present in order to provide coverage near the edges of FEs, and may be subject to different effects from ageing and radiation damage. Furthermore a dedicated set of comparison plots is generated, as demonstrated in Figure 3.7. This enables comparison between average values, as well as the RMS value, for each variable in each detector region.

Following DAQ expert requests, three other features are implemented:

- A comparison similar to that given for pixel types above, but for the number of a FE within the module. This was included in response to the finding of unusual

3. Experimental Setup

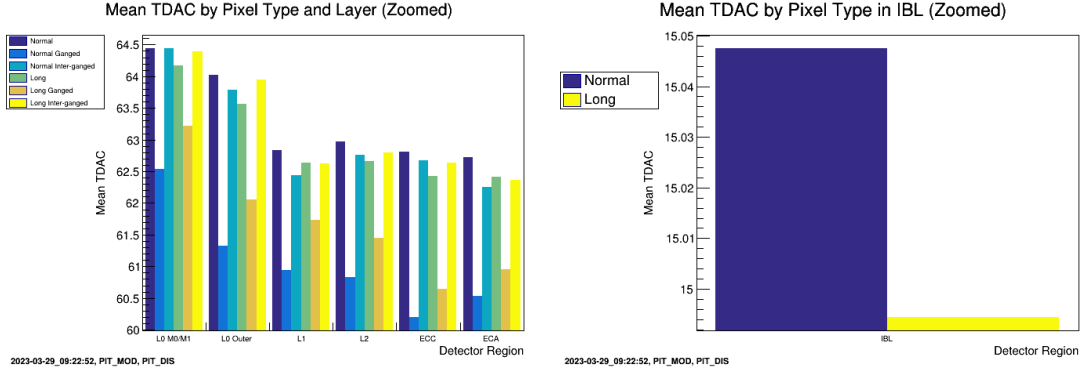


Figure 3.7.: Example plot comparing mean TDAC value by pixel type in each detector region. TDAC is a tuning variable controlling the threshold value per pixel. The definition of regions follows expert request, as the tuning behaviour is treated differently in each. The IBL also has a separate plot, as its TDAC value has a different range and it has two types of pixel rather than six.

row-based patterns in data already produced by the tool.

- Inclusion of a variable monitoring the enable/disable status of entire columns of pixels, as this is an option available to DAQ experts.
- Summary information, giving mean and, where relevant, RMS values for each variable, pixel type and detector region.

Perhaps the most important feature of the tool is the ability to visualise the evolution of detector tuning. With corresponding inputs, a series of plots are generated showing how tuning variables have changed over time. Two examples are shown in Figure 3.8. This enables a better understanding of how the tuning changes, as time and radiation damage impact the pixel detector throughout the remainder of Run 3. Evolution plots have a similar range of granularity to the 2D plots, being split where possible to enable detailed analysis, with a range of scaling options to see both small relative differences and large changes.

3.3.1. Calorimeters

The function of the ATLAS calorimeter system is to completely contain and measure the deposited energy of incident electrons, photons and hadronic jets. A necessary feature to contain all the energy is sufficient material, parameterised by radiation lengths χ_0 ³ and *interaction lengths*⁴. The term used for when energy escapes beyond the calorimeters is *punch – through*. There are two main calorimeter types: the liquid

³Defined as the amount of material such that the energy of a traversing electron will on average decrease by a factor of e^{-1} .

⁴Defined as the average length traversed by a hadronic particle before undergoing an inelastic scattering.

3.3. Monitoring of Pixel Detector tuning

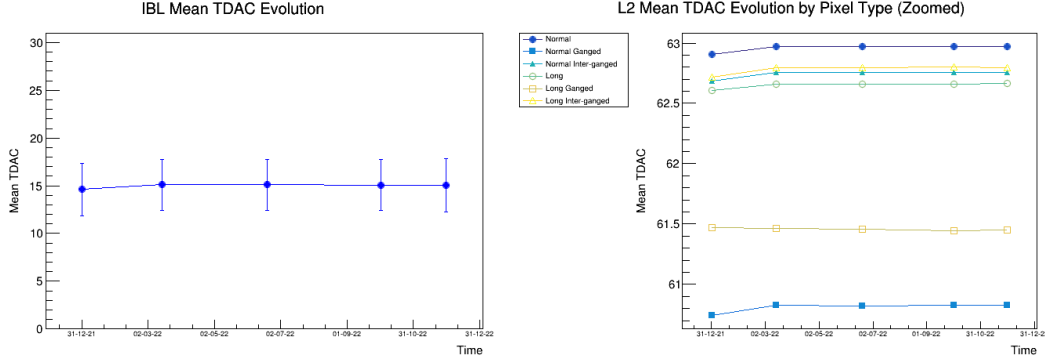


Figure 3.8.: Example plots showing evolution of the values of the TDAC variable, controlling pixel threshold values, over time. Plots are made separately for each detector region, and are generated both with (left) and without (right) error bars, denoting the RMS of the value. Where possible, additional plots are made split by pixel type, as shown on the right.

argon (LAr) calorimeter [145], which is adjacent to the inner detector and is specialised in electromagnetic calorimetry and therefore termed the ECAL; and the tile calorimeter [146], which lies outside the ECAL and is specialised for hadronic calorimetry, so known as the HCAL. At large pseudorapidities additional LAr components are also used for hadronic measurement, so also included in the HCAL system. A view of the ATLAS calorimeter system is shown in Figure 3.9.

The ECAL is a lead-LAr detector, consisting of a barrel section and two end-cap wheels. The lead absorber plates produce showers, which ionises the LAr. A voltage applied across the LAr then allows measurement of the charge produced. Its resolution is greater in the $|\eta| < 2.5$ region, corresponding to the coverage of the inner detector. This allows consistent good identification and measurement of electrons and photons. To prevent punch-through, its thickness is everywhere greater than 22 radiation lengths, and is approximately 9.7 interaction lengths in the barrel, with an additional 1.3 interaction lengths from the outer support.

In the $|\eta| < 1.8$ region, an additional presampler detector is present, consisting of an additional active LAr layer. It allows a correction for EM energy lost upstream.

The HCAL uses a hadronic sampling calorimeter, with steel as its absorber material and scintillating tiles as the active medium. These are read out by pairs of wave-length shifting optical fibres, which in turn go to readout photomultiplier tubes. The tiles are made from polystyrene, doped with fluors to shift the ultraviolet light produced in scintillation to the visible range. The tile hadronic calorimeter barrel section covers the range $|\eta| < 1.0$, with two extended barrels for the range $0.8 < |\eta| < 1.7$. Its barrel extends, radially, from 2.28 m to 4.25 m, and is everywhere segmented into three layers. At $\eta = 0$ its thickness corresponds to 9.7 interaction lengths.

Hadronic calorimetry in more forward regions is performed by two additional LAr end-cap detectors. The Hadronic End-Cap Calorimeter (HEC) extends from $1.5 < |\eta| <$

3. Experimental Setup

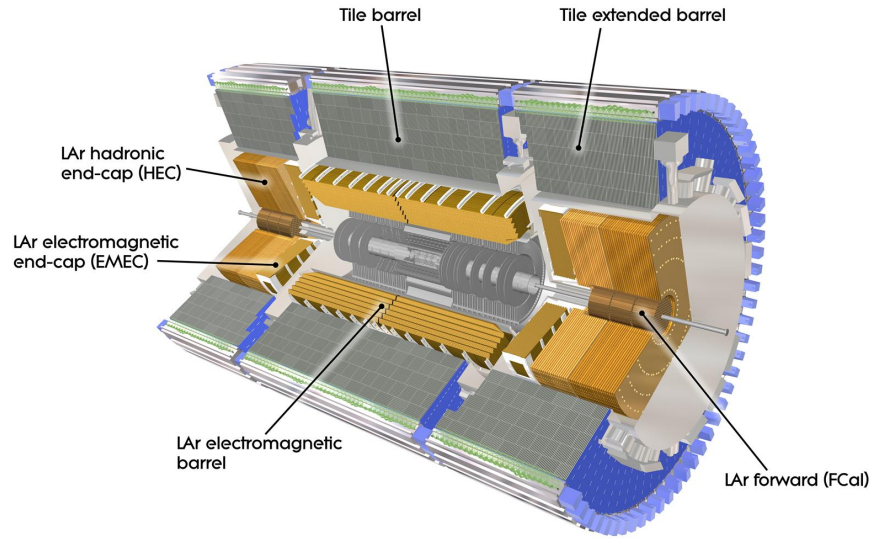


Figure 3.9.: Cut-away diagram showing the structure of the ATLAS calorimeter system. The two detector types shown are liquid Argon (LAr) and tile calorimeters, making up the ECAL and HCAL systems. Each of these has barrel and end-cap sections to cover a wider pseudorapidity range. Taken from Ref. [124].

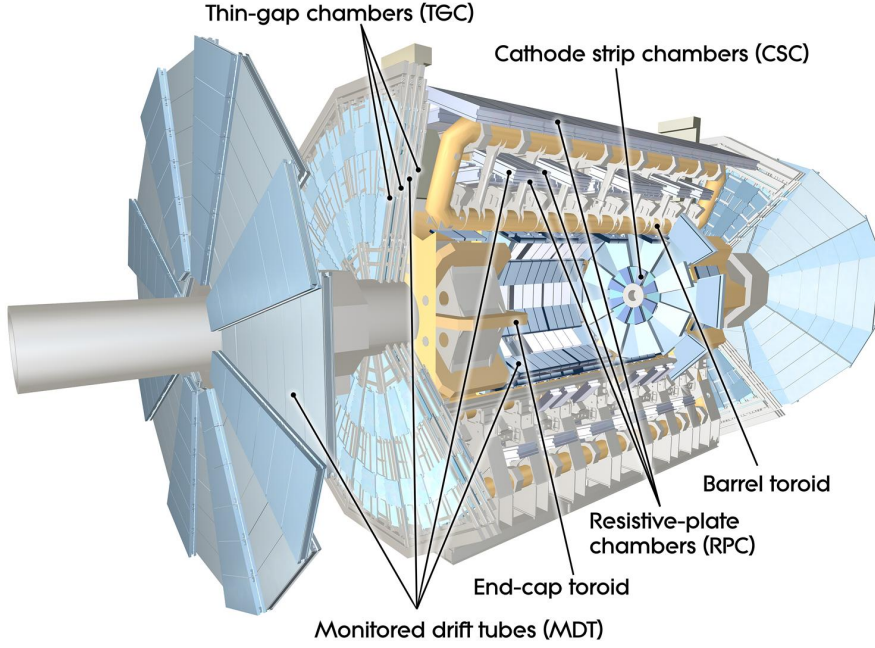


Figure 3.10.: Cut-away diagram showing the structure of the ATLAS muon spectrometer. Taken from Ref. [124].

3.2, overlapping at each end of the range with the tile calorimeter and the Forward Calorimeter (FCal). The absorber material used is copper, and a total of four layers are used per end-cap. The FCal has three layers, with copper acting as the absorber in the first, and tungsten in the second and third. The first layer is optimised for EM calorimetry, with the others optimised for hadronic calorimetry. It provides full coverage⁵ in the range $3.2 < |\eta| < 4.9$, and is designed to minimise issues caused by the large radiation flux experienced in this forward region.

3.3.2. Muon spectrometer

The measurement of muons poses a particular challenge as they are minimum ionising particles depositing very little energy in the previously described detector systems. Addressing this is the ATLAS detector's largest sub-detector: the muon spectrometer (MS) [147]. An overview of its structure is shown in Figure 3.10.

In order to measure muons' momenta, a magnetic field is needed. This is provided by three extremely large air-core toroids: one barrel toroid and two end-cap toroids, each consisting of eight coils. The barrel toroid covers the region $|\eta| < 1.4$ and the end-caps $1.6 < |\eta| < 2.7$. Muons traversing the transition region between these are bent by a combination of the two.

⁵Each layer has different coverage, with the first beginning at $\eta = 3.0$

3. Experimental Setup

The precision measurement of muons is done by two detector types: Monitored Drift Tubes (MDTs) in the region $|\eta| < 2.0$, and Cathode Strip Chambers (CSCs) for $2.0 < |\eta| < 2.7$. In this full range, three layers are present. The MDTs employ aluminium tubes containing a W-Re wire, and have a typical single-wire resolution of $80 \mu m$. The CSCs are multiwire proportional chambers with cathode strip readout, achieving a resolution in the bending direction of $60 \mu m$.

Another two sub-detectors are used for fast triggering, the process of which is discussed more in the following section. Together they cover $|\eta| < 2.4$. Resistive Plate Chambers (RPCs) are in the low pseudorapidity region, using narrow gaps between bakelite sheets filled with gas. High pseudorapidity regions use thin gap chambers (TGCs). These are similar to multiwire proportional chambers, with the difference that the separation between the anode wires and the cathode is smaller than that between wires. The precision of these is lower than the precision muon detectors, but provide information quickly to aid with bunch-crossing identification, and also give p_T thresholds. Furthermore they allow measurement of momentum in the orthogonal direction to that measured by the other systems.

3.3.3. Luminosity measurement and forward detectors

The instantaneous luminosity for observed events in the ATLAS detector can be written:

$$\mathcal{L} = \frac{f \langle \mu \rangle}{\sigma_{\text{incl}} \epsilon} \quad (3.4)$$

Where f is the frequency at which bunch crossings occur; $\langle \mu \rangle$ is the average number of inelastic interactions per bunch crossing, describing the pileup; σ_{incl} is the inclusive total cross section for interaction, and ϵ gives the average efficiency for detecting an event. Since the majority of ATLAS measurements aim to compare the observed number of a particular event type to those expected based on simulation, an accurate measurement of the luminosity is essential as it provides an overall scaling uncertainty on such measurements.

Luminosity measurement for Run 2 data is performed primarily using LUCID-2 (Luminosity Cherenkov Integrating Detector). It is a Cherenkov detector employing the quartz windows of photomultipliers as its Cherenkov medium. It performs a procedure known as charge integration, allowing it to measure the number of interactions in each bunch crossing. Its location is ≈ 17 m from the interaction point, at large pseudorapidity of $|\eta| \approx 5.6$. The *beam conditions monitor* (BCM) [148] was designed to also be a main source of luminosity data, but received limited use for this purpose in Run 2 data due to difficulties with the more challenging conditions with respect to Run 1. Instead its use was limited to certain checks during luminosity calibration. Additional information is provided by so-called *track counting*, measuring the number of tracks seen in the ID without applying the normal selection criteria for triggering described below. Furthermore the calorimeter systems can provide information on luminosity, averaged over a data-taking period.

3.3. Monitoring of Pixel Detector tuning

During Run 2, the luminosity measurement was calibrated once per year in dedicated fills using the van der Meer method [149, 150]. This uses a beam separation scan, and allows a direct measurement of the visible cross-section, $\sigma_{\text{vis}} = \sigma_{\text{incl}}\epsilon$. This in turn allows a calculation of the total luminosity, so the values from different luminosity detectors and algorithms can be compared to ensure consistency.

Additional forward detectors are present in ATLAS. The *Zero Degree Calorimeters* (ZDC) [151] are located along the beam-line at $|z| = 140$ m, and observe neutral particles produced from collisions in the forward regions. Additionally, the *Absolute Luminosity For ATLAS* (ALFA) detector [152], at $|z| = 240$ m, measures protons from elastic scattering using so-called “Roman Pots”.

The ATLAS *Forward Proton* (AFP) detectors [153] are at $|z| = 204$ m and $|z| = 217$ m, measure intact protons coming from collisions using silicon pixel detectors. It is specialised to perform physics measurements involving these objects, where proton interactions cause small deflections.

3.3.4. Trigger system and data acquisition

Given the collision rate of 40 MHz, it is impossible to fully analyse and store data from all events occurring inside the ATLAS detector. The process of reducing this rate and selecting, then storing, only those events likely to be of interest is performed by the trigger and data acquisition system (TDAQ). For Run 2, the trigger system has two components: the L1 trigger and high-level trigger (HLT).

The L1 trigger is hardware-based, to facilitate a maximum decision-making time of $2.5 \mu\text{s}$ [154–156]. This is a basic decision looking for objects with high transverse momentum, as well as a large total transverse energy or high missing transverse energy. Information on muons comes from the MS trigger chambers, while the calorimeter systems supply information with reduced granularity to simplify the calculation process. Further information comes from the LUCID Cherenkov counter, ZDC and *Minimum Bias Trigger Scintillators* (MBTSs) [157]. These are polystyrene scintillator discs mounted along the beam pipe at $|z| \approx 3.6$ m, covering the range $2.08 < |\eta| < 3.75$. The *central trigger processor* receives this information and selects those events passing a *menu* of possible selection criteria. It also applies a minimum dead-time between accepted events to allow sufficient time for readout of the data. Finally the central trigger processor can also define Regions-of-Interest (ROIs), the positions of notable features, which may be used in the next stage of processing of selected events. The L1 trigger passes data on selected events to the Read-Out System, which acts as a buffer.

Events passing selection by the L1 trigger are passed onto the HLT, which is software-based and performs a more full analysis [158]. It receives full information from the ID, calorimeters and MS. However to maintain performance most triggers have a two-stage selection which quickly rejects events definitely not of interest, then a fuller reconstruction is performed. During this process information on ROIs may be used. In the end, on the order of 100 events per second pass selection and are sent to CERN’s Tier-0 computing facility for full off-line reconstruction and storage.

Modelling of Signal and Background

In order to perform a meaningful measurement and compare observations to theory, MC events are simulated to compare with data from the ATLAS detector. These are created not only for the signal process in question, but for all categories of background events which may produce a similar response in the detector. Section 4.1 describes the simulation of $t\bar{t}$ events, including top quark pair production in association with charm quarks. Finally, Section 4.2 describes the process for simulating background processes.

The ATLAS detector response is simulated [159] with the GEANT4 [160] toolkit. For some MC samples a faster simulation method called ATLFAST-II is employed to improve computing performance, using the Fast ATLAS Tracking Simulation [161] and Fast Calorimeter Simulation [162]. The former employs a simplified version of the detector geometry, while the latter parameterises and reproduces shower shapes to produce a response similar to that from full simulation.

To account for pileup, additional minimum-bias pp collision events are overlaid on the simulated hard-scattering event. These are generated using PYTHIA 8.186 [163] with the A3 set of tuned parameters [164] with the NNPDF2.3_{LO} [51] PDF set. These are weighted to match the average number of interactions per bunch crossing observed in data for each data-taking period, following the procedure described in Refs. [165, 166]. For all processes the mass of the top quark is set to $m_t = 172.5$ GeV

4.1. $t\bar{t}$ events

Two different types of samples are used to model $t\bar{t}$ events. One is an inclusive sample, generated in a five-flavour-scheme (5FS), and the other is a dedicated sample of $t\bar{t}$ events with additional b quarks ($t\bar{t}b\bar{b}$), generated in a four-flavour-scheme (4FS) with the $b\bar{b}$ pair included in the matrix element. The flavour scheme describes how many quark flavours are treated as massless partons and included in PDFs, rather than treated as massive

4. Modelling of Signal and Background

and treated solely in perturbative QCD. The 4FS includes the u , d , c and s in this way, with the 5FS adding the b . In this analysis the purpose of the 5FS sample is to simulate $t\bar{t}$ events with additional jets coming from c and light-flavour quarks, while the 4FS sample is dedicated to the events with additional b quarks. A 3FS sample dedicated to modelling $t\bar{t}$ with c quarks was not available for this analysis. The 5FS $t\bar{t}$ sample and all variations are reweighted to a predicted $t\bar{t}$ cross-section of 832 ± 51 pb, as calculated using the Top++ program [167] at NNLO in QCD, with soft-gluon resummation at NNLL accuracy. The 4FS $t\bar{t}b\bar{b}$ samples are normalised to the cross-section calculated by the POWHEG BOX RES [168] generator with OPENLOOPS [169–171].

Unless otherwise specified, the parton shower (PS), hadronisation and MPIs for processes in this section are simulated using PYTHIA 8.2 [172] with the A14 set of tuned parameters [173] and the NNPDF2.3_{LO} [51] PDF set. Similarly unless otherwise specified the decays of b - and c -hadrons are simulated using the EVTGEN 1.6.0 [174] program.

4.1.1. $t\bar{t}$ 5FS sample

The 5FS $t\bar{t}$ inclusive sample is generated at NLO in QCD using the POWHEG Box2 [105–108] generator with the NNPDF3.0_{NLO} [51] PDF set. The h_{damp} parameter in POWHEG, which limits the p_T of the hardest gluon radiation emitted, is set to $1.5m_t$ [175]. Both μ_R and μ_F are set to the transverse mass of the top quark¹: $m_{T,t} = \sqrt{m_t^2 + p_{T,t}^2}$.

To enable the estimation of modelling uncertainties, a number of alternative samples or weightings are used. Here only separate samples are described; reweightings used for uncertainties are discussed in Section 8.3. One alternative sample is generated with h_{damp} doubled to a value of $3m_t$. Another uses a value of one for the POWHEG p_T^{hard} parameter rather than the default value of zero. This parameter controls the definition of the vetoed p_T region for showering in PYTHIA, based on information passed from POWHEG. To probe the choice of parton shower algorithm, an alternative sample is simulated interfacing POWHEG Box2 to HERWIG 7.1.3 [176–178] with the default HERWIG 7.1 tuned parameter set and the MMHT2014_{LO} [179] PDF set. Another sample uses MADGRAPH5_aMC@NLO v2.6.0 [110] with NNPDF3.0_{NLO} PDFs to calculate the matrix element. This employs MADSPIN [180, 181] to simulate the top quark decay, and is interfaced to HERWIG 7.1.3 with the same tuning as previously described.

4.1.2. $t\bar{t}b\bar{b}$ 4FS sample

$t\bar{t}b\bar{b}$ events are generated in the 4FS with the POWHEG BOX RES [168] generator alongside OPENLOOPS [169–171] and the NNPDF3.0_{NLO} PDF set [51]. The b quark mass is set to 4.95 GeV. The renormalisation and factorisation scales are set to $\mu_R = \frac{1}{2} \sqrt{m_{T,t} m_{T,\bar{t}} m_{T,b} m_{T,\bar{b}}}$ and $\mu_F = \frac{1}{2} \sum_{i=t,\bar{t},b,\bar{b},j} m_{T,i}$ where $m_{T,i}$ is the transverse mass of particle i , and j denotes any additional partons present. The value for h_{damp} used is

¹‘Transverse mass’ may be defined in different ways in different sources - for the purposes of this document this is the only definition used.

$h_{\text{damp}} = \frac{1}{2} \sum_{i=t,\bar{t},b,\bar{b}} m_{T,i}$, with the default value for zero used for p_T^{hard} . The POWHEG parameter h_{bzd} , which controls the splitting between the finite and singular parts of real emissions, is set to a value of five.

Alternative sets of events are generated with p_T^{hard} set to one; with h_{bzd} set to two; and another using a dipole recoil scheme in PYTHIA instead of the default global recoil scheme, which also has $h_{\text{bzd}} = 2$. The recoil scheme defines whether or not the entire system recoils from the emission of radiation. A sample is also generated with POWHEG BOX RES interfaced to HERWIG 7.1.6 with the default set of tuning parameters for that version. Finally, an alternative set of $t\bar{t}b\bar{b}$ events is generated using SHERPA 2.2.10 [182], with the NLO accuracy matrix element corrections provided by COMIX [183] and OPENLOOPS. In this setup the b quark mass used is 4.75 GeV. The SHERPA PS algorithm [184] is used with a set of tuned parameters as developed by the SHERPA authors. Matching between the ME and PS uses the MEPS@NLO procedure described in Refs. [185–188].

4.2. Background processes

4.2.1. Single top production

t -channel single top production is simulated following Ref. [189], using POWHEG Box2 in the 4FS with $\mu_R = \mu_F = \sqrt{m_b^2 + p_{T,b}^2}$. s -channel and tW events employ the same generator in the 5FS, with $\mu_R = \mu_F = m_t$. All use the NNPDF3.0_{NLO} PDF set corresponding to the given flavour-scheme. For tW production the diagram removal scheme is used to manage the interference between this process and $t\bar{t}$ production [190]. PS, hadronisation and MPIs are modelled identically to the nominal $t\bar{t}$ production above.

Alternative samples are generated using HERWIG 7.04 with the H7UE set of tuned parameters and the MMHT2014_{LO} PDF set, rather than PYTHIA. Another uses MADGRAPH5_aMC@NLO v2.6.2 [110] as the matrix element generator in the 5FS, with the same PDF set as the nominal setup. Finally in order to understand the impact of the handling of tW - $t\bar{t}$ interference, another tW sample using the diagram subtraction scheme is generated.

4.2.2. $t\bar{t}H$

The background sample for the $t\bar{t}H$ process is simulated in the 5FS using $m_H = 125$ GeV, employing POWHEG Box2 with the NNPDF3.0_{NLO} PDF set, interfaced to PYTHIA in the same way as previous samples. The QCD scales are set to $\mu_R = \mu_F = \sqrt[3]{m_{T,t}m_{T,\bar{t}}m_{T,H}}$, with $h_{\text{damp}} = \frac{3}{4}(m_t + m_{\bar{t}} + m_H)$. The cross-section value used is 507_{-50}^{+35} fb, calculated at NLO in QCD and the electroweak interaction as taken from Ref. [191].

4. Modelling of Signal and Background

4.2.3. $t\bar{t}W$, $t\bar{t}Z$, tZq and tWZ

The ME generator used to simulate these background processes is MADGRAPH5_aMC@NLO v2.3.3 with the NNPDF3.0_{NLO} PDF set, and interfaced with PYTHIA 8.2 with the A14 set of tuned parameters and the NNPDF2.3_{LO} PDF set.

Alternative $t\bar{t}W$ and $t\bar{t}Z$ samples were produced at LO accuracy using SHERPA 2.2.0 [182] in the MEPS@LO setup [187, 188], using the default SHERPA PS and the NNPDF3.0_{NNLO} PDF set.

4.2.4. W + jets and Z + jets

These processes are simulated using SHERPA 2.2.1, which uses NLO MEs for up to two partons, and LO MEs for up to four, implemented using Comix [183] and OPENLOOPS [169–171]. The PS and its matching use the same procedure as the $t\bar{t}b\bar{b}$ sample. The sample is normalised to the cross-section value from NNLO prediction [192]. For events with one reconstructed lepton and at least one heavy-flavour jet in the final state, as well as those with two reconstructed leptons and at least two heavy-flavour jets, a correction of +25% is applied to the cross-section. This accounts for mismodelling, which was observed in the 2022 ATLAS $t\bar{t}H(bb)$ analysis [193].

4.2.5. Diboson

Both SHERPA 2.2.1 and SHERPA 2.2.2 are used to simulate diboson background processes with either semi-leptonic or dileptonic final states². NLO accuracy is used for up to one additional parton emission, with LO accurate MEs for up to three additional partons. Samples for the $gg \rightarrow WW/ZZ$ processes use matrix elements which are LO accurate for up to one additional parton emission, in final states with either one or two leptons. OPENLOOPS supplies corrections for virtual QCD, and the procedure for PS simulation is the same as above using MEPS@NLO.

²These are defined in the same way as the decays of $t\bar{t}$ pairs.

Physics Object Identification and Reconstruction

The ATLAS detector, described in Section 3.2, ultimately measures a series of hit points and energy deposits. The process of accurately and efficiently interpreting this information is summarised in this chapter. Following reconstruction and identification, this results in physics objects which can be analysed: the most relevant ones for this thesis being electrons, muons, and hadronic jets (Sections 5.1 - 5.3). Sections 5.4 and 5.5 then describe the further steps used to experimentally identify those jets originating from b and c quarks: a crucial part of the analysis presented here. Section 5.6 briefly described the process used to determine the transverse momentum missing from the measured system, due to being carried by non-interacting neutrinos. Finally Section 5.7 lays out the ways in which overlapping objects are removed, preventing potential conflicting identifications of objects between the different reconstruction algorithms.

5.1. Electrons

Electrons¹, being electrically charged, leave tracks in the ID, and deposit the majority of their energy in the ECAL.

The reconstruction of tracks in the ID [194] is performed by first creating clusters in the pixel and SCT detectors [195, 196]. A pattern-recognition algorithm then runs, using either a pion hypothesis to model energy loss, or else an electron hypothesis which allows for losses to bremsstrahlung. Track candidates are fit using the ATLAS Global χ^2 Track Fitter [197], which also uses either pion or electron hypotheses. Additional fitting is performed using an optimised Gaussian-sum filter [198, 199], based on a generalisation of Kalman filtering [200]. This step further improves the accuracy of reconstructed track variables.

¹The description here applies to both electrons and positrons.

5. Physics Object Identification and Reconstruction

In the ECAL, a significant amount of energy loss occurs through bremsstrahlung, whereby the photon emitted may turn into an e^+e^- pair which interacts with matter in the ECAL. This typically occurs within a single topological cluster of connected calorimeter cells, termed a *topo-cluster* [201]. Reconstruction relies on matching such topo-clusters to track information from the ID. However there is not necessarily a neat one-to-one match: electrons may emit radiation in the ID, producing multiple tracks and multiple topo-clusters. The full procedure for reconstruction is described in Ref. [202].

The creation of a topo-cluster is seeded by a calorimeter cell which has energy E four times greater than its expected noise threshold E_{noise} , accounting for both electronic noise and pileup. The cluster is expanded in three dimensions, iteratively adding all neighbouring cells which have $E > 2E_{\text{noise}}$. Once no more cells meet this criterion, a final surrounding shell of cells is added to the cluster. Cells in the HCAL are included in this process, however only those clusters with over 400 MeV deposited in the ECAL, and more than half of the total topo-cluster energy there, are further considered.

Tracks are then matched to topo-clusters, potentially rescaling the momentum of the track to match the energy of the topo-cluster in question to allow for energy losses. In cases of multiple tracks matching a topo-cluster, a ranking is performed based on the precision of the match and quality of the track reconstruction.

Superclusters are formed using topo-clusters with matched tracks as seeds. Then nearby topo-clusters are considered as candidates to be satellite clusters and added to the supercluster, based on proximity and whether they share a matched track. Matching to ID tracks is re-done with the same procedure as above, but using the superclusters. This matched track and supercluster constitute a potential electron for the purposes of analysis. The energy is calibrated using the procedure described in Ref. [203].

A range of criteria are applied to improve the identification of electrons, described in detail in Refs. [194, 202]. The aim is to distinguish prompt electrons from deposits from hadronic jets, from converted photons and from electrons produced by decays of heavy-flavour hadrons. The variables considered relate to the ID track, the shape of the shower in the calorimeter, and the matching between the two. A discriminant is formed from signal and background likelihoods, themselves from *probability density functions* (pdfs) in the discriminating variables. The pdfs are derived in $Z \rightarrow ee$ and $J/\psi \rightarrow ee$ events using the tag-and-probe method [204]. For this analysis, the *TightLH* working point is used on the discriminant, defined in bins of $|\eta|$ and E_T with an efficiency of around 80%. This further requires that $E/p < 10$ and the track has $p_T > 2$ GeV. For this analysis it is also required that the electron candidate has $p_T > 10$ GeV, with $|\eta_{\text{cluster}}| < 2.47$. Additionally, candidates in the poorly-measured region $1.37 < |\eta_{\text{cluster}}| < 1.52$, corresponding to the transition between the barrel and end-cap, are discarded. The track must also have $|\frac{d_0}{\sigma_{d_0}}| < 5$ for transverse impact parameter d_0 and $|\Delta z_0 \sin \theta| < 0.5$ mm, with Δz_0 the longitudinal distance to the track from the primary vertex.

The criterion used for isolation is the **Tight_VarRad** operating point [205]. For calorimeter isolation this requires $E_T^{\text{cone20}}/p_T < 0.06$, the term cone20 denoting an angular cone

of $\Delta R = 0.2$, with:

$$E_T^{\text{cone20}} = E_{T,\text{raw}}^{\text{isol20}} - E_{T,\text{core}} - E_{T,\text{leakage}}(E_T, \eta) - E_{T,\text{pileup}}(\eta) \quad (5.1)$$

$E_{T,\text{raw}}^{\text{isol20}}$ is the total deposited energy in the calorimeter cells and $E_{T,\text{core}}$ is the energy in a simple rectangular area around the barycentre of the cluster. The latter estimate is made more accurate by the $E_{T,\text{leakage}}$ correction, parameterised as a function of E_T and η with values from MC simulation. For the term $E_{T,\text{pileup}}$, the pileup contribution is initially estimated with the same method as described in Ref. [206]². This estimate is corrected using a smooth function of η derived from $Z \rightarrow ee$ events, to account for the changing detector dimensions at different angles producing different pileup signals.

The **Tight_VarRad** operating point additionally applies a criterion for the track isolation of $p_T^{\text{varcone30}}/p_T < 0.06$. This is the scalar p_T sum of other tracks within a cone of angular size:

$$\Delta R = \min \left(\frac{10}{E_T[\text{GeV}]}, 0.3 \right) \quad (5.2)$$

5.2. Muons

Since muons act as minimum ionising particles at energy scales relevant for this work, they are not stopped in the calorimeters, depositing minimal energy. Instead they are mainly reconstructed from tracks in the ID and muon spectrometer (MS), which are created independently. ID track reconstruction is similar to that performed for electrons, as described in Ref. [196]. Reconstruction of MS tracks begins by identifying straight line segments in each MS station, which are combined, then a global χ^2 fit is performed, accounting for energy loss and the effect of the magnetic field present. Removal of outliers and other re-fitting is finally done, as described in Ref. [207]. ID, MS and calorimeter information can be used and combined in several different ways, leading to a total of five muon *types*, of which two are relevant for the *Medium* quality working point used for this analysis:

- *Combined* (CB) muons perform a combined track fit using matched MS and ID tracks, accounting for calorimeter energy loss information.
- *Inside-out combined* (IO) muons account for regions where MS coverage is poor, or for low p_T muons which may not leave a full MS track. They are created by extrapolating ID tracks to the MS, fitting a combination of the ID track, calorimeter energy loss and at least three loosely-aligned MS hits.

A requirement of $|\eta| < 2.5$ is used, corresponding to the region of full ID coverage. The ID track must have at least one hit in the pixel detector and at least five in the SCT detector, with a maximum of two locations where an active sensor is missing an

²See Section 5.3 below for a description of this method in the context of jet reconstruction.

5. Physics Object Identification and Reconstruction

expected hit. Furthermore this analysis applies the vertex association criteria $|\frac{d_0}{\sigma_{d_0}}| < 3$ and $|\Delta z_0 \sin \theta| < 0.5$ mm, defined in the same way as for electrons. To meet the Medium working point at least two *precision stations* are required, defined as those MS stations with at least three hits. Conversely a *precision hole station* has less than three hits, and at least three expected hits are missing. For the most central region $|\eta| < 0.1$ muons with one precision station are included, provided they have no more than one precision hole station. The other quality requirement is a *q/p compatibility* of less than seven, defined as:

$$q/p \text{ compatibility} = \frac{\left| \left(\frac{q}{p} \right)_{\text{ID}} - \left(\frac{q}{p} \right)_{\text{MS}} \right|}{\sqrt{\sigma^2 \left(\frac{q}{p} \right)_{\text{ID}} + \sigma^2 \left(\frac{q}{p} \right)_{\text{MS}}}} \quad (5.3)$$

with $(q/p)_{\text{ID/MS}}$ the ratio of muon charge to momentum as measured in the ID or MS.

The isolation WP used is *TightTrackOnly* [207], requiring $p_T^{\text{varcone30}}/p_T < 0.06$ with terms defined as for electrons above. A requirement of $p_T > 10$ GeV is also applied. Calibration of the muon momentum scale and resolution is performed by studying $Z \rightarrow \mu\mu$ and $J/\psi \rightarrow \mu\mu$ events, and using the observed resonance peaks, as described in Ref. [208].

5.3. Jets

Due to colour confinement, quarks and gluons produced in collisions are not observed as free particles, but undergo hadronisation. This results in a shower of collimated hadronic objects. Those which are charged leave tracks in the ID, while all objects then deposit their energy in the ECAL and HCAL. The object ultimately reconstructed from this information is termed a *jet*. The signals from individual calorimeter cells are combined into topo-clusters, using the same method as described for the reconstruction of electrons.

The *particle flow* algorithm³ [209] is then applied to the ID tracks and topo-clusters. Tracks which pass quality criteria and are not matched to candidate electrons or muons are considered one by one, and matched where possible to a topo-cluster. Based on momentum information from the track and the location of a topo-cluster, it can be calculated how much energy would be expected to be deposited. Successive topo-clusters can be added to the track/topo-cluster system until there is good agreement between the observed and expected energy deposited. Energy is then subtracted cell-by-cell from the topo-clusters up to the amount expected from the track. If the remaining energy is consistent with simply being fluctuations left over from the estimate, the topo-clusters in question are removed. Otherwise it is assumed that they must have energy from other particle(s) not associated with the track being considered. The first tracks processed are those matching exactly one topo-cluster, then the rest, with each group processed in

³‘Particle flow jets’ additionally is used for jets created using the entire jet-reconstruction procedure summarised here. Ref. [209] contains a complete description of this procedure.

order of decreasing p_T . The output of the algorithm is then a set of tracks and associated topo-clusters, and the remaining un-subtracted topo-clusters.

Jets are reconstructed using the anti- k_t [210] algorithm, implemented using the FAST-JET package [211, 212]. It considers all of the un-subtracted topo-clusters, as well as the sets of tracks/topo-cluster systems where the track passes within 2mm of the hard-scatter primary vertex. This step nominally removes the pileup contribution from charged particles from secondary vertices. At this point all position information is recalculated to be relative to the primary vertex. The anti- k_t algorithm uses a set of distance measures d_{ij} between entities i and j , and d_{iB} between entity i and the beam axis, defined as:

$$d_{ij} = \min \left(\frac{1}{p_{Ti}^2}, \frac{1}{p_{Tj}^2} \right) \frac{\Delta R_{ij}^2}{R^2} \quad (5.4)$$

$$d_{iB} = \frac{1}{p_{Ti}^2} \quad (5.5)$$

with ΔR_{ij} the angular separation between i and j and R a radius parameter. This analysis uses $R = 0.4$. The alternative jet-reconstruction k_t algorithm [213] uses the same procedure, but with terms p_T^2 in the distance measure in place of $\frac{1}{p_T^2}$.

The algorithm sequentially takes the smallest d value. If it is of the type d_{ij} , the two entities are combined into one. If it is of the type d_{iB} , this entity is labelled a jet, and is removed from consideration. Between each step the distances must be recalculated. This continues until all entities have been classified into jets. The effect of this system is that if there are several well-separated ($\Delta R > 2R$) hard particles and a large number of soft ones, each hard particle will be combined with all soft ones within radius R , forming conical jets. If the separation of hard particles is $R < \Delta R < 2R$ their cone shapes will be clipped in the middle region, with the boundary depending on their relative p_T s. Finally if $\Delta R < R$ they will be combined into a single jet with a more complex shape. For this analysis jets are only used in they have $|\eta| < 2.5$ and $p_T > 25$ GeV.

All ATLAS calorimeters are set to the electromagnetic scale, so the lower response seen to hadronic objects must be calibrated for, as well as a number of other physics effects. This is done through a series of steps:

1. The contribution from charged underlying-event hadrons, charged out-of-time events and neutral pileup components not removed through the particle flow algorithm's use of track information must be subtracted. The first step to do this uses the *jet ghost-area subtraction* method [214, 215]. This calculates an average transverse energy density ρ per-event using k_t jets. k_t jets are used for this because this algorithm tends to produce a number of large jets composed of soft particles. The measurement is performed in the central region of the calorimeter where occupancy is lower. The jet area A used is the *ghost area*. This adds a large number of evenly spaced, effectively infinitely soft *ghost* particles to the jet-finding procedure and uses the number ultimately associated with each jet as an area measure. This must additionally be done accounting for the effect of the particle flow algorithm's

5. Physics Object Identification and Reconstruction

removal of topo-clusters associated to tracks. The energy of each jet can then be corrected by subtracting $\rho \times A$.

2. A residual pileup correction is applied, calculated using the reconstructed and true p_T in MC-simulated events [216]. It accounts for the remaining dependence observed on the number of primary vertices N_{PV} and the amount of pileup μ , especially in more forward regions of the detector. For each of these, a linear dependence is seen, with coefficients α and β fit to them, producing an additional correction:

$$p_T^{\text{corrected}} = p_T^{\text{un-corrected}} - \alpha \times (N_{PV} - 1) - \beta \times \mu \quad (5.6)$$

3. The absolute jet energy scale (JES) is calibrated, based on the ratio of reconstructed to true energy in isolated jets in MC events after previous corrections have been applied. An additional correction is applied to correct an observed bias in the η distribution.
4. The *global sequential correction* scheme [217] corrects the jet four-momentum using MC events as a function of p_T and η , sequentially and independently in three observables. These are chosen to improve the JES resolution, accounting for the differences between quark and gluon-initiated jets, and the composition of hadrons in jet fragmentation.
5. Remaining mis-modelling of the detector and underlying physics is addressed through a final *in situ* calibration. The η intercalibration corrects the response of forward jets using well-measured central jets. Three further calibrations then correct the jet response further using well-measured objects in central regions, as described fully in Ref. [218].

Suppression of jets coming from pileup is improved through the use of the *jet-vertex-tagger* (JVT) [219] multivariate discriminant. This is based on two variables, both using track information to determine the extent to which the tracks and p_T associated to a jet are from the primary hard-scatter vertex. A two-dimensional likelihood is constructed based on the k -nearest neighbour algorithm [220] for the jet to come from the primary hard-scatter vertex. For this analysis the *Tight* JVT working point is used as a requirement for jets with $|\eta| < 2.4$ and $p_T < 60$ GeV.

5.4. Heavy flavour tagging

The underlying features enabling the identification of jets containing b and c -hadrons (b - and c -jets) were described briefly in 2.3.2. A number of low-level variables are constructed to measure these features, then combined into the high-level multivariate DL1r [53] classifier:

- Discriminating variables from the impact parameter (IP)-based IP2D and IP3D [221] algorithms are used. IP2D uses the ratio of the signed transverse IP to its

uncertainty⁴, while IP3D additionally uses the ratio of the signed longitudinal IP to its uncertainty. Log-likelihood ratio discriminants are formed for each of IP2D and IP3D defining the separation between each pairing of b -jets, c -jets and light jets.

- The **SV1** [222] secondary-vertex-tagging algorithm considers combinations of tracks and evaluates their compatibility with a χ^2 test to find a single secondary vertex consistent with decay of a b - or c -hadron. It produces eight discriminating variables to be used as inputs to **DL1r**.
- The **JetFitter** [223] algorithm aims to reconstruct the full decay chain of b - and c -hadrons inside the jet, exploiting the typical topology of weak hadronic $b \rightarrow c \rightarrow s$ decays. A modified Kalman filter [200] is used to approximate the flight path and positions of all decays vertices. Information about the kinematics and number of tracks matched at each vertex is passed to the high-level algorithm.
- A recurrent neural network (RNN) architecture, named **RNNIP** [224], considers a number of variables for each track in sequence by their importance. This allows it to exploit correlations and dependencies between the track variables, unlike the more simple algorithms described previously. The network outputs b -, c - and light jet probabilities, which are subsequently input into **DL1r**.

The **DL1r** tagger takes the outputs of the above as inputs to a fully connected multi-layer feed-forward neural network (NN) [225], the training of which is described in Ref. [53].

The outputs of **DL1r** are the probabilities to belong to the class of b -, c - or light jets, denoted $p_{b/c/\text{light}}$. In most $t\bar{t}$ analyses this is further optimised to perform as a b -tagging-only discriminant, defined:

$$\mathcal{D}_{\text{DL1r}} = \ln \left(\frac{p_b}{f_c \times p_c + (1 - f_c) \times p_{\text{light}}} \right) \quad (5.7)$$

where f_c is the fraction of c -jets in the background to b -jets, the value of which can be chosen to optimise performance. A standard choice is $f_c = 0.018$. A particular cut on the discriminant is referred to as a *working point* (WP), and is characterised by its *efficiency* in selecting b -jets. Commonly used WPs are at 60%, 70%, 77% and 85%, where the efficiencies are in MC $t\bar{t}$ events. They differ in their *rejection* of c and light jets. This is simply the inverse of the efficiency for these objects. The calibration is performed in bins of p_T and η .

⁴The transverse IP measures the closest distance between the track and primary vertex in the transverse plane. The ‘sign’ denotes whether the intersection between track and plane happens in front of or behind the primary vertex.

5.5. b/c -tagger

In order to jointly optimise for high-efficiency c - and b -tagging, a custom tool was developed for this analysis, termed the b/c -tagger. It uses the probability outputs from **DL1r** to define a set of two-dimensional working points, rather than the standard one-dimensional ones. The axes use b and c discriminants similar to the one above:

$$\mathcal{D}_{b/c} = \ln \left(\frac{p_{b/c}}{f_{c/b} \times p_{c/b} + (1 - f_{c/b}) \times p_{\text{light}}} \right) \quad (5.8)$$

The value of $f_c = 0.018$ is chosen to align with the standard calibration, then $f_b = 0.4$ is used due to the good balance of backgrounds seen following choices of binning. Five WPs are used in total: two optimised to select c -jets, two for b -jets and one untagged WP. This optimisation was performed using an independent subset of the same sample of non-all-hadronic⁵ $t\bar{t}$ events used to calculate the final efficiency and rejection rate values. The c -jet WPs both have the requirement $\mathcal{D}'_c \geq 0.625$ ⁶, and a looser ($c@22\%$) and tighter ($c@11\%$) are defined. Their names indicate their efficiencies in selecting c -jets, and $c@22\%$ is inclusive of $c@11\%$. $c@11\%$ has an additional requirement of $\mathcal{D}'_b \geq 0.825$ to improve light jet rejection. The b -jet WPs have the requirement $\mathcal{D}'_c < 0.625$, excluding the c -jet WPs. They are $b@70\%$ and $b@60\%$, requiring $\mathcal{D}'_b \geq 0.963$ and $\mathcal{D}'_b \geq 0.990$ respectively. All WPs are chosen to have efficiencies which are approximately independent of p_T and η . Their rejection rates for the other jet categories are given in Table 5.1. The remaining bin is termed ‘untagged’ and dominated by light jets. The distributions of jet categories and the working points chosen are shown in Figure 5.1.

Table 5.1.: Rejection rates for b/c -tagger WPs, the names of which indicate their efficiency in selecting their given jet category. Looser WPs are inclusive of their tighter counterparts.

Rejection rate for:	$c@22\%$	$c@11\%$	$b@70\%$	$b@60\%$
c -jets	-	-	12.2	37.1
b -jets	18.9	28.7	-	-
light jets	104	1051	573	2320

The calibration is performed using the same procedure as for the **DL1r** tagger, described in Refs. [226–228]. The first step is the determination of scale factors (SFs) to account for the differences between different MC generation setups [229]. The light jet calibration of WPs uses the *negative tag* method [230, 231], following the procedure of Ref. [228], in four p_T bins at each WP. This method is designed to allow calibration in bins with very high light jet rejection, hence very low statistics for light jets. It inverts

⁵Where at least one top quark decays via the leptonic channel.

⁶The prime indicates the application of the standard logistic function, $\mathcal{D}'_{b/c} = \frac{1}{1+\exp(-\mathcal{D}_{b/c})}$.

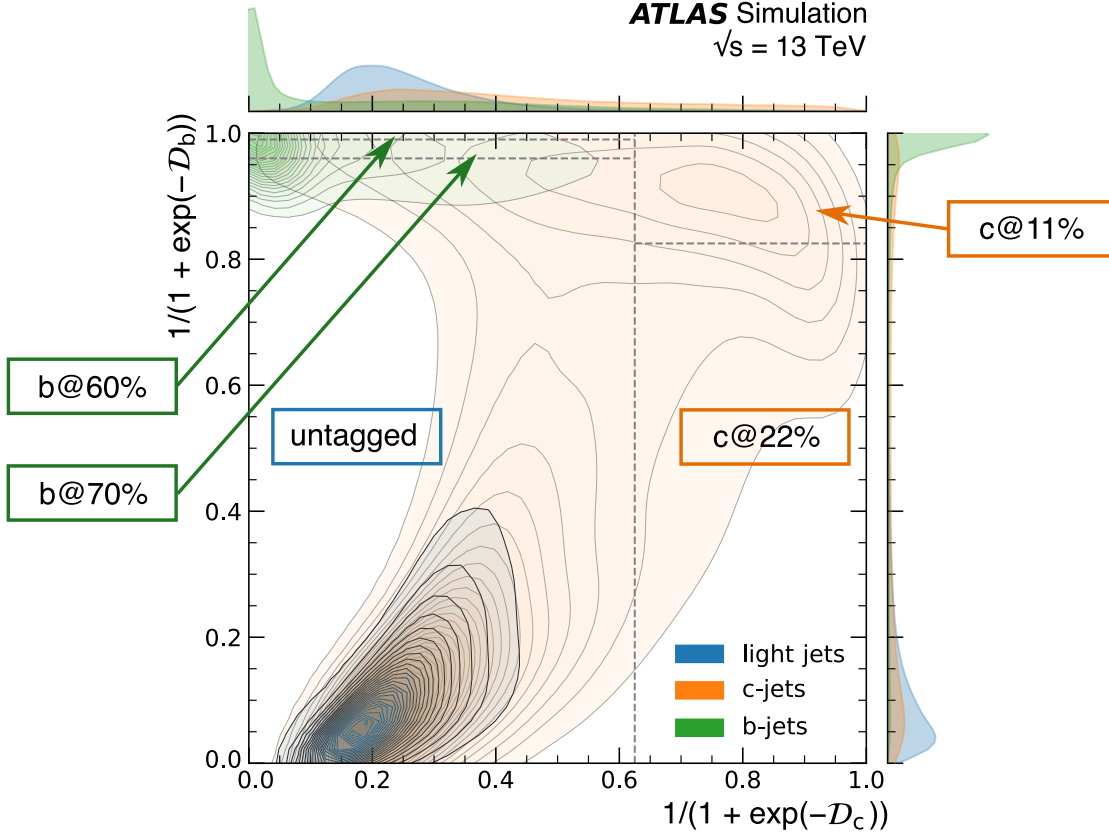


Figure 5.1.: Distribution of c -, b - and light jets with respect to discriminants, which have a logistic function applied to aid readability. Contours show lines of equal density, and are smoothed with a kernel density method. Grey dashed lines denote the boundaries of the five total working points used, with two b -tagging bins in the top left corner, two c -tagging bins on the right, and an untagged bin in the bottom left. The percentage values denote efficiency with respect to the given jet category at the given working point. Figure taken from Ref. [1].

5. Physics Object Identification and Reconstruction

the sign of all impact parameters, assuming that this leaves the light jet efficiency approximately unchanged, while the efficiency for b - and c -jets is lowered. Calibration SFs are extracted by fitting the invariant mass of secondary vertices in $Z + \text{jets}$ events. Once appropriate corrections are applied to account for the different b and c -jet behaviour, the data-MC SFs for light jets are all compatible with unity within uncertainties, with the exception of the $b@60\%$ WP. Here the number of light jets is too low, with too high heavy flavour contamination, so a value of unity is assumed and additional conservative systematic uncertainties are applied. The $c@11\%$ WP also has large uncertainties for similar reasons. In both cases these large uncertainties are expected to have a small impact on the final result, since they affect only a small number of light jets by definition. Uncertainties considered include MC modelling, an uncertainty linked to the negative tag method, statistics of data and MC events and one for the fitting procedure.

The events used for b -jet calibration [226] come from $t\bar{t}$ events decaying in the dileptonic $e\mu$ channel. The selection is similar to that for the main analysis described in Chapter 6, but with exactly two jets required, meaning it is statistically independent. It is assumed that the $t \rightarrow Wb$ branching fraction is 100%. Pairings are performed between the two jets and leptons, minimising $m_{\ell_a, j_1}^2 + m_{\ell_b, j_2}^2$, where the terms are invariant masses. For b -jets, the maximum value of $m_{\ell, j}$ will be around the mass of the top quark: 172.5 GeV. A signal region, targeting bb events, and control regions, targeting bl , lb and ll events⁷, are defined. In this process, b jets are those with $m_{\ell, j} < 175$ GeV, with l having $m_{\ell, j} \geq 175$ GeV. For example, the bl CR requires $m_{\ell_a, j_1} < 175$ GeV and $m_{\ell_b, j_2} \geq 175$ GeV. Regions are further split into nine jet p_T bins, and by the tagging bin in the signal region. An extended log-likelihood is then used to extract the b -jet tagging efficiencies in data. All resultant data-MC SFs are consistent with unity within uncertainties. In addition to experimental, modelling and statistical uncertainties, the uncertainties from the light jet calibration are propagated into the b -jet calibration uncertainties.

The c -jet calibration is performed in the $t\bar{t}$ lepton + jets channel, targeting those with $W \rightarrow cs$ decays⁸, with a requirement of exactly four jets making the selection applied similar but orthogonal to the event selection for the analysis presented here. SFs for each tagging bin, split further into four p_T bins, are derived by minimising a χ^2 function, considering the tagging status of jets originating from W decays. The assignment of which jets originate from top quark or W decays is performed using KLFitter [232], a likelihood-based reconstruction algorithm. A considerable number of the resultant SFs show deviation from unity outside uncertainty, particularly for jets tagged with $c@22\%$, exclusive of the tighter $c@11\%$ WP. The major source of uncertainty is related to MC modelling of the $t\bar{t}$ system, particularly the choice of parton shower algorithm. Large statistical uncertainties are additionally present in a number of bins at high p_T . In addition to a similar suite of uncertainties as the b -jet calibration, the previous calibration uncertainties are propagated to this procedure for c -jets.

For jets with p_T above the calibrated range, the uncertainty in the highest calibrated

⁷Ordering is based on jet p_T , and l here denotes any non- b jet.

⁸The SM branching fraction for this decay is assumed.

bin is doubled. This is chosen rather than a dedicated uncertainty as the number of jets in this range is small, being less than 2% for $t\bar{t}$ events decaying in the lepton + jets channel.

Figures showing the full range of data-MC SFs from calibration can be found in the auxiliary material of Ref. [1].

5.6. Missing transverse momentum

The missing transverse momentum, also referred to as missing transverse energy or $E_{\text{T}}^{\text{miss}}$, is used to estimate the transverse component of the momenta of particles which are not detected in the detector, notably neutrinos. In the case of multiple such particles being present, it naturally can only give the vector sum of these values.

The primary input to its calculation is the negative of the vector sum of p_{T} from all *hard-event* signals, comprising reconstructed objects such as leptons and jets. This simply relies on the principle of momentum conservation. A correction is applied for *soft-event* signals from ID tracks associated to the primary hard-scatter vertex, but not to any reconstructed objects. Finally a *signal ambiguity resolution* procedure is applied to resolve the same detector signal being reconstructed as two different objects, avoiding issues from double counting. The full procedure is given in Ref. [233].

5.7. Overlap removal

The reconstruction procedures described above are performed independently for each object type. Hence it is possible that a single detector signal may be reconstructed as two different objects. To account for this an *overlap removal* procedure is performed. For this purpose the measure of angular separation used is ΔR_y , defined identically to ΔR but using rapidity y rather than pseudorapidity η . If an electron and muon share a track, the electron is removed, as it is likely it was produced by bremsstrahlung. The closest jet within $\Delta R_y < 0.2$ of an electron is removed, but if any jets remain within $\Delta R_y < 0.4$ the electron is removed as it likely came from a weak decay inside the jet. Similarly, muons within $\Delta R_y < 0.4$ of a jet are removed. However in the case that this jet has fewer than three tracks associated with it, the jet is removed. This accounts for high- p_{T} muons which can deposit a large amount of energy in the calorimeter.

Event Selection and Classification

Two channels are used in this analysis, corresponding to different decay modes of the top quark pair, as introduced in Section 2.4. The dileptonic $t\bar{t}$ decay is relatively rare, with a branching ratio of around 4%, but the channel benefits from a pure signal with limited contamination from non- $t\bar{t}$ events. Meanwhile the lepton + jets channel is characterised by a greater number of events, reducing statistical uncertainty. However it has larger number of background events, and there is the possibility of the hadronically-decaying W boson producing a c -quark, which may be mistaken as additional to the $t\bar{t}$ system.

In this chapter the series of selection cuts and classifications are described, which are used to select events and structure their information so as to facilitate a sensitive measurement of $t\bar{t} + \geq 1c$ events. Section 6.1 sets out the preselection used to select data events in the the channels described above. Section 6.2 outlines the procedure used to estimate the contribution from background processes. In particular, it describes the steps taken to estimate the contribution from events with non-prompt, or ‘fake’, leptons. Then in Section 6.3 events are categorised by the types of jets they contain, thereby defining precisely the signal being measured. Finally in Section 6.4 it is described how the selected events are sorted into analysis regions to be used for fitting, also the variables chosen to further separate event categories within those regions.

6.1. Event pre-selection

The data used in this analysis comes from pp collisions recorded by ATLAS at $\sqrt{s} = 13\text{TeV}$ during Run 2, from 2015-2018. The quality of collision data is monitored both online and offline [234], forming what are known as *good run lists* (GRLs): periods of data taking when all detector components are judged to have been functioning to a high standard. This full dataset is used, corresponding to a total of 140fb^{-1} of integrated luminosity.

6. Event Selection

With simulated events in place to be compared to data, it is necessary to make a broad *pre-selection* of events which are likely to be of interest and used to define analysis regions. This also reduces the amount of data which must be processed further. For this analysis the aim is to have a large number of $t\bar{t}$ events with additional jets, with a bias towards heavy flavour jets. All selection criteria (including further selection criteria) are applied both to data and MC.

The ATLAS trigger system was described in Section 3.3.4. In this case since events both in the lepton + jets and dilepton channel feature leptons (electrons or muons), events are selected using single-lepton triggers [235, 236]. These triggers are organised into chains, where firing any one of them is sufficient for the event to be selected, and are listed in Table 6.1. The change in p_T threshold from 2015 to 2016-2018 data-taking periods was due to increased pileup in the detector. The higher threshold helped to reduce the number of events recorded and maintain a stable data-taking rate.

Table 6.1.: List of single-lepton triggers applied for each data-taking period of data used with associated p_T thresholds.

Year	Single- e trigger	p_T/GeV	Single- μ trigger	p_T/GeV
2015	HLT_E24_LHMEDIUM_L1EM20VH	24	HLT_mu20_loose_L1MU15	20
	HLT_E60_LHMEDIUM	60	HLT_mu50	50
	HLT_E120_LHLOOSE	120		
2016-2018	HLT_E26_LHTIGHT_NOD0_IVARLOOSE	26	HLT_mu26_ivarmedium	26
	HLT_E60_LHMEDIUM_NOD0	60	HLT_mu50	50
	HLT_E140_LHLOOSE_NOD0	140		

All objects must pass the quality criteria outlined in Section 5. Furthermore all events must have at least one primary vertex which is associated to at least two tracks having $p_T > 0.5$ GeV. In the case of multiple vertices matching this criterion, the hard-scattering vertex is taken to be the one with the highest value of $\sum p_T^2$ [237] over associated tracks.

Further pre-selections are split depending on the analysis channels studied.

In the lepton + jets channel, events are required to have exactly one electron or muon¹ with $p_T > 27$ GeV, ensuring they are above the trigger threshold. At least five jets must be present, with $p_T > 25$ GeV and $|\eta| < 2.5$. Finally at least two jets must be b -tagged using the DL1r tagging algorithm at a 70% efficiency working point, and at least three at the looser 85% working point. These are mainly natural requirements to select $t\bar{t}$ events decaying to lepton + jets, with at least one additional jet. The third b -tag is intended to enhance the contribution from heavy-flavour jets. Note that the pre-selection b -tag requirements in this channel use DL1r working points rather than those from b/c -tagger. This is done for technical reasons, and the relatively loose additional b -jet requirement does not remove a significant number of signal events.

¹As discussed in Section 2.4.2, these are the only particles considered when discussing ‘leptons’ for the purposes of this analysis.

In the dilepton channel, exactly two leptons of either flavour are required (i.e. they can be $ee, \mu\mu$ or $e\mu$), which must be of opposite charge. One of these leptons must have $p_T > 27$ GeV, and also be matched to a lepton of the same flavour reconstructed by the trigger system. Only for ee and $\mu\mu$ events, requirements are placed on the invariant mass of the lepton pair $m_{\ell\ell}$. These are that $m_{\ell\ell} > 15$ GeV, to reduce Drell-Yan production, and an additional veto in a window around the mass of the Z : $83 \text{ GeV} < m_{\ell\ell} < 99 \text{ GeV}$. There must be no reconstructed hadronically-decaying τ leptons. To select events with at least one additional jet, at least three jets are required in total, two of which must be b -tagged using the b/c -tagger $b@70\%$ working point.

6.2. Estimation of backgrounds

The majority of background processes have their contributions estimated using events passing pre-selection from the dedicated simulations described in Section 4.2. However a separate process is used for events containing ‘fake leptons’ or simply ‘fakes’. In this document these are defined as any leptons not originating from the original hard-scattering interaction. They may come from mis-reconstruction or mis-identification of another object, including mis-assigning the charge of a lepton of the correct flavour. Alternatively they may be real leptons produced by weak decays in jets, or by interactions of particles with the detector material. In MC events, generator information can be used to identify events containing fakes.

For the dilepton channel the contribution of fake leptons to the selected sample is estimated from MC, considering $t\bar{t}$ non-all-hadronic, V +jets, VV , $t\bar{t}V$ and single-top processes. However for the lepton + jets channel a data-driven approach is used, termed the *matrix method* [238]. This method in each of the lepton+jets channel analysis regions defined in Section 6.4, where a set of lepton isolation, identification and reconstruction quality criteria are applied. In each region two sets of criteria are defined: one is *tight*, the one used for analysis, and the other is *loose*, which is inclusive of tight leptons and has looser quality and identification requirements, with none on lepton isolation. All other requirements are the same. The quantity to be estimated is $N_{\text{fake}}^{\text{tight}}$: the number of fake leptons passing the tight selection in the analysis region. It can be expressed:

$$N_{\text{fake}}^{\text{tight}} = \frac{\epsilon_{\text{fake}}}{\epsilon_{\text{real}} - \epsilon_{\text{fake}}} \left(\epsilon_{\text{real}} N^{\text{loose}} - N^{\text{tight}} \right) \quad (6.1)$$

with the *efficiencies* $\epsilon_{\text{real/fake}} = \frac{N_{\text{real/fake}}^{\text{loose}}}{N_{\text{real/fake}}^{\text{tight}}}$ and $N^{\text{loose/tight}} = N_{\text{real}}^{\text{loose/tight}} + N_{\text{fake}}^{\text{loose/tight}}$.

To estimate ϵ_{real} , the tag-and-probe method is used in Z boson decays using only MC events. ϵ_{fake} uses both data and MC in a region selected to be enriched in fake leptons. This requires at least three jets, at least two jets b -tagged with the DL1r [53] tagger at the 70% efficiency WP, and one lepton fulfilling the loose criterion. Furthermore, to increase the fraction of fake leptons, the sum of the missing transverse momentum and leptonically-decaying W boson mass must be less than 60 GeV. The efficiency estimation is done in bins of p_T and $|\eta|$. To estimate a full binned distribution of fake lepton events

6. Event Selection

in data, a weight w_i is applied to those events satisfying the loose requirement in the analysis region, with efficiencies being taken from the appropriate bins for the event:

$$w_i = \frac{\epsilon_{\text{fake}}}{\epsilon_{\text{real}} - \epsilon_{\text{fake}}} (\epsilon_{\text{real}} - P_i) \quad (6.2)$$

where $P_i = 1$ if the tight criteria are met, and otherwise $P_i = 0$.

The final template for fake events produced has positive and negative contributions. When this procedure is performed in the lepton+jets regions, the statistical fluctuations are large. Some bins have a negative yield and the shapes of the distributions are distorted. To account for this, the shape of the fakes template is taken from events with negative weights flipped (i.e. taking the absolute values of weights). This ‘smoothed’ shape is rescaled in each region to the fake background already calculated, with statistical uncertainties kept for each bin of the distribution. These uncertainties are large and cover all discrepancies between the original and smoothed shapes.

6.3. Classification of simulated events

In the LHC, quarks produced in events are ultimately seen in the detector as jets following hadronisation, which contain a large number of different objects. How the flavour of the original quark is determined experimentally is discussed in Sections 5.4 and 5.5. However it is also necessary to classify MC events, thereby defining what is actually meant by ‘ $t\bar{t}$ in association with charm quarks’, in addition to the other $t\bar{t}$ event categories used. The procedure used for this is known as ‘heavy flavour classification’, which has been used by several ATLAS analyses [193, 239]. This common definition aids comparability and consistency across analyses.

The jets being classified are particle jets formed by the MC generator from stable particles². Similar to jets reconstructed from detector information as described in Section 5.3, they are constructed using the anti- k_t algorithm with radius parameter $R = 0.4$, and additionally must have $p_T > 15$ GeV and $|\eta| < 2.5$. Jets (see Section 5.3) are then matched with underlying hadrons (from MC generator information) at particle level using *ghost matching* [206, 240]. This method has been shown to have improved performance relative to *geometrical matching*, which simply uses the separation ΔR between objects [241]. In ghost matching an infinitesimally soft ($p_T = 1\text{eV}$) track is added corresponding to the hadron in question, thereby not affecting the event kinematics. Following anti- k_t clustering, it can be identified which jet this track was clustered into. In particular the number of b - and c - containing hadrons matched to a jet is used to define its flavour.

All events being classified are $t\bar{t}$ events, with associated decay products from the $t\bar{t}$ system. However the heavy flavour classification system is directed towards *additional* jets. Hence jets matched to the closest (in ΔR) b -hadron to a b quark from $t\bar{t}$ decay are neglected. The same is true for jets matched to the closest c -hadron to any c quarks from a W boson in this system. Following this, jets ghost matched to one or more b -hadrons

²Defined as having a mean lifetime $> 3 \times 10^{-11}$ s.

are considered b -jets, with a requirement that the leading b -hadron has $p_T > 5\text{GeV}$. This means that one b -jet may contain the hadronisation products from eg. both members of a $b\bar{b}$ pair. c -jets are defined analogously, but excluding those jets already labelled b -jets. This acts to exclude c -hadrons from the decay of b -hadrons.

Following the labelling of particle jets, events are exclusively categorised as one of:

- $t\bar{t} + 1b$ if they have exactly one b -jet
- $t\bar{t} + \geq 2b$ if they have two or more b -jets
- $t\bar{t} + 1c$ if they have exactly one c -jet, and no b -jets
- $t\bar{t} + \geq 2c$ if they have two or more c -jets, and no b -jets
- $t\bar{t} + \text{light}$ for all other $t\bar{t} + \text{jets}$ events

For most purposes of the analysis $t\bar{t} + 1b$ and $t\bar{t} + \geq 2b$ are grouped as $t\bar{t} + \geq 1b$. However certain systematic uncertainties are applied separately to these groups as described in Section 8.3.

Background events are also grouped in several plots and tables to aid readability. ‘Non-top’ refers to diboson, $W + \text{jets}$ and $Z + \text{jets}$ events. ‘Other top’ is used for all t -containing backgrounds, which are single-top production, $t\bar{t}W$, $t\bar{t}Z$, $t\bar{t}H$, tZq and tWZ processes. ‘Fakes’ contains events with misidentified or non-prompt leptons, as discussed in Section 6.2.

6.4. Definition of regions

The aim of defining regions for the analysis is to have some with a high fraction of $t\bar{t} + \geq 1c$ signal events, termed signal regions (SRs), while others are sensitive to the different background contributions, termed control regions (CRs). This allows an accurate measurement of all contributions once fitting is performed, as described in Section 7.1.

Regions are defined by the the number of tagged jets, using the outputs of b/c -tagger, as summarised in Table 6.2. As described in Section 5.5, the looser b/c working points ($b@70\%$ and $c@22\%$) are inclusive of the tighter working points ($b@60\%$ and $c@11\%$). Regions are further split by total jet multiplicity, into five-jet-exclusive ($N_{\text{jets}} = 5$) and six-jet-inclusive ($N_{\text{jets}} \geq 6$) regions in the lepton + jets channel, and into three-jet-exclusive ($N_{\text{jets}} = 3$) and four-jet-inclusive ($N_{\text{jets}} \geq 4$) regions in the dilepton channel. Although additional jets are normally produced in pairs, leading to an expected number of jets of six and four respectively for the lepton + jets and dilepton channels, this choice allows for cases where one jet is outside of the detector acceptance, or two jets are merged during the reconstruction process. In the names of regions, a ‘ 1ℓ ’ superscript denotes the lepton + jets channel, while ‘ 2ℓ ’ denotes the dilepton channel. Additional superscripts may be used to denote the jet multiplicity of the region, while subscripts denote the name or number of the region in question eg. $\text{CR}_1^{1\ell 5j}$, $\text{SR}_{\text{loose}}^{2\ell \geq 4j}$.

6. Event Selection

Table 6.2.: Definitions of signal regions (SRs) and control regions (CRs) in the lepton + jets (1ℓ) and dilepton (2ℓ) channels, by the multiplicity of jets tagged by b/c -tagger at different working points. Each region definition is further split by jet multiplicity, into five-jet-exclusive and six-jet-inclusive regions in the lepton + jets channel, and into three-jet-exclusive and four-jet-inclusive regions in the dilepton channel. Numbers without inequalities indicate an exact match in the number of tags is required. The main $t\bar{t}$ + jets event category targeted by each region is highlighted. * $\text{SR}_{\text{tight}}^{2\ell}$ is defined only with a four-jet-inclusive selection.

	$\text{CR}_1^{1\ell}$	$\text{CR}_2^{1\ell}$	$\text{CR}_3^{1\ell}$	$\text{SR}_{\text{loose}}^{1\ell}$	$\text{SR}_{\text{tight}}^{1\ell}$	$\text{CR}_1^{2\ell}$	$\text{CR}_2^{2\ell}$	$\text{CR}_3^{2\ell}$	$\text{SR}_{\text{loose}}^{2\ell}$	$\text{SR}_{\text{tight}}^{2\ell}$ *
$b@70\%$	2	-	-	2	2	2	-	≥ 3	2	2
$b@60\%$	-	≥ 3	3	-	-	-	≥ 3	≤ 2	-	-
$c@22\%$	1	0	1	≥ 2	-	0	-	-	1	≥ 2
$c@11\%$	1	-	1	1	≥ 2	-	-	-	-	-
Targeted category	$t\bar{t} + \text{light}$	$t\bar{t} + \geq 1b$	$t\bar{t} + \geq 1b$	$t\bar{t} + 1c$	$t\bar{t} + \geq 2c$	$t\bar{t} + \text{light}$	$t\bar{t} + \geq 1b$	$t\bar{t} + \geq 1b$	$t\bar{t} + 1c$	$t\bar{t} + \geq 2c$

Signal regions are defined to have a high purity of $t\bar{t} + \geq 1c$ signal events, with differing numbers of events from $t\bar{t} + 1c$ and $t\bar{t} + \geq 2c$, as well as non-identical backgrounds. For all signal regions, there is the shared requirement of exactly two b -jets tagged at the looser $b@70\%$ working point, thereby having the expected number of b -jets for a $t\bar{t}$ event, but no more. In the lepton + jets channel all SRs feature events with at least two c -jets tagged at the $c@22\%$ working point. These are split into $\text{SR}_{\text{loose}}^{1\ell}$ and $\text{SR}_{\text{tight}}^{1\ell}$, with $\text{SR}_{\text{loose}}^{1\ell}$ having exactly one c -jet tagged with $c@11\%$, and $\text{SR}_{\text{tight}}^{1\ell}$ having two or more c -jets tagged at this working point. For the dilepton channel no requirements are placed on $c@11\%$ tags, with $\text{SR}_{\text{loose}}^{2\ell}$ having exactly one jet tagged with $c@22\%$, and $\text{SR}_{\text{tight}}^{2\ell}$ having two or more. There is no $\text{SR}_{\text{tight}}^{2\ell}$ region for the three-jet-exclusive selection. This gives a total of nine SRs, with the tight signal regions having a higher fractional contribution from $t\bar{t} + \geq 2c$ events as shown in Figure 6.1.

A total of 12 CRs are used, defined so as to have differing contributions from $t\bar{t} + \text{light}$, $t\bar{t} + 1b$ and $t\bar{t} + \geq 2b$ events. The expected composition of these can also be seen in Figure 6.1. In the lepton + jets channel, $\text{CR}_1^{1\ell}$ requires exactly two jets tagged with $b@70\%$, and exactly one tagged with $c@11\%$, and no more additional jets tagged with $c@22\%$. This region is enriched in $t\bar{t} + \text{light}$ events, with some additional contribution from $t\bar{t} + 1c$ due to the c -tag requirement. $\text{CR}_2^{1\ell}$ and $\text{CR}_3^{1\ell}$ are both dominated by $t\bar{t} + \geq 1b$ events, with differing $t\bar{t} + \text{light}$ contributions. These also contain different fractions of $t\bar{t} + 1b$ and $t\bar{t} + \geq 2b$ events. $\text{CR}_2^{1\ell}$ requires at least three $b@60\%$ jets, and none which are c -tagged. $\text{CR}_3^{1\ell}$, meanwhile, requires exactly three jets tagged with $b@60\%$, and exactly one c -jet tagged with $c@11\%$, with a veto on any further c -jets.

In the dilepton channel, $\text{CR}_1^{2\ell}$ is highly enriched in $t\bar{t} + \text{light}$ events, and requires exactly two jets tagged with $b@70\%$, without any c -tagged jets. $\text{CR}_2^{2\ell}$ mostly contains $t\bar{t} + \geq 1b$ events, due to a requirement of three or more $b@60\%$ jets, and no requirement on c -jets. $\text{CR}_3^{2\ell}$ has a similar but orthogonal definition, with at least three b -jets at the looser $b@70\%$ working point, but less than three with the tighter $b@60\%$ tag. It similarly

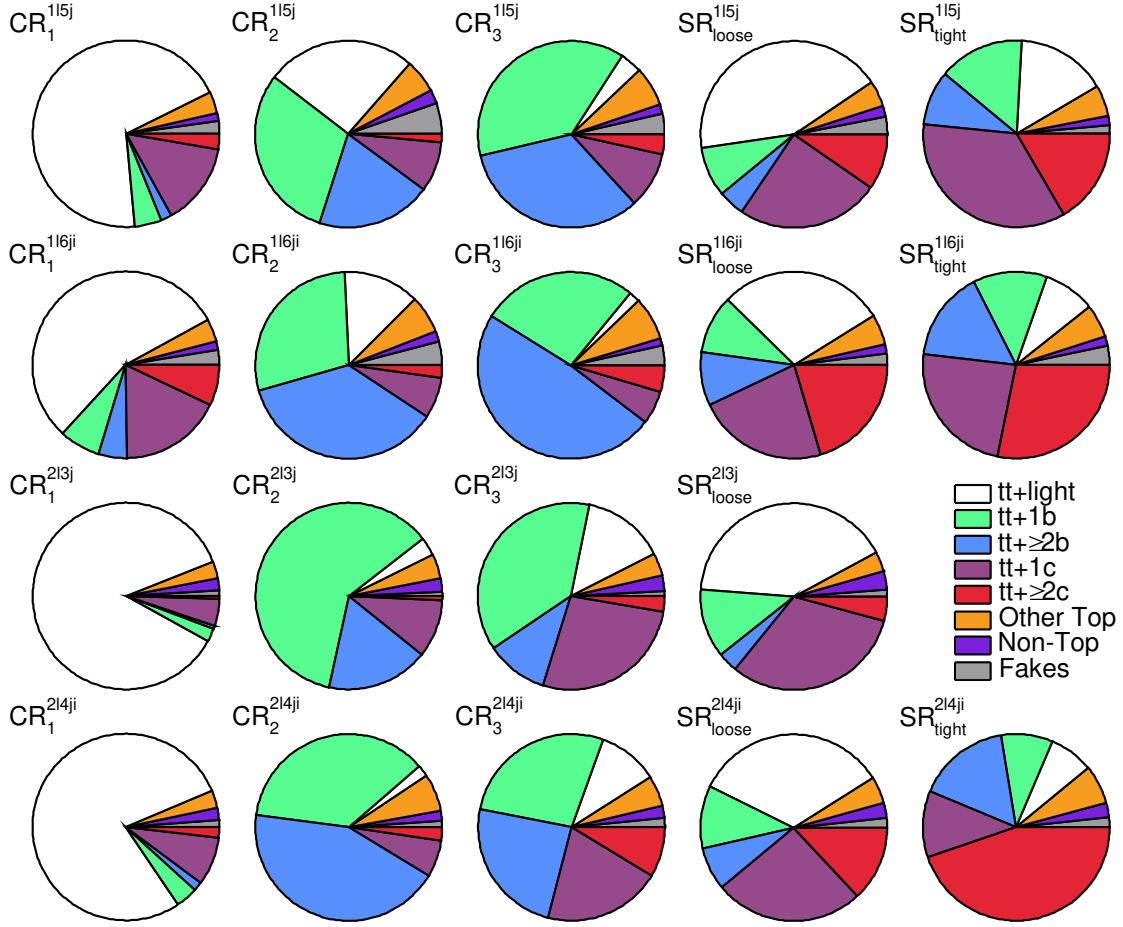


Figure 6.1.: Expected fraction of each event category in each analysis region.

is enriched in $t\bar{t} + \geq 1b$ events, but has a significantly higher contribution from $t\bar{t} + \geq 1c$, as well as slightly different fractions of $t\bar{t} + 1b$ and $t\bar{t} + \geq 2b$ events.

Given that both CR_2 and CR_3 target $t\bar{t} + \geq 1b$ events, a study was performed on possibilities to merge them, described in Section 9.3. This found a negative effect on the sensitivity of the final result, motivating the decision to retain the set of definitions presented.

It can be observed that all $t\bar{t} + \text{jets}$ categories have significant contributions in all analysis regions, though the fraction varies significantly. This cross-contamination is not entirely unexpected, given that the regions are defined by b/c -tagging, which does not have 100% efficiency. The fraction of non- $t\bar{t}$ backgrounds can be seen to be generally low, with the most significant category being single-top events. A full list of the expected event numbers by category in each region, alongside the number of data events, can be found in Appendix B.

6. Event Selection

6.4.1. Observables

Rather than simply counting events in each region, the sensitivity of the analysis to each $t\bar{t} + \text{jets}$ category can be enhanced by fitting their distributions. Such observables are here used only in the signal regions, with all control regions simply containing an overall event yield. In the regions $\text{SR}_{\text{loose}}^{1\ell 5j}$ and $\text{SR}_{\text{tight}}^{1\ell 5j}$, the observable used is the invariant mass of the two c -jets closest in ΔR , denoted $M_{cc}^{\text{min}\Delta R}$. For the region $\text{SR}_{\text{tight}}^{1\ell 5j}$ only those c -jets tagged with $c@11\%$ are considered. With this observable, the $t\bar{t} + \text{light}$ contribution shows an increase around the W boson mass, due to c -jets coming from their decay. For $\text{SR}_{\text{loose}}^{2\ell 3j}$ a similar variable is used, denoted $M_{cb}^{\text{min}\Delta R}$ and corresponding to the invariant mass of the event's c -tagged jet and the closest b -tagged jet. The pre-fit data/MC agreement for these regions is shown in Figure 6.2.

For the six- and four-jet-inclusive regions, the observable chosen to enhance the separation of $t\bar{t} + \text{jets}$ categories is the jet multiplicity, as shown in Figure 6.3. Upon visual inspection it is not immediately clear that this variable provides additional separation between event categories, but studies performed show that including this information does indeed improve the sensitivity of the analysis, as will be shown in Section 9.3.

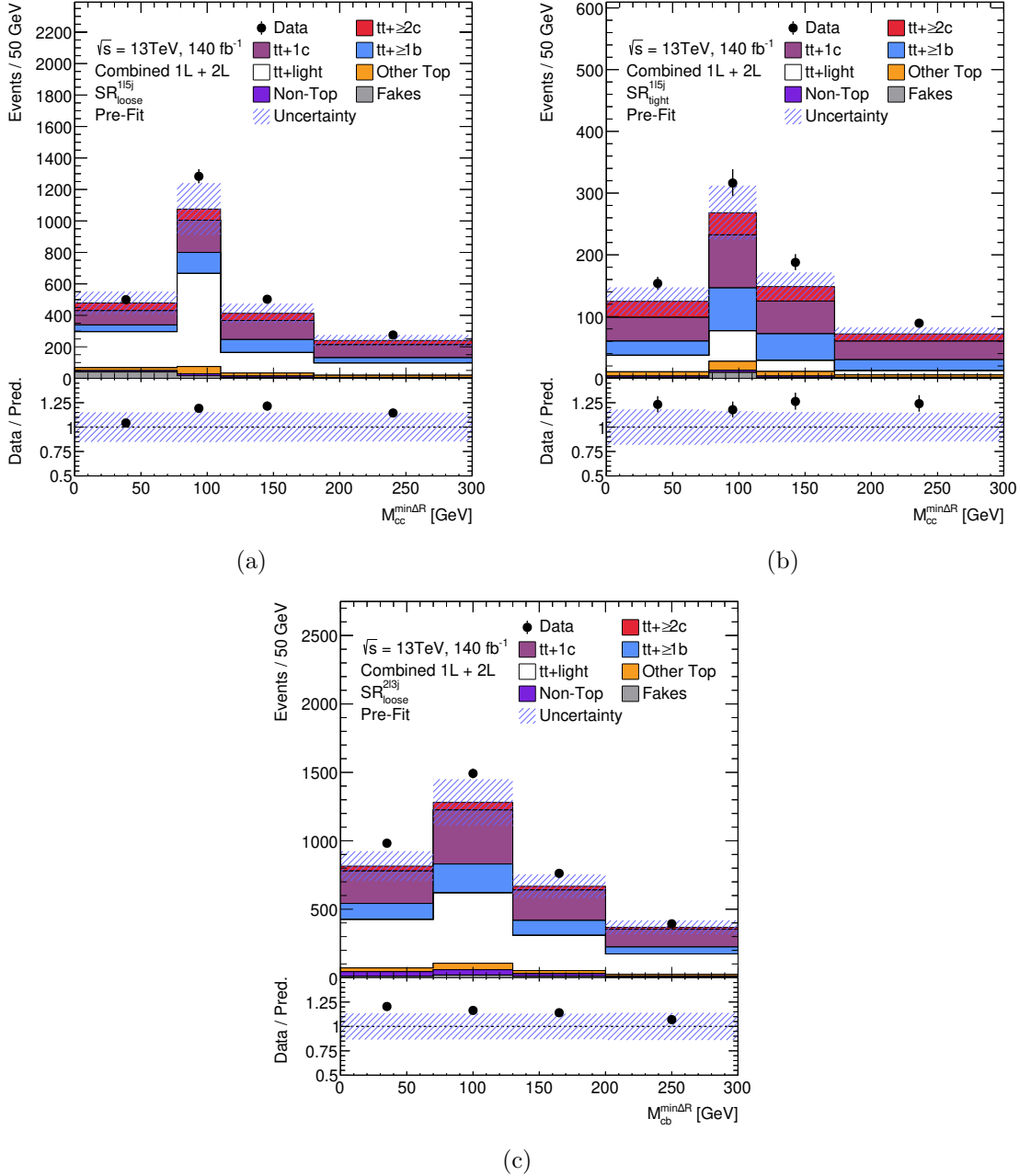


Figure 6.2.: Pre-fit plots comparing MC predictions and data in signal regions SR_{loose}^{1l5j} , SR_{tight}^{1l5j} and SR_{loose}^{2l3j} . The lepton + jets signal regions use the observable $M_{cc}^{\min\Delta R}$, the invariant mass of the two c -jets separated by the smallest ΔR . In SR_{tight}^{1l5j} only those c -jets tagged with $c@11\%$, the tighter c -tagging working point, are considered. Events in SR_{loose}^{2l3j} have only one c -jet, so the observable is $M_{cb}^{\min\Delta R}$, the invariant mass of it and the closest b -jet. Events outside the range are put into the first or last bin, and the blue uncertainty band includes both statistical and systematic uncertainties.

6. Event Selection

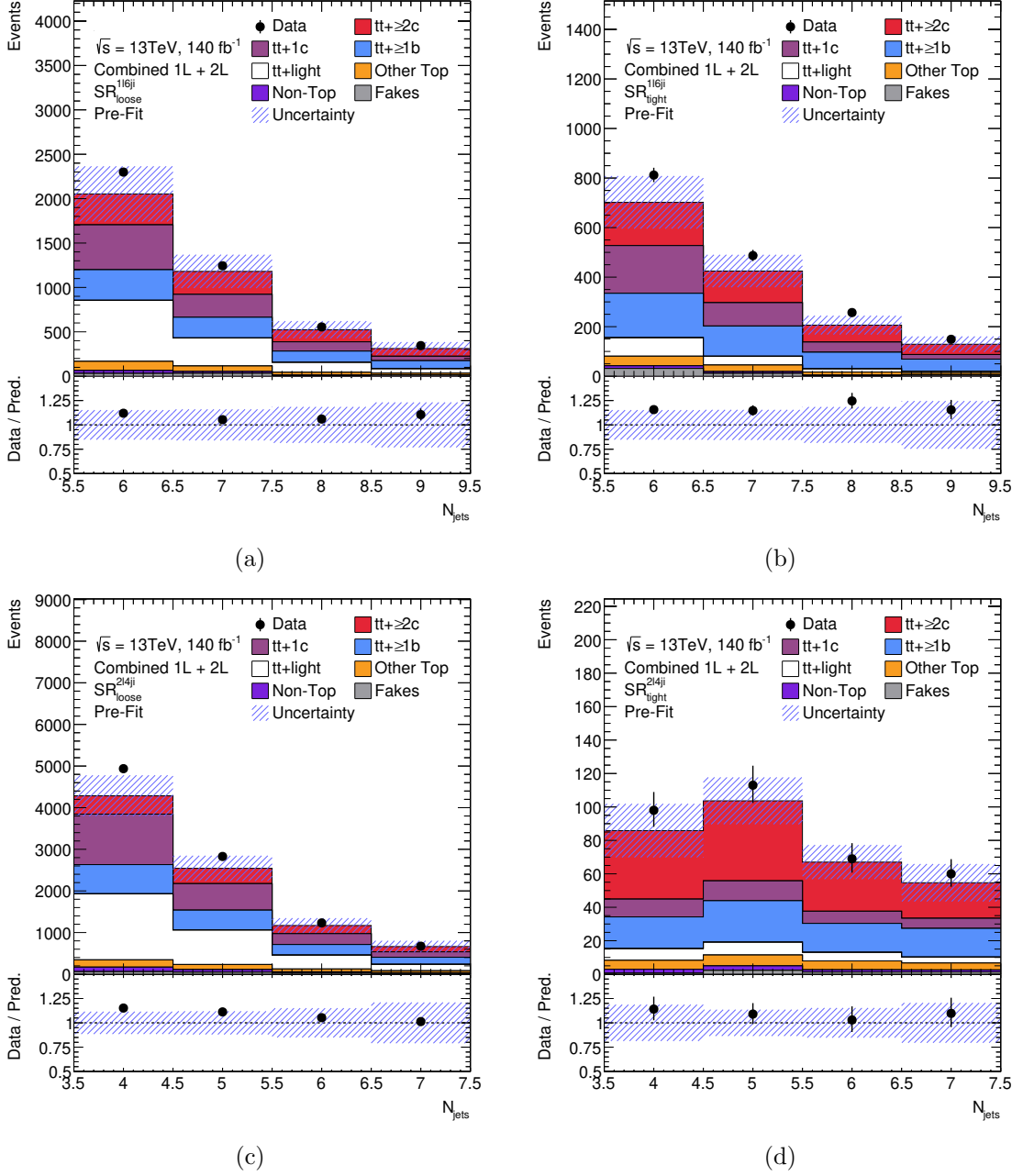


Figure 6.3.: Pre-fit plots comparing MC predictions and data in signal regions $\text{SR}_{\text{loose}}^{1\ell\geq 6j}$, $\text{SR}_{\text{tight}}^{1\ell\geq 6j}$ and $\text{SR}_{\text{loose}}^{2\ell\geq 4j}$ and $\text{SR}_{\text{tight}}^{2\ell\geq 4j}$. The observable used is the jet multiplicity. The last bin additionally contains events with jet multiplicities greater than the maximum shown, and the blue uncertainty band includes both statistical and systematic uncertainties.

Previous chapters described event selection and categorisation into regions following selection cuts. This chapter lays out the several closely related fitting procedures used to extract the $t\bar{t} + \geq 2c$ and $t\bar{t} + 1c$ cross-sections, in both a fiducial and inclusive phase space, as well as the ratio of these to all $t\bar{t} + \text{jets}$ events. Section 7.1 describes the profile likelihood fit applied to the data and simulated events, while Section 7.2 then defines the fiducial phase space in which the principal cross-section result is measured. Section 7.3 details the different parameterisations of events used in different fit setups, and finally Section 7.4 compares aspects of the strategy used to the only other similar published analysis, performed by the CMS Collaboration.

7.1. Fitting strategy

In order to obtain a measurement of the number of $t\bar{t} + \geq 1c$ events, the contribution of each event category to the observed data must be evaluated, whilst taking into account the full range of statistical and systematic uncertainties (see Chapter 8 for more detail on those considered). The method employed for this is a *profile likelihood fit*. In this section the theoretical basis for this method and its implementation will be laid out. It has theoretical strengths, as it tends to zero *bias* (the difference between expectation value produced and actual value) in the large sample limit [242]. Furthermore as used it satisfies the Cramér–Rao bound [243, 244] for minimum *variance* in an unbiased estimator. Practically, it provides an effective way to simultaneously handle a large number of parameters of interest and systematic parameters, as well as estimate their uncertainties.

The implementation of this method uses TREXFITTER, an ATLAS internal software package based on HISTFACTORY [245], in turn using tools from ROOSTATS [246] and ROOFIT [247], part of the ROOT [248] framework.

When performing any experiment, any individual observed value x can be thought of

7. Analysis Strategy

as a sample from a *probability distribution function* (pdf) $f(x)$, which is normalised to unity. Through performing a series of n independent measurements to make a dataset $\{\mathbf{x}\} = \{x_1 \dots x_n\}$, a *likelihood* $L(\boldsymbol{\alpha})$ can be defined for the given data. Here $\boldsymbol{\alpha}$ denotes the set of parameters which comprise a *model*, for example assumed values for certain cross-sections and detector properties.

$$L(\boldsymbol{\alpha}) = \text{Pois}(n|\nu(\boldsymbol{\alpha})) \prod_{i=1}^n f(x_i|\boldsymbol{\alpha}) \quad (7.1)$$

This is known as the marked Poisson model, where $\nu(\boldsymbol{\alpha})$ denotes the number of expected events given a particular set of parameters, and *Pois* denotes the Poisson distribution $\text{Pois}(a|b) = \frac{b^a e^{-b}}{a!}$. The form of Equation 7.1 can be changed into an *extended likelihood* [249]

$$-\ln L(\boldsymbol{\alpha}) = \nu(\boldsymbol{\alpha}) + \ln(n!) - n \ln \nu(\boldsymbol{\alpha}) - \sum_{i=1}^n f(x_i|\boldsymbol{\alpha}) \quad (7.2)$$

For the parameter list $\boldsymbol{\alpha}$, the values which minimise $-\ln L$ (equivalent to maximising L) are termed the *maximum likelihood estimates* (MLEs) denoted $\hat{\boldsymbol{\alpha}}$. Since only the relative value of the likelihood is of interest, the constant $\ln(n!)$ term can be dropped.

Then to test a particular value for one parameter out of the larger set, α_0 , the *profile likelihood ratio* can be used

$$\lambda(\mu) = \frac{L(\alpha_0, \hat{\boldsymbol{\alpha}})}{L(\hat{\alpha}_0, \hat{\boldsymbol{\alpha}})} \quad (7.3)$$

where $\hat{\boldsymbol{\alpha}}$ in the numerator denotes the MLE parameter values, given the particular value of α_0 . The denominator is simply the maximised likelihood value. Thus any model parameter, whether the main *parameter of interest* (POI) or systematic uncertainty, can have a likelihood profile extracted, allowing an estimate both of its ‘best fit’ value and uncertainty. The profile likelihood ratio is the *test statistic* used to drive fitting.

For practical purposes, instead of performing calculations event-by-event a *binned* dataset in the form of histograms is used, across several statistically independent analysis regions. The desired goal is to measure one (or more) of the POI, while the rest are labelled *nuisance parameters* (NPs). In many cases we may have some knowledge of the possible values of these NPs (for example the cross-section of a background process which has been measured previously). To reflect this, *constraints* are introduced, introducing penalty terms into the likelihood when NPs deviate from their expected value. This constraint implements some prior pdf describing its possible values. In HISTFACTORY model parameters act in three ways:

1. Free-floating normalisation parameters, here denoted μ_p , are introduced for each process p . In particular the cross-sections for $t\bar{t} + 1c$, $t\bar{t} + \geq 2c$, $t\bar{t} + \geq 1b$ and $t\bar{t} + \text{light}$ are each scaled by the corresponding normalisation factors, with $\mu_{t\bar{t}+1c/t\bar{t}+\geq 2c}$ being the POIs. They have no constraint applied, and are defined such that $\mu_p = 1$ corresponds to the predicted number of events from MC.

2. Statistical uncertainties for each bin and process considered are controlled by NPs denoted by γ . This is important since the MC predictions used have finite statistics, which these account for [250]. To avoid an extremely large number of NPs these are normally combined for several processes, with just one per bin γ_b . A Poisson distribution is used to constrain their values.
3. Systematic uncertainties are in general implemented through separate normalisation uncertainties $\eta_p(\theta)$, scaling the process in all bins, and a shape uncertainty $\sigma_{pb}(\theta)$, acting on each bin b . These systematic uncertainties are estimated through *templates*, whereby for each uncertainty (one NP θ), for each process, alternative predictions (termed an *up* and *down* variation) are provided. These are parameterised to $\theta = \theta_0 \pm \Delta\theta$, and correspond to $\pm 1\sigma$ in a Gaussian distribution constraining θ , with the nominal prediction θ_0 corresponding to the nominal prediction. To enable a continuous nuisance parameter, *interpolation* must be performed based on this limited information. For normalisation uncertainties $\eta_p(\theta)$ piecewise exponential interpolation is used, whereas for shape uncertainties $\sigma_{pb}(\theta)$ piecewise linear interpolation is employed [245]. For additional detail on the treatment of systematic templates see Section 8.1.

Once fitting has been performed, the MLE for θ , $\hat{\theta}$, may differ significantly from θ_0 . This is termed a *pull*, numerically parameterised by $\frac{\hat{\theta} - \theta_0}{\Delta\theta}$, so that a pull of -1 indicates that the down variation provided is ‘preferred’ by the fit. Additionally, the likelihood ratio can be used to estimate a post-fit uncertainty of θ : $\Delta\hat{\theta}$. If this is smaller than the prior uncertainty $\Delta\theta$ it is termed a *constraint*. The presence of pulls and constraints are not necessarily problematic, as it may be that the prior pdf was overly conservative, or the data being fit to is providing new information on the likely value of the systematic uncertainty. However they should ideally be well-motivated and/or understood.

Correlations between parameters are also calculated, and are taken into account when uncertainties are calculated.

A key tool in understanding the fit model is the so-called *Asimov* pseudo-dataset. This assumes that in each bin, the number of observed events is exactly equal to the expectation. When a fit is performed to this data the MLEs all have their nominal values: $\hat{\mu}_p = 1$, $\hat{\theta} = \theta_0$. The purpose of this process is to show the expected uncertainty on parameters (both the POIs and NPs), as well as to allow inspection of correlations in the fit model.

Saturated model for goodness-of-fit

The method used to determine the goodness-of-fit utilises a *saturated model* [251, 252]. This is a generalisation of the normal χ^2 goodness-of-fit, and can be applied to binned data not following a Gaussian distribution. The saturated model in question is one that has sufficient parameters to fit the data perfectly - typically this means the number of parameters is equal to the number of data points. The ratio can then be taken between

7. Analysis Strategy

the maximised likelihood from fitting the existing model, and that from the saturated model. By Wilks' theorem [253], this ratio will approach a χ^2 distribution asymptotically for large sample sizes, so it can be used as a rigorous metric for the goodness-of-fit. The implementation of this method is done using ROOFIT [247], and for fits performed here has been translated into a percentage probability.

7.2. Fiducial phase space definition

The measurement is performed for two phase space regions: the one used in event generation (termed the *inclusive* phase space), and the *fiducial* phase space, defined below. The fiducial phase space is defined at particle level, and is designed to mimic the event selection performed at detector level.

For electrons and muons, it is required that $|\eta| < 2.5$, and any of these which are close to a jet ($\Delta R < 0.4$) are removed. This aims to remove any electrons or muons which have been produced by decays in the jet, rather than from the original hard scattering. The remaining requirements on leptons are identical to those used in event pre-selections, as defined in Section 6.1. Jets must follow the pre-selection requirements for p_T and $|\eta|$, as well as jet multiplicity per event. Finally, at least two jets which have been ghost matched with a b -hadron must be present.

When calculating the value of the cross section in the fiducial phase space, it is necessary to take into account two factors: the *fiducial acceptance* ϵ and the *out-of-fiducial* fraction, f_{out} . The fiducial acceptance is the fraction of events in the fiducial phase space that also pass the cuts applied at reconstruction level (those described in Chapter 6). Meanwhile the out-of-fiducial fraction is the fraction of events which pass the reconstruction level cuts, but which are not in the fiducial phase space. The fitting of MC to data is performed with events passing the reconstruction level cuts, so to translate from the number of MC events measured there, N_{reco} , to the number of events in the fiducial phase space, N_{fid} , it is necessary to use the relation:

$$N_{\text{fid}} = \frac{1 - f_{\text{out}}}{\epsilon} N_{\text{reco}} \quad (7.4)$$

Once N_{fid} is known, it is then possible to use the cross-section value from MC in the fiducial phase space, and scale by the difference between measured and predicted number of events.

7.3. Fitting parameterisations

In each phase space, two fits are performed with different parameterisations of the contribution from each $t\bar{t}$ + jets category. In the first, the *signal strengths* $\mu_{t\bar{t}+\geq 2c}$, $\mu_{t\bar{t}+1c}$, $\mu_{t\bar{t}+\geq 1b}$ and $\mu_{t\bar{t}+\text{light}}$ are used. This is a simple scaling with $\mu = 1$ for the nominal prediction. In the second, the fit parameters are instead the ratios $R_{t\bar{t}+\geq 2c}$, $R_{t\bar{t}+1c}$ and

7.4. Comparison of strategy with the CMS analysis

$R_{t\bar{t}+\geq 1b}$, defined $R_{t\bar{t}+X} = \frac{N_{t\bar{t}+X}}{N_{t\bar{t}+\text{jets}}}$, as well as the inclusive $\mu_{t\bar{t}+\text{jets}}$ signal strength. The relationship between these signal strengths is given by:

$$\mu_{t\bar{t}+\text{jets}} = \mu_{t\bar{t}+\geq 2c} R_{t\bar{t}+\geq 2c} + \mu_{t\bar{t}+1c} R_{t\bar{t}+1c} + \mu_{t\bar{t}+\geq 1b} R_{t\bar{t}+\geq 1b} + \mu_{t\bar{t}+\text{light}} R_{t\bar{t}+\text{light}} \quad (7.5)$$

Since in the ratio fit $R_{t\bar{t}+\text{light}}$ is not included as a parameter, the overall scaling of $t\bar{t}+\text{light}$ events is $\mu_{t\bar{t}+\text{jets}} \times (1 - R_{t\bar{t}+\geq 2c} - R_{t\bar{t}+1c} - R_{t\bar{t}+\geq 1b})$.

Since they are simply different parameterisations of the same fundamental fit, the final predictions for each event category should be identical in each case. However in the ratio fit there is a possibility that correlations between individual uncertainties reduce the uncertainty on the ratio.

This results in a total of four fitting setups: the four signal strength parameterisation and ratio parameterisation in each of the fiducial and inclusive phase spaces described in the previous section.

7.4. Comparison of strategy with the CMS analysis

This analysis can be compared the one performed by CMS [104], the results of which are described in Section 2.5.1. This analysis is designed to use a similar fiducial phase space definition and similar reconstruction-level cuts. However there are several key differences in the CMS analysis strategy compared to the one performed here.

One prominent difference is the $t\bar{t}$ decay channels used: the CMS analysis uses only the dilepton channel, whereas this analysis utilises both dilepton and lepton + jets channels. Furthermore the principal measurement performed there is of $t\bar{t}$ with at least two c quarks, equivalent to the $t\bar{t} + \geq 2c$ category here. The $t\bar{t} + 1c$ category of this analysis (there termed $t\bar{t}cL$) is scaled by the same factor as $t\bar{t} + \geq 2c$, with an uncertainty used for the ratio. Thus while not stated explicitly, it is likely that the $t\bar{t} + 1c$ signal strength is not effectively a free floating parameter as in this analysis, and its value is not reported. The choice to measure $t\bar{t} + \geq 2c$ and $t\bar{t} + 1c$ separately is motivated by the desire to provide more information to future modelling studies, as these contributions may be sensitive to separate effects.

In the fiducial phase space definitions, the CMS analysis requires that jets have $p_T > 20$ GeV, while here the cut is placed at 25 GeV to better match the reconstruction-level cuts. While at least two b -jets are required as here, in that analysis they must be associated with the $t\bar{t}$ system. This is not used here so as to reduce reliance on generator-specific information. Furthermore the CMS analysis has a requirement of at least two jets additional to the $t\bar{t}$ system in the dilepton channel, whereas here only one is required. This more inclusive selection allows for jets which are either outside of detector acceptance or come from the combination of more than one b/c quark. As stated previously, the reconstruction level cut on jet p_T in this analysis is $p_T > 25$ GeV, whereas the CMS analysis places the cut at 30 GeV. Additionally that analysis uses different observables, fitting to the output of a neural network discriminator.

Systematic Uncertainties

A number of different systematic uncertainties must be considered when performing the measurement using the procedures described in the previous chapter. These enter the profile likelihood fit through nuisance parameters (NPs) (see Section 7.1 for a description of fitting setup), and describe a variation to the nominal template. In Section 8.1 the procedure for how these are handled in the fit is described. This is followed by a description of each uncertainty considered, split into experimental uncertainties (Section 8.2), related to the ATLAS detector, and theoretical uncertainties (Section 8.3), related to the modelling of processes in MC.

The variations used to generate each systematic template may come from reweighting the existing set of MC events, or from comparing the nominal prediction to an entirely new set of events (for example when considering an alternative choice of parton shower algorithm).

8.1. Handling of systematic templates

Each systematic variation may be labelled either *two-point* or *three-point*. The former indicates that there is just one alternative to the nominal template, while the latter has both up and down variations. Additionally, each template may be applied only to a certain sub-set of MC-generated events. Before they can be used, it may be helpful to first process the systematic templates through smoothing, symmetrisation and pruning as described below.

8.1.1. Smoothing

Some of the systematic templates come from sets of events with limited statistics. This may lead to fluctuations in the template, obscuring the true shape of the variation and

8. Systematic Uncertainties

potentially artificially constraining its NP in the fit. To mitigate this *smoothing* can be applied, using two methods: MAXVARIATION and parabolic rebinning.

MAXVARIATION sets out to limit the number of slope variations seen in the histogram formed by taking the ratio between the systematic and nominal templates. First, adjacent bins are merged until their statistical uncertainty is below a certain threshold (5%). Then if the number of slope variations seen is above a threshold - here four is used - the uncertainty threshold in the previous step is halved and the process repeats. After the number of slope variations satisfies the criterion, the ROOT [248] TH1::Smooth method is used, which in turn implements the 353QH TWICE algorithm [254].

This has several steps, beginning with smoothing using *medians of three*, then *medians of five* before repeating the medians of three step. These take the median of three or five adjacent neighbours in the sequence, i.e. for three:

$$z'_n = \text{median}(z_{n-1}, z_n, z_{n+1}) \quad (8.1)$$

Special conditions are applied at the endpoints of the sequence. Since the resulting sequence has all ‘peaks’ and ‘valleys’ converted to flat sections of length 3, the ‘Q’ step applies a quadratic interpolation to these sections. Then the ‘H’ step applies a Hanning mean:

$$z'_n = \frac{1}{4}z_{n-1} + \frac{1}{2}z_n + \frac{1}{4}z_{n+1} \quad (8.2)$$

to resolve any monotonic discontinuities. To prevent over-smoothing, *twicing* is applied, whereby the output is the sum of the input, smoothed by the 353QH algorithm, and a smoothed version of the difference between the input and the smoothed input.

PARABOLIC REBINNING This method considers the *extrema* of the distribution: local maxima or minima, or end points. It then rebins the distribution until only three extrema are remaining, and the distribution overall has a parabolic shape. Priority for which bins to merge is decided using the χ^2 value between the extremum bin and the average bin value between it and the next extremum. Once only three extrema remain, further rebinning is performed until all bins have a relative statistical uncertainty of less than 5%, or all bins are merged.

8.1.2. Symmetrisation

When using three-point systematics, the nominal prediction may lie exactly between the up and down variations. However in some cases these may be very asymmetric about the nominal template, and *symmetrisation* may be applied. For three-point systematics *two-sided smoothing* can be used. This simply takes, in each bin, half the difference between each variation and uses it as the new nominal uncertainty, i.e.:

$$\sigma_{\text{nominal}}^{\pm} = \pm \left| \frac{z_{\text{up}} - z_{\text{down}}}{2} \right| \quad (8.3)$$

where $\sigma_{\text{nominal}}^{\pm}$ are the values of the up and down uncertainties on the nominal prediction, and $z_{\text{up/down}}$ are the values of those variations in the given bin. This procedure leaves already-symmetric uncertainties unchanged.

For two-point systematics with only one variation, *one-sided symmetrisation* is used, whereby the difference between the systematic and nominal templates is simply reflected:

$$\sigma_{\text{nominal}}^{\pm} = \pm |z_{\text{syst}} - z_{\text{nominal}}| \quad (8.4)$$

8.1.3. Pruning

With a total of almost 300 systematic uncertainties considered, it would be impossible for the profile likelihood fit to converge in a timely manner in such a phase space. Therefore *pruning* is applied, which removes those components of uncertainties which have negligible impact - thereby simplifying fitting without significantly changing the result.

Pruning is performed separately for the *shape* and *normalisation* effect of each systematic template. Shape can be considered by first normalising the total number of events in each template before calculating the impact of the uncertainty. For normalisation only the total number of events is used.

The *pruning threshold* for this analysis is set to 0.5% for both shape and normalisation, chosen following dedicated studies. These showed a maximum difference in the expected sensitivity to the POIs of around 1%. Then for each systematic uncertainty, for each region, if the shape/normalisation effect is less than the threshold in all bins, the component is dropped from the fit for that sample and region. Figures showing the full results of pruning are included in Appendix C.

8.2. Experimental uncertainties

Given its size and complexity, there are a number of uncertainties related to the ATLAS detector itself. Many of these relate to reconstruction and identification, and to the calibration of the measurements made, eg. of a particle's energy. For more detail on these methods see Chapter 5.

Luminosity

The luminosity uncertainty for the entirety of Run 2 (2015-2018) data has been measured to be 0.83% [130]. This is a simple normalisation uncertainty, scaling all of the simulated events.

pileup reweighting

To account for additional *pp* collisions aside from the hard scattering of interest (*pileup*), minimum bias events are overlaid onto the hard scattering when creating MC simula-

8. Systematic Uncertainties

tions. These events are reweighted [165] to the observed patterns of pileup. This template reflects the uncertainties in this reweighting.

Charged lepton uncertainties

One category of lepton uncertainties concerns their reconstruction, identification, isolation and trigger efficiencies. Scale factors must be applied to electrons and muons in MC events to correct for observed differences between them in simulation and data. They are derived in statistically independent bins of p_T and η , with the uncertainties themselves kept correlated. Events with Z and W bosons, alongside those with J/ψ , are used to generate the scale factors using the *tag-and-probe* method. This method identifies one lepton with strict selection criteria (*tag*), then uses the other as an unbiased selection of leptons for study (*probe*). The procedure is described in more detail for electrons and muons respectively in Refs. [194] and [207]. Each lepton category has one uncertainty associated with each scale factor (reconstruction, identification, isolation and trigger), with muons having an additional uncertainty related to *track-to-vertex-association* (TTVA).

The second category of lepton uncertainties relates to lepton momentum scale and resolution. Similar to above, these may differ between simulation and data, and are checked by reconstructing the parent mass in $Z \rightarrow \ell^+\ell^-$ and $J/\psi \rightarrow \ell^+\ell^-$ decays. Additionally, for electrons $W \rightarrow e\nu$ events are used. As well as those for momentum scale and resolution, muons have two uncertainties related to *sagitta bias*, which would result in a charge-dependent difference in measured p_T . The methods used to account for this are described in Refs. [202] and [207] for electrons and muons respectively. In total there are three independent NPs used for electrons, and five for muons. All used two-sided symmetrisation.

Jet vertex fraction efficiency

An uncertainty is applied to account for differing efficiency of the JVT in data and simulation. JVT calibration is performed using the tag-and-probe method in $Z(\rightarrow \mu^+\mu^-) + \text{jets}$ events, with the leading jet recoiling from the Z boson as the probe [219]. Pileup jets are estimated using a control region where they predominate. The uncertainties in the calibration then relate to the hard-scattering contamination of the control region, taken to have 30% uncertainty, and variations depending on the choice of MC generator.

Jet energy scale

The JES calibration procedure is described in Section 5.3, and as a result of its complexity and large number of inputs (comprising test-beam data, collision data and simulation) has a large number of associated uncertainties. These reflect, in each of the principal event categories used for calibration ($Z/\gamma + \text{jets}$, dijet and multi-jet), uncertainties in physics modelling, in measurement of reference objects, and in modelling of p_T balance due to event topology. In general, there is also a p_T and η dependence on the degree of uncertainty. These must be propagated through the multi-step calibration, resulting in

a large set of over 100 NPs. This is reduced through eigenvector decomposition, which aims to maintain the most important components in all kinematic regions [255]. Furthermore a set of five additional uncertainties are included, relating to uncertainty handling the observed difference between quark and gluon jets. These uncertainties account for differences between different MC generators, applying MC/MC scale factors. In total this results in 35 independent NPs related to the JES, all symmetrised and with up and down variations.

Jet energy resolution

Jet energy resolution (JER) uncertainties come from the study of dijet events, where since the jets are produced back-to-back we would naively expect perfectly balanced p_T [255]. The method used requires one jet to lie in a well-calibrated region of the detector (the central region), then the other is treated as a probe. The asymmetry observed across p_T and η can be used to estimate the detector resolution. Additionally, a noise term is estimated by taking *random cones* in zero-bias data (random triggers). The principal uncertainties arising from this process are those propagated from the JES, dominant at lower p_T , and from observed non-closure between MC events and data for dijet events (significant at higher p_T). As for the JES, eigenvector decomposition is used to reduce the number of uncertainty components.

Smearing is applied to MC to match the JER in data when its resolution is lower. In cases where data have lower resolution, a separate uncertainty is introduced to account for the discrepancy. This preserves anti-correlations in the underlying JER NPs. In total 13 NPs are used to account for this uncertainty, all with two-sided symmetrisation.

Flavour tagging

Flavour-tagging uncertainties originate from the calibration procedure of the b/c -tagger, using the same procedure as the DL1r tagger [226–228]. This, as well as the uncertainties considered, are described in Section 5.5. They relate to uncertainties in modelling of the events used, in the fitting and calibration procedure itself, and to data and simulated event statistics. In total 45 NPs are used for b -jets, with 20 each for c -jets and light jets. Due to the decomposition process used to reduce the full number of uncertainties to this number of components, each does not have a straightforward physical interpretation.

8.3. Theoretical uncertainties

As this analysis is largely motivated by interest in better understanding the modelling of the top quark, the uncertainties regarding this are of particular importance. These theoretical uncertainties represent cases where there is ambiguity in the choice of MC parameters or algorithms. A description of many of the parameters which are varied here is given in Chapter 4.

8. Systematic Uncertainties

8.3.1. $t\bar{t}$ modelling

These uncertainties affect the main samples of interest: $t\bar{t} + 1c$, $t\bar{t} + \geq 2c$, $t\bar{t} + \geq 1b$ and $t\bar{t} + \text{light}$. Unless otherwise stated below, the three groupings of $t\bar{t} + \geq 1c$, $t\bar{t} + \geq 1b$ and $t\bar{t} + \text{light}$ are each decorrelated i.e. each uncertainty below represents three separate NPs for these groups. This allows for the fact that modelling changes may affect these categories in different ways, allowing the analysis to better constrain modelling choices. Since $t\bar{t} + \geq 1c$ and $t\bar{t} + \text{light}$ come from an inclusive 5FS $t\bar{t}$ sample and $t\bar{t} + \geq 1b$ comes from a dedicated 4FS $t\bar{t}b\bar{b}$ sample, the treatment differs in some cases.

Normalisation of $t\bar{t} + \text{jets}$ samples

The alternative samples used to determine modelling uncertainties in $t\bar{t}$ naturally predict different numbers of events in the $t\bar{t} + \geq 2c$, $t\bar{t} + 1c$, $t\bar{t} + \geq 1b$ and $t\bar{t} + \text{light}$ categories. However this analysis does not want to utilise this normalisation effect, rather only the shape effects and region migration seen. This is because ultimately results are compared to theoretical predictions of the cross-sections, and the uncertainties on those values will include these normalisation uncertainties.

To avoid probing these differences, the production rate of each $t\bar{t} + \text{jets}$ category is extracted at particle level from the nominal sample used and compared to the rate in the modelling variation in question. The rates are extracted in the relevant phase space in each fit setup (i.e. for the fiducial phase space after the fiducial event selection cuts have been applied). The ratio between the two is then applied as a reweighting to the reconstructed number of events in the variation.

Parton shower and hadronisation

To account for the uncertainty in choice of parton shower and hadronisation model, the nominal POWHEG + PYTHIA 8 samples are compared to alternatives generated using POWHEG+HERWIG7.1.3. These alternatives are generated using fast detector simulation [161, 162]. Therefore they cannot be directly compared to the main nominal samples, but instead the difference is taken with respect to a version of the nominal sample also using fast detector simulation. This two-point uncertainty is then smoothed and symmetrised.

For $t\bar{t} + \text{light}$ it was observed that the variation is consistently in opposite directions, predicting fewer events for five-jet-exclusive regions and more for six-jet-exclusive regions in the lepton+jets channel, as exemplified in Figure 8.1. If kept correlated between these groups, a large constraint would be observed on the NP and the true effect of the variation would be lost. Hence this uncertainty is decorrelated between five-jet-exclusive and six-jet-inclusive regions, and similarly between three-jet-exclusive and four-jet-inclusive dilepton channel regions.

It was similarly observed that this variation has differing effects on the sub-components of $t\bar{t} + \geq 1c$ and $t\bar{t} + \geq 1b$, so this uncertainty is decorrelated between $t\bar{t} + 1c$ and $t\bar{t} + \geq 2c$, and between $t\bar{t} + 1b$ and $t\bar{t} + \geq 2b$ samples. After all decorrelations a total of eight NPs are used to describe this uncertainty.

8.3. Theoretical uncertainties

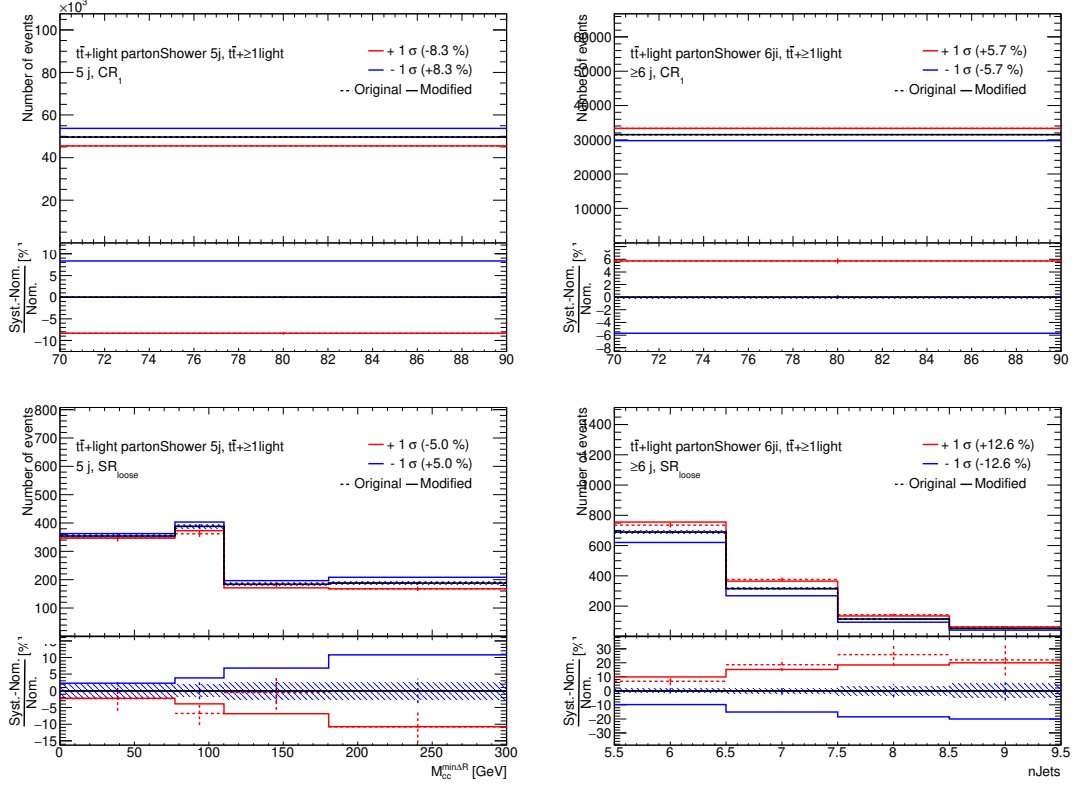


Figure 8.1.: Effect of the parton showering systematic variation on the $t\bar{t}$ + light sample in the lepton + jets channel for CR_1^{ℓ} and SR_{loose}^{ℓ} , for both five-jet-exclusive and six-jet-inclusive regions. The dashed lines show the variation before smoothing and symmetrisation, and the solid lines after. This shows an effect seen across all regions, whereby fewer events are predicted for 5-jet regions and more for ≥ 6 -jet regions.

8. Systematic Uncertainties

NLO matching

The uncertainty in NLO matching is estimated using the p_T^{hard} parameter, which changes the way information from POWHEG is used to define the possible p_T values used for showering in PYTHIA. The nominal samples with $p_T^{\text{hard}} = 0$ are compared to an alternative generated with $p_T^{\text{hard}} = 1$. As such, in figures the associated nuisance parameter is labelled ‘pthard’. The alternative sample employs fast detector simulation and is compared to a corresponding nominal sample. It is also smoothed and symmetrised.

It was observed that variations in this parameter impacted the contributions from $t\bar{t} + 1c$ and $t\bar{t} + \geq 2c$ events significantly differently, leading to large constraints in initial fit tests. A similar pattern was observed for $t\bar{t} + 1b$ and $t\bar{t} + \geq 2b$ events, so these components are decorrelated, being described by separate NPs. This allows the separate effects to be expressed in fitting.

Initial state radiation

Initial state radiation (ISR) modelling uncertainties are estimated by using a variation to the normal A14 tune of POWHEG+PYTHIA8, called **Var3c** [173]. In the simulation this acts to effectively vary the value of α_S used when producing ISR, and is applied as a reweighting to nominal events.

Final state radiation

An internal reweighting of events is performed, corresponding to changing the renormalisation scale used in simulating final state radiation (FSR): μ_R^{FSR} . This is in turn equivalent to varying α_S^{FSR} . A dedicated study showed that the scheme used by other similar analyses [70, 193] of using $0.5 \times \mu_R^{\text{FSR}}$ and $2 \times \mu_R^{\text{FSR}}$ is not suitable. This is due to the lower variation, where a significant tail of large weights causes statistical fluctuations following reweighting. Instead it was found that using $0.625 \times \mu_R^{\text{FSR}}$ as a lower variation mitigated this effect, so this is used. The variations are both smoothed and symmetrised.

Scale choices

The choice of renormalisation and factorisation scale, μ_R and μ_F , is a key uncertainty in modelling $t\bar{t} + 1c$ and related processes, as was described in Section 2.5. To assess their impact, reweightings of the nominal samples are used corresponding to multiplying μ_R and μ_F by 0.5 and 2, with one NP each. In particular, the variation of μ_R for $t\bar{t} + \geq 1b$ events is seen to have a large impact in $\text{CR}_2^{2\ell 3j}$ and $\text{CR}_2^{2\ell \geq 4j}$, both of which are predicted to be enriched in $t\bar{t} + \geq 1b$ events. Once symmetrised, variation of this NP to one standard deviation scales the expected $t\bar{t} + \geq 1b$ contribution by over 30% in each of these regions.

PDF uncertainty

Following the recommendations of Ref. [256], the PDF4LHC15_30 set of 30 NPs is used in this analysis. This comes from a combination of the CT14 [257], MMHT14 [179]

and NNPDF3.0 [258] PDF sets, then the uncertainties come from the process of *Hessian reduction* [259, 260]. These uncertainties are primarily driven by the experimental uncertainties in data used to derive the underlying PDF sets, as well as a number of modelling choices. In practice a reweighting is used, with each two-point systematic then symmetrised.

h_{damp} parameter

This uncertainty is only applied to the $t\bar{t} + \geq 1c$ and $t\bar{t} + \text{light}$ categories, taken from the inclusive $t\bar{t}$ sample. A dedicated alternative POWHEG+PYTHIA8 sample with $h_{\text{damp}} = 3m_{\text{top}}$ is compared to the nominal samples ($h_{\text{damp}} = 1.5m_{\text{top}}$), and the difference used as a two-point uncertainty (both with fast detector simulation). This is then smoothed and symmetrised.

Dipole recoil

This uncertainty is only considered for $t\bar{t} + \geq 1b$ events. In PYTHIA8 there is ambiguity in the choice of treatment of recoil against QCD initial state showering. Either a global scheme, where the entire final state recoils, or a dipole scheme, where only one final state parton recoils, may be used. It has been found that this choice has a noticeable impact on observables for $t\bar{t}b\bar{b}$ [261]. Due to the limited available samples this effect is estimated by comparing an alternative $t\bar{t}b\bar{b}$ sample with the dipole recoil scheme and $h_{\text{bzd}} = 2$, to a version of the nominal sample using the global recoil scheme, also with $h_{\text{bzd}} = 2$. The two-point uncertainty is smoothed and symmetrised.

8.3.2. Background modelling

Unless otherwise noted below, several categories of background process are simply assigned a conservative normalisation uncertainty. These are summarised in Table 8.1.

Single top

Due to the interference between Wt and $t\bar{t}$ production, LO $t\bar{t}$ diagrams must be removed when calculating Wt production beyond LO. There are two methods proposed for doing this: diagram removal (DR) and diagram subtraction (DS) [190]. DR involves removing those Wt diagrams which are *doubly resonant*, corresponding to cases where they can also be considered LO $t\bar{t}$ diagrams. DS, meanwhile, subtracts from the total matrix element a term designed to cancel the same contributions. However these methods are not equivalent, creating an uncertainty. The nominal sample uses DR, with an equivalent sample using DS used to estimate the uncertainty. This difference is then smoothed and symmetrised.

In the dilepton channel, the only way an s - or t -channel single top event can enter its selection is with a fake lepton. Therefore to account for their uncertainties a 25%

8. Systematic Uncertainties

normalisation uncertainty is placed on the fakes contribution in that channel. s - or t -channel uncertainties in the following paragraphs are hence applied only in the lepton + jets channel.

For each major single-top production channel (Wt , s - and t -channel), an uncertainty in the choice of parton shower and hadronisation model is estimated through comparison of the nominal POWHEG+PYTHIA8 to alternative POWHEG+HERWIG7 samples, followed by smoothing and symmetrisation. An additional uncertainty associated with the choice of matrix element generator is used for Wt events, through comparison to a MADGRAPH5_aMC@NLO + PYTHIA8 sample, followed by smoothing and symmetrisation. For s - and t -channels the equivalent alternative samples have very large fluctuations, resulting in negative values for some bins. Since the same comparison as for Wt is not possible, the normalisation uncertainty for these backgrounds is set to 50%.

Finally, an additional 5% cross-section uncertainty is applied to Wt events.

Fake lepton backgrounds

Fake lepton events in the dilepton region have a 25% uncertainty applied on the estimate from MC. In the lepton + jets channel, fake leptons are instead estimated using the *matrix method* [238] as described in Section 6.2. The statistical uncertainties in each bin (known as *gammas*) are used as uncertainties, in addition to an overall 50% normalisation uncertainty.

Other backgrounds

For $t\bar{t}W$ and $t\bar{t}Z$ backgrounds, one uncertainty is used for each combining the effect of both matrix element and parton shower/hadronisation choices, through comparing the nominal MADGRAPH5_aMC@NLO + PYTHIA8 samples with alternative SHERPA samples. This uncertainty is symmetrised. A further cross section uncertainty of $^{+13.3}_{-12.0}$ and $^{+10.4}_{-12.0}$ are applied for $t\bar{t}W$ and $t\bar{t}Z$ backgrounds, respectively.

A conservative 50% normalisation uncertainty is applied for $t\bar{t}H$ events, and the remaining rare single-top events (comprising tZq and tWZ events) also have one combined 50% normalisation uncertainty.

For electroweak backgrounds, W + jets (only a dedicated category in the lepton + jets channel) are split into three categories: those with ≥ 3 heavy flavour jets, those with exactly 2, and the remainder. Each of these has a separate 40% cross-section uncertainty. Z + jets and diboson backgrounds have cross-section uncertainties of 35% and 50% respectively.

8.3. Theoretical uncertainties

Table 8.1.: Summary of systematic uncertainties considered for background processes. ‘DR/DS’ denotes an uncertainty in the use of either the diagram removal or diagram subtraction scheme. ‘PS’ and ‘ME’ denote uncertainty in the choice of parton shower algorithm and matrix element generator, respectively.

Background	Norm. Uncertainty [%]	Note
Single top - Wt	5	+ DR/DS, PS & ME uncertainties
Single top - s -channel	50	lepton + jets channel only, +PS
Single top - t -channel	50	lepton + jets channel only, +PS
$t\bar{t}H$	50	-
$t\bar{t}W$	+13.3/-12.0	+ combined PS/ME uncertainty
$t\bar{t}Z$	+10.4/-12.0	+ combined PS/ME uncertainty
tZq & tWZ	50	-
W + jets	40	lepton + jets channel only
W + jets, 2 heavy flavour jets	40	lepton + jets channel only
W + jets, ≥ 3 heavy flavour jets	40	lepton + jets channel only
Z + jets	35	-
Diboson	50	-
Dilepton fakes	25	Accounts for s - & t -channel single top
lepton + jets fakes	50	+ per-bin statistical uncertainties

CHAPTER 9

Fit Studies

A significant part of the author’s work on this analysis involved studying the nature of the fit model. A number of large pulls and constraints were initially observed, so studies were undertaken to either validate the existing fit model, or to find improvements. However, given that the analysis is ultimately expected to be somewhat limited by modelling uncertainties, some tension related to the associated NPs may be expected. This chapter aims merely to give an overview of some of these studies. Note that in some cases minor changes were made to both the fit model and samples used following these studies. These do not affect the conclusions drawn here, but data presented in this chapter should not be regarded as showing the final results of the analysis unless otherwise indicated.

In order to give context to the description of the fit validation studies performed, one additional study not performed by the author is described here briefly. This is a study used to assess the flexibility of the model through a series of *pseudo-data* tests. In these tests, different nominal predictions for $t\bar{t}$ event categories are replaced by alternatives. A fit is then performed to the nominal predictions from simulation, as in an Asimov pseudo-data test. In this case, each of the $t\bar{t} + \text{light}$ and $t\bar{t} + \geq 1c$ samples are separately replaced by either the sample using HERWIG 7 as an alternative parton shower algorithm, or the one using MADGRAPH5_aMC@NLO as an alternative matrix element generator. These are introduced in Section 4.1. Additionally another test replaces $t\bar{t} + \geq 1b$ events with the alternative prediction generated using SHERPA. In all except one case the expected signal strength values are obtained after fitting, with one value incompatible with expectations at a level only slightly beyond one standard deviation. Additionally no significant pattern of problematic pulls and constraints are seen when examining the fitted NPs. This suggests that the fit model has sufficient flexibility to accurately reflect the patterns in data.

9. Fit Studies

9.1. Control plots of kinematic variables

One method of validating the modelling used is the production of control plots. These compare data to predictions in each control and signal region, across a range of kinematic observables related to the key analysis objects. The observables used, none of which are being directly fit to, are:

- p_T and η of the leading jet in the event¹
- p_T and η of a low- p_T jet: the fifth/third jet for five-/three-jet-exclusive regions, and the sixth/fourth for six-/four-jet-inclusive regions
- p_T and η of the leading lepton
- missing transverse momentum

Additionally, in regions in the lepton + jets channel, H_T is plotted, considering either only jets, or all objects. The variable H_T is defined as the total sum of transverse energy for the relevant objects. In dilepton channel regions, the p_T and η of the non-leading lepton are plotted.

The resulting set of plots is shown in Appendix D, both pre-fit and post-fit. These use the final fit model, as well as the finalised sets of data and simulated events.

The main value in these plots, with respect to validation of the fit performed, is gained by comparing them before and after fitting. If agreement worsens, this may indicate that the fit model is over-fitting to the specific regions and observables used, and that pulls or constraints of NPs may have no physical basis. However in this case agreement between predictions and data can be seen to clearly improve across the full range of variables, supporting the validity of the systematics model and selections used.

9.2. Individual pull/constraint studies

A large pull or constraint in an NP may indicate that the fit model is overconstrained, lacking sufficient degrees of freedom to describe the data. To judge the extent to which this was occurring, each of the NPs which were pulled and/or constrained, and were calculated to have a high impact on the POIs, were investigated. This was first done in the separate fits to each $t\bar{t}$ decay channel, then in the combined fit setup in cases where a new pull or constraint appeared following combination. The focus for investigation was those NPs associated with modelling uncertainties for the $t\bar{t}$ system, and the primary strategy was to *decorrelate* the NP. The principal decorrelations used were between shape and normalisation effects, and between each analysis region. This information could be compared to plots showing the effect of variations on the nominal template to understand the origin of the pull/constraint. In all cases, the pull or constraint was found to originate from an identifiable source. The results of some of such investigations will be referenced when discussing the results of the analysis in the following chapter.

¹Ordering of objects here is done with respect to p_T .

9.3. Studies of region and observable changes

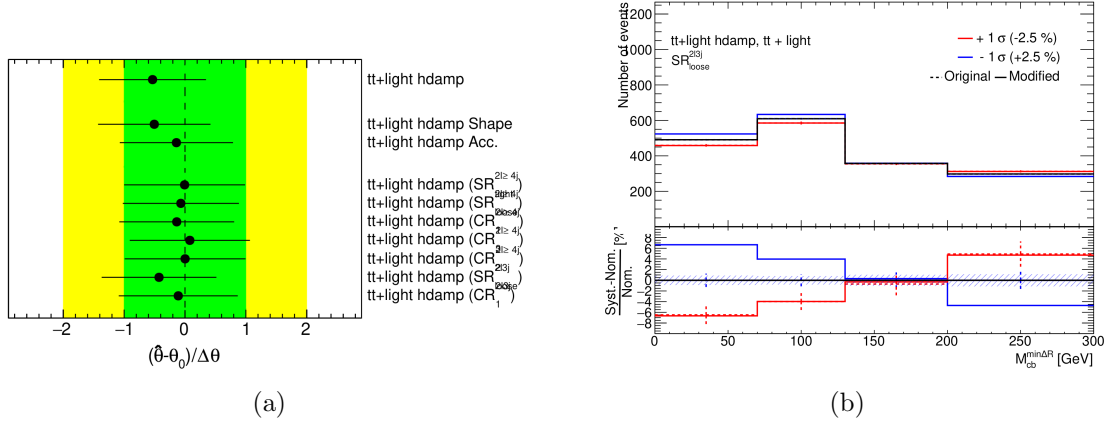


Figure 9.1.: Pre-fit plots comparing MC predictions and data in signal regions $\text{SR}_{\text{loose}}^{1\ell 5j}$, $\text{SR}_{\text{tight}}^{1\ell 5j}$ and $\text{SR}_{\text{loose}}^{2\ell 3j}$. The lepton + jets signal regions use the observable $M_{cc}^{\min\Delta R}$, the invariant mass of the two c -jets separated by the smallest ΔR . In $\text{SR}_{\text{tight}}^{1\ell 5j}$ only those c -jets tagged with $c@11\%$, the tighter c -tagging working point, are considered. Events in $\text{SR}_{\text{loose}}^{2\ell 3j}$ have only one c -jet, so the observable is $M_{cb}^{\min\Delta R}$, the invariant mass of it and the closest b -jet. Events outside the range are put into the first or last bin, and the blue uncertainty band includes both statistical and systematic uncertainties.

As an example of this, one investigation conducted in the dilepton-channel-only fit, looking at the h_{damp} uncertainty for $t\bar{t} + \text{light}$ events, is given here. It was performed in a fit to data, in the fiducial phase space. Figure 9.1a shows the associated NP's post-fit value, with a pull of $\frac{\hat{\theta}-\theta_0}{\Delta\theta} \approx 0.5$ and a moderate constraint. The decorrelated NPs are shown in the same figure, decorrelated by shape and acceptance effect, then by region. These suggest the original pull is associated with the shape effect of the uncertainty, and that the region responsible is $\text{SR}_{\text{loose}}^{2\ell 3j}$. Figure 9.1b then shows the effect of the systematic variation in this region. The negative variation, as preferred by the fit model, can be seen to produce a slope increasing the $t\bar{t} + \text{light}$ contribution at low values of $M_{cb}^{\min\Delta R}$ and decreasing it at higher values. Examining the pre-fit comparison of data and prediction for this region in Figure 6.2, a similar shape can be seen in the ratio of the two. Therefore this pull can likely be understood as acting to compensate for this discrepancy.

9.3. Studies of region and observable changes

One possibility studied was changing the definitions of the analysis regions, as well as the observables fit to within them. If a fit is overconstrained, removing regions or observables may allow it to then converge without a large number of problematic pulls or constraints. The blinding strategy implemented at this point involved blinding only the

9. Fit Studies

value of $t\bar{t} + \geq 2c$ and $t\bar{t} + 1c$ signal strengths and their absolute uncertainties. Therefore one of the key checks for the effect of each modelling study below was the shift in the central value of the POIs, and the change in their relative uncertainties. Additionally, changes in pulls and constraints were examined. All studies were performed in the fiducial phase space, and using the signal strength fit setup.

Removing jet-exclusive regions

One option involved removing the nine jet-exclusive regions². These regions are less key to the analysis, covering cases where either one jet is out-of-acceptance or two jets are merged, and were not used in the comparable CMS analysis [104].

Table 9.1 compares the resultant signal strengths to the nominal values. A shift is seen in the fitted value for $\mu_{t\bar{t}+1c}$, most likely on the order of one to two standard deviations, alongside large increases in the uncertainties of the $t\bar{t} + \geq 1c$ signal strengths. Amongst pulls and constraints, observed pulls are lessened in NPs related to $t\bar{t} + \geq 1b$ FSR and $t\bar{t} + \text{light } h_{\text{damp}}$ uncertainties. Additionally, a constraint is lessened for the $t\bar{t} + \geq 1b \mu_R$ uncertainty.

Table 9.1.: Comparison showing the effect on fitted signal strengths of removing jet-exclusive regions from the fit model. The central value and absolute uncertainties of the POIs were blinded at the time of the study, so only relative changes are shown.

Signal strength	Nominal value	Jet-exclusive regions removed
$\mu_{t\bar{t}+\text{light}}$	$0.90^{+0.05}_{-0.05}$	$0.92^{+0.06}_{-0.06}$
$\mu_{t\bar{t}+\geq 1b}$	$1.11^{+0.08}_{-0.08}$	$1.13^{+0.09}_{-0.08}$
$\mu_{t\bar{t}+\geq 2c}$	$X^{+20.9\%}_{-18.7\%}$	$(X - 0.04)^{+24.0\%}_{-21.0\%}$
$\mu_{t\bar{t}+1c}$	$X^{+14.9\%}_{-14.0\%}$	$(X + 0.26)^{+19.4\%}_{-17.3\%}$

Removing signal region observables

A test was performed removing the observables described in Section 6.4.1 from different sets of SRs, and instead simply fitting to a yield in those regions. The sets of regions considered for this procedure were:

- the two five-jet-exclusive SRs in the lepton + jets channel
- all four SRs in the lepton + jets channel
- all seven SRs across both channels

²Five-jet-exclusive regions for the lepton + jets channel and three-jet-exclusive regions for the dilepton channel

9.3. Studies of region and observable changes

Table 9.2 compares the fitted signal strengths for each of these cases. A trend can be observed that as shape information is removed from more regions, the relative uncertainties in the POIs rise, from around 20% and 14% for $\mu_{t\bar{t}+\geq 2c}$ and $\mu_{t\bar{t}+1c}$ respectively, to 22% and 18%. A shift is also seen in the central value of the μ_{ttc} signal strength for the most extreme scenario. When considering pulls and constraints of uncertainties, the effects observed are similar for all changes, also increasing in degree when more regions are modified. A number of $t\bar{t}$ modelling pulls are lessened, however a smaller number are also introduced. In particular, a large pull is introduced in the NP corresponding to uncertainty in the choice of the dipole recoil scheme for modelling of $t\bar{t} + \geq 1b$ events.

Table 9.2.: Comparison showing the effect on fitted signal strengths of removing removing fit observables, and instead fitting a yield, from different groups of signal regions. The central value and absolute uncertainties of the POIs were blinded at the time of the study, so only relative changes are shown.

Signal strength	Nominal value	Five-jet signal regions	Lepton + jets signal regions	All signal regions
$\mu_{t\bar{t}+\text{light}}$	$0.90^{+0.05}_{-0.05}$	$0.92^{+0.05}_{-0.05}$	$0.92^{+0.05}_{-0.05}$	$0.91^{+0.06}_{-0.05}$
$\mu_{t\bar{t}+\geq 1b}$	$1.11^{+0.08}_{-0.08}$	$1.13^{+0.09}_{-0.09}$	$1.17^{+0.09}_{-0.09}$	$1.18^{+0.10}_{-0.09}$
$\mu_{t\bar{t}+\geq 2c}$	$X^{+20.9\%}_{-18.7\%}$	$(X + 0.05)^{+21.1\%}_{-18.9\%}$	$(X - 0.03)^{+22.5\%}_{-19.9\%}$	$(X - 0.03)^{+23.3\%}_{-19.7\%}$
$\mu_{t\bar{t}+1c}$	$X^{+14.9\%}_{-14.0\%}$	$(X + 0.03)^{+15.7\%}_{-14.8\%}$	$(X + 0.02)^{+15.7\%}_{-14.8\%}$	$(X + 0.14)^{+18.8\%}_{-16.5\%}$

Merging CR₂ and CR₃

A study was undertaken to see the effect of merging the sets of CR₂ and CR₃, while maintaining the regions' definitions otherwise, eg. merging CR₂^{1ℓ5j} and CR₃^{1ℓ5j}. The motivation for choosing these as candidates for merging was their broadly similar composition, being enriched in $t\bar{t} + \geq 1b$ events. This can be seen in Figure 6.1. There it can also be seen, however, that this similarity is greater in the lepton + jets channel. Therefore two options were tested: merging these regions in both channels; and merging only in the lepton + jets channel. The fitted signal strengths can be seen in Table 9.3.

In the case of merging in both channels, the main POIs see a loss of sensitivity of approximately 2%. A large number of changes to NPs result, especially those related to $t\bar{t} + \geq 1b$ modelling. In most cases this results in the lessening of pulls and constraints. Additionally pulls in the NPs for uncertainties in the calibration of c -tagging are lessened.

For the merging performed only in the lepton + jets channel, a smaller impact is seen on the fitted norm factors. This is mirrored in a minimal change to the values of NPs.

Conclusions

While some of the tested alternatives saw an improvement in problematic pulls and constraints (particularly the merging of CR₂ and CR₃), all corresponded to a loss in

9. Fit Studies

Table 9.3.: Comparison showing the effect on fitted signal strengths of merging CR₂ and CR₃, either only in the lepton + jets channel, or also in the dilepton channel. The central value and absolute uncertainties of the POIs were blinded at the time of the study, so only relative changes are shown.

Signal strength	Nominal value	Merged in both channels	Merged in lepton + jets channel
$\mu_{tt+light}$	$0.90^{+0.05}_{-0.05}$	$0.92^{+0.05}_{-0.05}$	$0.91^{+0.05}_{-0.05}$
$\mu_{tt+\geq 1b}$	$1.11^{+0.08}_{-0.08}$	$1.09^{+0.08}_{-0.08}$	$1.09^{+0.08}_{-0.08}$
$\mu_{tt+\geq 2c}$	$X^{+20.9\%}_{-18.7\%}$	$(X - 0.14)^{+24.1\%}_{-20.8\%}$	$(X - 0.04)^{+21.1\%}_{-19.2\%}$
μ_{tt+1c}	$X^{+14.9\%}_{-14.0\%}$	$(X - 0.09)^{+16.5\%}_{-15.0\%}$	$(X - 0.02)^{+15.2\%}_{-13.9\%}$

sensitivity in the POIs. Ultimately, given the other fit validation tests performed, it was decided that any improvements seen were not worth the corresponding sacrifice in sensitivity.

9.4. MPI/FSR studies

A study was performed to better understand the role played by MPI and FSR in the production of heavy flavour jets. The physics of these effects was described in Section 2.3. There is potential ambiguity in how MPI jets should be handled conceptually, since this production mechanism is separate, and it may be argued that measuring this contribution on its own could improve the ability of the analysis to provide inputs to future modelling. Furthermore it was possible that providing a separate template for events with MPI/FSR c -/ b -jets could improve the quality of the fitting, as it is possible their shape and normalisation may behave differently. This study aimed to characterise the number of these events, and to investigate whether such a division of events would be feasible.

The study used simulated events, specifically the MC generator record, labelling the origin of the heavy flavour quark ghost associated to a given jet. A dedicated reprocessing of events was performed to add this information, which due to practical constraints was performed only in the dilepton channel. The study was performed separately for $t\bar{t} + \geq 1c/t\bar{t} + \geq 1b$ events looking at c -/ b - jets respectively. In each event the number of MPI, FSR and ‘prompt’ jets was counted, where ‘prompt’ denotes all other production modes, and the fraction of $t\bar{t} + \geq 1c/t\bar{t} + \geq 1b$ events containing at least one MPI/FSR c -/ b -jet was recorded.

c -jets

The contribution from FSR was found to be negligible, being found in $< 0.1\%$ of events in all analysis regions. However this was not the case for MPI, which had a prevalence of over 10% in all regions, as shown in Table 9.4. The overall proportion of MPI-containing events was seen to be relatively consistent across each region. To further profile these

Table 9.4.: Fraction of c -jet events in each region containing at least one c -jet from MPI in the dilepton channel, in the combined fit.

Region	$t\bar{t} + 1c$ MPI /%	$t\bar{t} + \geq 2c$ MPI /%
$\text{CR}_1^{2\ell 3j}$	16.74	17.53
$\text{CR}_2^{2\ell 3j}$	12.92	14.11
$\text{CR}_3^{2\ell 3j}$	13.74	15.74
$\text{SR}_{\text{loose}}^{2\ell 3j}$	13.43	15.44
$\text{CR}_1^{2\ell \geq 4j}$	15.72	15.38
$\text{CR}_2^{2\ell \geq 4j}$	13.34	15.00
$\text{CR}_3^{2\ell \geq 4j}$	13.46	13.95
$\text{SR}_{\text{loose}}^{2\ell \geq 4j}$	13.49	13.76
$\text{SR}_{\text{tight}}^{2\ell \geq 4j}$	13.23	12.67

events, plots were produced comparing the shape of the distribution of events containing MPI to those that did not. This was done in the signal regions, using the dilepton channel signal regions, using the corresponding observable. Each was normalised to the same area, and the resulting distributions are shown in Figure 9.2. Comparing these shapes shows that with the existing definition of regions and fit observables, there is no significant shape difference which could be exploited to extract a normalisation for MPI-containing jets. As such, and given the similar fraction of MPI events in each region, it is likely that attempting to measure an MPI contribution would significantly increase the uncertainty on the POIs. It may have been possible to choose new regions or fit variables so as to better separate MPI-containing events, but given the limited motivation to perform this additional measurement, it was decided to not define this as a separate process.

b -jets

Similar to the case for c -jets, the contribution from FSR was found to be negligible, being found in $< 0.2\%$ of events in each analysis region. However MPI was not negligible, with $2 - 6\%$ of $t\bar{t} + \geq 1b$ events containing a jet originating from MPI as shown in Table 9.5. Figure 9.3 compares the shape of the templates of MPI-containing/all-prompt $t\bar{t} + \geq 1b$ events in dilepton signal regions, normalised to the same areas. A strong shape effect is seen in $\text{SR}_{\text{loose}}^{2\ell 3j}$ and $\text{SR}_{\text{tight}}^{2\ell \geq 4j}$, with almost none in $\text{SR}_{\text{loose}}^{2\ell \geq 4j}$. This suggested that fitting a separate MPI template for $t\bar{t} + \geq 1b$ events might be feasible in the current fit setup. However the low absolute number of such events, as well as its status as a background to the main measurement, meant that the inclusion of a separate template for these events was not considered likely to significantly improve the sensitivity of the principal measurement.

9. Fit Studies

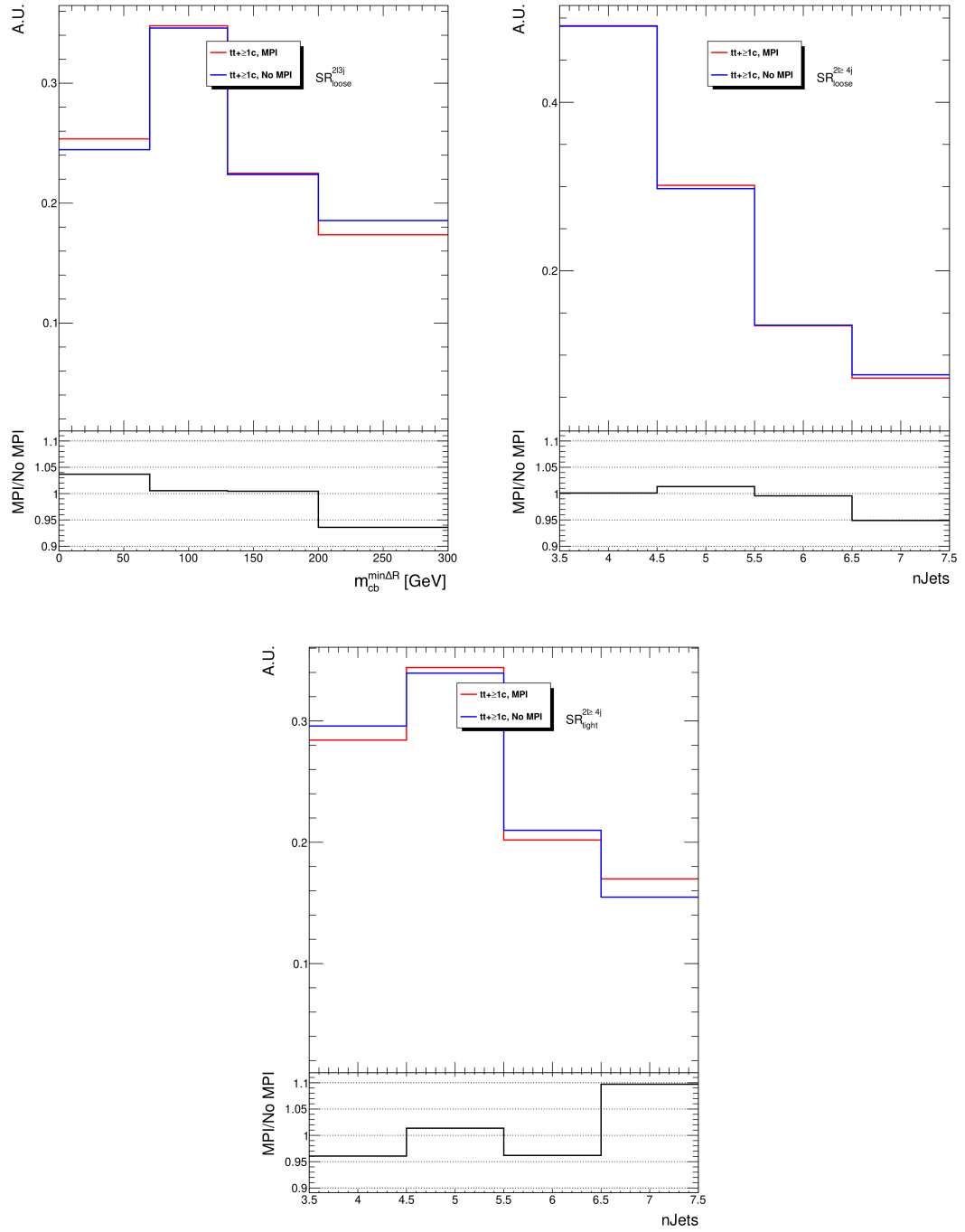


Figure 9.2.: Distributions of $t\bar{t} + \geq 1c$ events either containing at least one or lacking any c -jets from MPI, in dilepton channel signal regions, normalised to equal areas in each region to allow shape comparison.

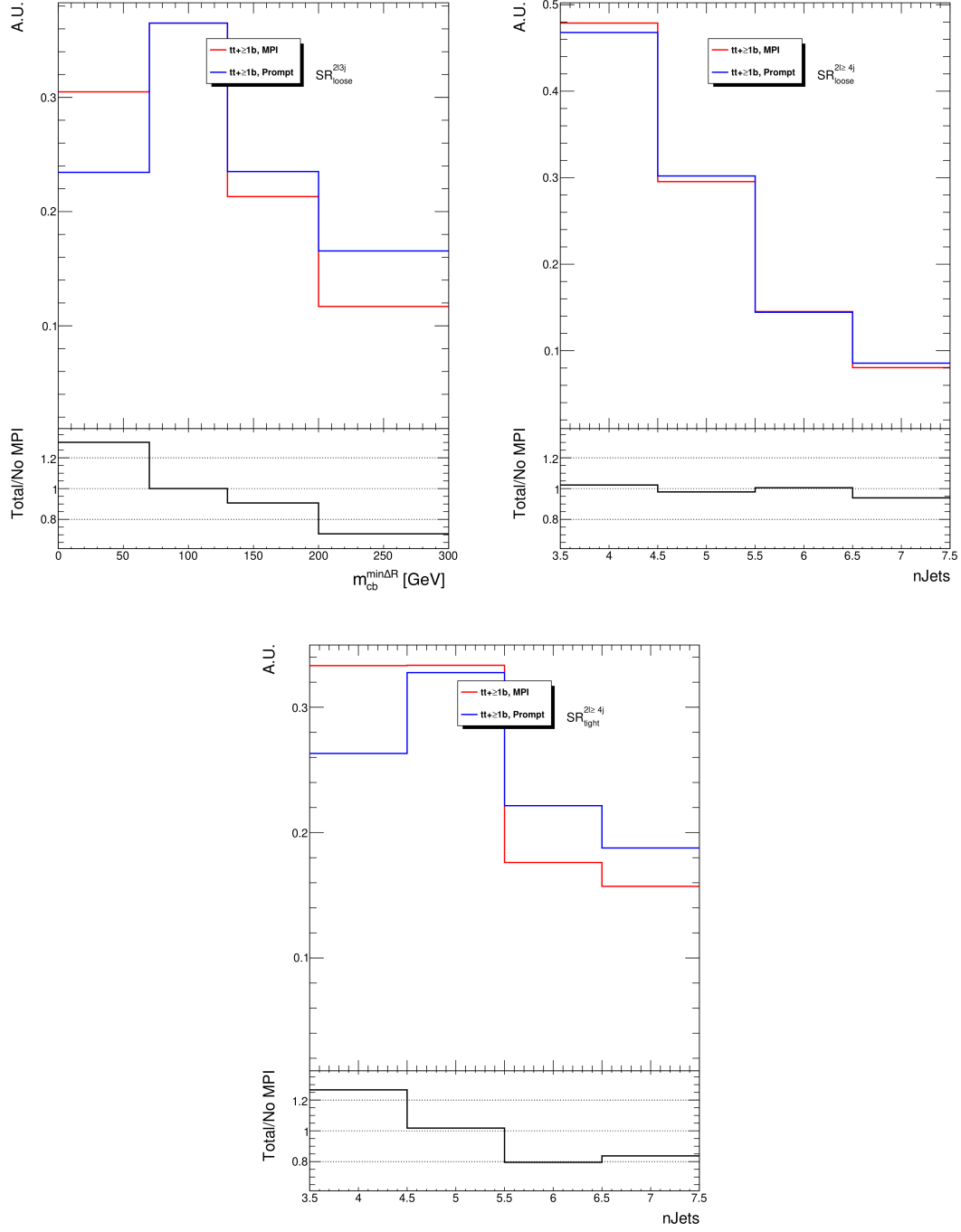


Figure 9.3.: Distributions of $t\bar{t} + \geq 1b$ events either containing at least one or lacking any b -jets from MPI, in dilepton channel signal regions, normalised to equal areas in each region to allow shape comparison.

9. Fit Studies

Table 9.5.: Fraction of b -jet events containing at least one b -jet from MPI in the dilepton channel, in the combined fit.

Region	$t\bar{t} + 1b$ MPI /%	$t\bar{t} + \geq 2b$ MPI /%
$\text{CR}_1^{2\ell 3j}$	6.21	4.12
$\text{CR}_2^{2\ell 3j}$	2.76	2.81
$\text{CR}_3^{2\ell 3j}$	2.86	2.89
$\text{SR}_{\text{loose}}^{2\ell 3j}$	2.97	3.01
$\text{CR}_1^{2\ell \geq 4j}$	5.45	3.35
$\text{CR}_2^{2\ell \geq 4j}$	2.72	2.30
$\text{CR}_3^{2\ell \geq 4j}$	3.16	2.47
$\text{SR}_{\text{loose}}^{2\ell \geq 4j}$	3.39	2.58
$\text{SR}_{\text{tight}}^{2\ell \geq 4j}$	3.06	2.27

In this chapter the results are shown of performing profile likelihood fits in both a fiducial and inclusive phase space as described in Chapter 7, fitting the expected number of events from the MC simulations described in Chapter 4. The pre-selection and choice of regions and observables are as laid out in Chapter 6, using the systematics model described in Chapter 8.

10.1. Fiducial phase space measurement

Here the results found for the measurements in the fiducial phase space are presented. Two parameterisations are used: one employing signal strengths for each $t\bar{t}$ + jets category and one using ratios. However since they converge to the same cross-section values, only one: the fit using signal strengths for each $t\bar{t}$ + jets category ($\mu_{t\bar{t}+\geq 2c}$, $\mu_{t\bar{t}+1c}$, $\mu_{t\bar{t}+\geq 1b}$ and $\mu_{t\bar{t}+\text{light}}$) is presented in full. The fit using the ratios $R_{t\bar{t}+\geq 2c}$, $R_{t\bar{t}+1c}$, $R_{t\bar{t}+\geq 1b}$ and the overall normalisation $\mu_{t\bar{t}+\text{jets}}$ has the same fitted values for NPs and the same set of correlations between them, so only its measured values are discussed.

Fit to Asimov pseudo-dataset

A profile likelihood fit is performed to an Asimov pseudo-dataset, defined in Section 7.1. The fitted values from both parameterisations are shown in Figure 10.1, with all values equal to one as expected. The expected uncertainties obtained for $\mu_{t\bar{t}+\geq 2c}$ and $\mu_{t\bar{t}+1c}$ are $^{+0.215}_{-0.189}$ and $^{+0.183}_{-0.165}$ respectively, with uncertainties of around 7% and 5% for the $t\bar{t}+\geq 1b$ and $t\bar{t}+\text{light}$ contributions respectively. The ratios have slightly smaller relative uncertainties than their comparable signal strength, with an expected uncertainty for the overall $t\bar{t}$ + jets signal strength of around 5%. This reduction is likely due to the effective

10. Results

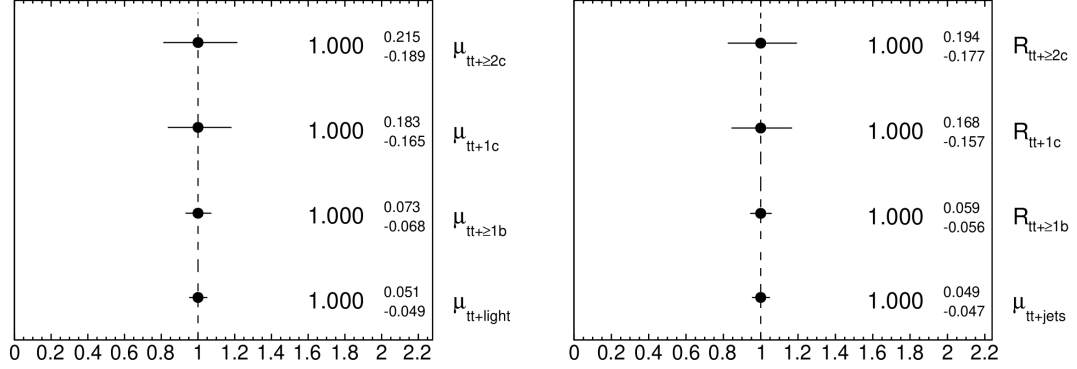


Figure 10.1.: Signal strengths for each $t\bar{t} + \text{jets}$ category in fits to an Asimov pseudo-dataset, in a fiducial phase space. Central values are all one, as expected in this fit test. Uncertainties include both statistical and systematic uncertainties. Left: fitted signal strengths for each event category. Right: Ratios of each category except $t\bar{t} + \text{light}$, with a signal strength describing the overall $t\bar{t} + \text{jets}$ normalisation.

cancellation of uncertainties related to detector effects, since those due to modelling are decorrelated between categories.

All systematic uncertainties show no pulls in their NPs, as expected. However some notable constraints are seen. Table 10.1 shows all constraints below the threshold $\frac{\Delta\hat{\theta}}{\Delta\theta} = 0.9$, with the most constrained shown first. The large majority are related to the modelling of the $t\bar{t}$ system, in particular uncertainties in the choice of parton showering simulation and NLO matching. Several of the NPs related to the calibration of the b/c -tagger are also constrained.

The most constrained have been the subject of dedicated investigations, as described in Section 9.2. Looking at the two most strongly constrained NPs, it was determined that the constraint on the $t\bar{t} + \text{light}$ parton shower uncertainty affecting three-jet-exclusive regions was primarily due to its shape effect in $\text{SR}_{\text{loose}}^{2\ell 3j}$. In this region, systematic variations act in opposite directions in different bins of the distribution, so this strong shape effect may be ‘disfavoured’ during fitting. Regarding the constrained NP related to μ_R for $t\bar{t} + \geq 1b$ events, as mentioned in Section 8.3.1, in certain regions the variation of the NP to one standard deviation has a very large impact on the predicted number of events. Therefore it is unsurprising that such a constraint is seen post-fit, as a large variation of the NP would significantly change the final data/prediction agreement.

Fit to ATLAS data

The fit to ATLAS data in a fiducial phase space is detailed here. This result is the principal one of the analysis as presented in Ref. [1].

The calculated correlations between each NP and signal strength (where at least one

10.1. Fiducial phase space measurement

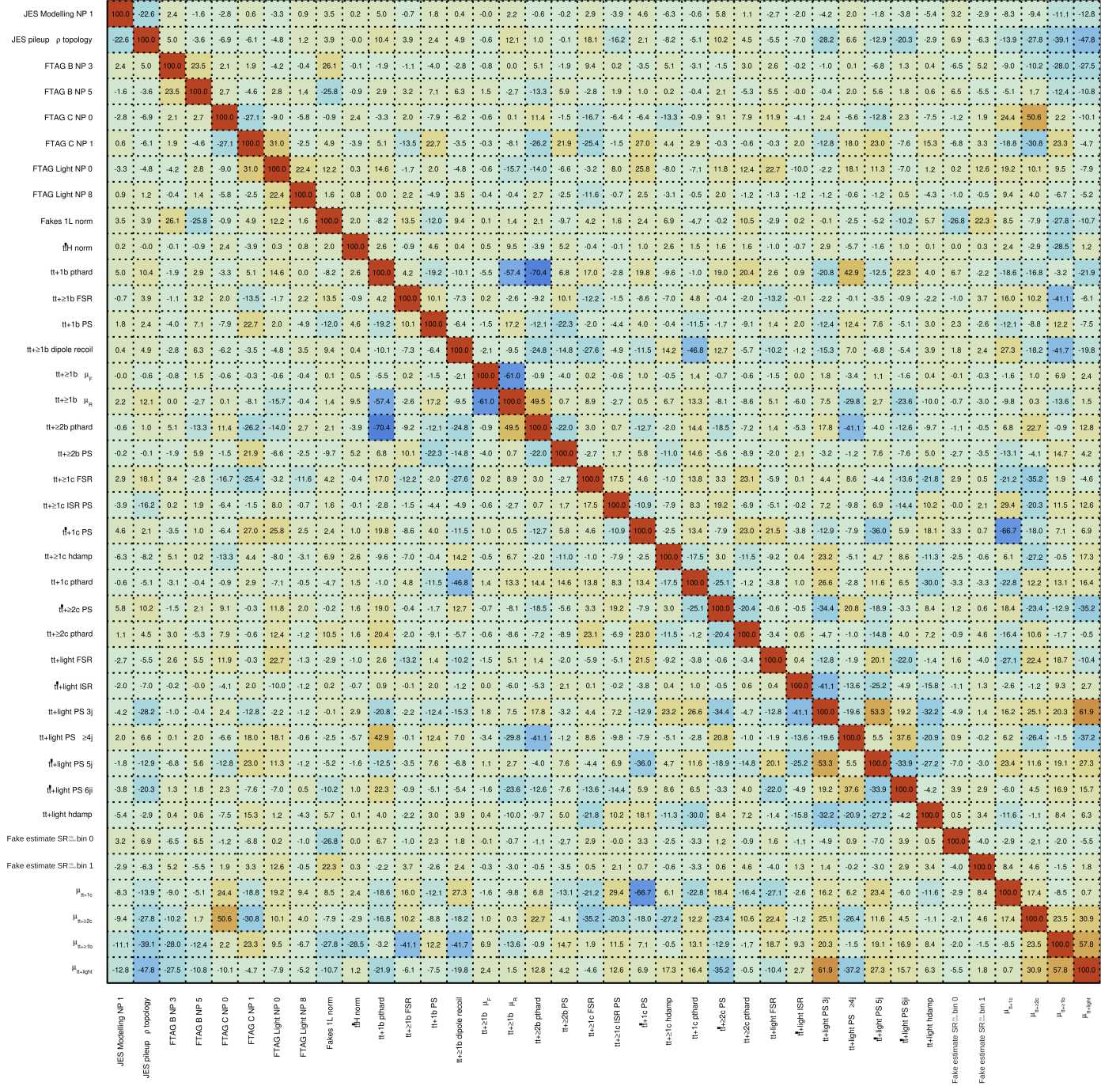
Table 10.1.: Constraints $\frac{\Delta\hat{\theta}}{\Delta\theta}$ of nuisance parameters in a fit to an Asimov pseudo-dataset in a fiducial phase space. Only those with $\frac{\Delta\hat{\theta}}{\Delta\theta} < 0.9$ are shown, ordered from most to least constrained.

Nuisance Parameter	Constraint $\Delta\hat{\theta}/\Delta\theta$	Nuisance Parameter	Constraint $\Delta\hat{\theta}/\Delta\theta$
$t\bar{t}$ + light parton shower 3j	0.330	$t\bar{t}$ + 1c NLO matching	0.704
$t\bar{t}$ + $\geq 1b$ μ_R	0.347	$t\bar{t}$ + $\geq 1c$ FSR	0.726
$t\bar{t}$ + 1b NLO matching	0.421	$t\bar{t}$ + light NLO matching	0.744
$t\bar{t}$ + light parton shower 5j	0.494	JES pileup ρ topology	0.752
FTAG Light NP 0	0.589	$t\bar{t}$ + $\geq 2c$ NLO matching	0.779
$t\bar{t}$ + $\geq 1b$ dipole recoil	0.597	$t\bar{t}$ + light FSR	0.797
$t\bar{t}$ + $\geq 2b$ NLO matching	0.601	$t\bar{t}$ + $\geq 2b$ parton shower	0.802
$t\bar{t}$ + light parton shower $\geq 4j$	0.618	$t\bar{t}$ + 1b parton shower	0.847
FTAG C NP 1	0.625	$t\bar{t}$ + $\geq 1c$ hdamp	0.847
$t\bar{t}$ + 1c parton shower	0.628	FTAG C NP 0	0.863
lepton + jets fakes normalisation	0.679	FTAG B NP 5	0.879
$t\bar{t}$ + light parton shower $\geq 6j$	0.685	FTAG Light NP 3	0.883
$t\bar{t}$ + $\geq 2c$ parton shower	0.695	FTAG Light NP 1	0.888
$t\bar{t}$ + light hdamp	0.701	FTAG B NP 3	0.899

correlation is $\geq 20\%$) is shown in Figure E.4, which uses the fit setup with individual signal strengths. The correlation between the signal strengths $\mu_{t\bar{t}+\geq 2c}$ and $\mu_{t\bar{t}+1c}$ is +17.4%. This is notable as one could expect a negative correlation if these categories behaved interchangeably in fitting. This underscores that, as modelled, they behave as distinct processes, supporting the decision to measure them separately in this analysis. Strong (anti-)correlations appear between some of the key $t\bar{t} + \geq 1b$ modelling uncertainties: specifically between the uncertainty on the p_T^{hard} parameter for $t\bar{t} + 1b$ events, and both the $t\bar{t} + \geq 2b$ p_T^{hard} and $t\bar{t} + \geq 1b$ μ_R uncertainties. Similarly a strong anti-correlation is seen between the $t\bar{t} + \geq 1b$ μ_R and μ_F NPs. The majority of these show a constraint on their NP, with the $t\bar{t} + 1b$ p_T^{hard} NP also having a pull $\frac{\hat{\theta}-\theta_0}{\Delta\theta} \approx 0.8$. The study described in Section 9.3 was partly aimed at lessening these, but did not find an alternative fit model without significant sacrifices in sensitivity.

Figure 10.3 shows the ten most significant NPs ranked by their impact on the POIs: the signal strength for $t\bar{t} + \geq 2c$ and $t\bar{t} + 1c$ events, as well as their respective ratios to the $t\bar{t}$ + jets cross-section. The impact of each NP is calculated using the linear correlation coefficient between the NP and POI, as well as the post-fit uncertainty of the NP and POI [262]. In each case the rankings are similar between the signal strengths and ratios. For $t\bar{t} + \geq 2c$, the most significant NP is the first one related to the calibration of c -tagging WPs, with the second one also featuring in the ranking. The first is also highly ranked for $t\bar{t} + 1c$ POIs, reflecting that these NPs impact the definition of the signal regions, and highlighting the key nature of HF tagging in this analysis. The majority of the other highly ranked systematic uncertainties for $t\bar{t} + \geq 2c$ and $t\bar{t} + 1c$ relate to the modelling of the $t\bar{t}$ + jets system, especially modelling of $t\bar{t} + \geq 1c$.

10. Results



10.1. Fiducial phase space measurement

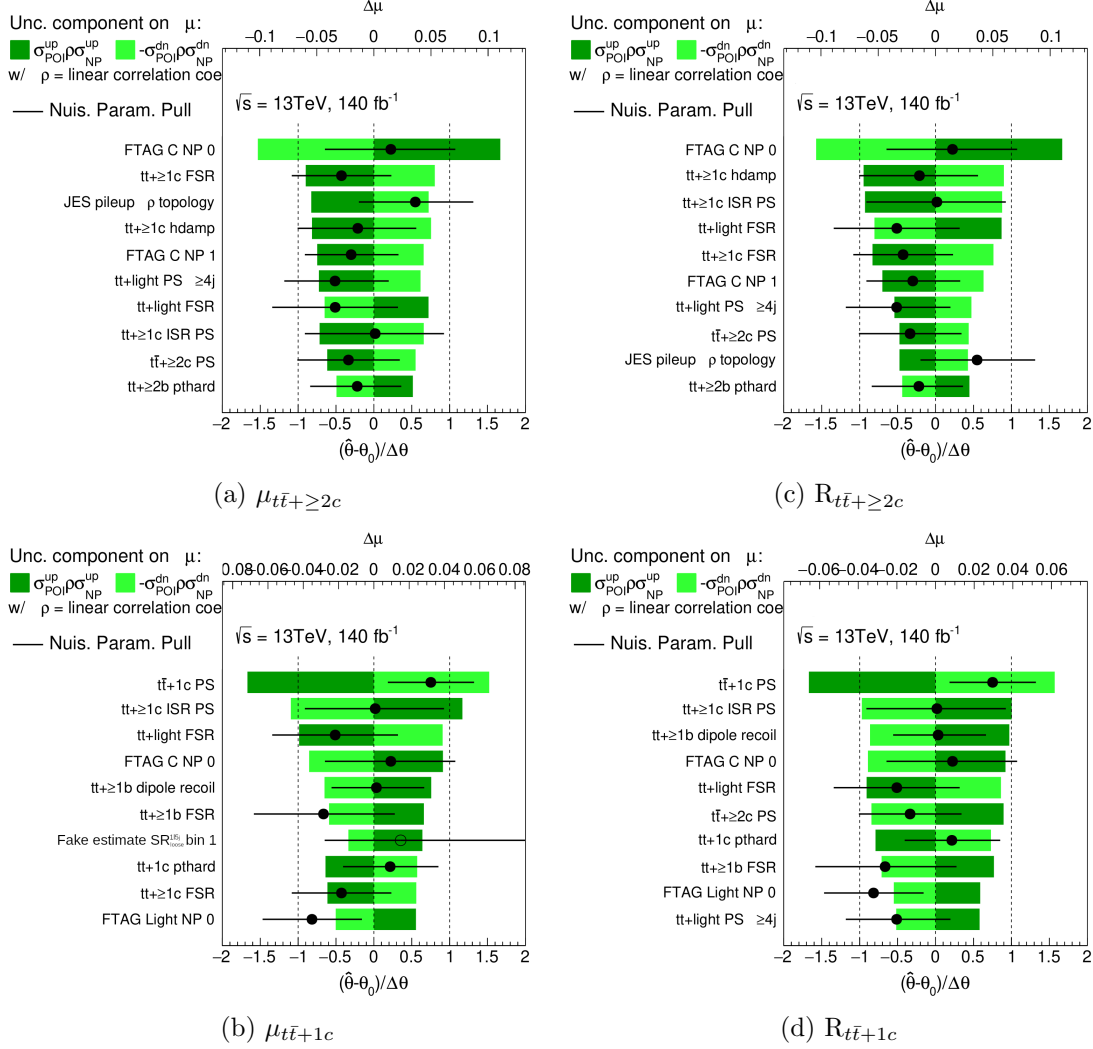


Figure 10.3.: Plots showing a ranking of the ten most impactful systematic uncertainties, in fits to ATLAS data in a fiducial phase space, on a) $t\bar{t} + \geq 2c$ signal strength b) $t\bar{t} + 1c$ signal strength c) $R_{t\bar{t}+\geq 2c}$ d) $R_{t\bar{t}+1c}$. The latter two denote the fraction of events in that category relative to all $t\bar{t} + \text{jets}$ events. The impact is calculated using the covariance matrix and the uncertainties of parameters, and is shown in green. The post-fit values and uncertainties of these nuisance parameters is also shown, relative to their pre-fit values.

10. Results

Among these, a notable constraint ($\frac{\Delta\hat{\theta}}{\Delta\theta} = 0.57$) can be seen on the NP related to the choice of parton shower algorithm for $t\bar{t} + 1c$, as well as a pull of $\frac{\hat{\theta}-\theta_0}{\Delta\theta} = 0.75$. When the effect of the ‘preferred’ upward variation of this NP is examined, it produces a significant increase in the $t\bar{t} + 1c$ contribution across all signal regions. These regions are highly enriched in $t\bar{t} + 1c$ events, and pre-fit data/prediction comparisons show an under-prediction there. Therefore the pull can be interpreted as acting to improve agreement, with the constraint related to the large impact of the pre-fit uncertainty. Also highly ranked and constrained, albeit less so ($\frac{\Delta\hat{\theta}}{\Delta\theta} = 0.66$), is the NP associated with $t\bar{t} + \geq 1c$ FSR modelling uncertainty. Investigation of this constraint suggested the constraint is linked to the uncertainty’s effect on $t\bar{t} + 1c$ events in lepton + jets channel signal regions, and the large impact variation of this NP has there. Similar rankings, calculated using two different methods, can be found in the Appendix E and show a similar set of the most highly ranked uncertainties, with slightly differing orderings in some cases.

The other highly impactful non-modelling NPs are the ones related to JES pileup ρ topology, impactful for $t\bar{t} + \geq 2c$, and the uncertainty of the fake lepton contribution in one bin of the $\text{SR}_{\text{loose}}^{1\ell 5j}$ region, for $t\bar{t} + 1c$. The former is less significant for the ratio $R_{t\bar{t}+\geq 2c}$, as may be expected given that it scales all $t\bar{t} + \text{jets}$ contributions, allowing cancellation in the ratio setup. Its NP shows a moderate pull of $\frac{\hat{\theta}-\theta_0}{\Delta\theta} = 0.63$. The full set of NP pulls and constraints can be found in Figures 10.4 and 10.5.

The goodness-of-fit value for this fit, calculated using a saturated model, is 98.2%, indicating good agreement.

Figures 10.6 and 10.7 show a post-fit comparison between data and simulation in the signal regions, which can be compared to the pre-fit plots in Figures 6.2 and 6.3. These also show good agreement in the final fit.

The fiducial cross-section values calculated from the signal strengths are:

$$\begin{aligned}\sigma_{t\bar{t}+\geq 2c}^{\text{fid}} &= 1.28_{-0.10}^{+0.16} \text{ (stat)} \text{ }_{-0.22}^{+0.21} \text{ (syst)} \text{ pb} = 1.28_{-0.24}^{+0.27} \text{ pb} \\ \sigma_{t\bar{t}+1c}^{\text{fid}} &= 6.5_{-0.4}^{+0.5} \text{ (stat)} \pm 0.8 \text{ (syst)} \text{ pb} = 6.4_{-0.9}^{+1.0} \text{ pb}\end{aligned}\tag{10.1}$$

The overall impact of each group of uncertainties is given in Table 10.2. This also uses the correlations as the basis for calculating impact, and the uncertainties can be combined by addition in quadrature. Among systematic uncertainties, the most significant group is the one concerning modelling of $t\bar{t} + \geq 1c$ events, contributing a 9% uncertainty to the $t\bar{t} + \geq 2c$ cross-section and 8% for $t\bar{t} + 1c$. Notably, c -tagging calibration uncertainties contribute significantly more to the uncertainty of $\sigma_{t\bar{t}+\geq 2c}$ than $\sigma_{t\bar{t}c}$ (9% vs. 4%). This follows the pattern observed in the highly ranked individual NPs, and likely originates from the observed mis-match between data and MC prediction in the c -dominated signal regions, as shown in Figures 6.2 and 6.3. The data statistical uncertainty of 11% and 7% for $\sigma_{t\bar{t}+\geq 2c}$ and $\sigma_{t\bar{t}c}$ respectively includes the uncertainties in the normalisation of $t\bar{t} + \geq 1b$ and $t\bar{t} + \text{light}$. Of the analysis regions, the greatest data statistical uncertainty is observed in the ‘tight’ signal regions requiring two jets tagged with the $c@11\%$ working point. The overall uncertainties seen are similar to the expected values from the fit to an Asimov pseudo-dataset.

10.1. Fiducial phase space measurement

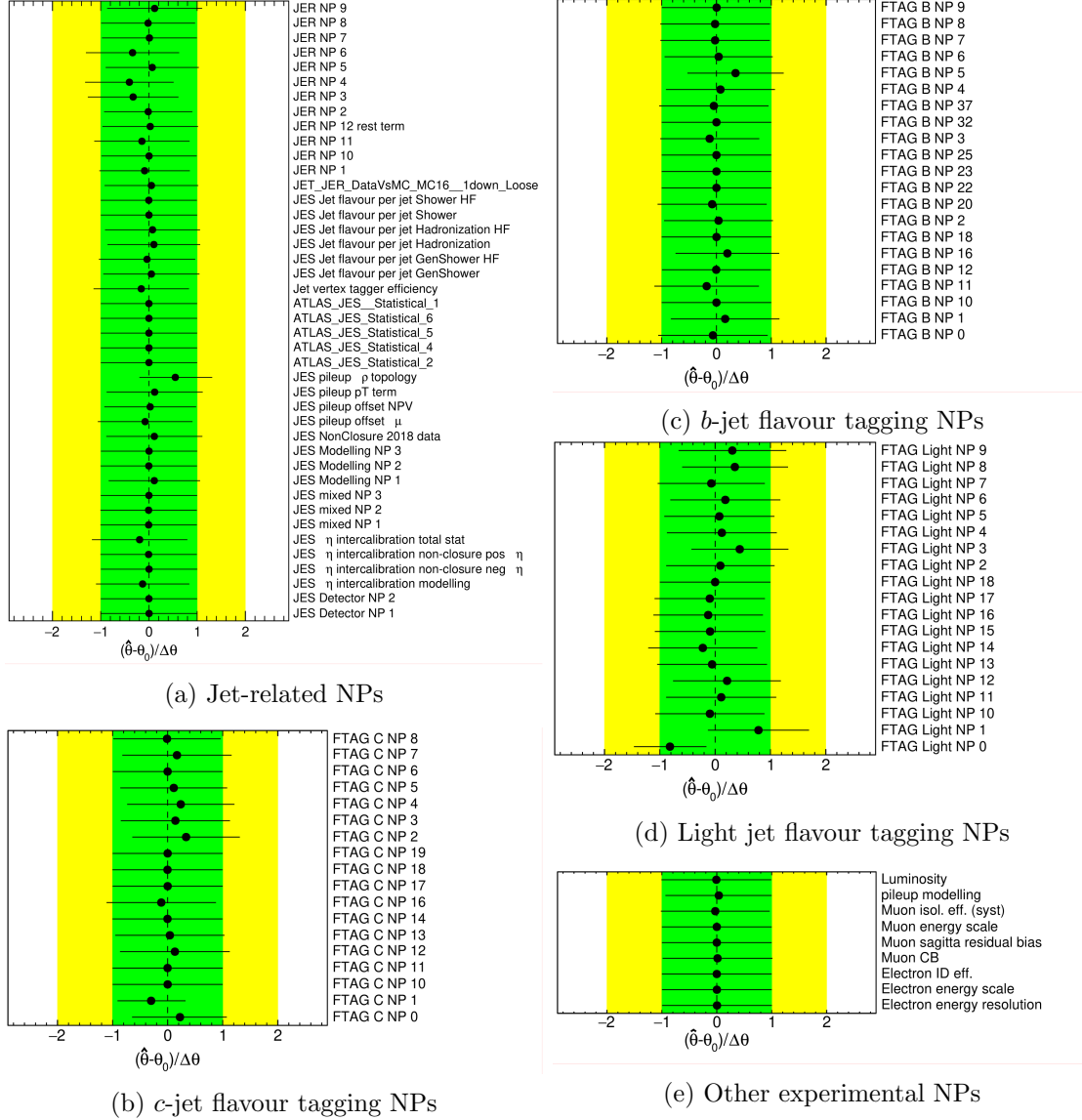


Figure 10.4.: Pulls of instrumental NPs in a fit to data in a fiducial phase space, grouped into those related to a) jets b) c -jet flavour tagging c) b -jet flavour tagging d) light jet flavour tagging e) other experimental NPs.

10. Results

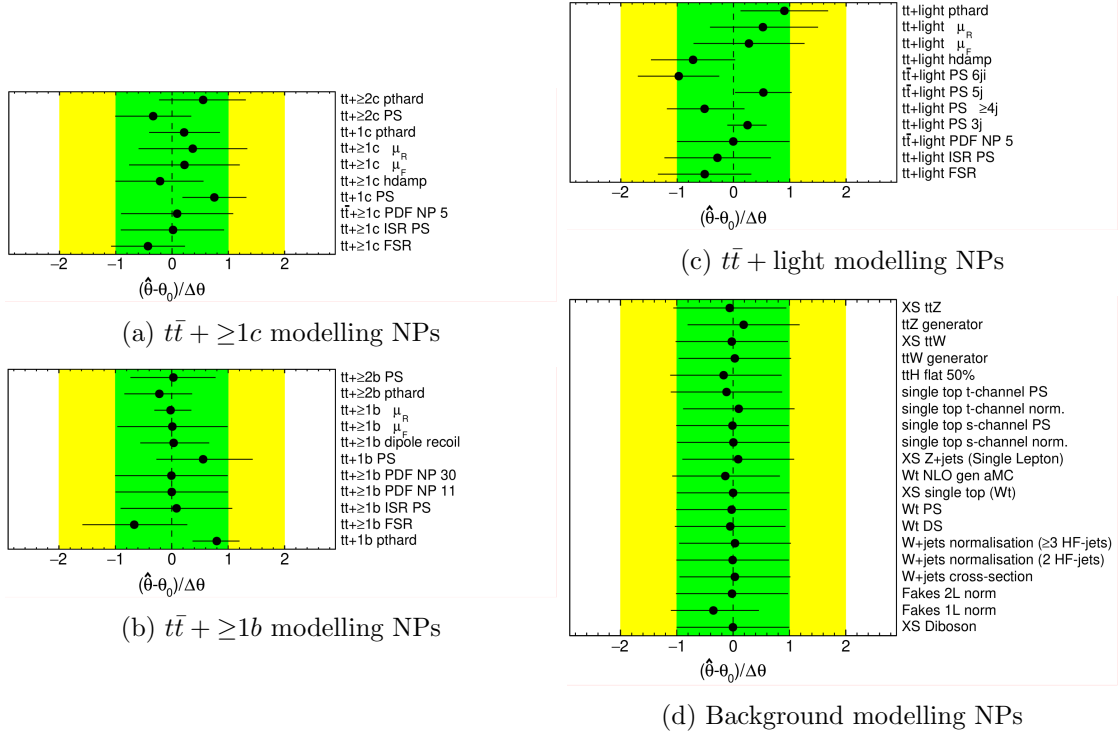


Figure 10.5.: Pulls of modelling NPs in a fit to data in a fiducial phase space, grouped into those related to a) $t\bar{t} + \geq 1c$ b) $t\bar{t} + \geq 1b$ c) $t\bar{t} + \text{light}$ d) background processes.

10.1. Fiducial phase space measurement

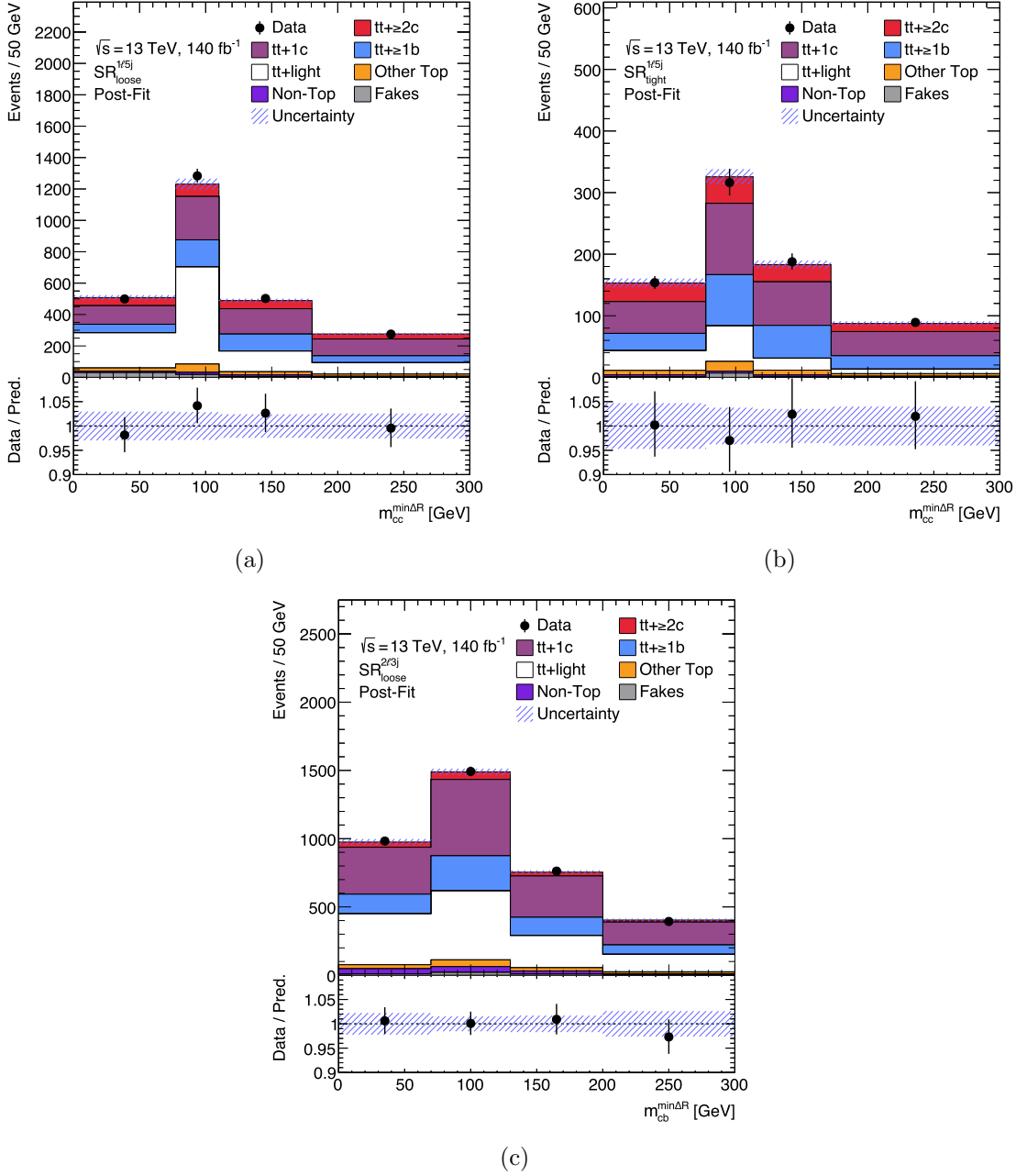


Figure 10.6.: Post-fit plots comparing MC predictions and data in signal regions $SR_{loose}^{1\ell 5j}$, $SR_{tight}^{1\ell 5j}$ and $SR_{loose}^{2\ell 3j}$. The lepton + jets signal regions use the observable $M_{cc}^{min\Delta R}$, the invariant mass of the two c -jets separated by the smallest ΔR . In $SR_{tight}^{1\ell 5j}$ only those c -jets tagged with $c@11\%$, the tighter c -tagging working point, are considered. Events in $SR_{loose}^{2\ell 3j}$ have only one c -jet, so the observable is $M_{cb}^{min\Delta R}$, the invariant mass of it and the closest b -jet. Events outside the range are put into the first or last bin, and the blue uncertainty band includes both statistical and systematic uncertainties.

10. Results

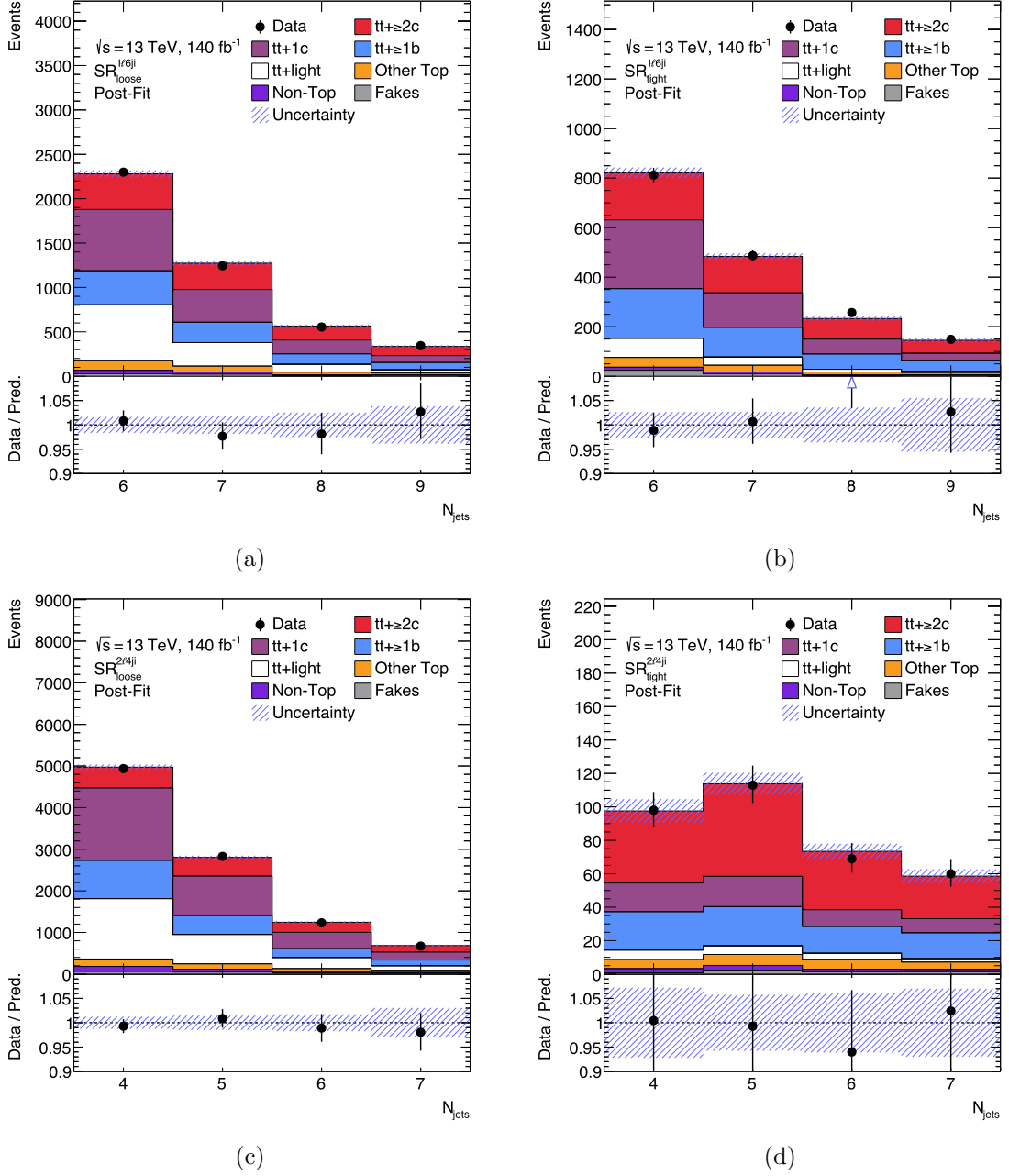


Figure 10.7.: Post-fit plots comparing MC predictions and data in signal regions $\text{SR}_{\text{loose}}^{1\ell \geq 6j}$, $\text{SR}_{\text{tight}}^{1\ell \geq 6j}$ and $\text{SR}_{\text{loose}}^{2\ell \geq 4j}$ and $\text{SR}_{\text{tight}}^{2\ell \geq 4j}$. The observable used is the jet multiplicity. The last bin additionally contains events with jet multiplicities greater than the maximum shown, and the blue uncertainty band includes both statistical and systematic uncertainties.

Table 10.2.: Fractional uncertainty contributed by different uncertainty groups to the measured fiducial cross section values of $t\bar{t} + \geq 2c$ and $t\bar{t} + 1c$. Values are estimated from the covariance matrix between parameters. Uncertainties on the normalisation of $t\bar{t} + \geq 1b$ and $t\bar{t} + \text{light}$ events are included in the ‘Data statistical uncertainty’ category. Data taken from Ref. [1].

Uncertainty group	Fractional uncertainty [%] on	
	$\sigma_{t\bar{t}+\geq 2c}$	$\sigma_{t\bar{t}+1c}$
$t\bar{t} + \geq 1c$ modelling	9	8
Background modelling:		
$t\bar{t} + \geq 1b$	4	4
$t\bar{t} + \text{light}$	6	4
Others	2.5	1.7
Instrumental:		
b -tagging	2.2	1.8
c -tagging	9	4
light mis-tagging	2.2	3.4
JES/JER	6	3.5
Others	1.3	0.9
MC statistics	3.1	2.5
Total systematic uncertainty	17	12
Data statistical uncertainty	11	7
Total	20	14

10. Results

Table 10.3.: Comparison of the measured and predicted values for cross-sections of $t\bar{t} + \geq 1b$, $t\bar{t} + \geq 2c$ and $t\bar{t} + 1c$, and for the ratios of these to inclusive $t\bar{t} + \text{jets}$ production, measured in a fiducial phase space. Measurement uncertainties include statistical and systematic uncertainties, and prediction uncertainties include variations of the μ_R and μ_F scale choices (independent and simultaneous), as well as uncertainties in the choice of PDF set. Predictions are from the nominal inclusive $t\bar{t}$ simulation or dedicated $t\bar{t}b\bar{b}$ simulation, both using POWHEG+PYTHIA8.

	Measured	$t\bar{t}$ or $t\bar{t}b\bar{b}$ POWHEG+PYTHIA8
$\sigma_{t\bar{t}+\geq 1b}$ [pb]	3.46 ± 0.24	3.2 ± 1.6
$\sigma_{t\bar{t}+\geq 2c}$ [pb]	1.28 ± 0.25	1.04 ± 0.18
$\sigma_{t\bar{t}+1c}$ [pb]	6.4 ± 0.9	5.1 ± 0.8
$R_{t\bar{t}+\geq 1b}$ [%]	7.2 ± 0.4	6.5 ± 3.3
$R_{t\bar{t}+\geq 2c}$ [%]	2.7 ± 0.5	2.1 ± 0.4
$R_{t\bar{t}+1c}$ [%]	13.7 ± 1.8	10.3 ± 1.6

For the ratio fit setup, the values obtained for $t\bar{t} + \geq 2c$ and $t\bar{t} + 1c$ are $R_{t\bar{t}+\geq 2c} = (2.7 \pm 0.5)\%$ and $R_{t\bar{t}+1c} = (13.7 \pm 1.8)\%$. As expected, the relative uncertainties on the POIs are slightly lower than in the signal strength fit due to cancellation of uncertainties. However the difference is fairly small, due to the limited correlations between the most important modelling uncertainties across different $t\bar{t} + \text{jets}$ categories.

In Table 10.3, the measured cross sections and ratios for $t\bar{t} + \geq 2c$, $t\bar{t} + 1c$ and $t\bar{t} + \geq 1b$ are compared to their predicted values, taken from the nominal MC samples described in Section 4.1. For $t\bar{t} + \geq 2c$ and $t\bar{t} + 1c$, the relevant sample is a 5FS $t\bar{t}$ inclusive one, while the $t\bar{t} + \geq 1b$ values are compared to dedicated 4FS $t\bar{t}b\bar{b}$ samples, both employing POWHEG+PYTHIA8.

In all cases, the measured values agree with the predictions within one to two standard deviations, but exceed them. This pattern is consistent with that seen in the previous CMS analysis [104], as well as other recent ATLAS analyses, such as the measurement of $t\bar{t}$ with additional b -jets in the $e\mu$ $t\bar{t}$ final state [263]. A broader comparison is shown in Figure 10.8, which includes all measured cross-section values: inclusive $t\bar{t} + \text{jets}$, $t\bar{t} + \text{light}$, $t\bar{t} + 1c$, $t\bar{t} + \geq 2c$ and $t\bar{t} + \geq 1b$. These are compared to the predictions from the full range of $t\bar{t}$ and $t\bar{t}b\bar{b}$ MC samples, including those with alternative generation setups used to estimate systematic uncertainties. The uncertainties of the predictions include variations of the μ_R and μ_F scale choices (independent and simultaneous), as well as uncertainties in the choice of PDF set. The values plotted are given in Table E.1 in Appendix E.

The $t\bar{t} + \text{jets}$ and $t\bar{t} + \text{light}$ predicted cross-sections mainly agree within one standard deviation, though show a tendency to slightly over-predict the measured value. In particular for the $t\bar{t} + \text{light}$ cross-section, the measured value is approximately one standard

10.1. Fiducial phase space measurement

deviation lower than the predictions. For $t\bar{t} + \geq 1b$, all predictions show good agreement with the measured value, with those from dedicated $t\bar{t}b\bar{b}$ simulations having notably larger uncertainties. Nonetheless all except one under-predict this cross-section. For the $t\bar{t} + 1c$ cross-section, all POWHEG + PYTHIA 8 setups show a similar level of under-prediction, though considering both measurement and prediction uncertainties agree within 0.9 to 1.1 standard deviations. However the setups using POWHEG + HERWIG 7 and MADGRAPH5_aMC@NLO + HERWIG 7 show larger disagreement, under-predicting at the level of two standard deviations.

A similar pattern is seen for $t\bar{t} + \geq 2c$, with POWHEG + PYTHIA 8 setups agreeing within 0.5 to 0.8 standard deviations, and the others having larger under-predictions at a level above one standard deviation.

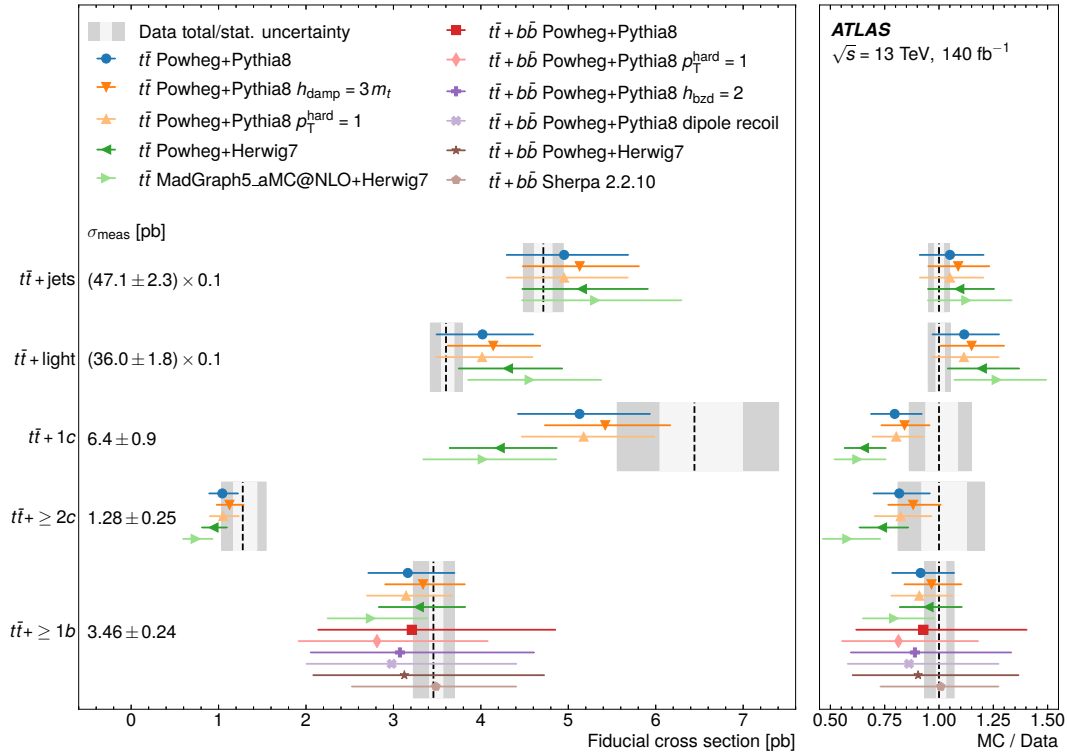


Figure 10.8.: Comparison of cross-section values, measured in a fiducial phase space, to predicted values taken from MC simulation. Some cross-section values are multiplied by 0.1 for ease of visualisation. The nominal predicted values are either from a 5FS inclusive $t\bar{t}$ simulation, or a dedicated 4FS $t\bar{t}b\bar{b}$ simulation, both using POWHEG+PYTHIA8. Alternative samples use different simulation setups. The uncertainties of the predictions include variations of the μ_R and μ_F scale choices (independent and simultaneous), as well as uncertainties in the choice of PDF set. Figure taken from Ref. [1].

Additional fit setups

Alternative fit setups are also used in the fiducial phase space to validate the results. In one, the $t\bar{t} + \geq 2c$ and $t\bar{t} + 1c$ signal strengths are separated between the lepton + jets and dilepton channels, testing the compatibility between the fits in each channel. This measures values of $\sigma_{t\bar{t}+\geq 2c}^{1\ell} = 1.5 \pm 0.4$ pb and $\sigma_{t\bar{t}+1c}^{1\ell} = 6.4 \pm 1.1$ pb for the lepton + jets channel, and $\sigma_{t\bar{t}+\geq 2c}^{2\ell} = 1.18 \pm 0.25$ pb and $\sigma_{t\bar{t}+1c}^{2\ell} = 6.4 \pm 1.0$ pb for the dilepton channel, which are consistent with the nominal result within uncertainties. A χ^2 test performed on the difference in each setup's log-likelihood yields a value of 58%, indicating good compatibility between the setups.

Another fit is performed using a single signal strength to scale both $t\bar{t} + \geq 2c$ and $t\bar{t} + 1c$ events. The systematic uncertainties related to NLO matching and choice of parton shower algorithm, which are decorrelated between $t\bar{t} + \geq 2c$ and $t\bar{t} + 1c$ in the nominal setup, are also recorrelated. This gives a cross-section value of $\sigma_{t\bar{t}+\geq 1c} = 8.2 \pm 0.9$ pb. The result is consistent within uncertainties with the sums of the nominal values, and has a slightly lower relative uncertainty.

10.2. Inclusive phase space measurement

Here the results are presented from the fits performed in an inclusive phase space, without the fiducial phase space cuts described in Section 7.2. Otherwise, the fit is performed in an identical way to the previously described fiducial phase space fit. Since the fitted NPs follow a similar pattern of correlations, pulls and constraints as that principal result, it is here discussed in less detail, only considering the fit to data. A more complete set of figures related to this fit are included in Appendix E.

Figure 10.9 shows the impact of the most significant uncertainties on the $t\bar{t} + \geq 2c$ and $t\bar{t} + 1c$ signal strengths and ratios, alongside their pulls. Both of these are largely similar to those in the fiducial fit, being dominated by uncertainties related to $t\bar{t}$ modelling (especially $t\bar{t} + \geq 1c$ modelling) and the calibration of the b/c -tagger.

The goodness-of-fit in this setup, using a saturated model, is 99.5%, slightly higher than the fiducial fit setup.

The calculated cross-sections and ratios are shown in Table 10.4, alongside comparisons to the values from the relevant nominal MC simulation. Notably, the ratios $R_{t\bar{t}+\geq 2c}$ and $R_{t\bar{t}+1c}$ are significantly lower than in the fiducial phase space. This is a natural consequence of the different phase space considered, without requirements on the transverse momentum of the objects. The fractional uncertainties are slightly larger than those in the fiducial measurement. The measured values are under-predicted by simulation to a similar extent, agreeing with the nominal predicted values at a level of around one standard deviation.

10.2. Inclusive phase space measurement

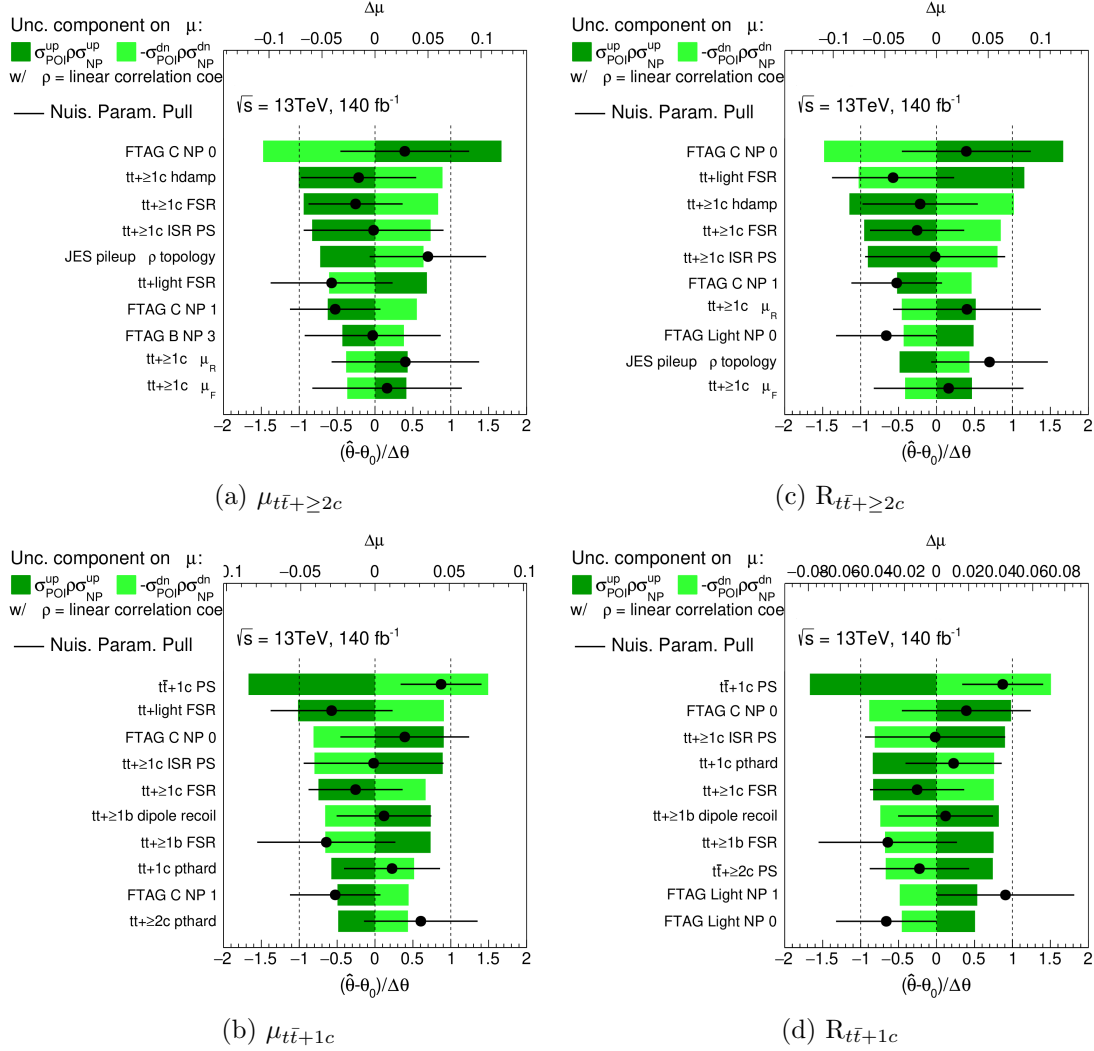


Figure 10.9.: Plots showing a ranking of the ten most impactful systematic uncertainties, in fits to ATLAS data in an inclusive phase space, on a) $t\bar{t} + \geq 2c$ signal strength b) $t\bar{t} + 1c$ signal strength c) $R_{t\bar{t}+\geq 2c}$ d) $R_{t\bar{t}+1c}$. The latter two denote the fraction of events in that category relative to all $t\bar{t}$ + jets events. The impact is calculated using the covariance matrix, and the uncertainties of parameters, and is shown in green. The post-fit values and uncertainties of these nuisance parameters is also shown, relative to their pre-fit values.

10. Results

Table 10.4.: Comparison of the measured and predicted values for cross-sections of $t\bar{t} + \geq 1b$, $t\bar{t} + \geq 2c$ and $t\bar{t} + 1c$, and for the ratios of these to inclusive $t\bar{t} + \text{jets}$ production, measured in an inclusive phase space. Measurement uncertainties include statistical and systematic uncertainties, and prediction uncertainties include variations of the μ_R and μ_F scale choices (independent and simultaneous), as well as uncertainties in the choice of PDF set. Predictions are from the nominal inclusive $t\bar{t}$ simulation or dedicated $t\bar{t}b\bar{b}$ simulation, both using POWHEG+PYTHIA8.

	Measured	$t\bar{t}$ or $t\bar{t}b\bar{b}$ POWHEG+PYTHIA8
$\sigma_{t\bar{t}+\geq 1b}$ [pb]	13.0 ± 0.9	12 ± 4
$\sigma_{t\bar{t}+\geq 2c}$ [pb]	5.4 ± 1.1	4.4 ± 0.7
$\sigma_{t\bar{t}+1c}$ [pb]	38 ± 6	31 ± 4
$R_{t\bar{t}+\geq 1b}$ [%]	3.14 ± 0.23	2.6 ± 0.8
$R_{t\bar{t}+\geq 2c}$ [%]	1.23 ± 0.25	0.97 ± 0.16
$R_{t\bar{t}+1c}$ [%]	8.8 ± 1.3	6.9 ± 1.0

10.3. Comparison of uncertainties and results to the CMS analysis

A comparison is made in Section 7.4 of the event selections, fit parameterisations and fiducial phase space definition in this analysis with those of the CMS analysis [104]. Here the uncertainties considered and results are compared.

In addition to differences in instrumental uncertainties due to detector differences, the set of modelling uncertainties employed has some notable differences. Those used here are described in detail in Section 8.3.1, and are mostly common to other ATLAS analyses in this area. The CMS analysis includes dedicated b - and c -fragmentation uncertainties, which are not used here. It does not include uncertainties dedicated to the use of an alternative parton shower algorithm, or those related to NLO matching. Furthermore, as indicated in the publication, all uncertainties are correlated within $t\bar{t} + \geq 2c/t\bar{t} + 1c$ and $t\bar{t} + \geq 2b/t\bar{t} + 1b$ categories, whereas in this analysis the NLO matching and parton shower variation uncertainties are decorrelated between these groups (with further decorrelation of the parton shower variation uncertainty for $t\bar{t} + \text{light events}$). This is motivated by a desire to account for these categories being sensitive to systematic effects in different ways, the same motivation for measuring $t\bar{t} + \geq 2c$ and $t\bar{t} + 1c$ separately. The lack of correlation between their signal strengths, and the high impact of these uncertainties.

Due to the differences in phase spaces and signal definitions between the analyses, the measured cross-section and ratio values from the CMS analysis, shown in Appendix A, cannot be compared directly to these results. However they show a similar pattern of NLO+PS simulation under-predicting the measured values at the level of one to two standard deviations. The relative uncertainty of those measured values for $\sigma_{t\bar{t}+\geq 2c}$ are slightly lower, being approximately 18% compared a relative uncertainty of 20% in this

10.3. Comparison of uncertainties and results to the CMS analysis

analysis. These fractional uncertainties are similar across both phase spaces used.

To give an indication of the effect of the differing systematics models between analyses, an additional fit is performed, neglecting parton shower algorithm and NLO matching uncertainties. This makes the systematic uncertainty model employed more similar to the CMS analysis. It is performed in the fiducial phase space. The relative uncertainty for the $t\bar{t} + \geq 2c$ contribution decreases to 18%, and the value agrees with that from the nominal fit model. However the fitted $t\bar{t} + 1c$ contribution, despite a larger decrease in uncertainty of five percentage points, only agrees with the nominal value at the level of two standard deviations. The goodness-of-fit for this setup, evaluated using a saturated model, is significantly decreased at 36.8%. Additionally, a significant number of new and increased pulls are seen on NPs. Therefore it can be concluded that neglecting parton shower and NLO matching uncertainties would not provide a feasible alternative without other significant changes to the fit setup.

Summary and Conclusions

The production of top quark pairs in association with charm quarks presents a challenge in the modelling of QCD processes at different energy scales. Additionally, it represents a major background to searches for rare processes, including those beyond the SM. Experimentally, the efficient identification of c -jets presents an even greater challenge than the equivalent process for b -jets, especially when the two are performed simultaneously.

This thesis presents the first dedicated ATLAS measurement of this process, and the first overall to separately measure the cross-sections of $t\bar{t} + \geq 2c$ and $t\bar{t} + 1c$ events. The definition of these event types in simulation, as well as other $t\bar{t} + \text{jets}$ categories, is provided by the ‘heavy flavour classification’ scheme. The dataset used was collected by the ATLAS experiment at the LHC at $\sqrt{s} = 13$ TeV from 2015-2018, with a corresponding integrated luminosity of 140 fb^{-1} . Two top quark decay channels are considered: lepton + jets and dilepton. To address the challenges in flavour-tagging, a custom algorithm, the b/c -tagger, is employed. Based on the existing ATLAS DL1r tagger, it uses new 2D working points requiring custom calibration. A total of 12 control regions and 7 signal regions are defined across both channels, using the overall multiplicity of jets, as well as the number of b/c -tagged jets. In this way the control regions are enriched in $t\bar{t} + 1b$ and $t\bar{t} + \text{light}$ events, while the signal regions contain a large $t\bar{t} + \geq 2c$ contribution.

A profile likelihood fit is then applied in two different phase spaces: one fiducial phase space with cuts applied at generator level to mimic detector acceptance, and one inclusive phase space without such cuts. In each case separate fits either directly measure the cross-sections for $t\bar{t} + \geq 2c$, $t\bar{t} + 1c$, $t\bar{t} + \geq 1b$ and $t\bar{t} + \text{light}$ events; or the inclusive $t\bar{t} + \text{jets}$ cross-section alongside the fractional contribution of $t\bar{t} + \geq 2c$, $t\bar{t} + 1c$ and $t\bar{t} + \geq 1b$ events. A significant amount of work was done to validate and understand the fit model, in light of the pulls and constraints seen on nuisance parameters; particularly those associated with modelling.

In the fiducial phase space, the measured cross-sections are $\sigma_{t\bar{t} + \geq 2c} = 1.28^{+0.27}_{-0.24} \text{ pb}$

11. Summary and Conclusions

and $\sigma_{t\bar{t}+1c} = 6.4^{+1.0}_{-0.9}$ pb. Predicted values from a range of NLO+PS simulations show agreement within 0.5-2 standard deviations, but tend to under-predict the measured values. The limiting factors of the analysis are modelling of the $t\bar{t}$ and $t\bar{t}b\bar{b}$ systems, as well as uncertainties from flavour-tagging calibration and data statistics.

While direct comparison or combination of the results with those from other analyses is not possible due to the phase spaces and selections used, the observed under-prediction is consistent with previous analyses, including the CMS measurement of $t\bar{t} + \geq 2c$ events [104]. The sensitivity achieved in this measurement of $t\bar{t} + \geq 2c$ is comparable to that analysis, while providing the first measurement of $t\bar{t} + 1c$.

These results, and the comparison to a large range of MC simulation setups, provide crucial input for future work on the modelling of top quark pairs in association with charm quarks, as well as the modelling of multi-scale QCD processes more broadly. In particular, the separate measurement of $t\bar{t} + \geq 2c$ and $t\bar{t} + 1c$ provides more granular information than has previously been published. While not definitive, this measurement adds to the suggestion of some tension between data and current NLO+PS simulations of the $t\bar{t}$ system in association with additional heavy-flavour jets.

Future measurements of this process would likely benefit from the production of dedicated $t\bar{t} + c\bar{c}$ simulations in the 3FS, similar to the existing 4FS $t\bar{t}b\bar{b}$ samples. These would include gluons splitting to $c\bar{c}$ directly in the matrix element. The fact that $t\bar{t}$ modelling is the most significant source of uncertainty highlights the need for further work on the modelling of this system.

Furthermore, benefit may be derived from the use of the latest ATLAS flavour-tagging algorithms, based on graph neural networks [264]. These boast significantly improved performance, with development and calibration being completed at time of writing of the next-generation GN2 tagger. These should allow purer selections of signal regions with higher statistics - important since $t\bar{t} + \geq 1c$ events in these regions are the only significant source of statistical uncertainty in the analysis.

The addition of the ITk inner detector for the future HL-LHC, scheduled to begin operation in 2030, should further improve the performance of flavour-tagging due to enhanced tracking capabilities [265]. The combination of more data, improved algorithms, and higher-quality tracking should provide significant opportunities to more precisely measure this process. It may also become feasible to perform a high-quality differential measurement of the $t\bar{t} + \geq 2c$ and $t\bar{t} + 1c$ processes, providing more information for the use of future studies.

Bibliography

- [1] ATLAS Collaboration, *Measurement of top-quark pair production in association with charm quarks in proton–proton collisions at $s=13$ TeV with the ATLAS detector*, *Phys. Lett. B* **860** (2025) 139177, Auxiliary figures available at: <https://atlas.web.cern.ch/Atlas/GROUPS/PHYSICS/PAPERS/TOPQ-2021-26/>.
- [2] A. A. Michelson and E. W. Morley, *On the Relative Motion of the Earth and the Luminiferous Ether*, *Am. J. Sci.* **34** (1887) 333–345.
- [3] S. L. Glashow, *Partial-symmetries of weak interactions*, *Nucl. Phys.* **22** (1961) 579–588.
- [4] S. Weinberg, *A Model of Leptons*, *Phys. Rev. Lett.* **19** (1967) 1264–1266.
- [5] A. Salam, *Weak and Electromagnetic Interactions*, *Conf. Proc. C* **680519** (1968) 367–377.
- [6] H. Georgi and S. L. Glashow, *Unified Weak and Electromagnetic Interactions without Neutral Currents*, *Phys. Rev. Lett.* **28** (1972) 1494–1497.
- [7] G. Hooft, *Renormalizable Lagrangians for massive Yang-Mills fields*, *Nucl. Phys. B* **35** (1971) 167–188.
- [8] G. 't Hooft and M. Veltman, *Regularization and renormalization of gauge fields*, *Nucl. Phys. B* **44** (1972) 189–213.
- [9] G. 't Hooft and M. Veltman, *Combinatorics of gauge fields*, *Nucl. Phys. B* **50** (1972) 318–353.
- [10] D. J. Gross and F. Wilczek, *Asymptotically Free Gauge Theories. I*, *Phys. Rev. D* **8** (1973) 3633–3652.

BIBLIOGRAPHY

- [11] D. J. Gross and F. Wilczek, *Asymptotically free gauge theories. II*, [Phys. Rev. D **9** \(1974\) 980–993](#).
- [12] H. Fritzsch, M. Gell-Mann, and H. Leutwyler, *Advantages of the color octet gluon picture*, [Phys. Lett. B **47** \(1973\) 365–368](#).
- [13] S. Weinberg, *Non-Abelian Gauge Theories of the Strong Interactions*, [Phys. Rev. Lett. **31** \(1973\) 494–497](#).
- [14] P. Higgs, *Broken symmetries, massless particles and gauge fields*, [Physics Letters **12** \(1964\) 132–133](#).
- [15] F. Englert and R. Brout, *Broken Symmetry and the Mass of Gauge Vector Mesons*, [Phys. Rev. Lett. **13** \(1964\) 321–323](#).
- [16] Particle Data Group Collaboration, S. Navas et al., *Review of particle physics*, [Phys. Rev. D **110** \(2024\) 030001](#).
- [17] C. N. Yang and R. L. Mills, *Conservation of Isotopic Spin and Isotopic Gauge Invariance*, [Phys. Rev. **96** \(1954\) 191–195](#).
- [18] C. S. Wu, et al., *Experimental Test of Parity Conservation in Beta Decay*, [Phys. Rev. **105** \(1957\) 1413–1415](#).
- [19] M. Kobayashi and T. Maskawa, *CP-Violation in the Renormalizable Theory of Weak Interaction*, [Prog. Theor. Phys. **49** \(1973\) 652–657](#).
- [20] N. Cabibbo, *Unitary Symmetry and Leptonic Decays*, [Phys. Rev. Lett. **10** \(1963\) 531–533](#).
- [21] ATLAS Collaboration, *Observation of a new particle in the search for the Standard Model Higgs boson with the ATLAS detector at the LHC*, [Phys. Lett. B **716** \(2012\) 1–29](#).
- [22] CMS Collaboration, *Observation of a New Boson at a Mass of 125 GeV with the CMS Experiment at the LHC*, [Phys. Lett. B **716** \(2012\) 30–61](#).
- [23] D. J. Gross and F. Wilczek, *Ultraviolet Behavior of Non-Abelian Gauge Theories*, [Phys. Rev. Lett. **30** \(1973\) 1343–1346](#).
- [24] H. D. Politzer, *Reliable Perturbative Results for Strong Interactions?*, [Phys. Rev. Lett. **30** \(1973\) 1346–1349](#).
- [25] BESIII Collaboration, *Observation of a Charged Charmoniumlike Structure in $e^+e^- \rightarrow \pi^+\pi^- J/\psi$ at $\sqrt{s}=4.26$ GeV*, [Phys. Rev. Lett. **110** \(2013\) 252001](#).
- [26] Belle Collaboration, *Study of $e^+e^- \rightarrow \pi^+\pi^- J/\psi$ and Observation of a Charged Charmoniumlike State at Belle*, [Phys. Rev. Lett. **110** \(2013\) 252002](#).

- [27] LHCb Collaboration, *Observation of J/ψ Resonances Consistent with Pentaquark States in $\Lambda_b^0 \rightarrow J/\psi K^- p$ Decays*, [Phys. Rev. Lett. **115** \(2015\) 072001](#).
- [28] K. G. Wilson, *Confinement of quarks*, [Phys. Rev. D **10** \(1974\) 2445–2459](#).
- [29] D. Britzger, et al., *Calculations for deep inelastic scattering using fast interpolation grid techniques at NNLO in QCD and the extraction of α_s from HERA data*, [Eur. Phys. J. C **79** \(2019\)](#).
- [30] ATLAS Collaboration, *Measurement of dijet azimuthal decorrelations in pp collisions at $\sqrt{s} = 8$ TeV with the ATLAS detector and determination of the strong coupling*, [Phys. Rev. D **98** \(2018\) 092004](#).
- [31] ATLAS Collaboration, *Determination of the strong coupling constant from transverse energy–energy correlations in multijet events at $\sqrt{s} = 13$ TeV with the ATLAS detector*, [JHEP **07** \(2023\) 085](#).
- [32] CMS Collaboration, *Measurement and QCD analysis of double-differential inclusive jet cross sections in pp collisions at $\sqrt{s} = 8$ TeV and cross section ratios to 2.76 and 7 TeV*, [JHEP **03** \(2017\) 156](#).
- [33] T. Klijnsma, et al., *Determination of the strong coupling constant $\alpha_s(m_Z)$ from measurements of the total cross section for top-antitop quark production*, [Eur. Phys. J. C **77** \(2017\) 778](#).
- [34] P. D. Group, *Review of Particle Physics*, [Progress of Theoretical and Experimental Physics **2022** \(2022\) 083C01](#).
- [35] D. Boito, et al., *Strong coupling from $e^+e^- \rightarrow$ hadrons below charm*, [Phys. Rev. D **98** \(2018\) 074030](#).
- [36] S. Narison, $\alpha_s(\mu)$ from $M_{\chi_{0c(0b)}} - M_{\eta_{c(b)}}$ @N²LO, in *21st High-Energy Physics International Conference in Quantum Chromodynamics*. 12, 2018. [arXiv:1812.09360 \[hep-ph\]](#).
- [37] G. Dissertori, et al., *Determination of the strong coupling constant using matched NNLO+NLLA predictions for hadronic event shapes in $e+e^-$ annihilations*, [JHEP **08** \(2009\) 036](#).
- [38] OPAL Collaboration, *Determination of α_s using OPAL hadronic event shapes at $\sqrt{s} = 91 - 209$ GeV and resummed NNLO calculations*, [Eur. Phys. J. C **71** \(2011\) 1733](#).
- [39] JADE Collaboration, S. Bethke, et al., *Determination of the Strong Coupling $\alpha(s)$ from hadronic Event Shapes with $O(\alpha^3(s))$ and resummed QCD predictions using JADE Data*, [Eur. Phys. J. C **64** \(2009\) 351–360](#).

BIBLIOGRAPHY

- [40] JADE Collaboration, J. Schieck, et al., *Measurement of the strong coupling α_s from the three-jet rate in e^+e^- - annihilation using JADE data*, [Eur. Phys. J. C **73** \(2013\) 2332](#).
- [41] DØ Collaboration, *Determination of the strong coupling constant from the inclusive jet cross section in $p\bar{p}$ collisions at $\sqrt{s}=1.96$ TeV*, [Phys. Rev. D **80** \(2009\) 111107](#).
- [42] DØ Collaboration, *Measurement of angular correlations of jets at $\sqrt{s} = 1.96$ TeV and determination of the strong coupling at high momentum transfers*, [Phys. Lett. B **718** \(2012\) 56–63](#).
- [43] CMS Collaboration, *Measurement of the inclusive 3-jet production differential cross section in proton–proton collisions at 7 TeV and determination of the strong coupling constant in the TeV range*, [Eur. Phys. J. C **75** \(2015\) 186](#).
- [44] Y. L. Dokshitzer, *Calculation of the Structure Functions for Deep Inelastic Scattering and e^+e^- Annihilation by Perturbation Theory in Quantum Chromodynamics.*, *Sov. Phys. JETP* **46** (1977) 641–653.
- [45] V. N. Gribov and L. N. Lipatov, *Deep inelastic $e p$ scattering in perturbation theory*, *Sov. J. Nucl. Phys.* **15** (1972) 438–450.
- [46] G. Altarelli and G. Parisi, *Asymptotic Freedom in Parton Language*, [Nucl. Phys. B **126** \(1977\) 298–318](#).
- [47] J. C. Collins, D. E. Soper, and G. F. Sterman, *Factorization of Hard Processes in QCD*, [Adv. Ser. Direct. High Energy Phys. **5** \(1989\) 1–91](#).
- [48] S. Alekhin, et al., *The new ABMP16 PDF*, [PoS DIS2016 \(2016\) 016](#).
- [49] T.-J. Hou et al., *New CTEQ global analysis of quantum chromodynamics with high-precision data from the LHC*, [Phys. Rev. D **103** \(2021\) 014013](#).
- [50] S. Bailey, et al., *Parton distributions from LHC, HERA, Tevatron and fixed target data: MSHT20 PDFs*, [Eur. Phys. J. C **81** \(2021\) 341](#).
- [51] R. D. Ball et al., *Parton distributions with LHC data*, [Nucl. Phys. B **867** \(2013\) 244–289](#).
- [52] P. Bartalini et al., *Multi-Parton Interactions at the LHC*, 11, 2011. [arXiv:1111.0469 \[hep-ph\]](#).
- [53] ATLAS Collaboration, *ATLAS flavour-tagging algorithms for the LHC Run 2 pp collision dataset*, [Eur. Phys. J. C **83** \(2023\) 681](#).
- [54] H. Harari, *A new quark model for hadrons*, [Phys. Lett. B **57** \(1975\) 265–269](#).

- [55] J. H. Christenson, et al., *Evidence for the 2π Decay of the K_2^0 Meson*, *Phys. Rev. Lett.* **13** (1964) 138–140.
- [56] M. L. Perl, et al., *Evidence for Anomalous Lepton Production in $e^+ - e^-$ Annihilation*, *Phys. Rev. Lett.* **35** (1975) 1489–1492.
- [57] S. W. Herb, et al., *Observation of a Dimuon Resonance at 9.5 GeV in 400-GeV Proton-Nucleus Collisions*, *Phys. Rev. Lett.* **39** (1977) 252–255.
- [58] CDF Collaboration, *Observation of Top Quark Production in $\bar{p}p$ Collisions with the Collider Detector at Fermilab*, *Phys. Rev. Lett.* **74** (1995) 2626–2631.
- [59] DØ Collaboration, *Observation of the Top Quark*, *Phys. Rev. Lett.* **74** (1995) 2632–2637.
- [60] ATLAS Collaboration and CMS Collaboration, *Combination of Measurements of the Top Quark Mass from Data Collected by the ATLAS and CMS Experiments at $\sqrt{s}=7$ and 8 TeV*, *Phys. Rev. Lett.* **132** (2024) 261902.
- [61] G. Degrandi, et al., *Higgs mass and vacuum stability in the Standard Model at NNLO*, *JHEP* **08** (2012) 098.
- [62] G. Isidori, G. Ridolfi, and A. Strumia, *On the metastability of the Standard Model vacuum*, *Nucl. Phys. B* **609** (2001) 387–409.
- [63] M. Czakon, P. Fiedler, and A. Mitov, *Total Top-Quark Pair-Production Cross Section at Hadron Colliders Through $\mathcal{O}(\alpha_s^4)$* , *Phys. Rev. Lett.* **110** (2013) 252004.
- [64] CDF Collaboration and DØ Collaboration, *Combination of Measurements of the Top-Quark Pair Production Cross Section from the Tevatron Collider*, *Phys. Rev. D* **89** (2014) 072001.
- [65] ATLAS Collaboration, *Measurement of the $t\bar{t}$ production cross-section in pp collisions at $\sqrt{s} = 5.02$ TeV with the ATLAS detector*, *JHEP* **06** (2023) 138.
- [66] CMS Collaboration, *Measurement of the inclusive $t\bar{t}$ cross section in final states with one lepton and additional jets at 5.02 TeV with 2017 data*, 2024. <https://cds.cern.ch/record/2895219>.
- [67] ATLAS Collaboration and CMS Collaboration, *Combination of inclusive top-quark pair production cross-section measurements using ATLAS and CMS data at $\sqrt{s} = 7$ and 8 TeV*, *JHEP* **07** (2023) 213.
- [68] ATLAS Collaboration, *Inclusive and differential cross-sections for dilepton $t\bar{t}$ production measured in $\sqrt{s} = 13$ TeV pp collisions with the ATLAS detector*, *JHEP* **07** (2023) 141.

BIBLIOGRAPHY

- [69] CMS Collaboration, *Measurement of the $t\bar{t}$ production cross section, the top quark mass, and the strong coupling constant using dilepton events in pp collisions at $\sqrt{s} = 13$ TeV*, *Eur. Phys. J. C* **79** (2019) 368.
- [70] ATLAS Collaboration, *Measurement of the $t\bar{t}$ production cross-section in the lepton+jets channel at $\sqrt{s} = 13$ TeV with the ATLAS experiment*, *Phys. Lett. B* **810** (2020) 135797.
- [71] CMS Collaboration, *Measurement of differential $t\bar{t}$ production cross sections in the full kinematic range using lepton+jets events from proton-proton collisions at $\sqrt{s} = 13$ TeV*, *Phys. Rev. D* **104** (2021) 092013.
- [72] ATLAS Collaboration, *Measurement of the $t\bar{t}$ cross section and its ratio to the Z production cross section using pp collisions at $s=13.6$ TeV with the ATLAS detector*, *Phys. Lett. B* **848** (2024) 138376.
- [73] CMS Collaboration, *First measurement of the top quark pair production cross section in proton-proton collisions at $\sqrt{s} = 13.6$ TeV*, *JHEP* **08** (2023) 204.
- [74] LHC Top Working Group, *LHCTopWG Summary Plots*, <https://twiki.cern.ch/twiki/bin/view/LHCPhysics/LHCTopWGSummaryPlots>, Accessed 13/12/2024.
- [75] J. Campbell, T. Neumann, and Z. Sullivan, *Single-top-quark production in the t -channel at NNLO*, *JHEP* **02** (2021) 040.
- [76] E. L. Berger, J. Gao, and H. X. Zhu, *Differential Distributions for t -channel Single Top-Quark Production and Decay at Next-to-Next-to-Leading Order in QCD*, *JHEP* **11** (2017) 158.
- [77] N. Kidonakis, *NNLL resummation for s -channel single top quark production*, *Phys. Rev. D* **81** (2010) 054028.
- [78] N. Kidonakis, *Two-loop soft anomalous dimensions for single top quark associated production with a W^- or H^-* , *Phys. Rev. D* **82** (2010) 054018.
- [79] C. D. White, et al., *Isolating Wt production at the LHC*, *JHEP* **11** (2009) 074.
- [80] ATLAS Collaboration and CMS Collaboration, *Combinations of single-top-quark production cross-section measurements and $-f_{LV} V_{tb}$ determinations at $\sqrt{s} = 7$ and 8 TeV with the ATLAS and CMS experiments*, *JHEP* **05** (2019) 088.
- [81] L.-B. Chen, et al., *Analytic result for the top-quark width at next-to-next-to-leading order in QCD*, *Phys. Rev. D* **108** (2023) 054003.
- [82] CMS Collaboration, *Measurement of the ratio $\mathcal{B}(t \rightarrow Wb)/\mathcal{B}(t \rightarrow Wq)$ in pp collisions at $\sqrt{s} = 8$ TeV*, *Phys. Lett. B* **736** (2014) 33–57.

- [83] CMS Collaboration, *Measurement of the Single-Top-Quark t -Channel Cross Section in pp Collisions at $\sqrt{s} = 7$ TeV*, [JHEP **12** \(2012\) 035](#).
- [84] I. Bigi, et al., *Production and decay properties of ultra-heavy quarks*, [Phys. Lett. B **181** \(1986\) 157–163](#).
- [85] CMS Collaboration, *Search for heavy pseudoscalar and scalar bosons decaying to top quark pairs in proton-proton collisions at $\sqrt{s} = 13$ TeV*, 2024.
<https://cds.cern.ch/record/2911775>.
- [86] ATLAS Collaboration, *Observation of quantum entanglement with top quarks at the ATLAS detector*, [Nature **633** \(2024\) 542–547](#).
- [87] CMS Collaboration, *Observation of quantum entanglement in top quark pair production in proton-proton collisions at $\sqrt{s} = 13$ TeV*, [Rept. Prog. Phys. **87** \(2024\) 117801](#).
- [88] R. H. Dalitz and G. R. Goldstein, *Decay and polarization properties of the top quark*, [Phys. Rev. D **45** \(1992\) 1531–1543](#).
- [89] L. Sonnenschein, *Algebraic approach to solve $t\bar{t}$ dilepton equations*, [Phys. Rev. D **72** \(2005\) 095020](#).
- [90] L. Sonnenschein, *Analytical solution of $t\bar{t}$ dilepton equations*, [Phys. Rev. D **73** \(2006\) 054015](#).
- [91] B. A. Betchart, R. Demina, and A. Harel, *Analytic solutions for neutrino momenta in decay of top quarks*, [Nucl. Instrum. Meth. A **736** \(2014\) 169–178](#).
- [92] T. Ježo, et al., *New NLOPS predictions for $t\bar{t} + b$ -jet production at the LHC*, [Eur. Phys. J. C **78** \(2018\) 502](#).
- [93] A. Bredenstein, et al., *NLO QCD corrections to t anti- t b anti- b production at the LHC: 1. Quark-antiquark annihilation*, [JHEP **08** \(2008\) 108](#).
- [94] A. Bredenstein, et al., *NLO QCD corrections to $pp \rightarrow t$ anti- t b anti- b + X at the LHC*, [Phys. Rev. Lett. **103** \(2009\) 012002](#).
- [95] F. Cascioli, et al., *NLO matching for $t\bar{t}b\bar{b}$ production with massive b -quarks*, [Phys. Lett. B **734** \(2014\) 210–214](#).
- [96] F. Buccioni, et al., *NLO QCD predictions for $t\bar{t}b\bar{b}$ production in association with a light jet at the LHC*, [JHEP **12** \(2019\) 015](#).
- [97] ATLAS Collaboration, *Study of heavy-flavor quarks produced in association with top-quark pairs at $\sqrt{s} = 7$ TeV using the ATLAS detector*, [Phys. Rev. D **89** \(2014\) 072012](#).

BIBLIOGRAPHY

- [98] ATLAS Collaboration, *Measurements of fiducial cross-sections for $t\bar{t}$ production with one or two additional b-jets in pp collisions at $\sqrt{s}=8$ TeV using the ATLAS detector*, [Eur. Phys. J. C **76** \(2016\) 11](#).
- [99] CMS Collaboration, *Measurement of $t\bar{t}$ production with additional jet activity, including b quark jets, in the dilepton decay channel using pp collisions at $\sqrt{s}=8$ TeV*, [Eur. Phys. J. C **76** \(2016\) 379](#).
- [100] CMS Collaboration, *Measurement of the cross section ratio $\sigma_{t\bar{t}b\bar{b}}/\sigma_{t\bar{t}jj}$ in pp collisions at $\sqrt{s}=8$ TeV*, [Phys. Lett. B **746** \(2015\) 132–153](#).
- [101] ATLAS Collaboration, *Measurements of inclusive and differential fiducial cross-sections of $t\bar{t}$ production with additional heavy-flavour jets in proton-proton collisions at $\sqrt{s}=13$ TeV with the ATLAS detector*, [JHEP **04** \(2019\) 046](#).
- [102] CMS Collaboration, *Measurements of $t\bar{t}$ cross sections in association with b jets and inclusive jets and their ratio using dilepton final states in pp collisions at $\sqrt{s}=13$ TeV*, [Phys. Lett. B **776** \(2018\) 355–378](#).
- [103] CMS Collaboration, *Measurement of the $t\bar{t}b\bar{b}$ production cross section in the all-jet final state in pp collisions at $\sqrt{s}=13$ TeV*, [Phys. Lett. B **803** \(2020\) 135285](#).
- [104] CMS Collaboration, *First measurement of the cross section for top quark pair production with additional charm jets using dileptonic final states in pp collisions at $s=13$ TeV*, [Phys. Lett. B **820** \(2021\) 136565](#).
- [105] S. Frixione, G. Ridolfi, and P. Nason, *A positive-weight next-to-leading-order Monte Carlo for heavy flavour hadroproduction*, [JHEP **2007** \(2007\) 126](#).
- [106] P. Nason, *A new method for combining NLO QCD with shower Monte Carlo algorithms*, [JHEP **2004** \(2004\) 040](#).
- [107] S. Frixione, P. Nason, and C. Oleari, *Matching NLO QCD computations with parton shower simulations: the POWHEG method*, [JHEP **2007** \(2007\) 070](#).
- [108] S. Alioli, et al., *A general framework for implementing NLO calculations in shower Monte Carlo programs: the POWHEG BOX*, [JHEP **2010** \(2010\)](#).
- [109] J. M. Campbell, et al., *Top-Pair Production and Decay at NLO Matched with Parton Showers*, [JHEP **04** \(2015\) 114](#).
- [110] J. Alwall, et al., *The automated computation of tree-level and next-to-leading order differential cross sections, and their matching to parton shower simulations*, [JHEP **07** \(2014\) 079](#).

- [111] ATLAS Collaboration, *Measurement of the associated production of a top-antitop-quark pair and a Higgs boson decaying into a $b\bar{b}$ pair in pp collisions at $\sqrt{s} = 13$ TeV using the ATLAS detector at the LHC*, [arXiv:2407.10904 \[hep-ex\]](#).
- [112] ATLAS Collaboration, *Measurement of $t\bar{t}$ production in association with additional b -jets in the $e\mu$ final state in proton–proton collisions at $\sqrt{s} = 13$ TeV with the ATLAS detector*, [JHEP 01 \(2025\) 068](#).
- [113] A. E. van de Ven, *Two-loop quantum gravity*, [Nucl. Phys. B 378 \(1992\) 309–366](#).
- [114] M. Persic, P. Salucci, and F. Stel, *The Universal rotation curve of spiral galaxies: 1. The Dark matter connection*, [Mon. Not. Roy. Astron. Soc. 281 \(1996\) 27](#).
- [115] A. J. S. Hamilton and M. Tegmark, *The Real Space Power Spectrum of the PSCz Survey from 0.01 to 300 $h\text{Mpc}^{-1}$* , [Mon. Not. Roy. Astron. Soc. 330 \(2002\) 506](#).
- [116] R. Davis, D. S. Harmer, and K. C. Hoffman, *Search for Neutrinos from the Sun*, [Phys. Rev. Lett. 20 \(1968\) 1205–1209](#).
- [117] SNO Collaboration, *Measurement of the Rate of $\nu_e + d \rightarrow p + p + e^-$ Interactions Produced by ^8B Solar Neutrinos at the Sudbury Neutrino Observatory*, [Phys. Rev. Lett. 87 \(2001\) 071301](#).
- [118] S. Dimopoulos and H. Georgi, *Softly broken supersymmetry and $SU(5)$* , [Nucl. Phys. B 193 \(1981\) 150–162](#).
- [119] S. Weinberg, *Baryon- and Lepton-Nonconserving Processes*, [Phys. Rev. Lett. 43 \(1979\) 1566–1570](#).
- [120] W. Buchmüller and D. Wyler, *Effective lagrangian analysis of new interactions and flavour conservation*, [Nucl. Phys. B 268 \(1986\) 621–653](#).
- [121] B. Grzadkowski, et al., *Dimension-Six Terms in the Standard Model Lagrangian*, [JHEP 10 \(2010\) 085](#).
- [122] L. Evans and P. Bryant, *LHC Machine*, [Journal of Instrumentation 3 \(2008\) S08001](#).
- [123] <https://cds.cern.ch/record/2800984>. Accessed 04/01/2025.
- [124] ATLAS Collaboration, *The ATLAS Experiment at the CERN Large Hadron Collider*, [JINST 3 \(2008\) S08003](#).
- [125] CMS Collaboration, *The CMS Experiment at the CERN LHC*, [JINST 3 \(2008\) S08004](#).
- [126] ALICE Collaboration, *The ALICE experiment at the CERN LHC*, [JINST 3 \(2008\) S08002](#).

BIBLIOGRAPHY

- [127] LHCb Collaboration, *The LHCb Detector at the LHC*, **JINST** **3** (2008) S08005.
- [128] ATLAS Collaboration, *Improved luminosity determination in pp collisions at $\sqrt{s} = 7$ TeV using the ATLAS detector at the LHC*, **Eur. Phys. J. C** **73** (2013) 2518.
- [129] ATLAS Collaboration, *Luminosity determination in pp collisions at $\sqrt{s} = 8$ TeV using the ATLAS detector at the LHC*, **Eur. Phys. J. C** **76** (2016) 653.
- [130] ATLAS Collaboration, *Luminosity determination in pp collisions at $\sqrt{s} = 13$ TeV using the ATLAS detector at the LHC*, **Eur. Phys. J. C** **83** (2023) 982.
- [131] <https://twiki.cern.ch/twiki/bin/view/AtlasPublic/LuminosityPublicResultsRun3>. Accessed 13/01/2025.
- [132] ATLAS Collaboration, *ATLAS inner detector: Technical Design Report, 1*, 1997. <https://cds.cern.ch/record/331063>.
- [133] ATLAS Collaboration, *ATLAS inner detector: Technical Design Report, 2*, 1997. <https://cds.cern.ch/record/331064>.
- [134] A. Yamamoto, et al., *The ATLAS central solenoid*, **Nucl. Instrum. Meth. A** **584** (2008) 53–74.
- [135] ATLAS Collaboration, *ATLAS pixel detector: Technical Design Report*, 1998. <https://cds.cern.ch/record/381263>.
- [136] ATLAS Collaboration, *ATLAS Insertable B-Layer Technical Design Report*, 2010. <https://cds.cern.ch/record/1291633>.
- [137] ATLAS Collaboration, *ATLAS Insertable B-Layer Technical Design Report Addendum*, 2012. <https://cds.cern.ch/record/1451888>.
- [138] A. La Rosa on behalf of the ATLAS Collaboration, *The ATLAS Insertable B-Layer: from construction to operation*, **JINST** **11** (2016) C12036.
- [139] A. Ahmad et al., *The Silicon microstrip sensors of the ATLAS semiconductor tracker*, **Nucl. Instrum. Meth. A** **578** (2007) 98–118.
- [140] The ATLAS TRT Collaboration, *The ATLAS Transition Radiation Tracker (TRT) proportional drift tube: design and performance*, **JINST** **3** (2008) P02013.
- [141] ATLAS Collaboration, *Technical Design Report for the ATLAS Inner Tracker Strip Detector*, 2017. <https://cds.cern.ch/record/2257755>.
- [142] ATLAS Collaboration, *Technical Design Report for the ATLAS Inner Tracker Pixel Detector*, 2017. <https://cds.cern.ch/record/2285585>.
- [143] ATLAS Collaboration, *Threshold Tuning of the ATLAS Pixel Detector*, 2010. <https://cds.cern.ch/record/1283928>.

- [144] Maria Elena Stramaglia on behalf of the ATLAS Collaboration, *Calibration analysis software for the ATLAS Pixel Detector*, *Nucl. Instrum. Meth. A* **824** (2016) 50–52, Frontier Detectors for Frontier Physics: Proceedings of the 13th Pisa Meeting on Advanced Detectors.
- [145] ATLAS Collaboration, *ATLAS liquid-argon calorimeter: Technical Design Report*, 1996. <https://cds.cern.ch/record/331061>.
- [146] ATLAS Collaboration, *ATLAS tile calorimeter: Technical Design Report*, 1996. <https://cds.cern.ch/record/331062>.
- [147] ATLAS Collaboration, *ATLAS muon spectrometer: Technical Design Report*, 1997. <https://cds.cern.ch/record/331068>.
- [148] V. Cindro, et al., *The ATLAS Beam Conditions Monitor*, *JINST* **3** (2008) P02004.
- [149] S. van der Meer, *Calibration of the effective beam height in the ISR*, 1968. <https://cds.cern.ch/record/296752>.
- [150] P. Grafström and W. Kozanecki, *Luminosity determination at proton colliders*, *Prog. Part. Nucl. Phys.* **81** (2015) 97–148.
- [151] ATLAS Collaboration, *Zero Degree Calorimeters for ATLAS*, 2007. <https://cds.cern.ch/record/1009649>.
- [152] ATLAS Collaboration, *ATLAS Forward Detectors for Measurement of Elastic Scattering and Luminosity*, <https://cds.cern.ch/record/1095847>.
- [153] ATLAS Collaboration, *Letter of Intent for the Phase-I Upgrade of the ATLAS Experiment*, 2011. <https://cds.cern.ch/record/1402470>.
- [154] ATLAS Collaboration, *Performance of the ATLAS Trigger System in 2010*, *Eur. Phys. J. C* **72** (2012) 1849.
- [155] ATLAS Collaboration, *Performance of electron and photon triggers in ATLAS during LHC Run 2*, *Eur. Phys. J. C* **80** (2020) 47.
- [156] ATLAS Collaboration, *Performance of the ATLAS muon triggers in Run 2*, *JINST* **15** (2020) P09015.
- [157] A. Sidoti, *Minimum Bias Trigger Scintillators in ATLAS Run II*, *JINST* **9** (2014) C10020.
- [158] ATLAS Collaboration, *Performance of the ATLAS Trigger System in 2015*, *Eur. Phys. J. C* **77** (2017) 317.
- [159] ATLAS Collaboration, *The ATLAS Simulation Infrastructure*, *Eur. Phys. J. C* **70** (2010) 823–874.

BIBLIOGRAPHY

- [160] S. Agostinelli, et al., *Geant4—a simulation toolkit*, *Nucl. Instrum. Meth. A* **506** (2003) 250–303.
- [161] K. Edmonds, et al., *The Fast ATLAS Track Simulation (FATRAS)*, 2008.
<https://cds.cern.ch/record/1091969>.
- [162] ATLAS Collaboration, M. Beckingham, et al., *The simulation principle and performance of the ATLAS fast calorimeter simulation FastCaloSim*,
<https://cds.cern.ch/record/1300517>.
- [163] T. Sjostrand, S. Mrenna, and P. Z. Skands, *A Brief Introduction to PYTHIA 8.1*, *Comput. Phys. Commun.* **178** (2008) 852–867.
- [164] ATLAS Collaboration, *The Pythia 8 A3 tune description of ATLAS minimum bias and inelastic measurements incorporating the Donnachie-Landshoff diffractive model*, 2016. <https://cds.cern.ch/record/2206965>.
- [165] Z. Marshall and ATLAS Collaboration, *Simulation of Pile-up in the ATLAS Experiment*, *J. Phys. Conf. Ser.* **513** (2014) 022024.
- [166] W. Buttinger, *Using Event Weights to account for differences in Instantaneous Luminosity and Trigger Prescale in Monte Carlo and Data*, 2015.
<https://cds.cern.ch/record/2014726>.
- [167] M. Czakon and A. Mitov, *Top++: A program for the calculation of the top-pair cross-section at hadron colliders*, *Comput. Phys. Commun.* **185** (2014) 2930–2938.
- [168] T. Ježo, et al., *New NLOPS predictions for $t\bar{t} + b$ -jet production at the LHC*, *Eur. Phys. J. C* **78** (2018) 502.
- [169] F. Cascioli, P. Maierhofer, and S. Pozzorini, *Scattering Amplitudes with Open Loops*, *Phys. Rev. Lett.* **108** (2012) 111601.
- [170] A. Denner, S. Dittmaier, and L. Hofer, *Collier: a fortran-based Complex One-Loop Library in Extended Regularizations*, *Comput. Phys. Commun.* **212** (2017) 220–238.
- [171] F. Buccioni, et al., *OpenLoops 2*, *Eur. Phys. J. C* **79** (2019) 866.
- [172] T. Sjöstrand, et al., *An introduction to PYTHIA 8.2*, *Comput. Phys. Commun.* **191** (2015) 159–177.
- [173] ATLAS Collaboration, *ATLAS Pythia 8 tunes to 7 TeV data*, 2014.
<https://cds.cern.ch/record/1966419>.
- [174] D. J. Lange, *The EvtGen particle decay simulation package*, *Nucl. Instrum. Meth. A* **462** (2001) 152–155, BEAUTY2000, Proceedings of the 7th Int. Conf. on B-Physics at Hadron Machines.

- [175] ATLAS Collaboration, *Studies on top-quark Monte Carlo modelling for Top2016*, tech. rep., CERN, Geneva, 2016. <https://cds.cern.ch/record/2216168>.
- [176] M. Bahr et al., *Herwig++ Physics and Manual*, *Eur. Phys. J. C* **58** (2008) 639–707.
- [177] J. Bellm et al., *Herwig 7.0/Herwig++ 3.0 release note*, *Eur. Phys. J. C* **76** (2016) 196.
- [178] J. Bellm et al., *Herwig 7.1 Release Note*, [arXiv:1705.06919](https://arxiv.org/abs/1705.06919) [[hep-ph](#)].
- [179] L. A. Harland-Lang, et al., *Parton distributions in the LHC era: MMHT 2014 PDFs*, *Eur. Phys. J. C* **75** (2015).
- [180] S. Frixione, et al., *Angular correlations of lepton pairs from vector boson and top quark decays in Monte Carlo simulations*, *JHEP* **2007** (2007) 081.
- [181] P. Artoisenet, et al., *Automatic spin-entangled decays of heavy resonances in Monte Carlo simulations*, *JHEP* **03** (2013) 015.
- [182] Sherpa Collaboration, E. Bothmann et al., *Event Generation with Sherpa 2.2*, *SciPost Phys.* **7** (2019) 034.
- [183] T. Gleisberg and S. Höche, *Comix, a new matrix element generator*, *JHEP* **2008** (2008) 039.
- [184] S. Schumann and F. Krauss, *A parton shower algorithm based on Catani-Seymour dipole factorisation*, *JHEP* **03** (2008) 038.
- [185] S. Hoeche, et al., *A critical appraisal of NLO+PS matching methods*, *JHEP* **09** (2012) 049.
- [186] S. Hoeche, et al., *QCD matrix elements + parton showers: The NLO case*, *JHEP* **04** (2013) 027.
- [187] S. Catani, et al., *QCD matrix elements + parton showers*, *JHEP* **11** (2001) 063.
- [188] S. Hoeche, et al., *QCD matrix elements and truncated showers*, *JHEP* **05** (2009) 053.
- [189] R. Frederix, E. Re, and P. Torrielli, *Single-top t-channel hadroproduction in the four-flavour scheme with POWHEG and aMC@NLO*, *JHEP* **09** (2012) 130.
- [190] S. Frixione, et al., *Single-top hadroproduction in association with a W boson*, *JHEP* **2008** (2008) 029–029.
- [191] LHC Higgs Cross Section Working Group, *Handbook of LHC Higgs Cross Sections: 4. Deciphering the Nature of the Higgs Sector*, [arXiv:1610.07922](https://arxiv.org/abs/1610.07922) [[hep-ph](#)].

BIBLIOGRAPHY

- [192] C. Anastasiou, et al., *High precision QCD at hadron colliders: Electroweak gauge boson rapidity distributions at NNLO*, *Phys. Rev. D* **69** (2004) 094008.
- [193] ATLAS Collaboration, *Measurement of Higgs boson decay into b -quarks in associated production with a top-quark pair in pp collisions at $\sqrt{s} = 13$ TeV with the ATLAS detector*, *JHEP* **06** (2022) 097.
- [194] ATLAS Collaboration, *Electron reconstruction and identification in the ATLAS experiment using the 2015 and 2016 LHC proton–proton collision data at $\sqrt{s} = 13$ TeV*, *Eur. Phys. J. C* **79** (2019).
- [195] ATLAS Collaboration, *Performance of the ATLAS Track Reconstruction Algorithms in Dense Environments in LHC Run 2*, *Eur. Phys. J. C* **77** (2017) 673.
- [196] T. Cornelissen, et al., *The new ATLAS track reconstruction (NEWT)*, *J. Phys. Conf. Ser.* **119** (2008) 032014.
- [197] T. G. Cornelissen, et al., *The global χ^2 track fitter in ATLAS*, *J. Phys. Conf. Ser.* **119** (2008) 032013.
- [198] ATLAS Collaboration, *Improved electron reconstruction in ATLAS using the Gaussian Sum Filter-based model for bremsstrahlung*, 2012.
<https://cds.cern.ch/record/1449796>.
- [199] R. Frühwirth, *A Gaussian-mixture approximation of the Bethe–Heitler model of electron energy loss by bremsstrahlung*, *Comput. Phys. Commun.* **154** (2003) 131–142.
- [200] R. Frühwirth, *Application of Kalman filtering to track and vertex fitting*, *Nucl. Instrum. Meth. A* **262** (1987) 444–450.
- [201] ATLAS Collaboration, *Topological cell clustering in the ATLAS calorimeters and its performance in LHC Run 1*, *Eur. Phys. J. C* **77** (2017) 490.
- [202] ATLAS Collaboration, *Electron and photon performance measurements with the ATLAS detector using the 2015–2017 LHC proton–proton collision data*, *JINST* **14** (2019) P12006.
- [203] ATLAS Collaboration, *Electron and photon energy calibration with the ATLAS detector using 2015–2016 LHC proton–proton collision data*, *JINST* **14** (2019) P03017.
- [204] ATLAS Collaboration, *Electron efficiency measurements with the ATLAS detector using 2012 LHC proton–proton collision data*, *Eur. Phys. J. C* **77** (2017) 195.
- [205] ATLAS Collaboration, *Electron and photon efficiencies in LHC Run 2 with the ATLAS experiment*, *JHEP* **05** (2024) 162.

- [206] M. Cacciari and G. P. Salam, *Pileup subtraction using jet areas*, [Phys. Lett. B **659** \(2008\) 119–126](#).
- [207] ATLAS Collaboration, *Muon reconstruction and identification efficiency in ATLAS using the full Run 2 pp collision data set at $\sqrt{s} = 13$ TeV*, [Eur. Phys. J. C **81** \(2021\)](#).
- [208] ATLAS Collaboration, *Studies of the muon momentum calibration and performance of the ATLAS detector with pp collisions at $\sqrt{s} = 13$ TeV*, [Eur. Phys. J. C **83** \(2023\) 686](#).
- [209] ATLAS Collaboration, *Jet reconstruction and performance using particle flow with the ATLAS Detector*, [Eur. Phys. J. C **77** \(2017\) 466](#).
- [210] M. Cacciari, G. P. Salam, and G. Soyez, *The anti-kt jet clustering algorithm*, [JHEP **2008** \(2008\) 063](#).
- [211] M. Cacciari, G. P. Salam, and G. Soyez, *FastJet User Manual*, [Eur. Phys. J. C **72** \(2012\) 1896](#).
- [212] M. Cacciari and G. P. Salam, *Dispelling the N^3 myth for the kt jet-finder*, [Phys. Lett. B **641** \(2006\) 57–61](#).
- [213] S. Catani, et al., *Longitudinally invariant K_t clustering algorithms for hadron hadron collisions*, [Nucl. Phys. B **406** \(1993\) 187–224](#).
- [214] M. Cacciari, G. P. Salam, and G. Soyez, *The Catchment Area of Jets*, [JHEP **04** \(2008\) 005](#).
- [215] M. Cacciari and G. P. Salam, *Pileup subtraction using jet areas*, [Phys. Lett. B **659** \(2008\) 119–126](#).
- [216] ATLAS Collaboration, *Monte Carlo Calibration and Combination of In-situ Measurements of Jet Energy Scale, Jet Energy Resolution and Jet Mass in ATLAS*, <https://cds.cern.ch/record/2044941>.
- [217] ATLAS Collaboration, *Jet global sequential corrections with the ATLAS detector in proton-proton collisions at $\sqrt{s} = 8$ TeV*, <https://cds.cern.ch/record/2001682>.
- [218] ATLAS Collaboration, *Jet energy scale measurements and their systematic uncertainties in proton-proton collisions at $\sqrt{s} = 13$ TeV with the ATLAS detector*, [Phys. Rev. D **96** \(2017\) 072002](#).
- [219] ATLAS Collaboration, *Tagging and suppression of pileup jets with the ATLAS detector*, 2014. <https://cds.cern.ch/record/1700870>.
- [220] A. Hoecker, et al., *TMVA - Toolkit for Multivariate Data Analysis*, 2009. <https://arxiv.org/abs/physics/0703039>.

BIBLIOGRAPHY

- [221] ATLAS Collaboration, *Optimisation and performance studies of the ATLAS b-tagging algorithms for the 2017-18 LHC run*, <https://cds.cern.ch/record/2273281>.
- [222] ATLAS Collaboration, *Secondary vertex finding for jet flavour identification with the ATLAS detector*, <https://cds.cern.ch/record/2270366>.
- [223] ATLAS Collaboration, *Topological b-hadron decay reconstruction and identification of b-jets with the JetFitter package in the ATLAS experiment at the LHC*, <https://cds.cern.ch/record/2645405>.
- [224] ATLAS Collaboration, *Identification of Jets Containing b-Hadrons with Recurrent Neural Networks at the ATLAS Experiment*, <https://cds.cern.ch/record/2255226>.
- [225] I. H. Witten, et al., *Chapter 10 - Deep learning*, <https://www.sciencedirect.com/science/article/pii/B9780128042915000106>.
- [226] ATLAS Collaboration, *ATLAS b-jet identification performance and efficiency measurement with $t\bar{t}$ events in pp collisions at $\sqrt{s} = 13$ TeV*, *Eur. Phys. J. C* **79** (2019) 970.
- [227] ATLAS Collaboration, *Measurement of the c-jet mistagging efficiency in $t\bar{t}$ events using pp collision data at $\sqrt{s} = 13$ TeV collected with the ATLAS detector*, *Eur. Phys. J. C* **82** (2022) 95.
- [228] ATLAS Collaboration, *Calibration of the light-flavour jet mistagging efficiency of the b-tagging algorithms with Z+jets events using 139 fb^{-1} of ATLAS proton-proton collision data at $\sqrt{s} = 13$ TeV*, *Eur. Phys. J. C* **83** (2023) 728.
- [229] ATLAS Collaboration, *Monte Carlo to Monte Carlo scale factors for flavour tagging efficiency calibration*, <https://cds.cern.ch/record/2718610>.
- [230] ATLAS Collaboration, *Calibration of the performance of b-tagging for c and light-flavour jets in the 2012 ATLAS data*, <https://cds.cern.ch/record/1741020>.
- [231] DØ Collaboration, *Measurement of the $t\bar{t}$ production cross section in $p\bar{p}$ collisions at $\sqrt{s} = 1.96$ TeV using secondary vertex b tagging*, *Phys. Rev. D* **74** (2006) 112004.
- [232] J. Erdmann, et al., *A likelihood-based reconstruction algorithm for top-quark pairs and the KLfitter framework*, *Nuclear Instruments and Methods in Physics Research Section A: Accelerators, Spectrometers, Detectors and Associated Equipment* **748** (2014) 18–25.
- [233] ATLAS Collaboration, *The performance of missing transverse momentum reconstruction and its significance with the ATLAS detector using 140 fb^{-1} of $\sqrt{s} = 13$ TeV pp collisions*, [arXiv:2402.05858 \[hep-ex\]](https://arxiv.org/abs/2402.05858).

- [234] ATLAS Collaboration, *ATLAS data quality operations and performance for 2015–2018 data-taking*, [JINST **15** \(2020\) P04003](#).
- [235] ATLAS Collaboration, *Performance of electron and photon triggers in ATLAS during LHC Run 2*, [Eur. Phys. J. C **80** \(2020\) 47](#).
- [236] ATLAS Collaboration, *Performance of the ATLAS muon triggers in Run 2*, [JINST **15** \(2020\) P09015](#).
- [237] ATLAS Collaboration, *Vertex Reconstruction Performance of the ATLAS Detector at $\sqrt{s} = 13$ TeV*, 2015. <https://cds.cern.ch/record/2037717>.
- [238] ATLAS Collaboration, *Tools for estimating fake/non-prompt lepton backgrounds with the ATLAS detector at the LHC*, [JINST **18** \(2023\) T11004](#).
- [239] ATLAS Collaboration, *Search for the Standard Model Higgs boson produced in association with top quarks and decaying into $b\bar{b}$ in pp collisions at $\sqrt{s} = 8$ TeV with the ATLAS detector*, [Eur. Phys. J. C **75** \(2015\) 349](#).
- [240] M. Cacciari, G. P. Salam, and G. Soyez, *The Catchment Area of Jets*, [JHEP **04** \(2008\) 005](#).
- [241] ATLAS Collaboration, *Performance of jet substructure techniques for large- R jets in proton-proton collisions at $\sqrt{s} = 7$ TeV using the ATLAS detector*, [JHEP **09** \(2013\) 076](#).
- [242] G. Cowan, et al., *Asymptotic formulae for likelihood-based tests of new physics*, [Eur. Phys. J. C **71** \(2011\) 1554](#), [Erratum: Eur.Phys.J.C 73, 2501 (2013)].
- [243] H. Cramér, *Mathematical Methods of Statistics*. Goldstine Printed Materials. Princeton University Press, 1946.
- [244] C. R. Rao, *Minimum variance and the estimation of several parameters*, [Math. Proc. Camb. Philos. Soc. **43** \(1947\) 280–283](#).
- [245] ROOT Collaboration, K. Cranmer, et al., *HistFactory: A tool for creating statistical models for use with RooFit and RooStats*, 2012. <https://cds.cern.ch/record/1456844>.
- [246] L. Moneta, et al., *The RooStats project*, [PoS ACAT2010 \(2011\) 057](#).
- [247] W. Verkerke and D. P. Kirkby, *The RooFit toolkit for data modeling*, eConf [C0303241](#) (2003) MOLT007.
- [248] R. Brun and F. Rademakers, *ROOT — An object oriented data analysis framework*, [Nucl. Instrum. Meth. A **389** \(1997\) 81–86](#), New Computing Techniques in Physics Research V.

BIBLIOGRAPHY

- [249] R. Barlow, *Extended maximum likelihood*, [Nucl. Instrum. Meth. A](#) **297** (1990) 496–506.
- [250] R. Barlow and C. Beeston, *Fitting using finite Monte Carlo samples*, [Comput. Phys. Commun.](#) **77** (1993) 219–228.
- [251] J. Lindsey, *Parametric Statistical Inference*. 1996.
- [252] S. Baker and R. D. Cousins, *Clarification of the use of CHI-square and likelihood functions in fits to histograms*, [Nucl. Instrum. Methods Phys. Res.](#) **221** (1984) 437–442.
- [253] S. S. Wilks, *The Large-Sample Distribution of the Likelihood Ratio for Testing Composite Hypotheses*, [Annals Math. Statist.](#) **9** (1938) 60–62.
- [254] *1974 CERN School of Computing, Godoyssund, Norway, 11-24 Aug 1974: Proceedings*, CERN Yellow Reports: School Proceedings. 11, 1974.
- [255] ATLAS Collaboration, *Jet energy scale and resolution measured in proton-proton collisions at $\sqrt{s} = 13$ TeV with the ATLAS detector*, 2021. <https://arxiv.org/abs/2007.02645>.
- [256] J. Butterworth et al., *PDF4LHC recommendations for LHC Run II*, [J. Phys. G](#) **43** (2016) 023001.
- [257] S. Dulat, et al., *New parton distribution functions from a global analysis of quantum chromodynamics*, [Phys. Rev. D](#) **93** (2016).
- [258] R. D. Ball, et al., *Parton distributions for the LHC run II*, [JHEP](#) **2015** (2015).
- [259] J. Gao and P. Nadolsky, *A meta-analysis of parton distribution functions*, [JHEP](#) **2014** (2014).
- [260] S. Carrazza, et al., *An unbiased Hessian representation for Monte Carlo PDFs*, [Eur. Phys. J. C](#) **75** (2015).
- [261] ATLAS Collaboration, *Studies of Monte Carlo predictions for the $t\bar{t}b\bar{b}$ process*, 2022. <https://cds.cern.ch/record/2802806>.
- [262] A. Pinto, et al., *Uncertainty components in profile likelihood fits*, [Eur. Phys. J. C](#) **84** (2024) 593.
- [263] ATLAS Collaboration, *Measurement of $t\bar{t}$ production in association with additional b-jets in the $e\mu$ final state in proton-proton collisions at $\sqrt{s}=13$ TeV with the ATLAS detector*, [arXiv:2407.13473 \[hep-ex\]](#).
- [264] ATLAS Collaboration, *Graph Neural Network Jet Flavour Tagging with the ATLAS Detector*, 2022. <https://cds.cern.ch/record/2811135>.

BIBLIOGRAPHY

- [265] ATLAS Collaboration, *Expected tracking and related performance with the updated ATLAS Inner Tracker layout at the High-Luminosity LHC*, 2021.
<https://cds.cern.ch/record/2776651>.

Appendices

APPENDIX A

CMS Analysis Results

Table A.1.: Summary of results from CMS measurement of top quark pairs in association with charm quarks [104]. Measured results have their statistical and systematic uncertainties listed in that order, and are compared to predictions from $t\bar{t}$ samples generated using POWHEG BOXv2 and MADGRAPH5_aMC@NLO v2.4.2 matrix element generators.

	Result	POWHEG BOX	MADGRAPH5_aMC@NLO
Fiducial phase space			
$\sigma_{t\bar{t}c\bar{c}}$ [pb]	$0.207 \pm 0.025 \pm 0.027$	0.187 ± 0.038	0.189 ± 0.032
$\sigma_{t\bar{t}b\bar{b}}$ [pb]	$0.132 \pm 0.010 \pm 0.015$	0.097 ± 0.021	0.101 ± 0.023
$\sigma_{t\bar{t}LL}$ [pb]	$5.15 \pm 0.12 \pm 0.41$	5.95 ± 1.02	6.32 ± 0.94
R_c [%]	$3.01 \pm 0.34 \pm 0.31$	2.53 ± 0.18	2.43 ± 0.17
R_b [%]	$1.93 \pm 0.15 \pm 0.18$	1.31 ± 0.12	1.30 ± 0.16
Full phase space			
$\sigma_{t\bar{t}c\bar{c}}$ [pb]	$10.1 \pm 1.2 \pm 1.4$	9.1 ± 1.8	8.9 ± 1.5
$\sigma_{t\bar{t}b\bar{b}}$ [pb]	$4.54 \pm 0.35 \pm 0.56$	3.34 ± 0.72	3.39 ± 0.66
$\sigma_{t\bar{t}LL}$ [pb]	$220 \pm 5 \pm 19$	255 ± 43	261 ± 37
R_c [%]	$3.36 \pm 0.38 \pm 0.34$	2.81 ± 0.20	2.72 ± 0.19
R_b [%]	$1.51 \pm 0.11 \pm 0.16$	1.03 ± 0.08	1.03 ± 0.09

APPENDIX B

Expected Number of Events in Analysis Regions

Table B.1.: Expected and observed number of events in the control regions of the lepton+jets channel. All uncertainty components are included.

	$\text{CR}_1^{1\ell 5j}$	$\text{CR}_1^{1\ell \geq 6j}$	$\text{CR}_2^{1\ell 5j}$	$\text{CR}_2^{1\ell \geq 6j}$	$\text{CR}_3^{1\ell 5j}$	$\text{CR}_3^{1\ell \geq 6j}$
$t\bar{t} + \geq 2c$	1920 \pm 180	4060 \pm 370	369 \pm 38	780 \pm 100	40 \pm 8	120 \pm 19
$t\bar{t} + 1c$	10 200 \pm 1100	10 200 \pm 1300	2380 \pm 210	2520 \pm 380	115 \pm 21	150 \pm 33
$t\bar{t} + \geq 2b$	1400 \pm 400	2760 \pm 340	5400 \pm 1600	13 000 \pm 1200	390 \pm 130	1250 \pm 150
$t\bar{t} + 1b$	3400 \pm 1200	4100 \pm 1000	8300 \pm 3200	10 200 \pm 1700	440 \pm 210	700 \pm 130
$t\bar{t} + \text{light}$	49 600 \pm 6000	32 000 \pm 4000	7100 \pm 900	4700 \pm 800	45 \pm 16	51 \pm 26
Diboson	54 \pm 28	57 \pm 29	38 \pm 19	40 \pm 20	1 \pm 1	2 \pm 1
$W + \text{jets}$	730 \pm 360	640 \pm 320	490 \pm 240	510 \pm 260	14 \pm 7	24 \pm 12
$Z + \text{jets}$	192 \pm 70	151 \pm 57	145 \pm 53	136 \pm 50	4 \pm 2	6 \pm 2
$t\bar{t}W$	105 \pm 15	192 \pm 28	20 \pm 3	53 \pm 8	1 \pm 0	5 \pm 1
$t\bar{t}Z$	125 \pm 16	267 \pm 34	166 \pm 20	392 \pm 56	12 \pm 2	38 \pm 6
$t\bar{t}H$	120 \pm 60	270 \pm 140	380 \pm 190	900 \pm 400	28 \pm 14	90 \pm 50
Single top Wt	1900 \pm 500	1300 \pm 500	660 \pm 210	670 \pm 280	28 \pm 14	46 \pm 21
Single top s -channel	28 \pm 15	14 \pm 8	28 \pm 16	17 \pm 10	1 \pm 1	1 \pm 1
Single top t -channel	380 \pm 220	250 \pm 170	360 \pm 240	310 \pm 240	10 \pm 8	15 \pm 12
Single top other	3 \pm 1	4 \pm 2	1 \pm 0	1 \pm 1	0 \pm 0	0 \pm 0
Fakes electron	1790 \pm 900	1700 \pm 900	1300 \pm 700	1400 \pm 700	39 \pm 24	100 \pm 50
Fakes muon	0 \pm 15	0 \pm 13	170 \pm 90	25 \pm 27	3 \pm 5	0 \pm 3
Total MC	72 000 \pm 7000	57 000 \pm 6000	27 000 \pm 4000	35 700 \pm 3300	1170 \pm 280	2600 \pm 270
Data	69 136	56 277	30 388	37 209	1345	2728

B. Expected Number of Events in Analysis Regions

Table B.2.: Expected and observed number of events in the control regions of the dilepton channel. All uncertainty components are included.

	$\text{CR}_1^{2\ell 3j}$	$\text{CR}_1^{2\ell \geq 4j}$	$\text{CR}_2^{2\ell 3j}$	$\text{CR}_2^{2\ell \geq 4j}$	$\text{CR}_3^{2\ell 3j}$	$\text{CR}_3^{2\ell \geq 4j}$
$t\bar{t} + \geq 2c$	950 \pm 140	2860 \pm 240	17 \pm 4	139 \pm 21	54 \pm 13	410 \pm 40
$t\bar{t} + 1c$	10 600 \pm 1100	13 400 \pm 1700	226 \pm 29	390 \pm 70	570 \pm 100	970 \pm 200
$t\bar{t} + \geq 2b$	1200 \pm 400	2580 \pm 170	400 \pm 120	2700 \pm 400	230 \pm 70	1150 \pm 90
$t\bar{t} + 1b$	5000 \pm 2400	6100 \pm 900	1400 \pm 700	2230 \pm 260	800 \pm 400	1300 \pm 130
$t\bar{t} + \text{light}$	192 000 \pm 24 000	125 000 \pm 10 000	72 \pm 14	121 \pm 33	300 \pm 70	500 \pm 110
Diboson	70 \pm 40	80 \pm 40	1 \pm 1	2 \pm 1	1 \pm 0	2 \pm 1
$Z + \text{jets}$	4700 \pm 1600	3100 \pm 1100	50 \pm 18	97 \pm 34	56 \pm 21	99 \pm 35
$t\bar{t}W$	167 \pm 33	410 \pm 60	1 \pm 0	10 \pm 1	3 \pm 1	17 \pm 2
$t\bar{t}Z$	170 \pm 60	540 \pm 100	10 \pm 2	80 \pm 11	7 \pm 1	51 \pm 7
$t\bar{t}H$	100 \pm 50	340 \pm 170	25 \pm 13	180 \pm 90	14 \pm 7	80 \pm 40
Single top Wt	6200 \pm 1200	3700 \pm 1100	61 \pm 27	130 \pm 60	58 \pm 19	100 \pm 40
Single top other	19 \pm 0	30 \pm 1	1 \pm 0	3 \pm 0	1 \pm 0	2 \pm 0
Fakes	2100 \pm 500	2000 \pm 500	17 \pm 4	74 \pm 19	20 \pm 5	75 \pm 19
Total MC	223 000 \pm 24 000	160 000 \pm 12 000	2200 \pm 700	6100 \pm 500	2100 \pm 400	4800 \pm 400
Data	213 185	152 931	2682	6725	2640	5655

Table B.3.: Expected and observed number of events in the signal regions of the lepton + jets channel. All uncertainty components are included.

	$\text{SR}_{\text{loose}}^{1\ell 5j}$	$\text{SR}_{\text{loose}}^{1\ell \geq 6j}$	$\text{SR}_{\text{tight}}^{1\ell 5j}$	$\text{SR}_{\text{tight}}^{1\ell \geq 6j}$
$t\bar{t} + \geq 2c$	250 \pm 52	830 \pm 150	124 \pm 27	410 \pm 70
$t\bar{t} + 1c$	640 \pm 120	920 \pm 230	260 \pm 50	350 \pm 100
$t\bar{t} + \geq 2b$	120 \pm 40	380 \pm 60	70 \pm 28	227 \pm 35
$t\bar{t} + 1b$	230 \pm 110	410 \pm 110	110 \pm 40	190 \pm 50
$t\bar{t} + \text{light}$	1110 \pm 210	1170 \pm 290	117 \pm 39	130 \pm 50
Diboson	3 \pm 2	5 \pm 3	1 \pm 1	2 \pm 2
$W + \text{jets}$	35 \pm 18	49 \pm 26	8 \pm 5	16 \pm 9
$Z + \text{jets}$	10 \pm 4	13 \pm 5	3 \pm 1	5 \pm 2
$t\bar{t}W$	7 \pm 2	23 \pm 4	3 \pm 0	8 \pm 2
$t\bar{t}Z$	12 \pm 2	42 \pm 7	6 \pm 1	18 \pm 3
$t\bar{t}H$	12 \pm 6	41 \pm 21	6 \pm 3	22 \pm 11
Single top Wt	73 \pm 32	86 \pm 37	19 \pm 7	30 \pm 20
Single top s -channel	1 \pm 1	1 \pm 0	0 \pm 0	0 \pm 0
Single top t -channel	0 \pm 0	1 \pm 0	0 \pm 0	0 \pm 0
Fakes electron	94 \pm 52	98 \pm 55	15 \pm 12	48 \pm 29
Fakes muon	0 \pm 3	0 \pm 4	0 \pm 2	1 \pm 3
Total MC	2620 \pm 370	4100 \pm 600	750 \pm 110	1460 \pm 220
Data	2976	4443	913	1705

Table B.4.: Expected and observed number of events in the signal regions of the dilepton channel. All uncertainty components are included.

	$\text{SR}_{\text{loose}}^{2\ell 3j}$	$\text{SR}_{\text{loose}}^{2\ell \geq 4j}$	$\text{SR}_{\text{tight}}^{2\ell \geq 4j}$
$t\bar{t} + \geq 2c$	180 ± 50	1130 ± 80	139 ± 23
$t\bar{t} + 1c$	1380 ± 300	2200 ± 600	36 ± 13
$t\bar{t} + \geq 2b$	150 ± 50	650 ± 50	50 ± 5
$t\bar{t} + 1b$	520 ± 240	950 ± 80	28 ± 9
$t\bar{t} + \text{light}$	1780 ± 320	2900 ± 500	24 ± 12
Diboson	2 ± 1	8 ± 4	0 ± 0
$Z + \text{jets}$	140 ± 50	210 ± 80	7 ± 3
$t\bar{t}W$	12 ± 2	62 ± 9	2 ± 0
$t\bar{t}Z$	11 ± 1	90 ± 12	7 ± 1
$t\bar{t}H$	12 ± 6	80 ± 40	6 ± 3
Single top Wt	110 ± 40	180 ± 60	5 ± 4
Single top other	1 ± 0	4 ± 0	0 ± 0
Fakes	53 ± 14	150 ± 40	6 ± 2
Total MC	4300 ± 500	8700 ± 900	310 ± 40
Data	5015	9668	340

APPENDIX C

Pruning of Systematic Uncertainties

C. Pruning of Systematic Uncertainties



Figure C.1.: Pruning of systematic uncertainties in (from left to right) $CR_1^{2\ell 3j}$, $CR_1^{2\ell \ge 4j}$, $CR_1^{1\ell 5j}$ and $CR_1^{1\ell \ge 6j}$. Continued on following page. Colour key and list of samples shown in Figure C.4.

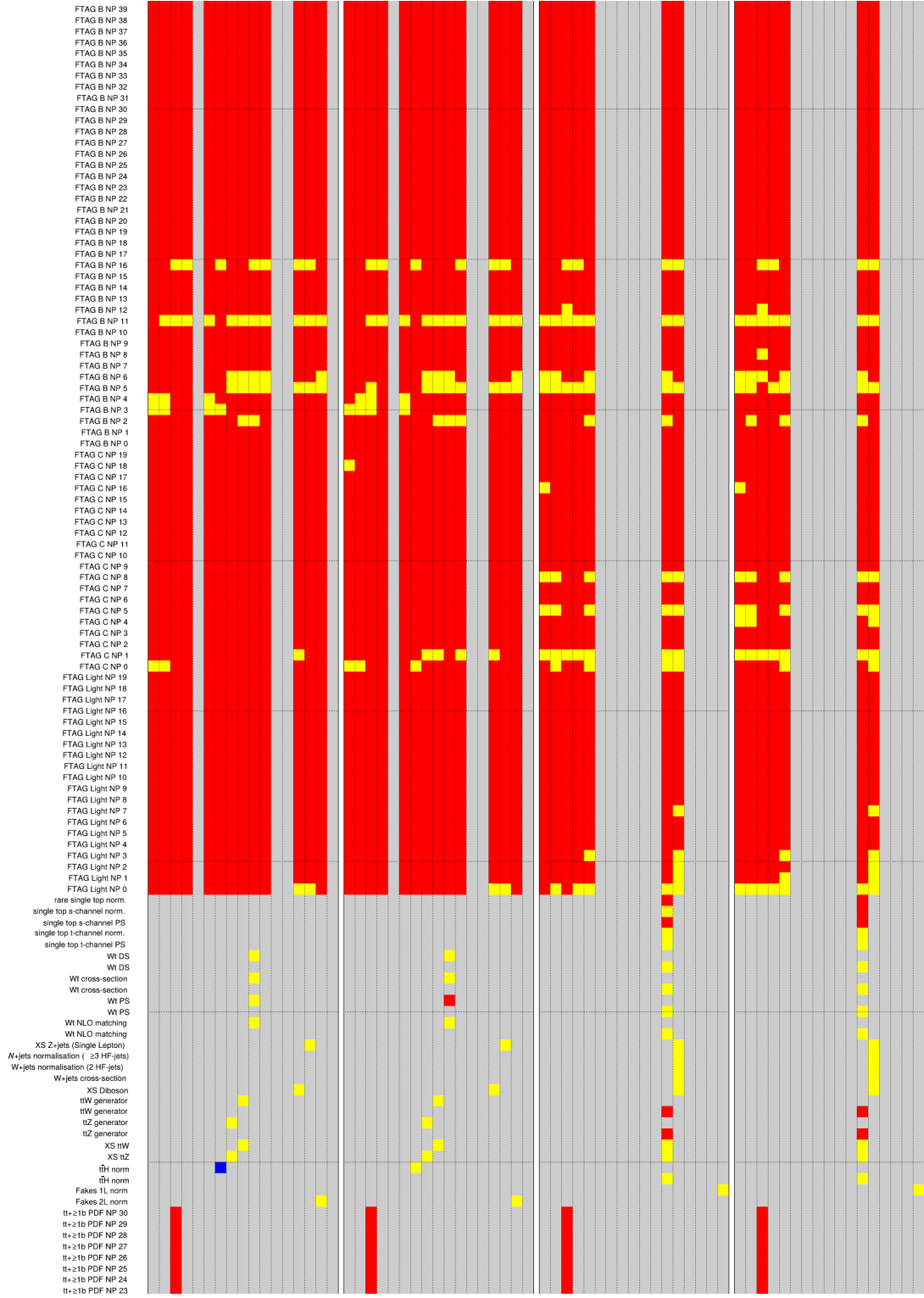


Figure C.2.: Pruning of systematic uncertainties in (from left to right) $CR_1^{2\ell 3j}$, $CR_1^{2\ell \geq 4j}$, $CR_1^{1\ell 5j}$ and $CR_1^{1\ell \geq 6j}$. Continued on following page. Colour key and list of samples shown in Figure C.4.

C. Pruning of Systematic Uncertainties

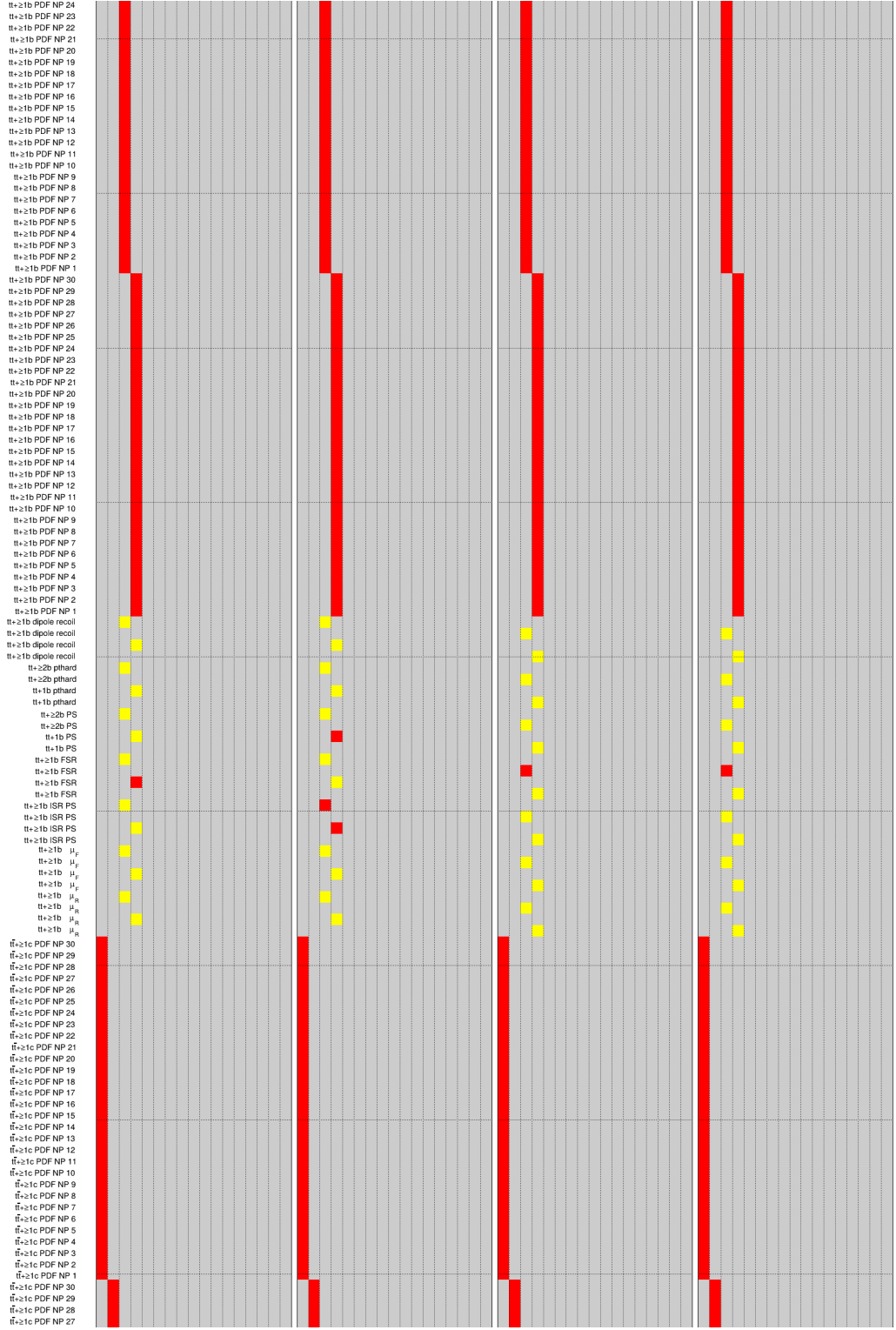


Figure C.3.: Pruning of systematic uncertainties in (from left to right) $CR_1^{2\ell 3j}$, $CR_1^{2\ell \geq 4j}$, $CR_1^{1\ell 5j}$ and $CR_1^{1\ell \geq 6j}$. Continued on following page. Colour key and list of samples shown in Figure C.4.

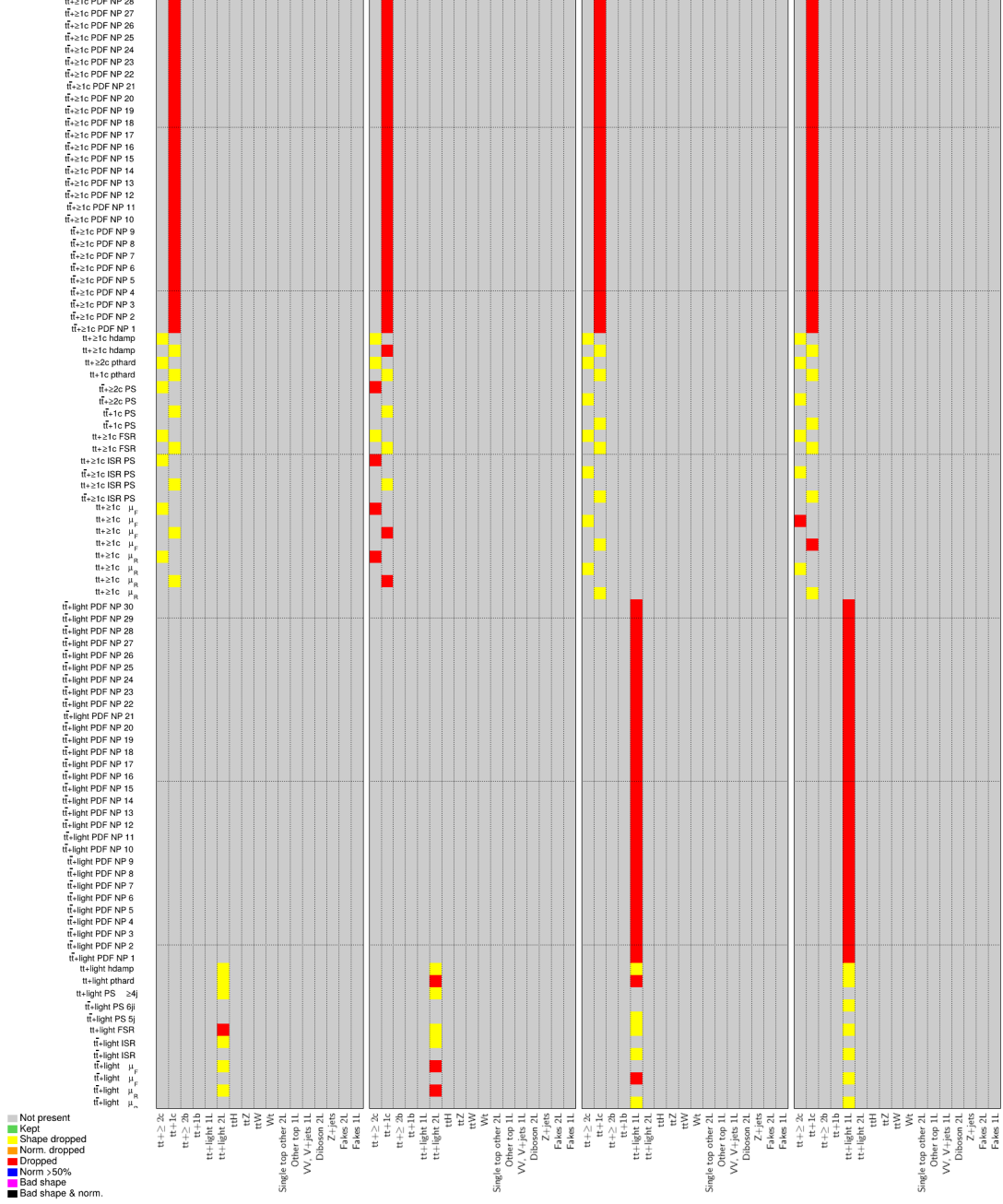


Figure C.4.: Pruning of systematic uncertainties in (from left to right) $CR_1^{2\ell 3j}$, $CR_1^{2\ell \geq 4j}$, $CR_1^{\ell 5j}$ and $CR_1^{1\ell \geq 6j}$, showing colour scheme and samples considered in each region.

C. Pruning of Systematic Uncertainties



Figure C.5.: Pruning of systematic uncertainties in (from left to right) CR₂^{2l3j}, CR₂^{2l≥4j}, CR₂^{1l5j} and CR₂^{1l≥6j}. Continued on following page. Colour key and list of samples shown in Figure C.8.

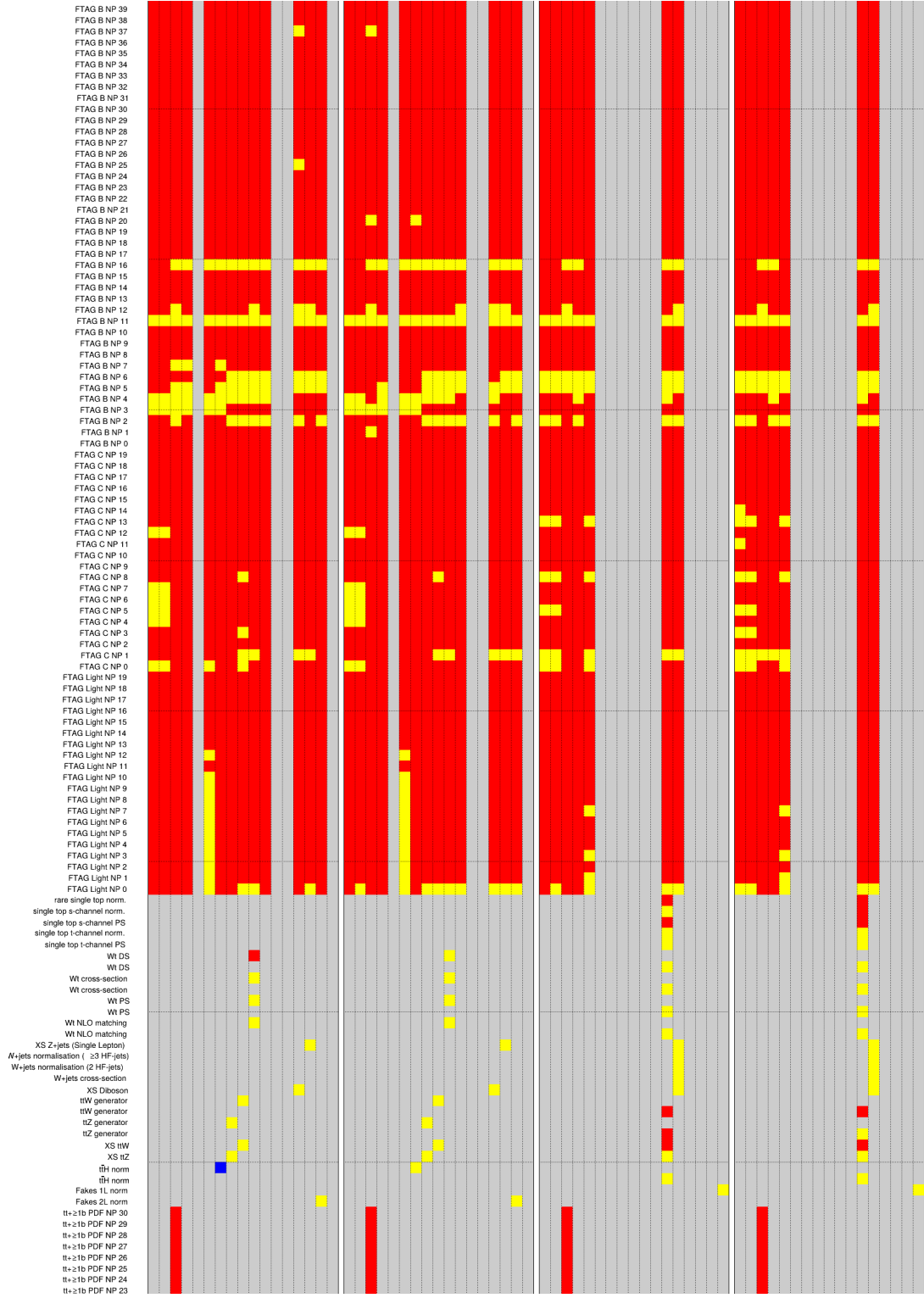


Figure C.6.: Pruning of systematic uncertainties in (from left to right) $CR_2^{2\ell 3j}$, $CR_2^{2\ell \geq 4j}$, $CR_2^{1\ell 5j}$ and $CR_2^{1\ell \geq 6j}$. Continued on following page. Colour key and list of samples shown in Figure C.8.

C. Pruning of Systematic Uncertainties

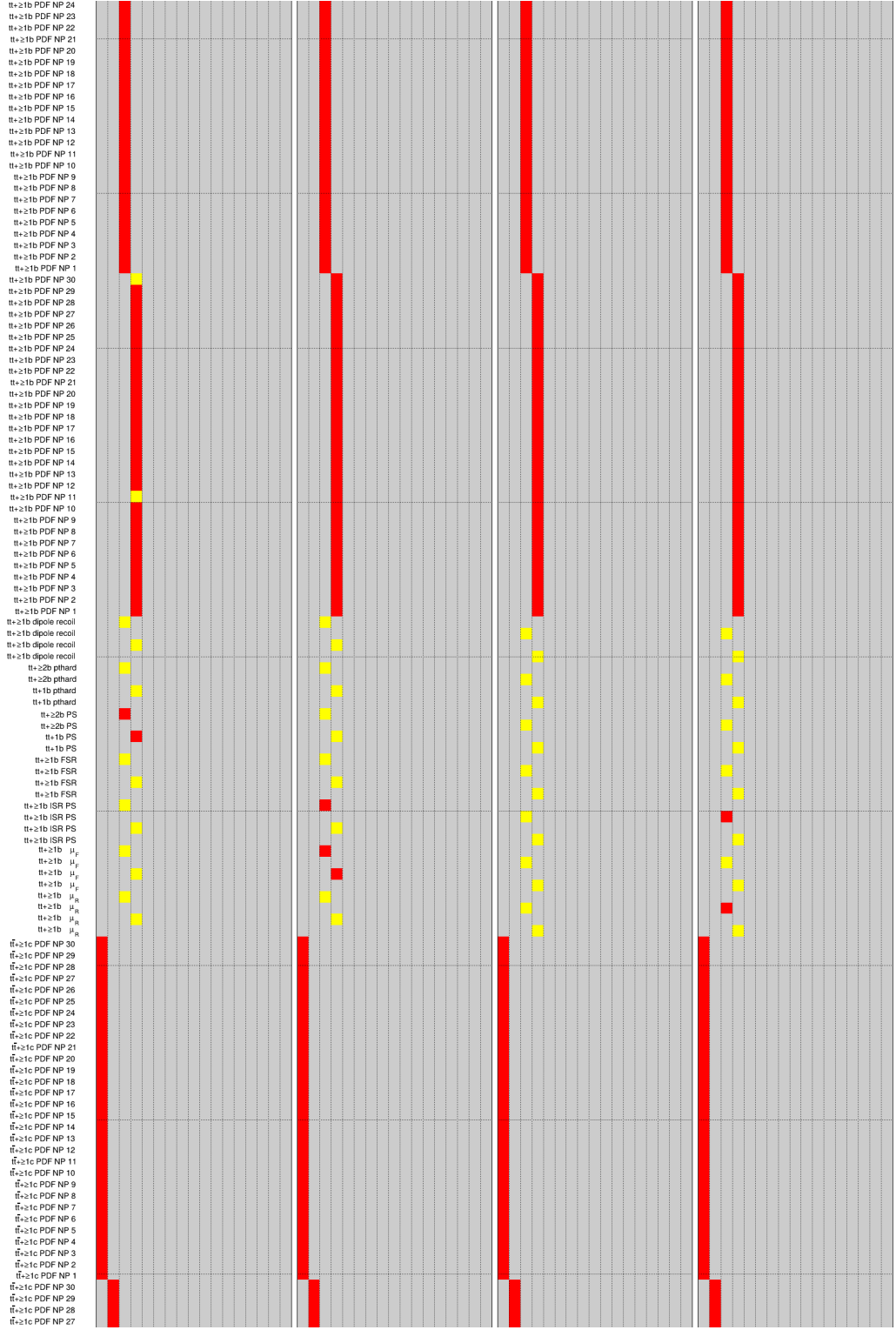


Figure C.7.: Pruning of systematic uncertainties in (from left to right) $CR_2^{2\ell 3j}$, $CR_2^{2\ell \geq 4j}$, $CR_2^{1\ell 5j}$ and $CR_2^{1\ell \geq 6j}$. Continued on following page. Colour key and list of samples shown in Figure C.8.

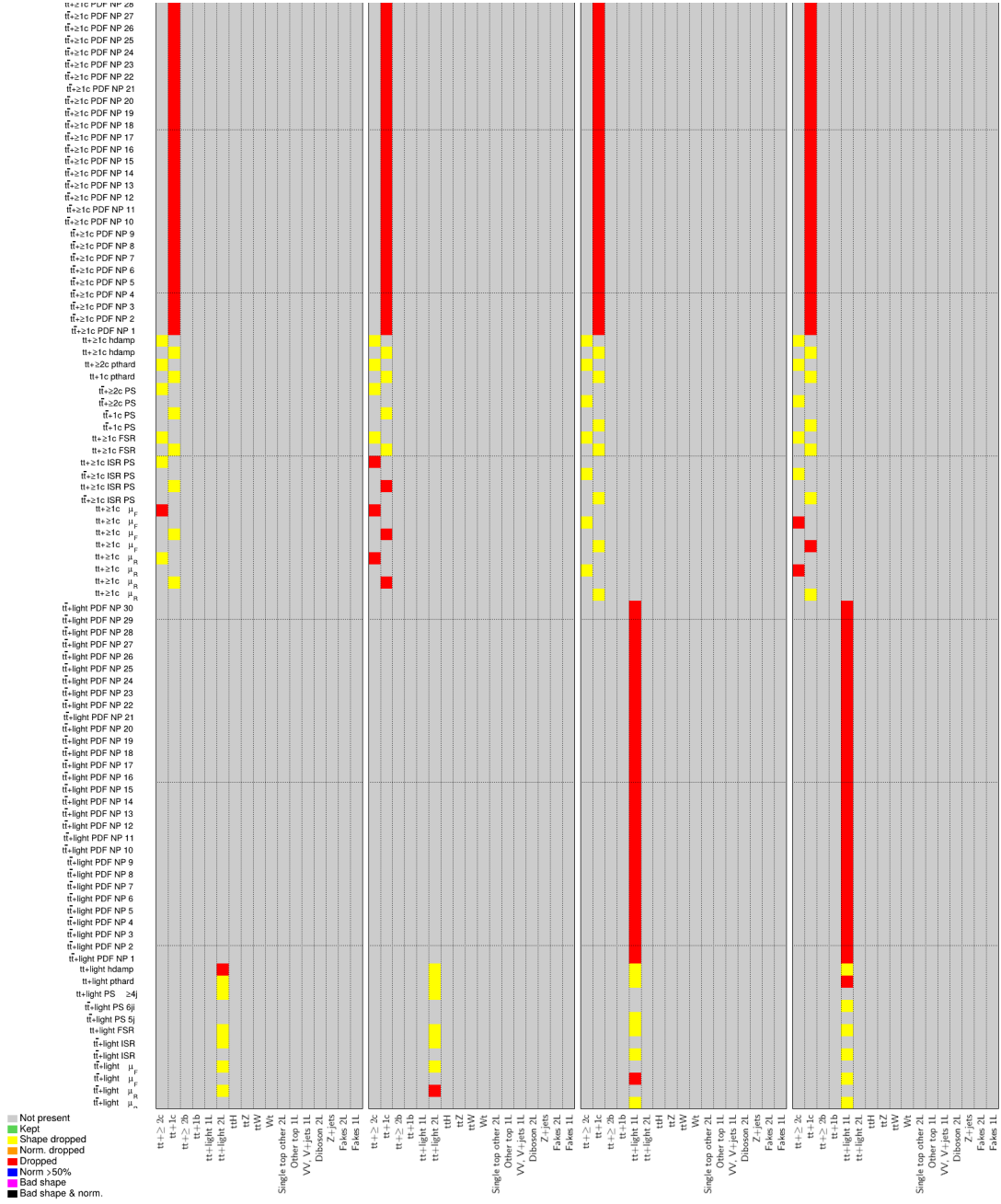


Figure C.8.: Pruning of systematic uncertainties in (from left to right) $CR_2^{2\ell 3j}$, $CR_2^{2\ell \geq 4j}$, $CR_2^{1\ell 5j}$ and $CR_2^{1\ell \geq 6j}$, showing colour scheme and samples considered in each region.

C. Pruning of Systematic Uncertainties

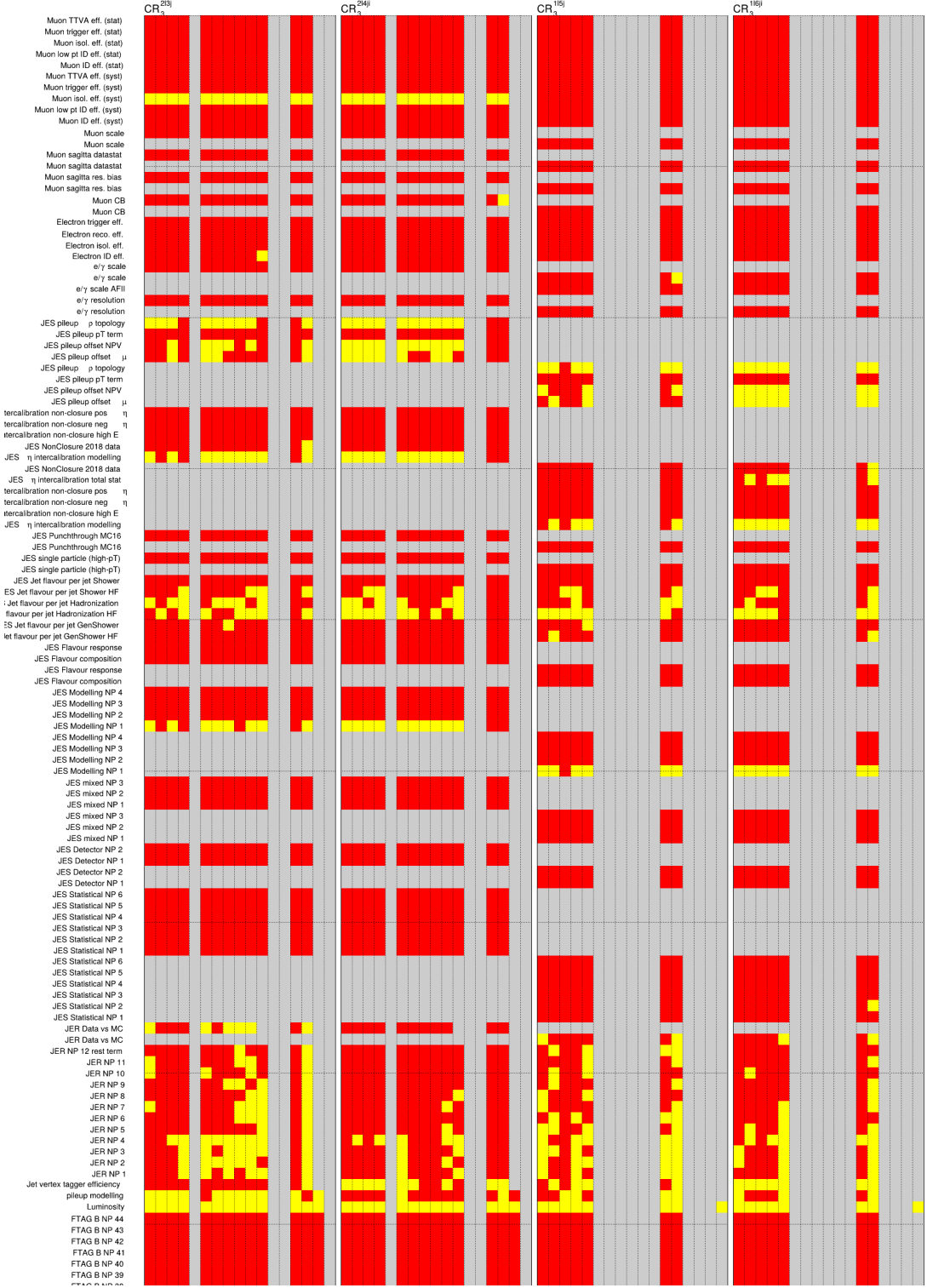


Figure C.9.: Pruning of systematic uncertainties in (from left to right) CR_3^{2l3j} , $CR_3^{2l\ge4j}$, CR_3^{1l5j} and $CR_3^{1l\ge6j}$. Continued on following page. Colour key and list of samples shown in Figure C.12.

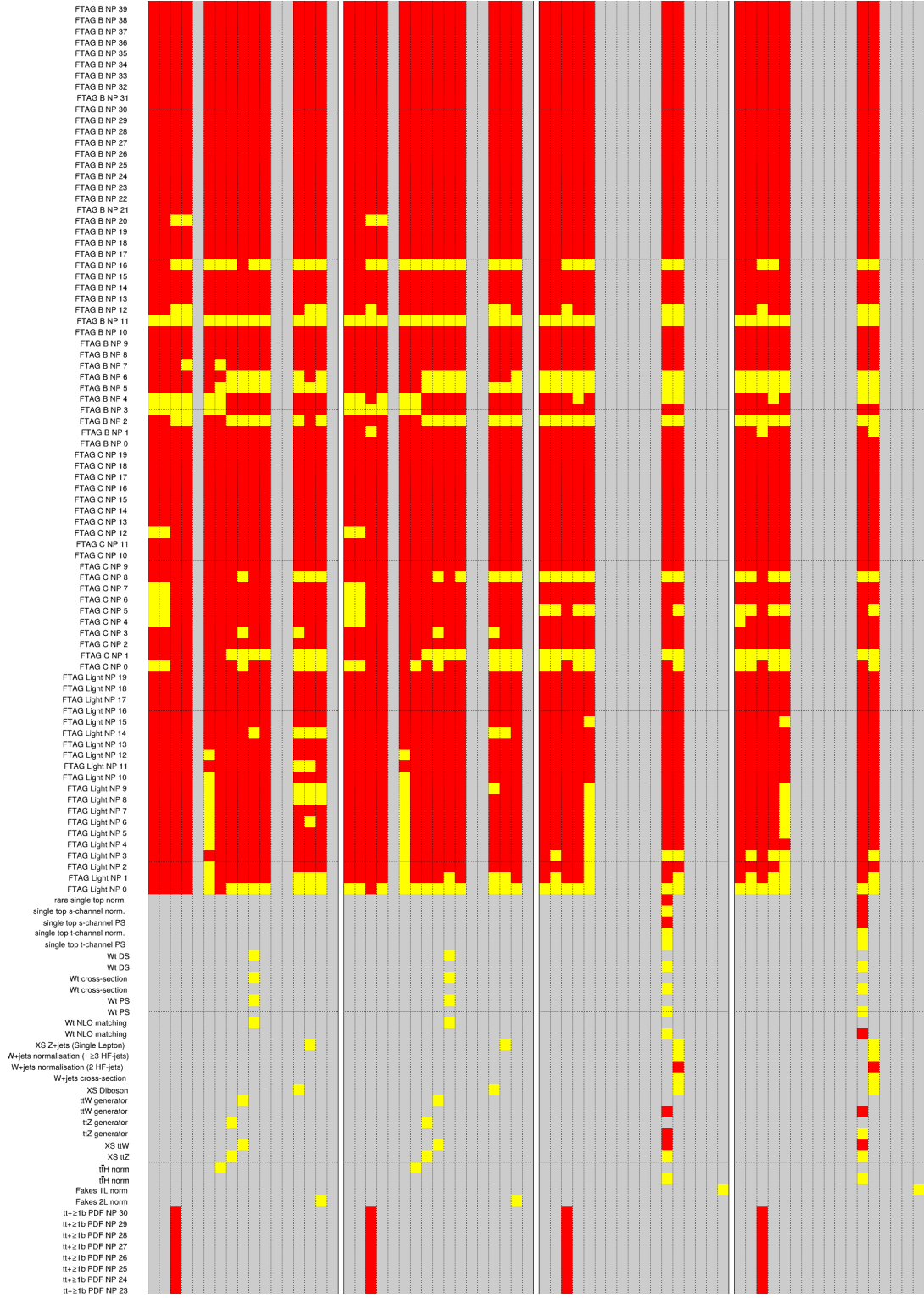


Figure C.10.: Pruning of systematic uncertainties in (from left to right) $\text{CR}_3^{2\ell 3j}$, $\text{CR}_3^{2\ell \geq 4j}$, $\text{CR}_3^{1\ell 5j}$ and $\text{CR}_3^{1\ell \geq 6j}$. Continued on following page. Colour key and list of samples shown in Figure C.12.

C. Pruning of Systematic Uncertainties

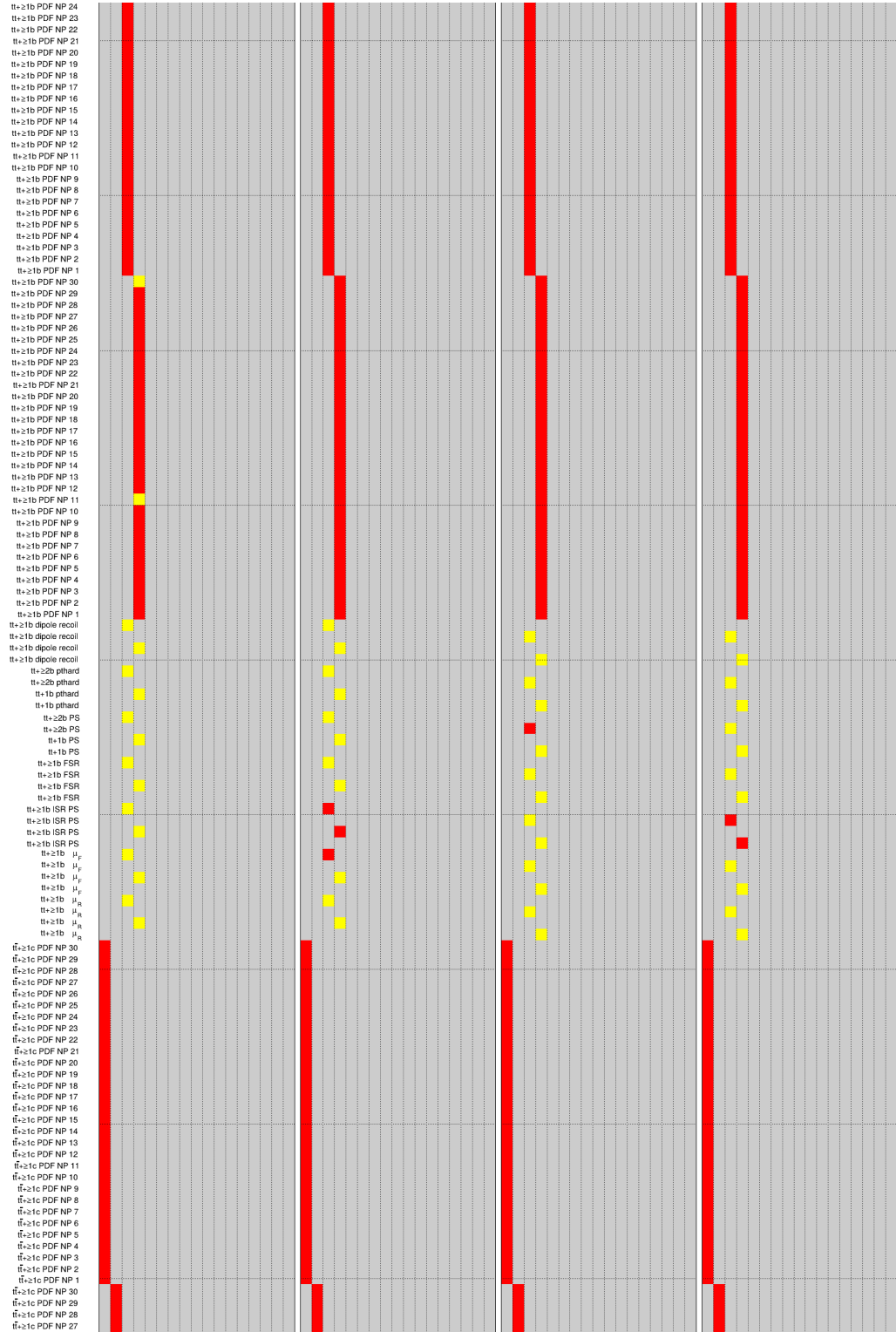


Figure C.11.: Pruning of systematic uncertainties in (from left to right) $\text{CR}_3^{2\ell 3j}$, $\text{CR}_3^{2\ell \geq 4j}$, $\text{CR}_3^{1\ell 5j}$ and $\text{CR}_3^{1\ell \geq 6j}$. Continued on following page. Colour key and list of samples shown in Figure C.12.

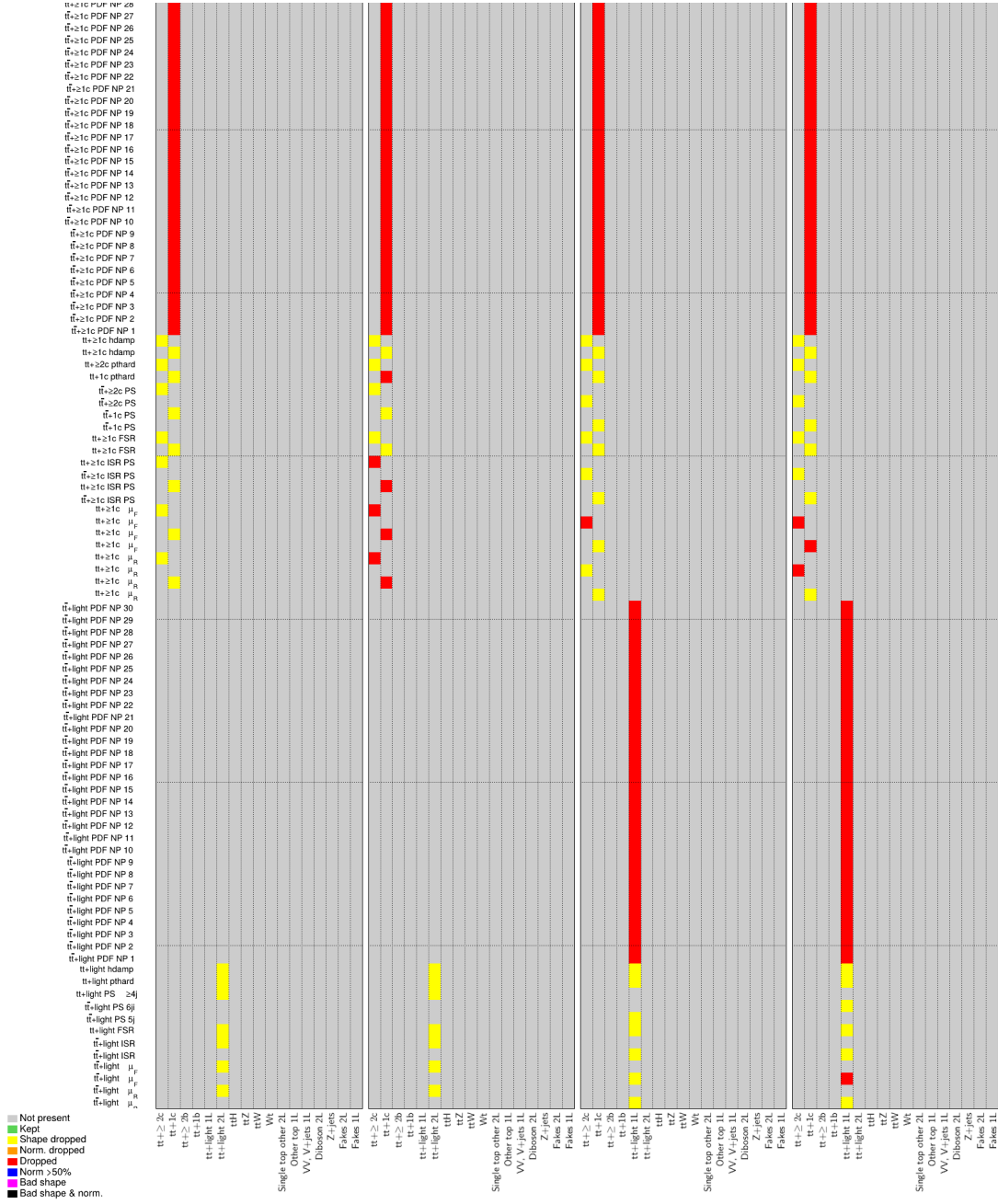


Figure C.12.: Pruning of systematic uncertainties in (from left to right) $CR_3^{2\ell 3j}$, $CR_3^{2\ell \geq 4j}$, $CR_3^{1\ell 5j}$ and $CR_3^{1\ell \geq 6j}$, showing colour scheme and samples considered in each region.

C. Pruning of Systematic Uncertainties



Figure C.13.: Pruning of systematic uncertainties in (from left to right) SR_{loose}^{2l3j} , $SR_{loose}^{2l\ge 4j}$, SR_{loose}^{1l5j} and $SR_{loose}^{1l\ge 6j}$. Continued on following page. Colour key and list of samples shown in Figure C.16.

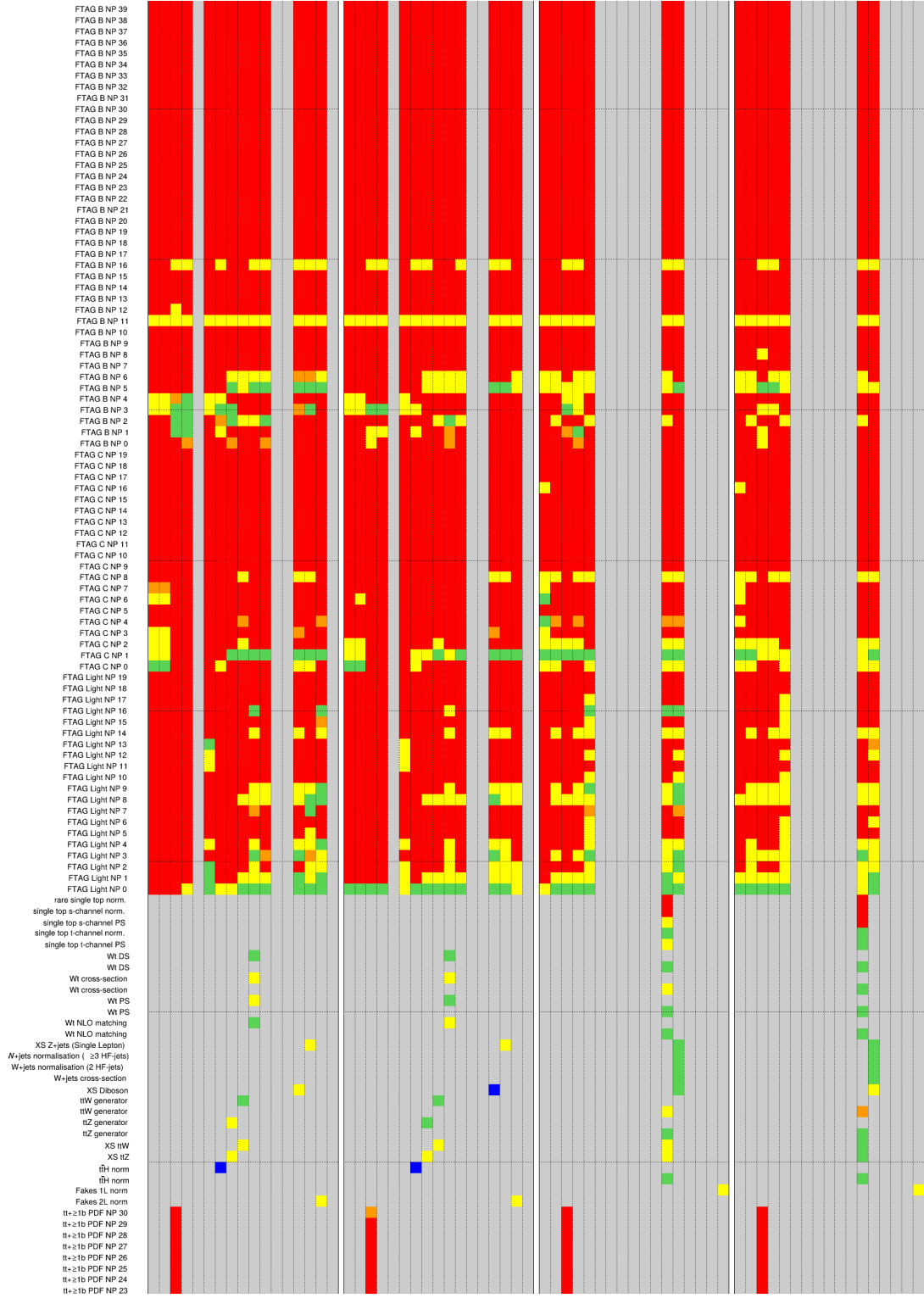


Figure C.14.: Pruning of systematic uncertainties in (from left to right) SR_{loose}^{2l3j} , $SR_{loose}^{2l\geq 4j}$, SR_{loose}^{1l5j} and $SR_{loose}^{1l\geq 6j}$. Continued on following page. Colour key and list of samples shown in Figure C.16.

C. Pruning of Systematic Uncertainties

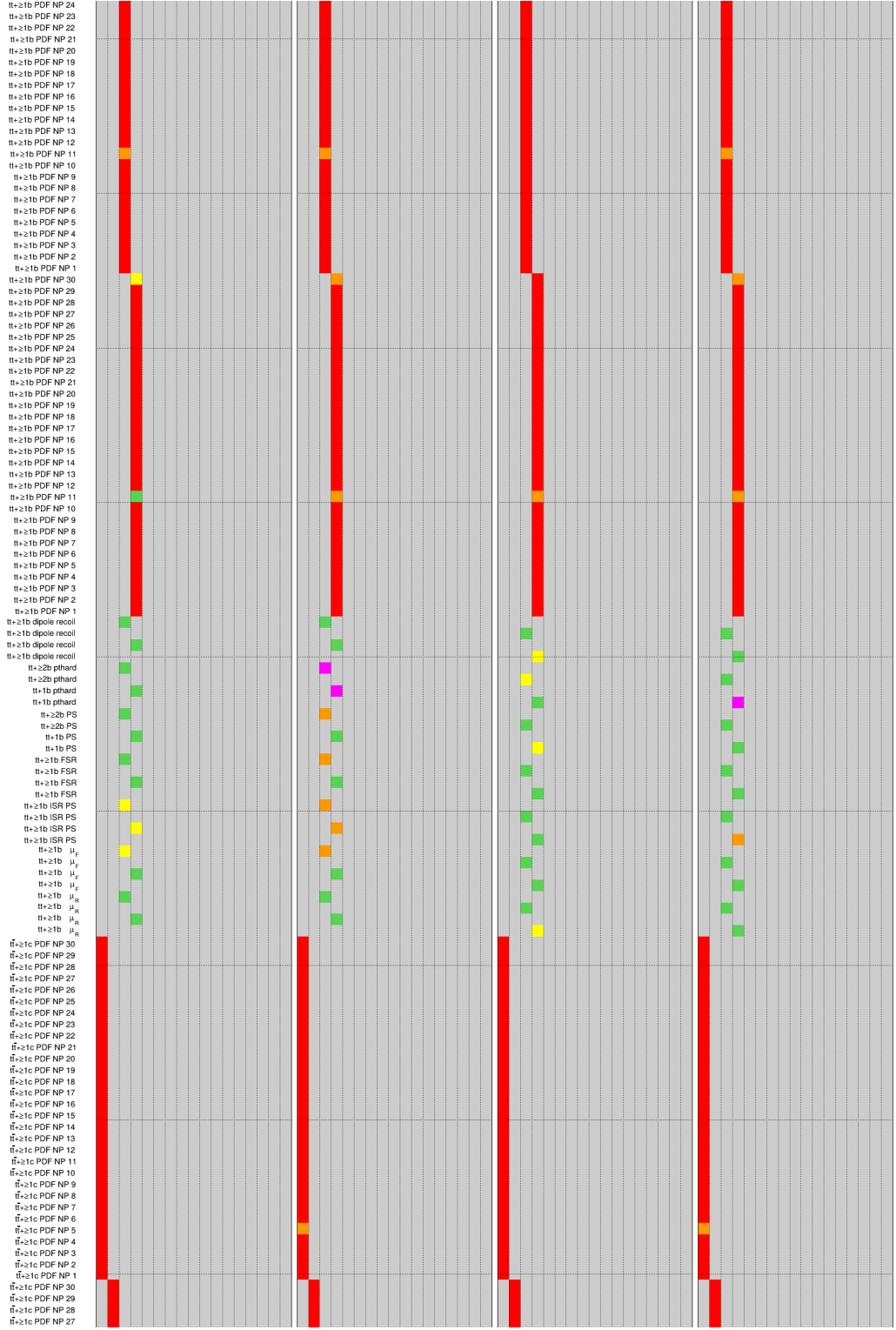


Figure C.15.: Pruning of systematic uncertainties in (from left to right) $SR_{\text{loose}}^{2\ell 3j}$, $SR_{\text{loose}}^{2\ell \geq 4j}$, $SR_{\text{loose}}^{1\ell 5j}$ and $SR_{\text{loose}}^{1\ell \geq 6j}$. Continued on following page. Colour key and list of samples shown in Figure C.16.

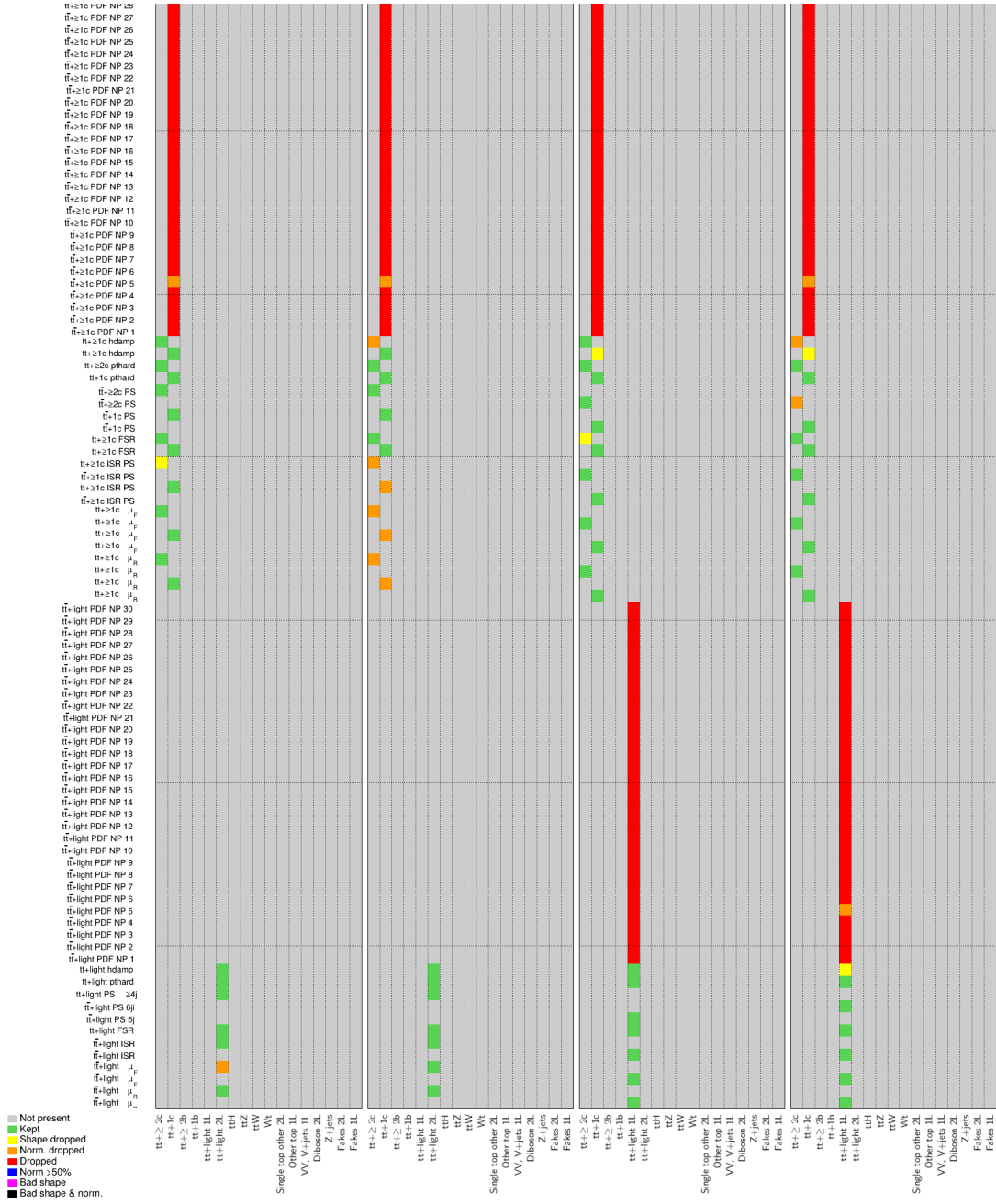


Figure C.16.: Pruning of systematic uncertainties in (from left to right) SR_{loose}^{2l3j} , $SR_{loose}^{2l\ge4j}$, SR_{loose}^{1l5j} and $SR_{loose}^{1l\ge6j}$, showing colour scheme and samples considered in each region.

C. Pruning of Systematic Uncertainties



Figure C.17.: Pruning of systematic uncertainties in (from left to right) $SR_{\text{tight}}^{2\ell 3j}$, $SR_{\text{tight}}^{1\ell 5j}$ and $SR_{\text{tight}}^{1\ell \geq 6j}$. Continued on following page. Colour key and list of samples shown in Figure C.20.

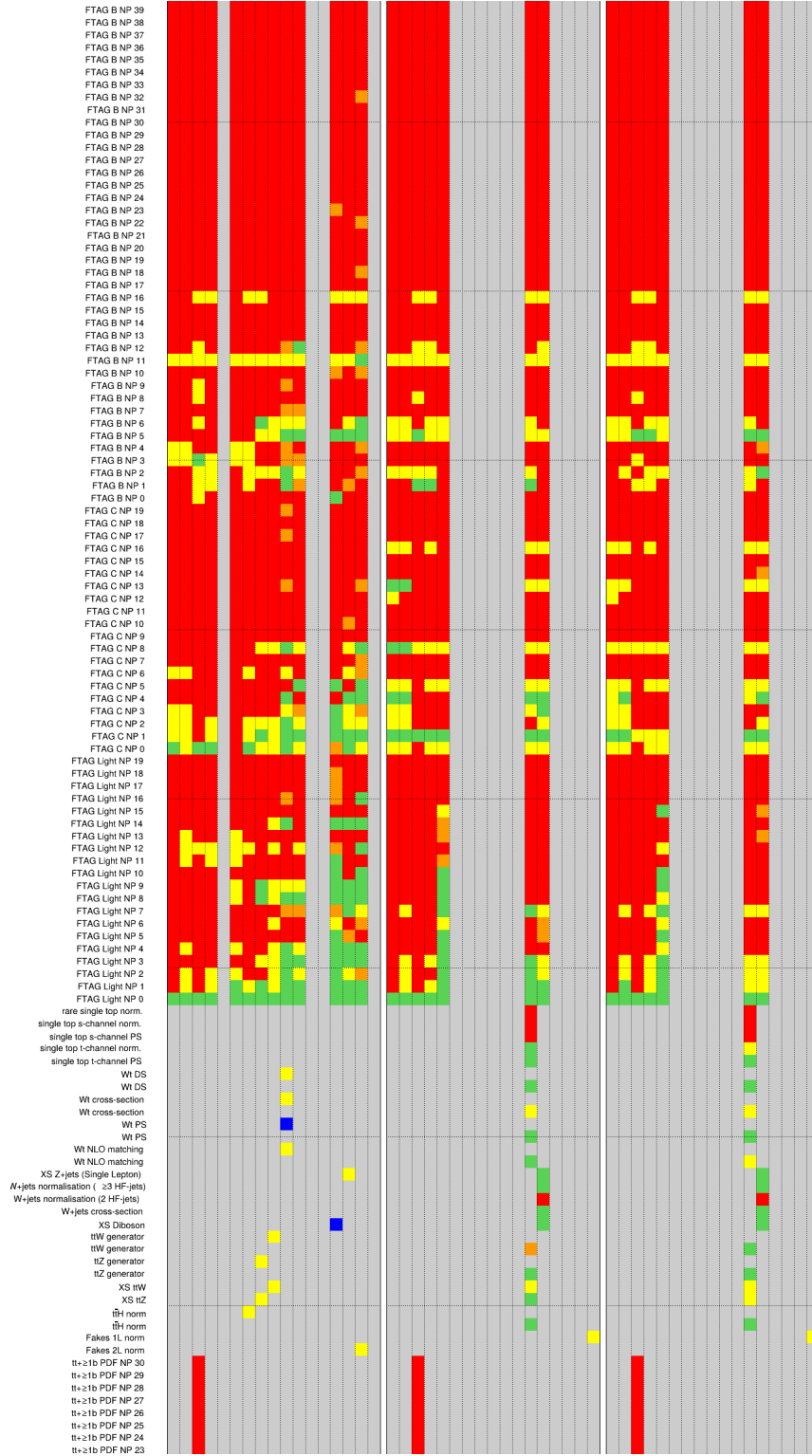


Figure C.18.: Pruning of systematic uncertainties in (from left to right) $\text{SR}_{\text{tight}}^{2\ell 3j}$, $\text{SR}_{\text{tight}}^{1\ell 5j}$ and $\text{SR}_{\text{tight}}^{1\ell \geq 6j}$. Continued on following page. Colour key and list of samples shown in Figure C.20.

C. Pruning of Systematic Uncertainties

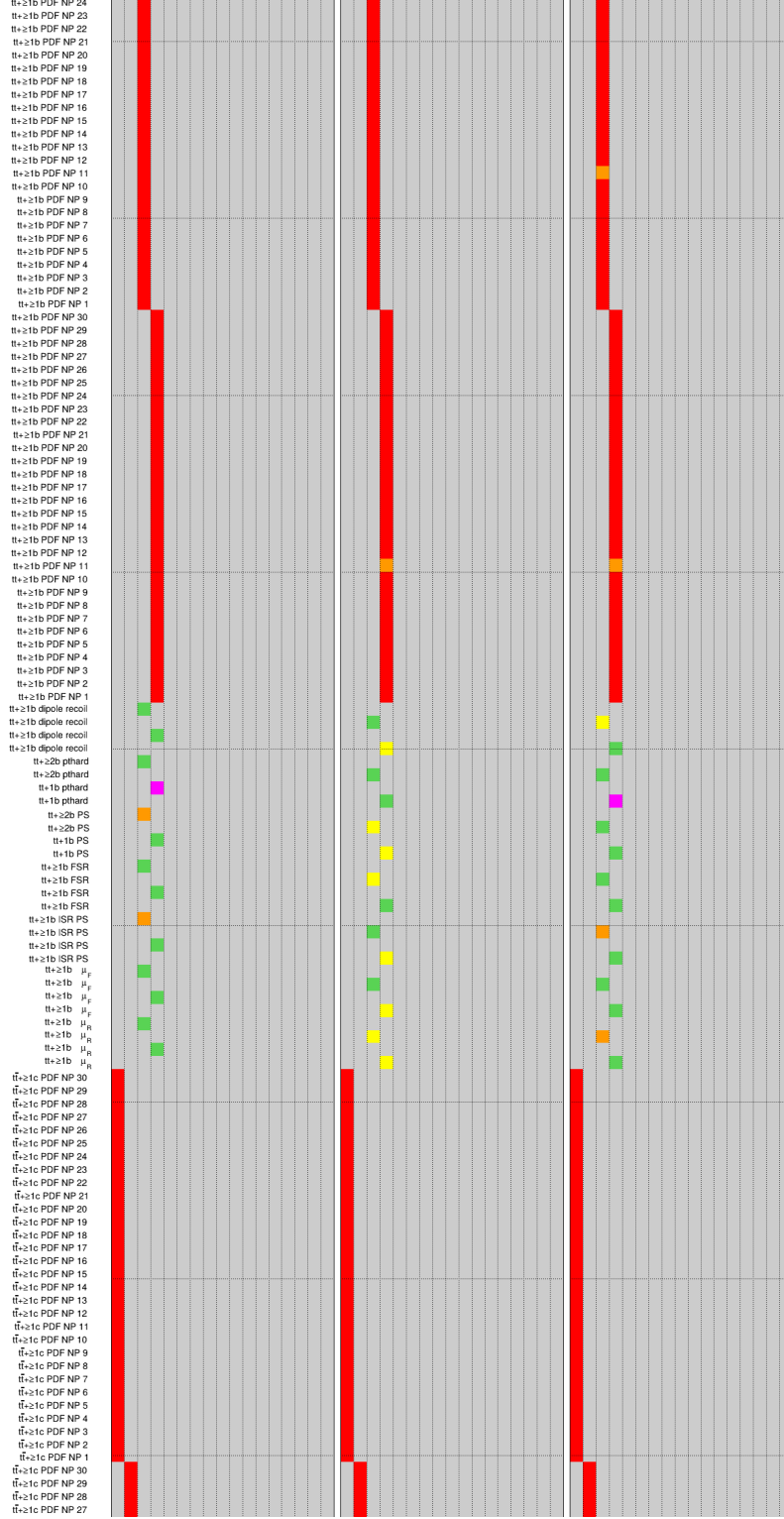


Figure C.19.: Pruning of systematic uncertainties in (from left to right) $SR_{\text{tight}}^{2\ell 3j}$, $SR_{\text{tight}}^{1\ell 5j}$ and $SR_{\text{tight}}^{1\ell \ge 6j}$. Continued on following page. Colour key and list of samples shown in Figure C.20.

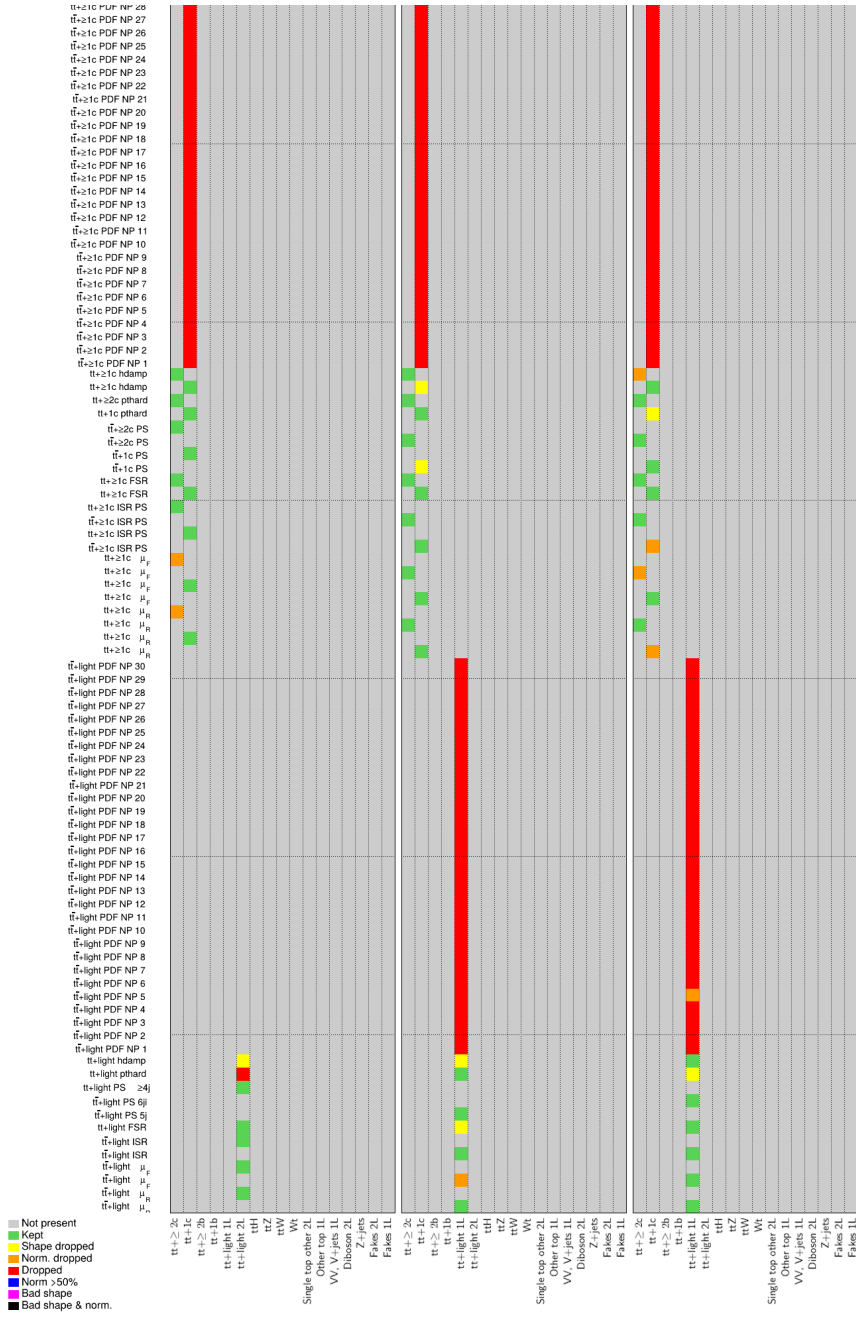


Figure C.20.: Pruning of systematic uncertainties in (from left to right) $SR^{2\ell 3j}_{tight}$, $SR^{1\ell 5j}_{tight}$ and $SR^{1\ell \ge 6j}_{tight}$, showing colour scheme and samples considered in each region.

APPENDIX D

Kinematics Control Plots

D.1. Pre-fit plots - lepton + jets channel

D. Kinematics Control Plots

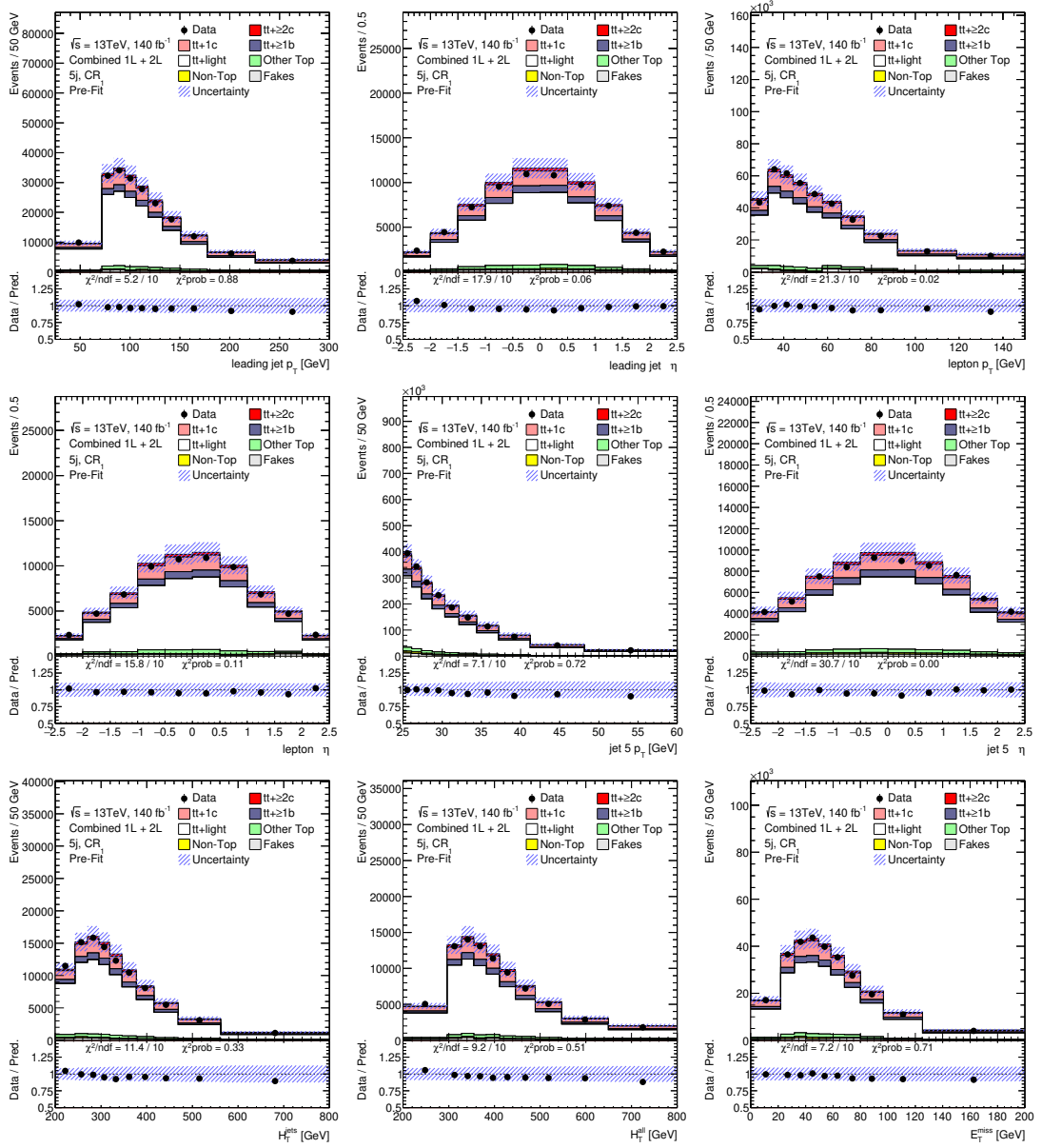


Figure D.1.: Pre-fit agreement between data and prediction for basic kinematic variables in $CR_1^{1\ell5j}$. The hashed band includes all prediction uncertainties. Overflow and underflow events are contained in the first and last bin respectively.

D.1. Pre-fit plots - lepton + jets channel

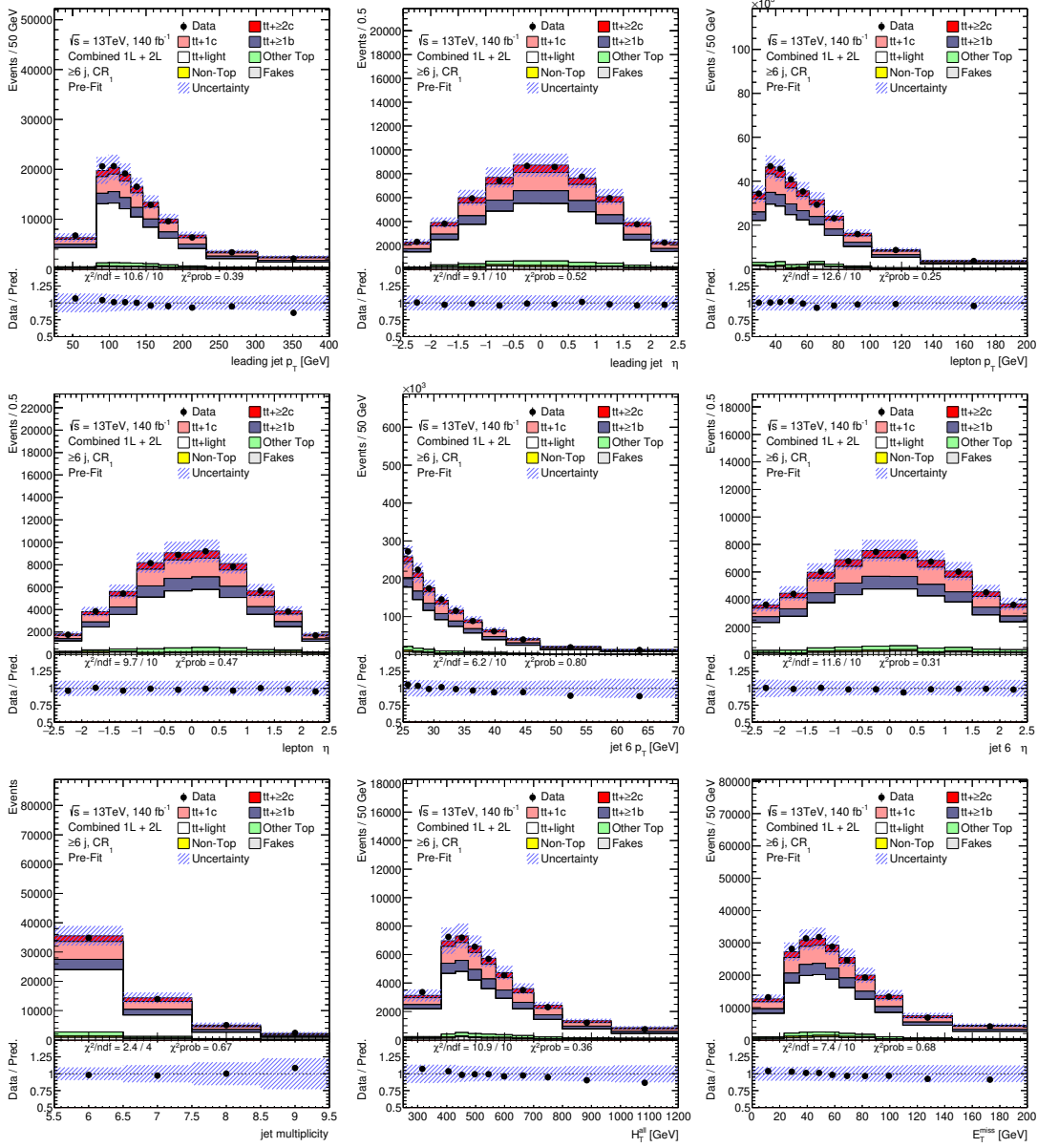


Figure D.2.: Pre-fit agreement between data and prediction for basic kinematic variables in $CR_1^{1\ell \geq 6j}$. The hashed band includes all prediction uncertainties. Overflow and underflow events are contained in the first and last bin respectively.

D. Kinematics Control Plots

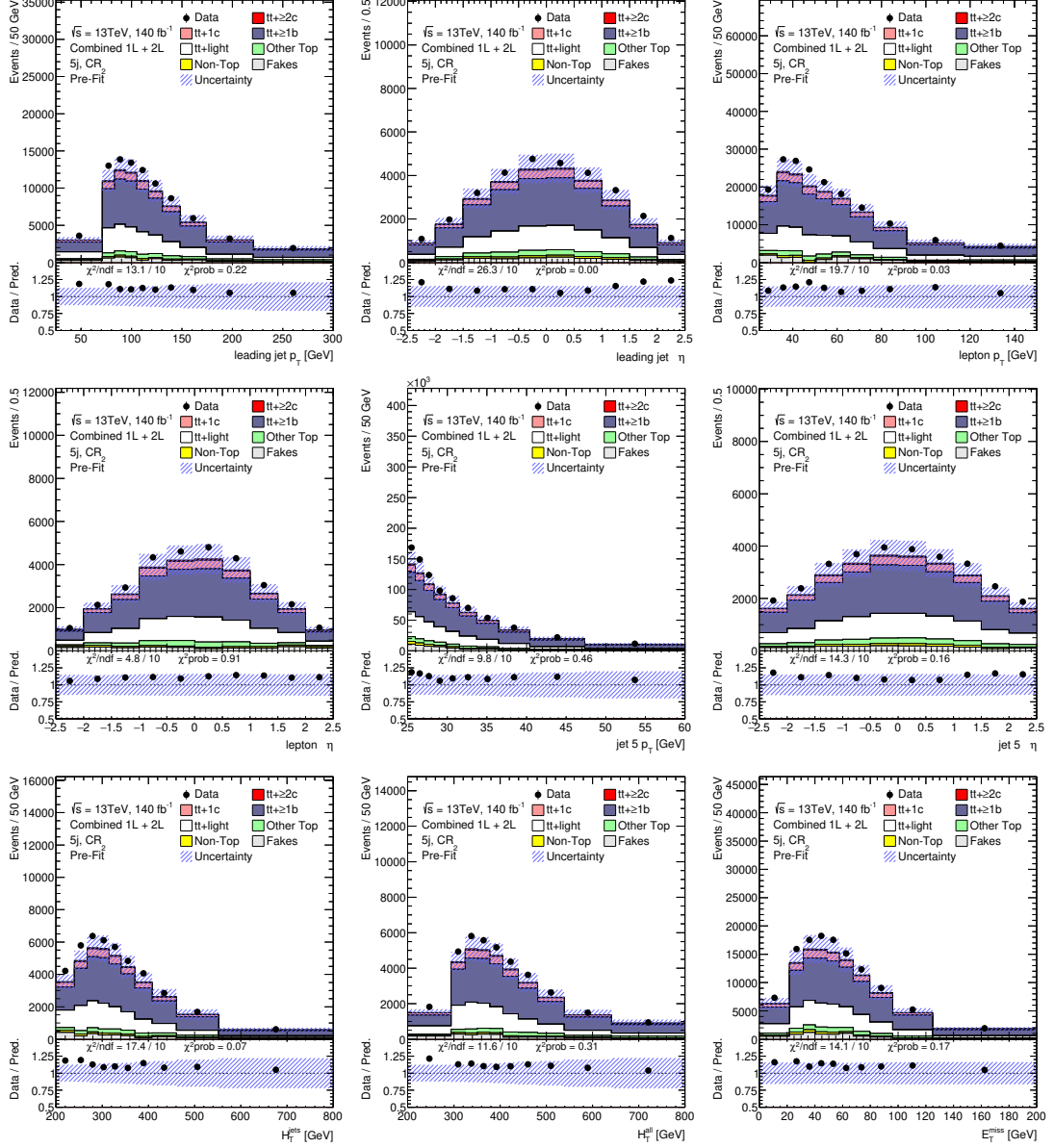


Figure D.3.: Pre-fit agreement between data and prediction for basic kinematic variables in $\text{CR}_2^{1\ell 5j}$. The hashed band includes all prediction uncertainties. Overflow and underflow events are contained in the first and last bin respectively.

D.1. Pre-fit plots - lepton + jets channel

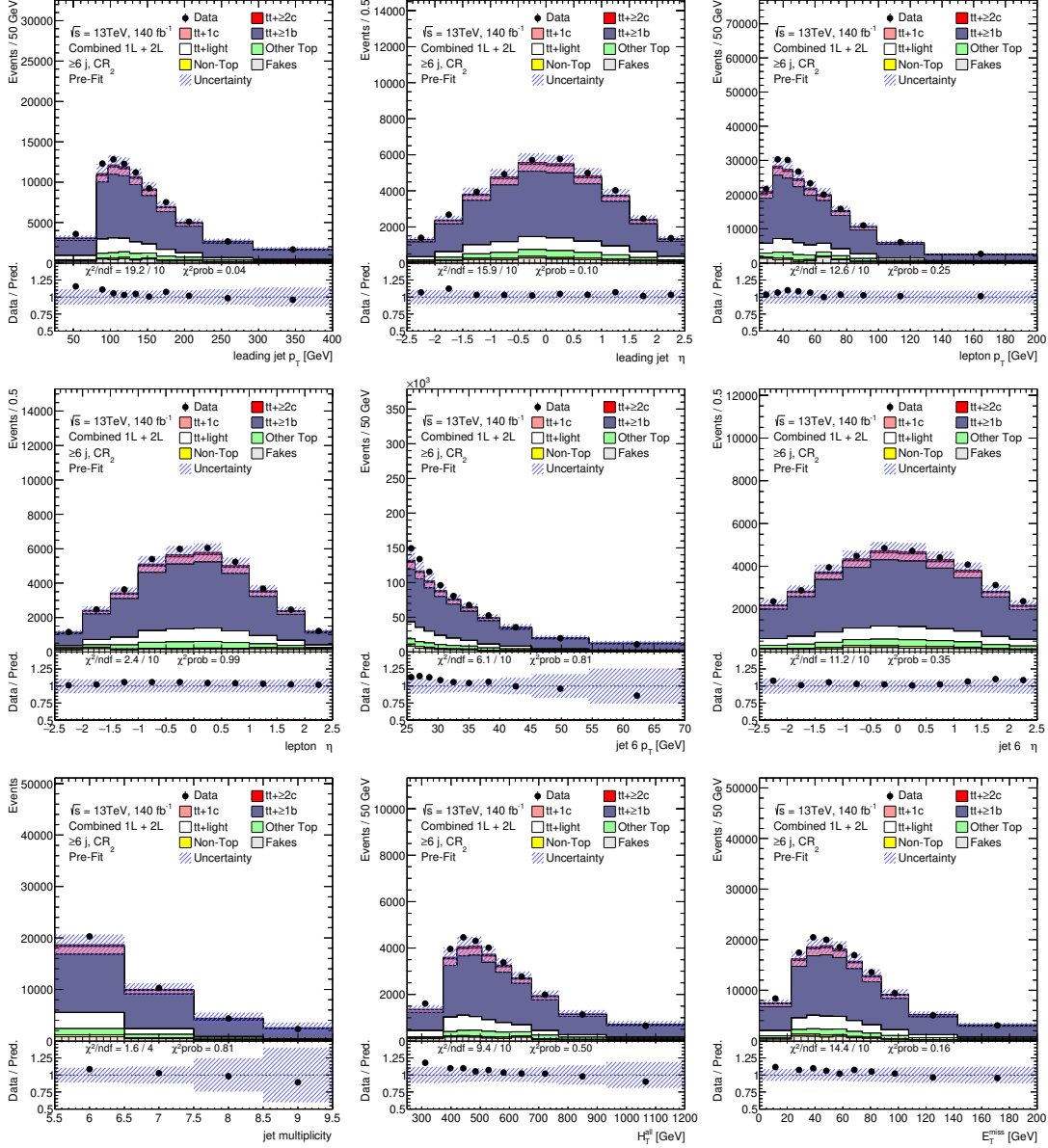


Figure D.4.: Pre-fit agreement between data and prediction for basic kinematic variables in $CR_2^{1\ell \geq 6j}$. The hashed band includes all prediction uncertainties. Overflow and underflow events are contained in the first and last bin respectively.

D. Kinematics Control Plots

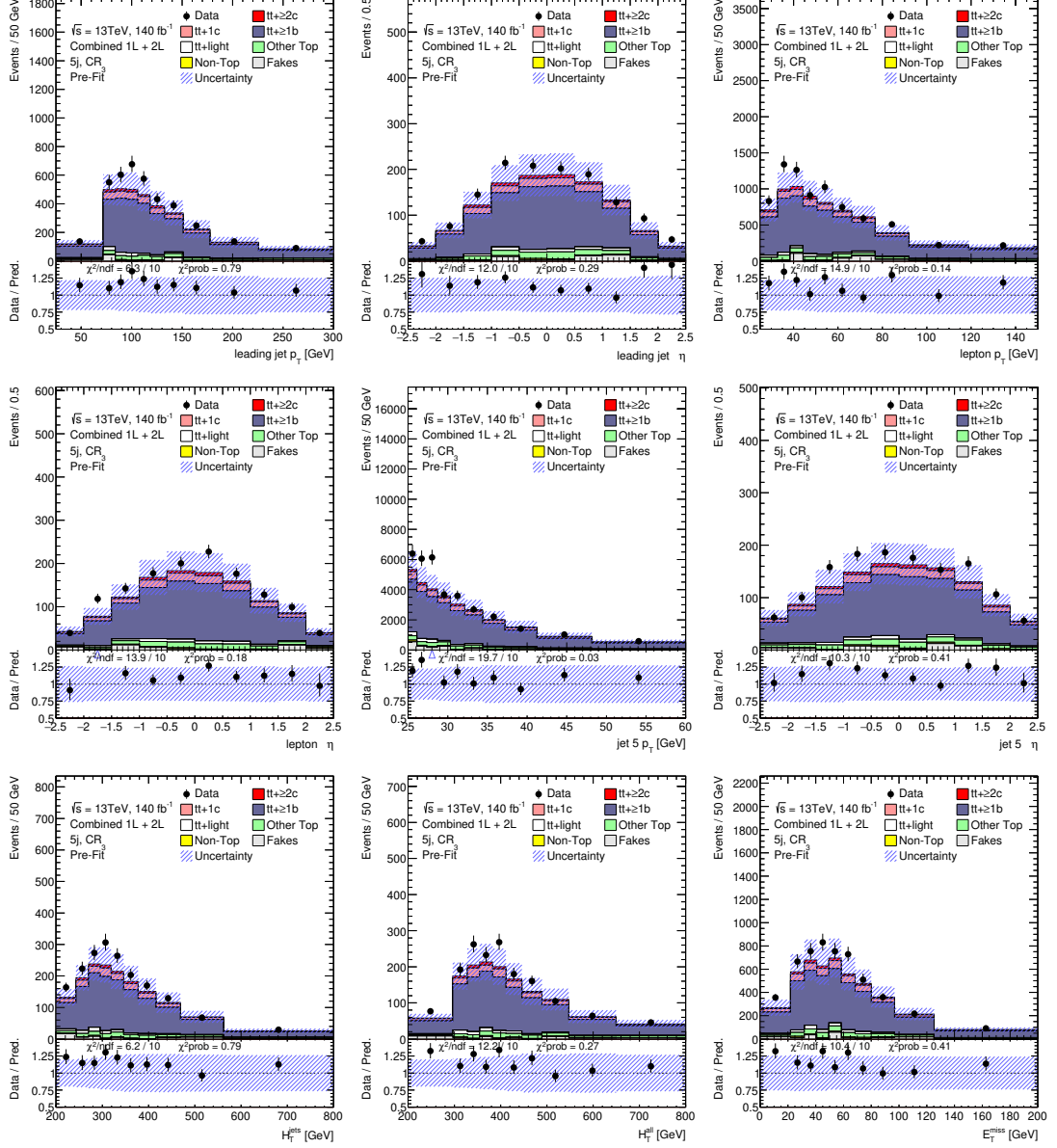


Figure D.5.: Pre-fit agreement between data and prediction for basic kinematic variables in $CR_3^{1/5j}$. The hashed band includes all prediction uncertainties. Overflow and underflow events are contained in the first and last bin respectively.

D.1. Pre-fit plots - lepton + jets channel

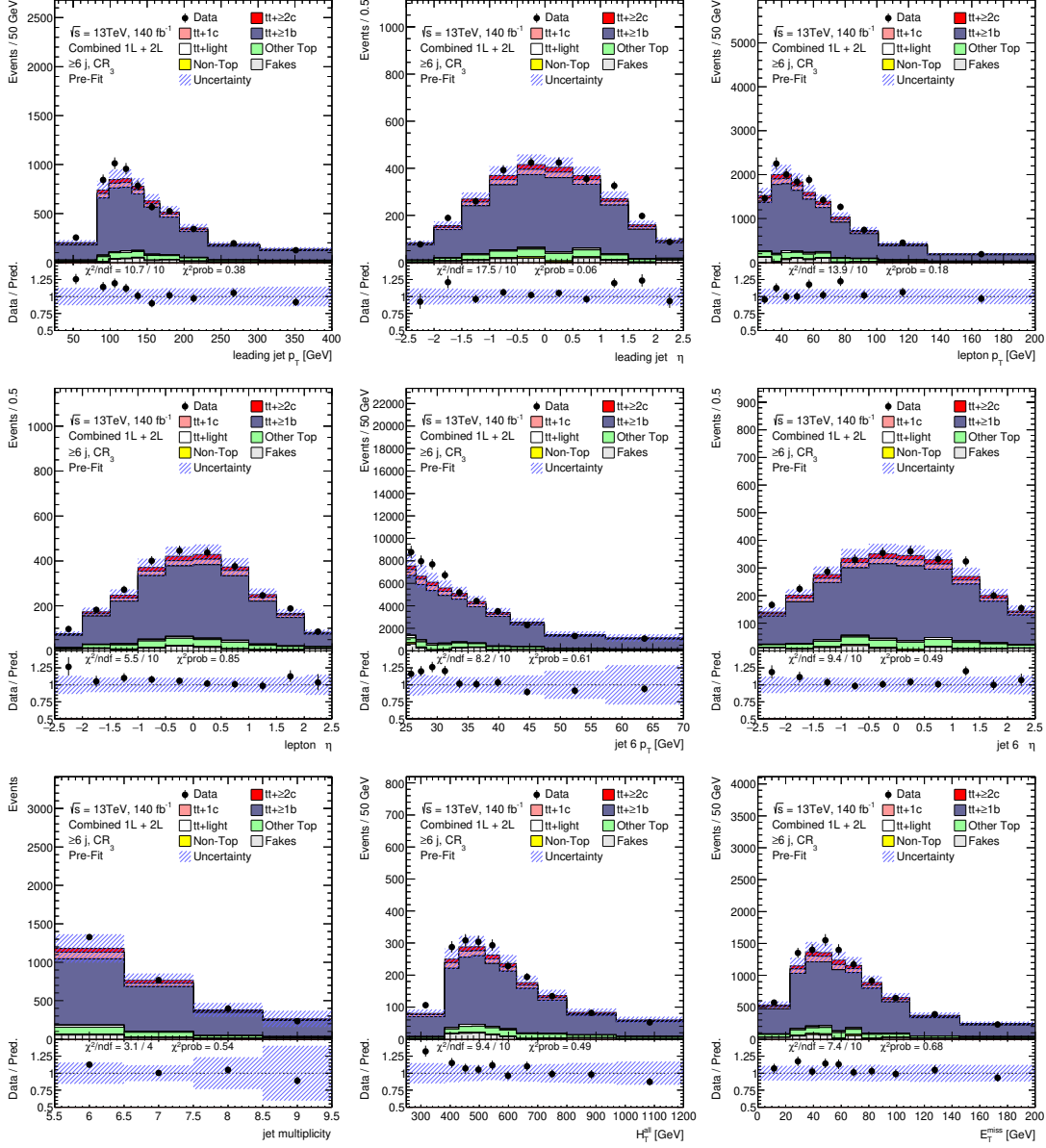


Figure D.6.: Pre-fit agreement between data and prediction for basic kinematic variables in $CR_3^{1\ell \geq 6j}$. The hashed band includes all prediction uncertainties. Overflow and underflow events are contained in the first and last bin respectively.

D. Kinematics Control Plots

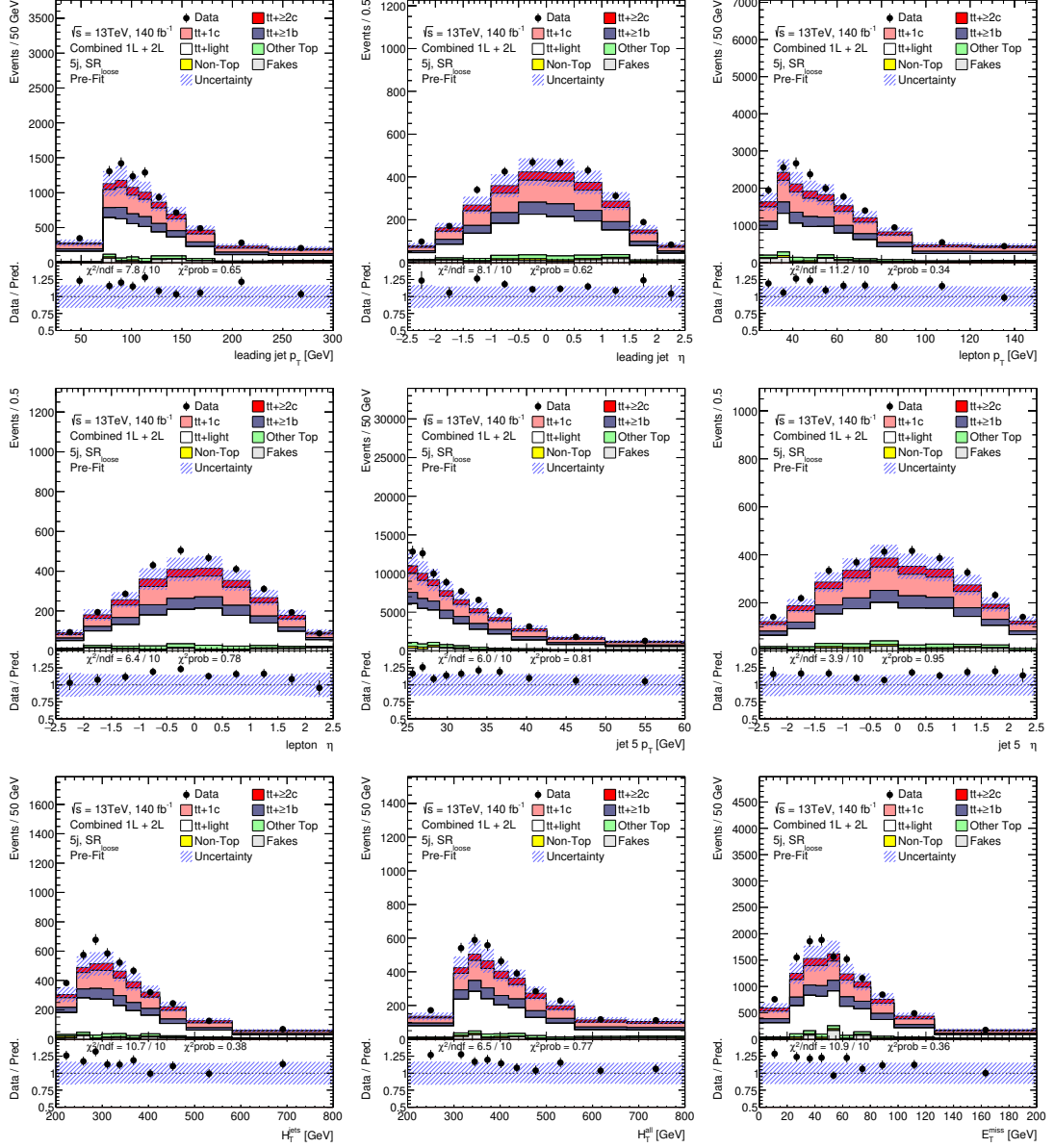


Figure D.7.: Pre-fit agreement between data and prediction for basic kinematic variables in $\text{SR}_{1\ell 5j}^{\text{loose}}$. The hashed band includes all prediction uncertainties. Overflow and underflow events are contained in the first and last bin respectively.

D.1. Pre-fit plots - lepton + jets channel

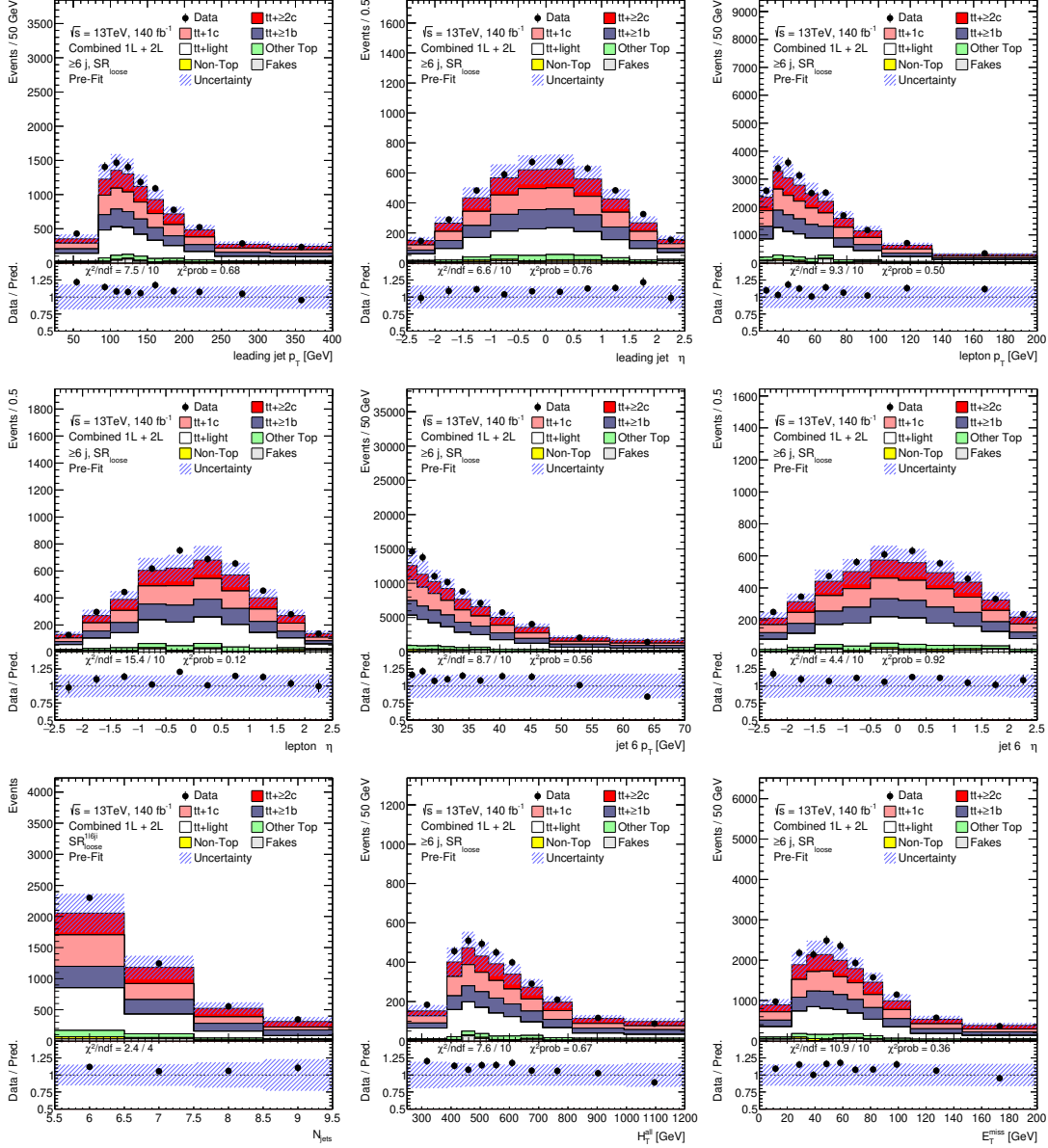


Figure D.8.: Pre-fit agreement between data and prediction for basic kinematic variables in $SR_{1\ell \geq 6j}^{loose}$. The hashed band includes all prediction uncertainties. Overflow and underflow events are contained in the first and last bin respectively.

D. Kinematics Control Plots

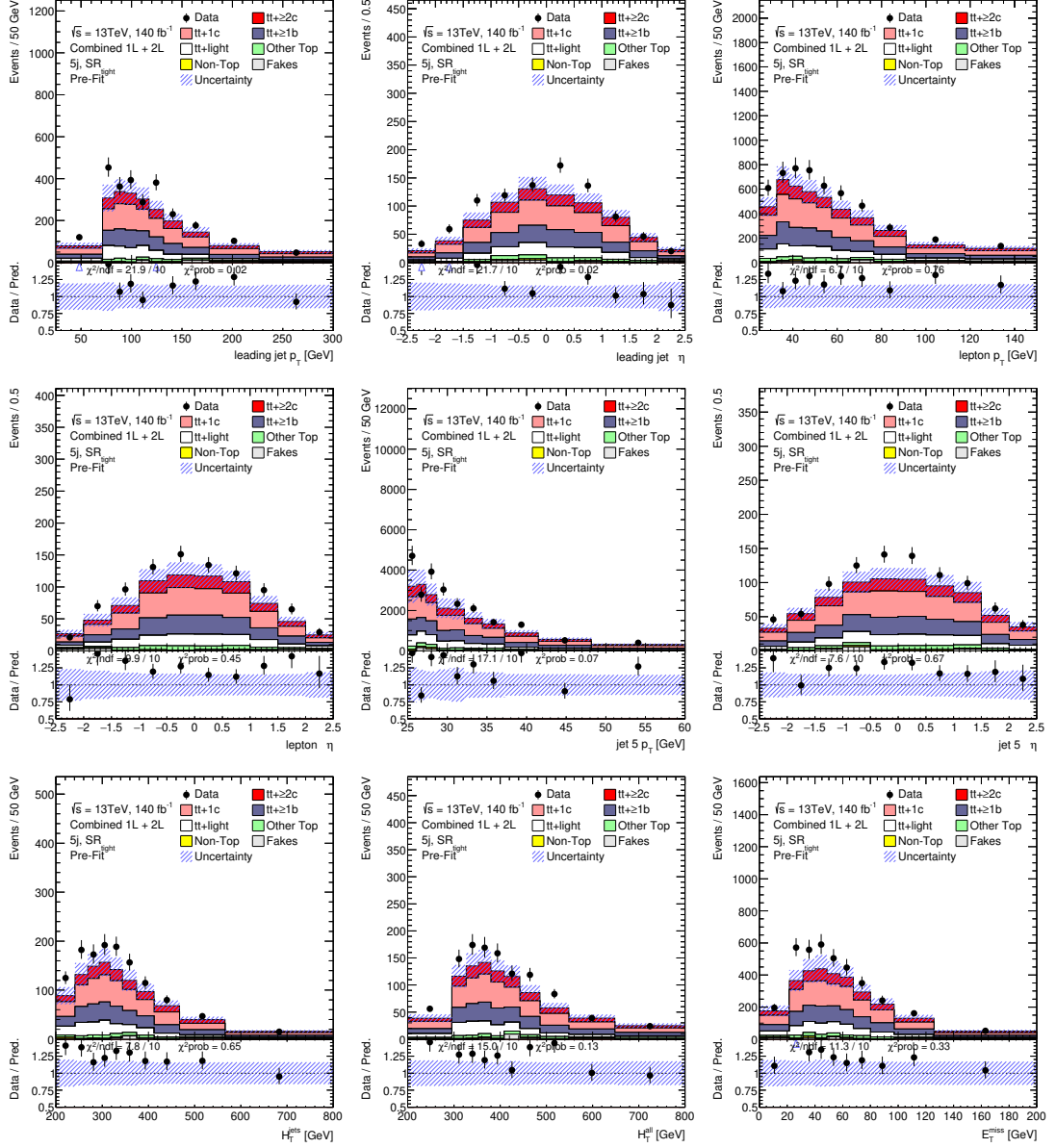


Figure D.9.: Pre-fit agreement between data and prediction for basic kinematic variables in $SR^{1\ell 5j}_{tight}$. The hashed band includes all prediction uncertainties. Overflow and underflow events are contained in the first and last bin respectively.

D.1. Pre-fit plots - lepton + jets channel

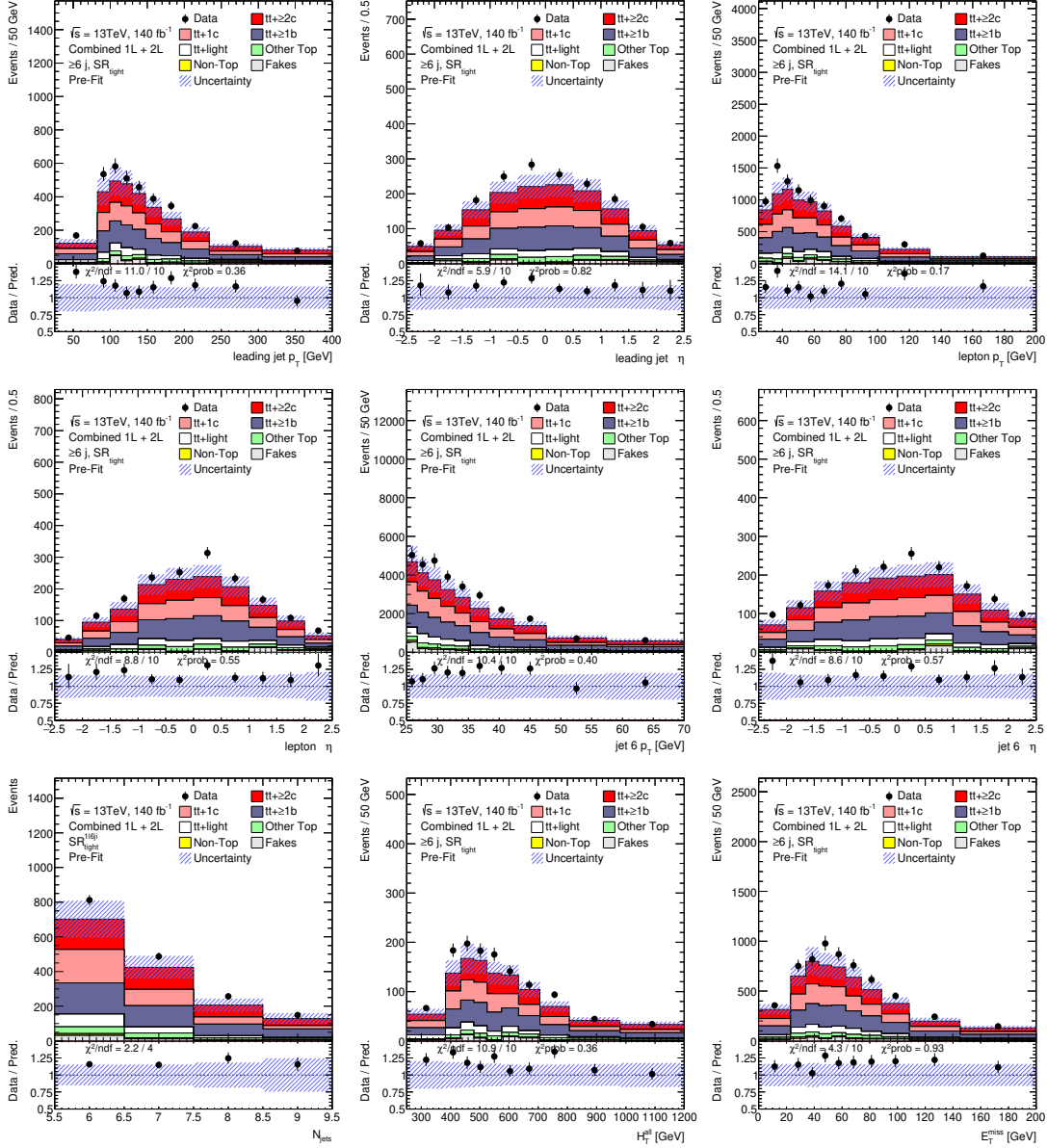


Figure D.10.: Pre-fit agreement between data and prediction for basic kinematic variables in $SR_{tight}^{1\ell \ge 6j}$. The hashed band includes all prediction uncertainties. Overflow and underflow events are contained in the first and last bin respectively.

D. Kinematics Control Plots

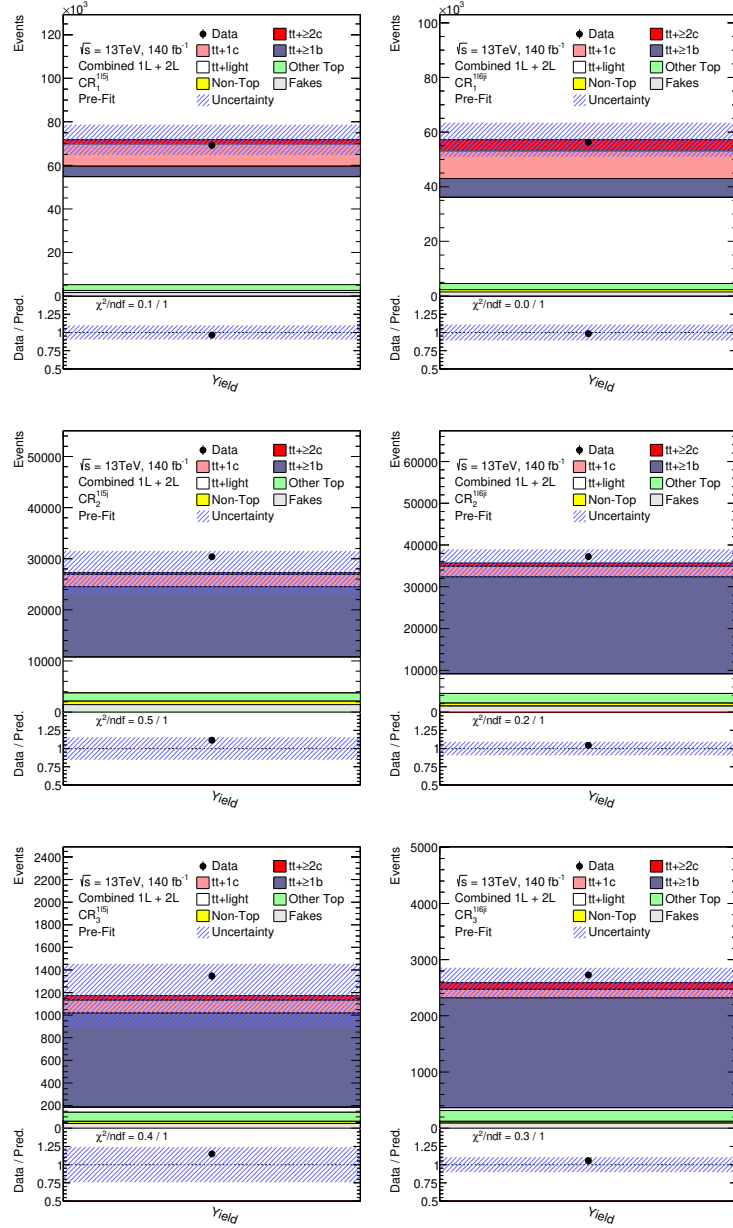


Figure D.11.: Pre-fit agreement between data and prediction for observables used in fitting in lepton + jets channel control regions. The hashed band includes all prediction uncertainties.

D.1. Pre-fit plots - lepton + jets channel

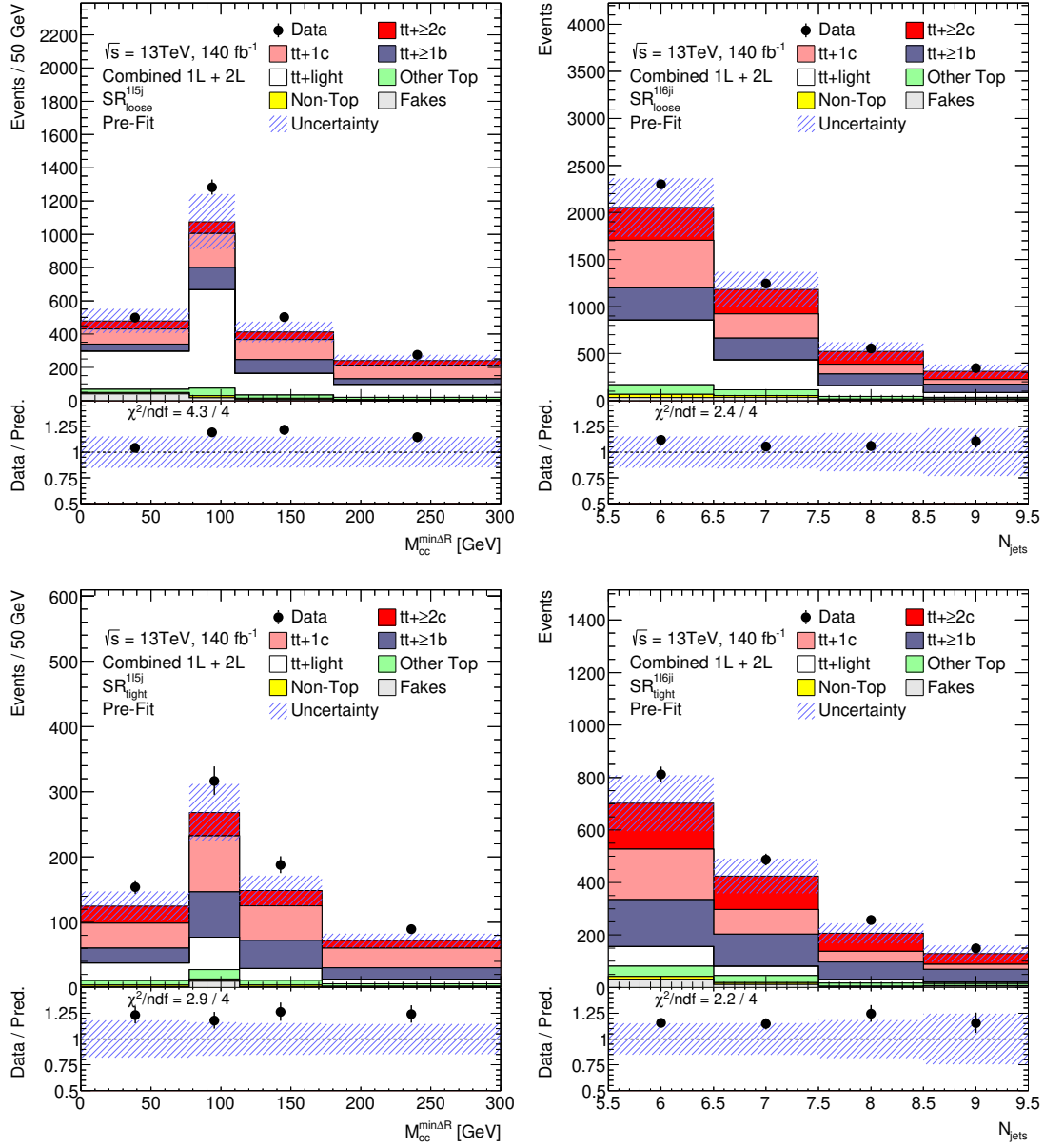


Figure D.12.: Pre-fit agreement between data and prediction for observables used in fitting in lepton + jets channel signal regions. The hashed band includes all prediction uncertainties. Overflow and underflow events are contained in the first and last bin respectively.

D. Kinematics Control Plots

D.2. Pre-fit plots - dilepton channel

D.2. Pre-fit plots - dilepton channel

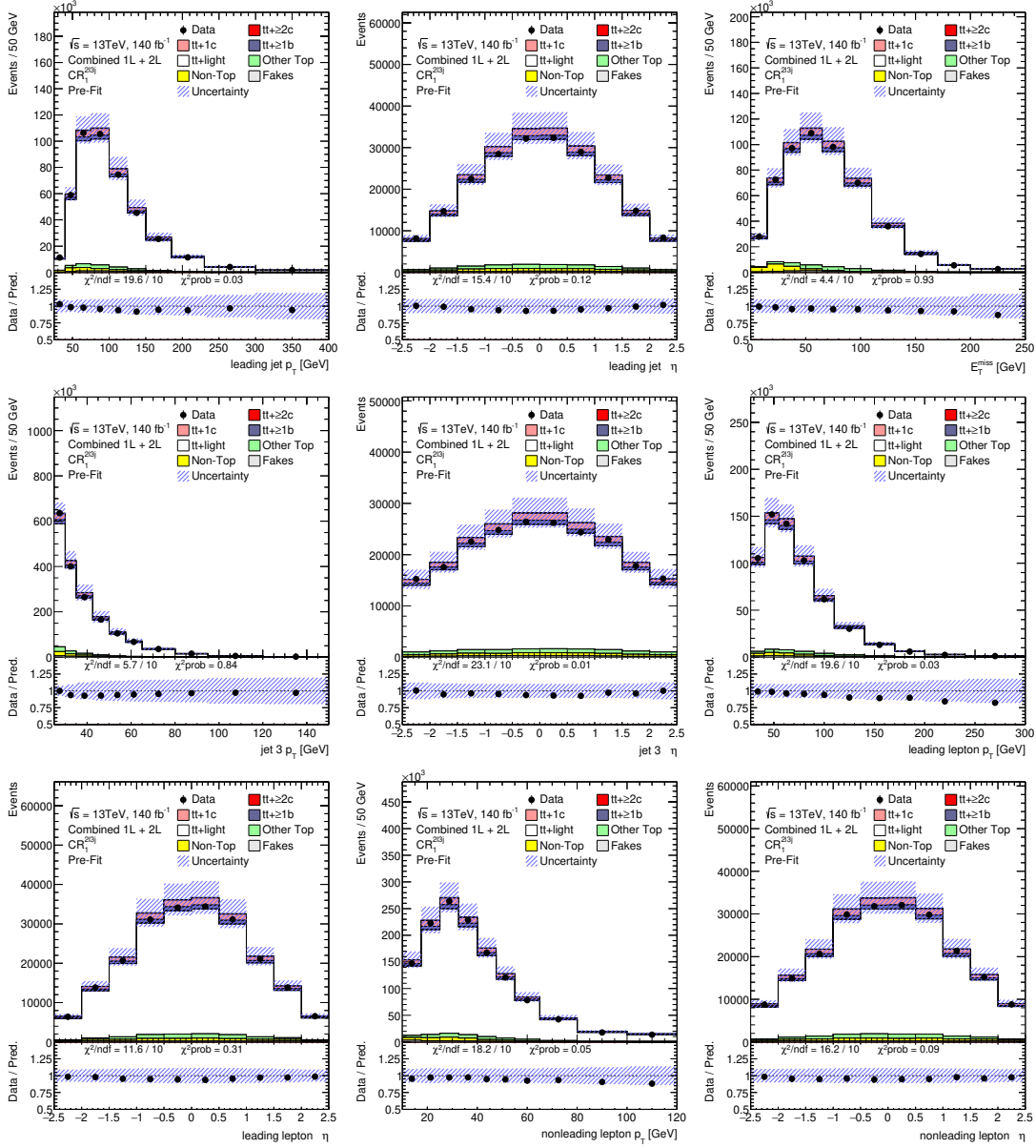


Figure D.13.: Pre-fit agreement between data and prediction for basic kinematic variables in $CR_1^{2\ell 3j}$. The hashed band includes all prediction uncertainties. Overflow and underflow events are contained in the first and last bin respectively.

D. Kinematics Control Plots

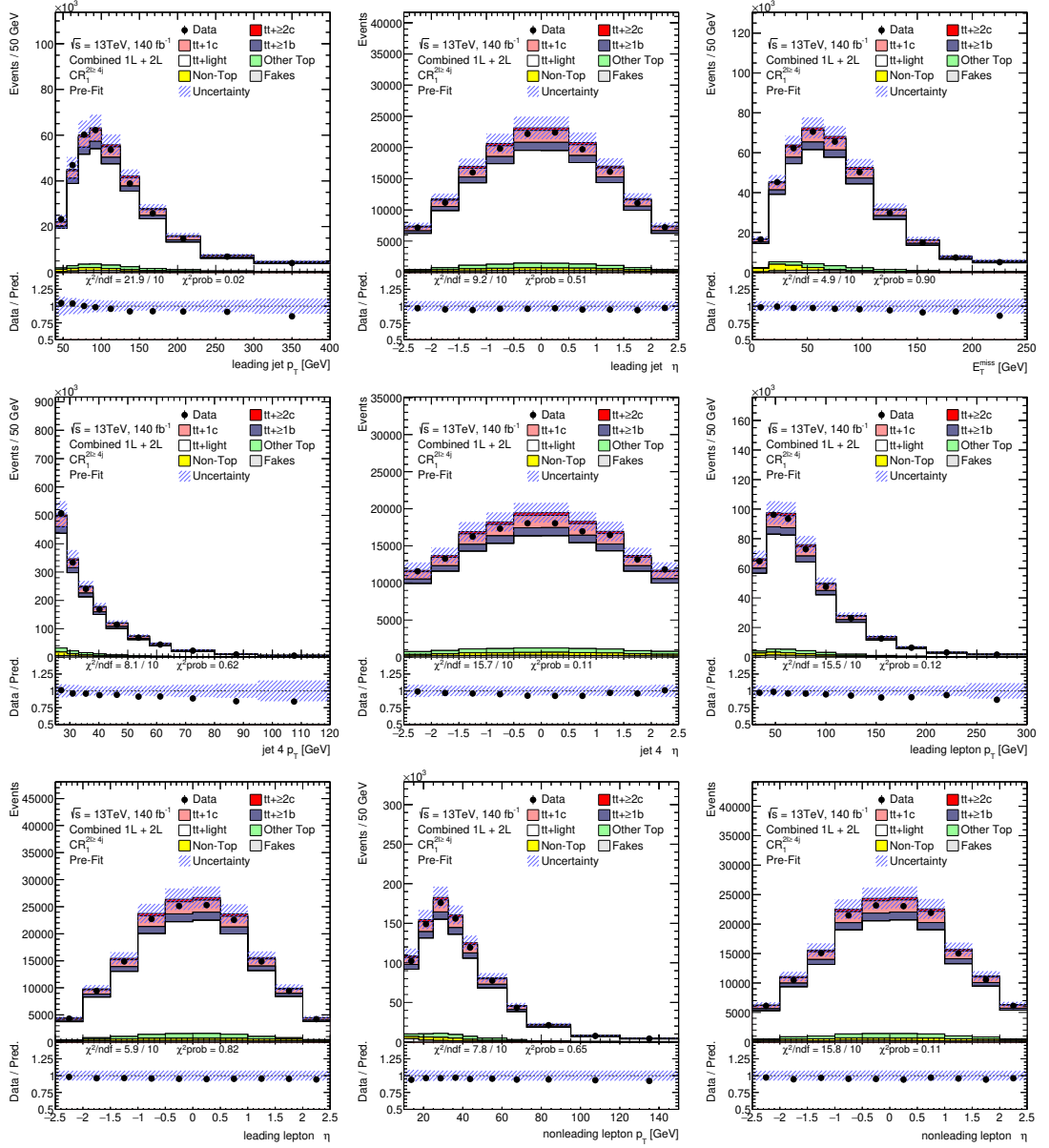


Figure D.14.: Pre-fit agreement between data and prediction for basic kinematic variables in $CR_1^{2\ell\geq 4j}$. The hashed band includes all prediction uncertainties. Overflow and underflow events are contained in the first and last bin respectively.

D.2. Pre-fit plots - dilepton channel

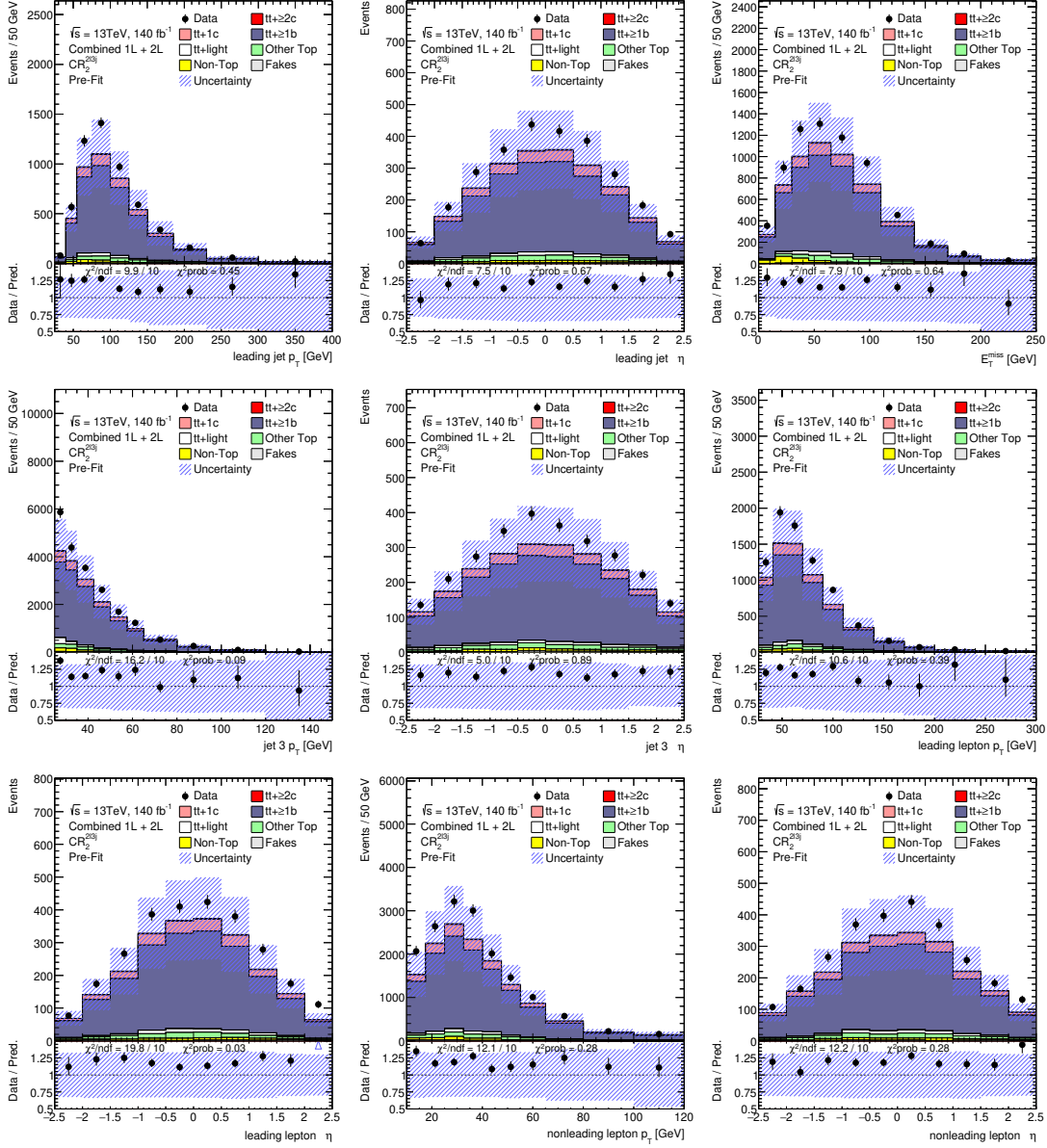


Figure D.15.: Pre-fit agreement between data and prediction for basic kinematic variables in $CR_2^{2\ell 3j}$. The hashed band includes all prediction uncertainties. Overflow and underflow events are contained in the first and last bin respectively.

D. Kinematics Control Plots

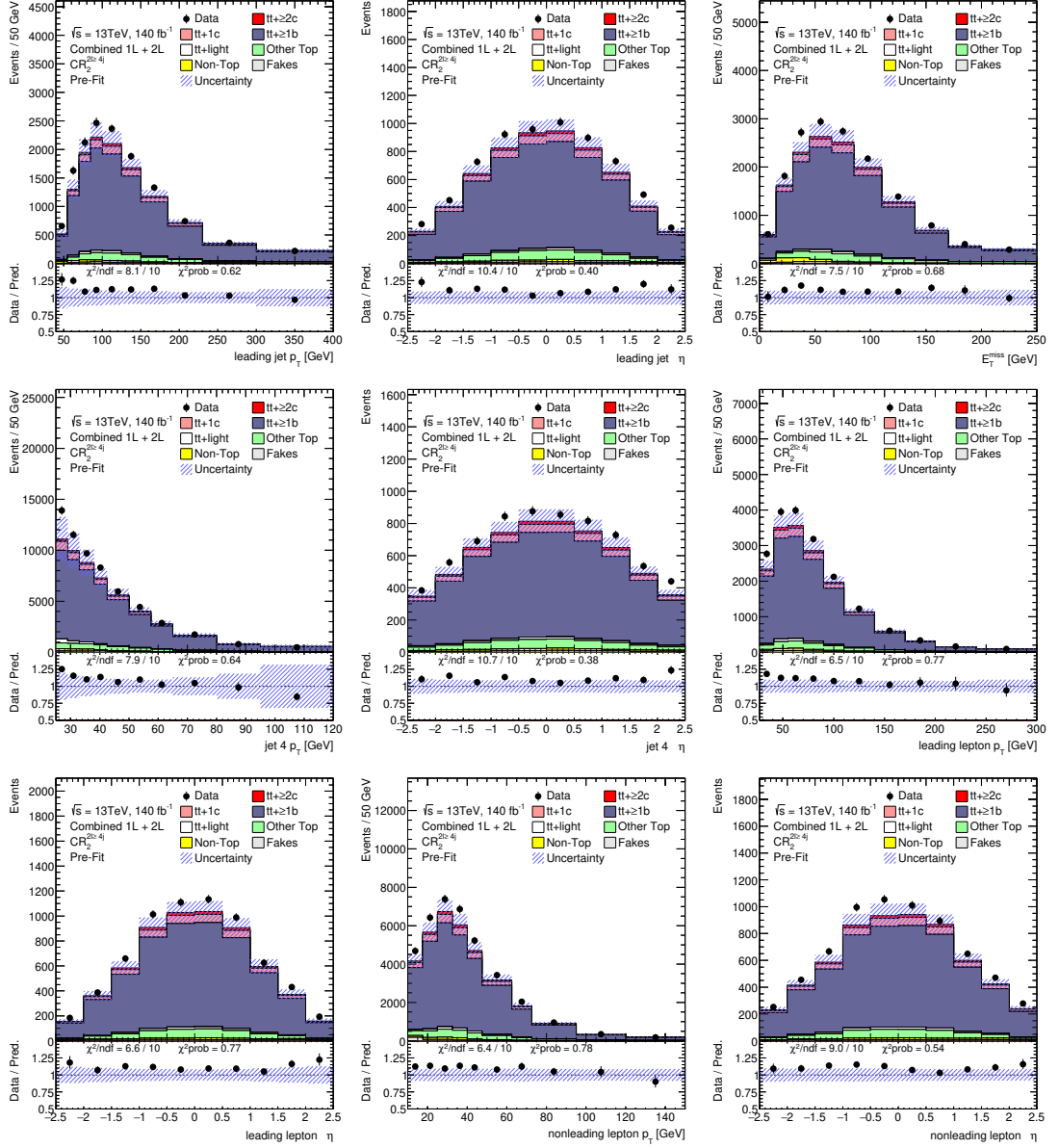


Figure D.16.: Pre-fit agreement between data and prediction for basic kinematic variables in $CR_2^{2\ell\geq 4j}$. The hashed band includes all prediction uncertainties. Overflow and underflow events are contained in the first and last bin respectively.

D.2. Pre-fit plots - dilepton channel

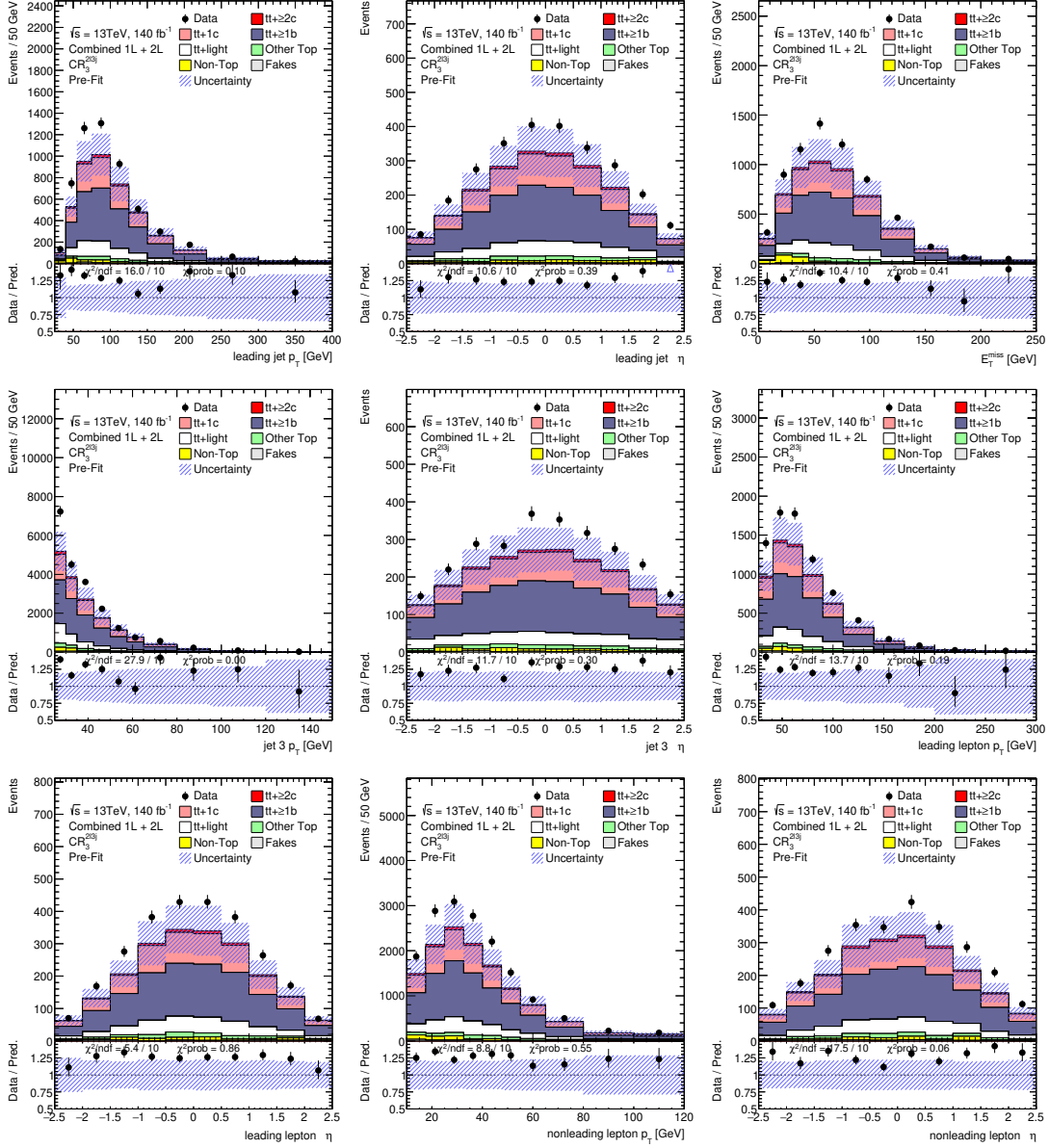


Figure D.17.: Pre-fit agreement between data and prediction for basic kinematic variables in $CR_3^{2\ell 3j}$. The hashed band includes all prediction uncertainties. Overflow and underflow events are contained in the first and last bin respectively.

D. Kinematics Control Plots

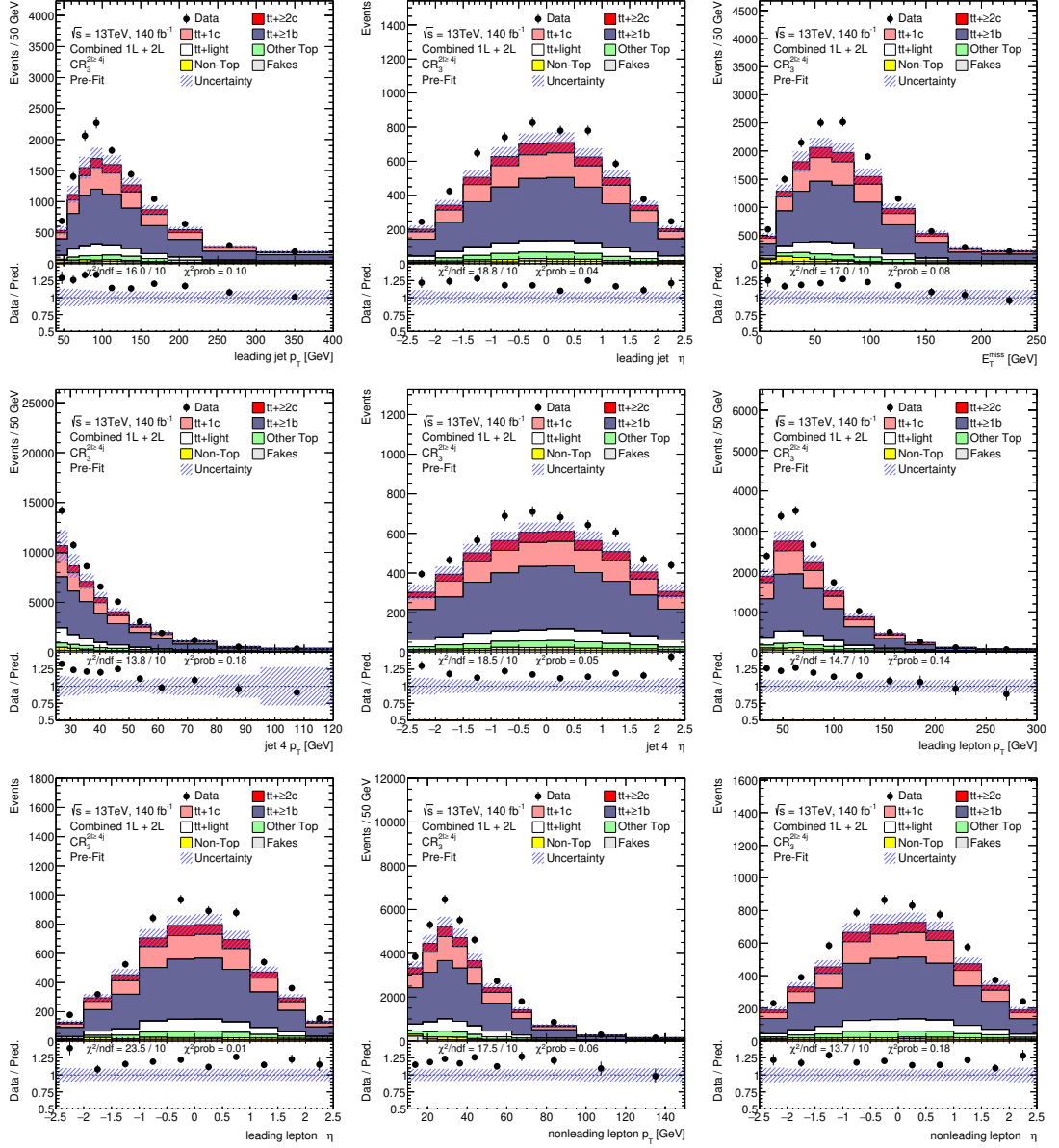


Figure D.18.: Pre-fit agreement between data and prediction for basic kinematic variables in $CR_3^{2\ell\geq 4j}$. The hashed band includes all prediction uncertainties. Overflow and underflow events are contained in the first and last bin respectively.

D.2. Pre-fit plots - dilepton channel

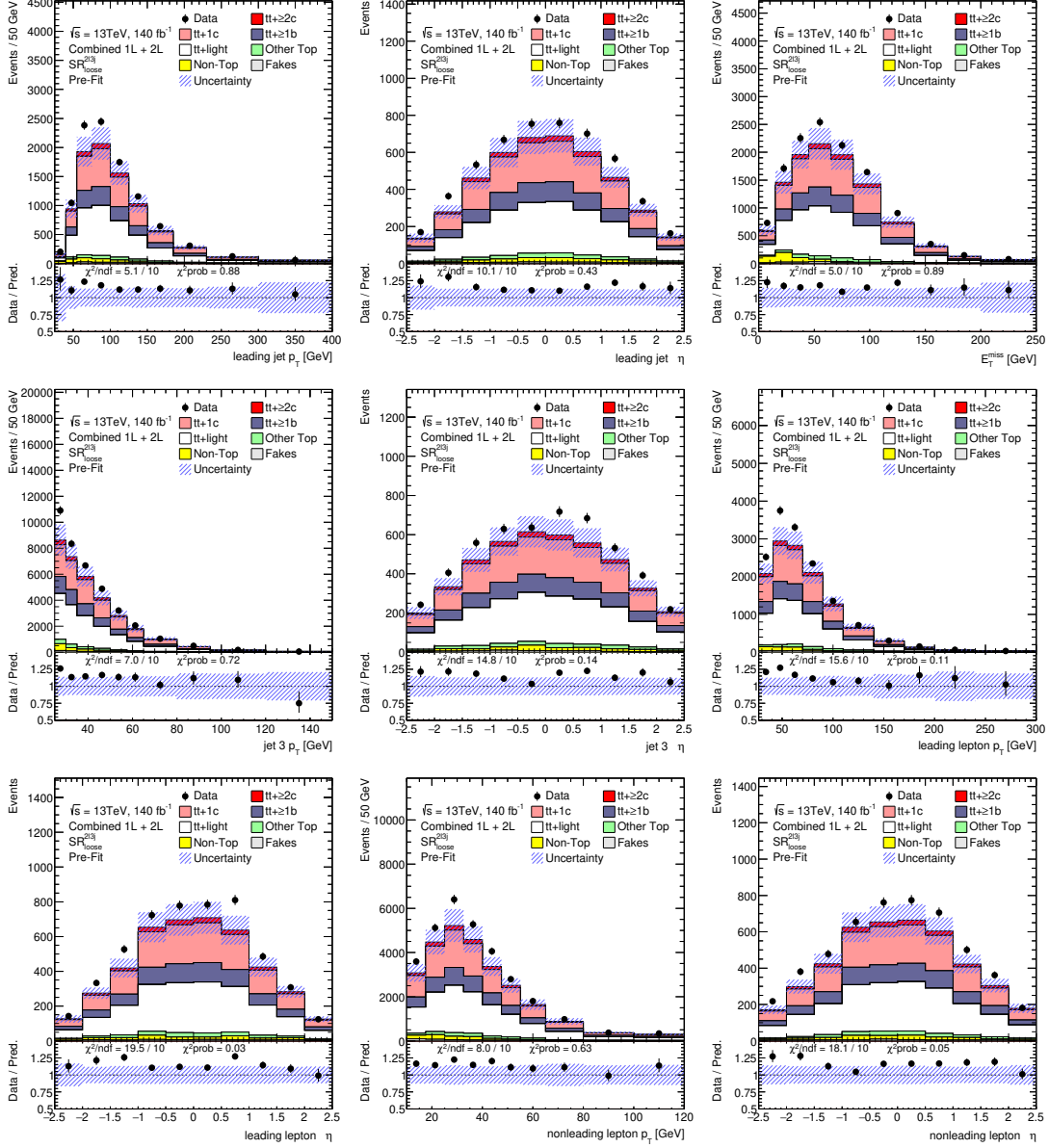


Figure D.19.: Pre-fit agreement between data and prediction for basic kinematic variables in $SR_{loose}^{2\ell 3j}$. The hashed band includes all prediction uncertainties. Overflow and underflow events are contained in the first and last bin respectively.

D. Kinematics Control Plots

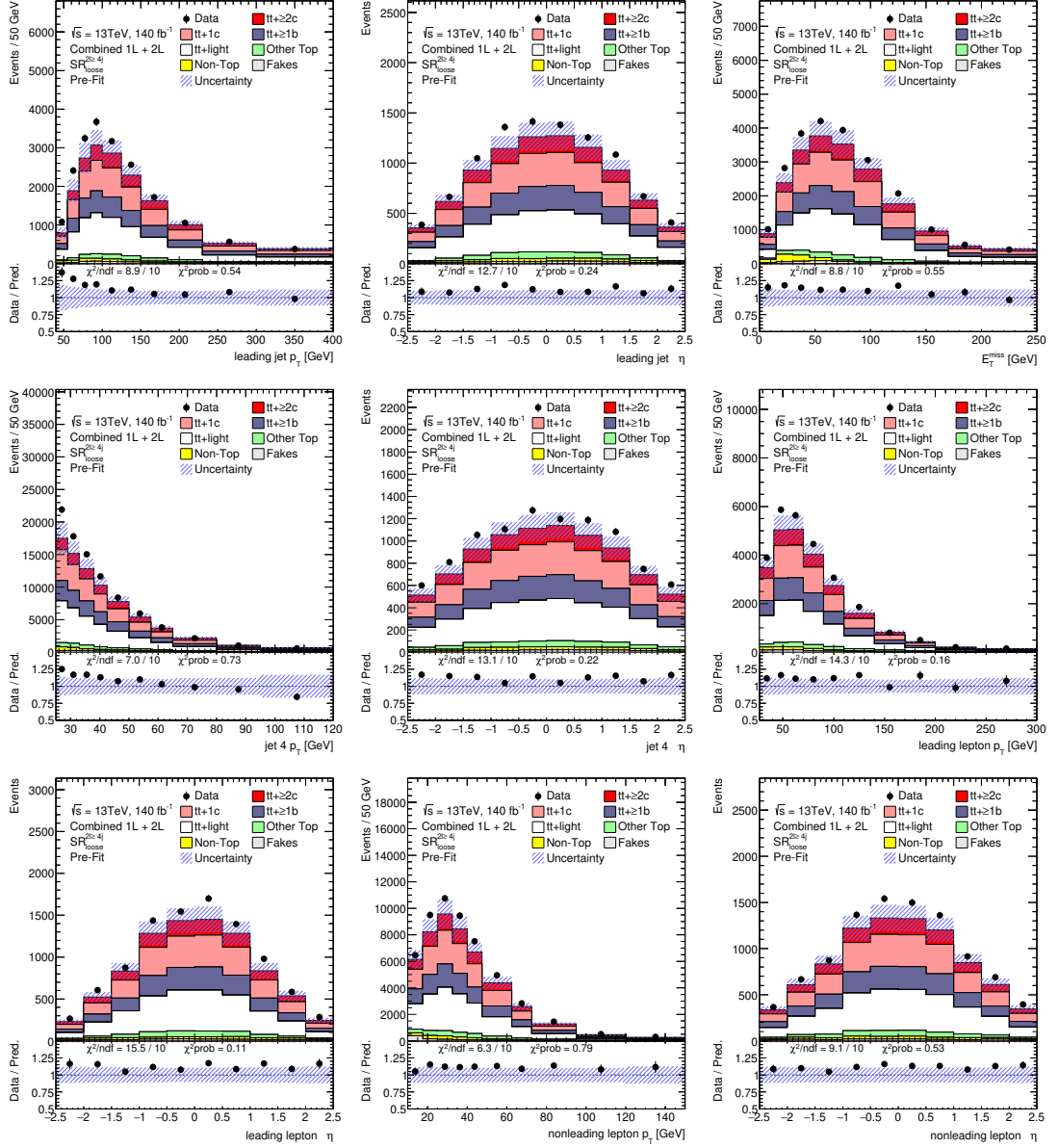


Figure D.20.: Pre-fit agreement between data and prediction for basic kinematic variables in $SR_{loose}^{2\ell \geq 4j}$. The hashed band includes all prediction uncertainties. Overflow and underflow events are contained in the first and last bin respectively.

D.2. Pre-fit plots - dilepton channel

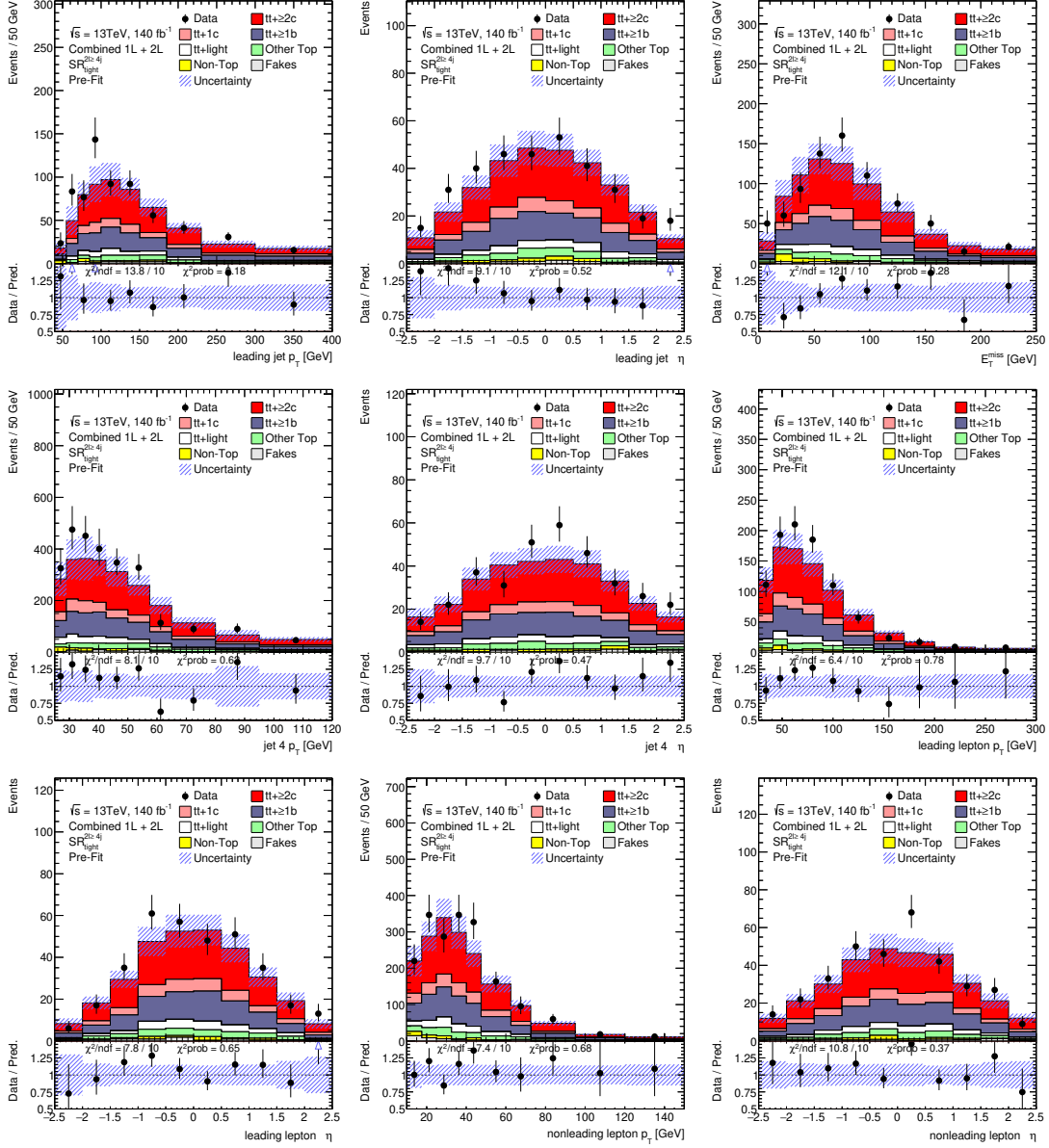


Figure D.21.: Pre-fit agreement between data and prediction for basic kinematic variables in $SR^{2\ell\geq 4j}_{\text{tight}}$. The hashed band includes all prediction uncertainties. Overflow and underflow events are contained in the first and last bin respectively.

D. Kinematics Control Plots

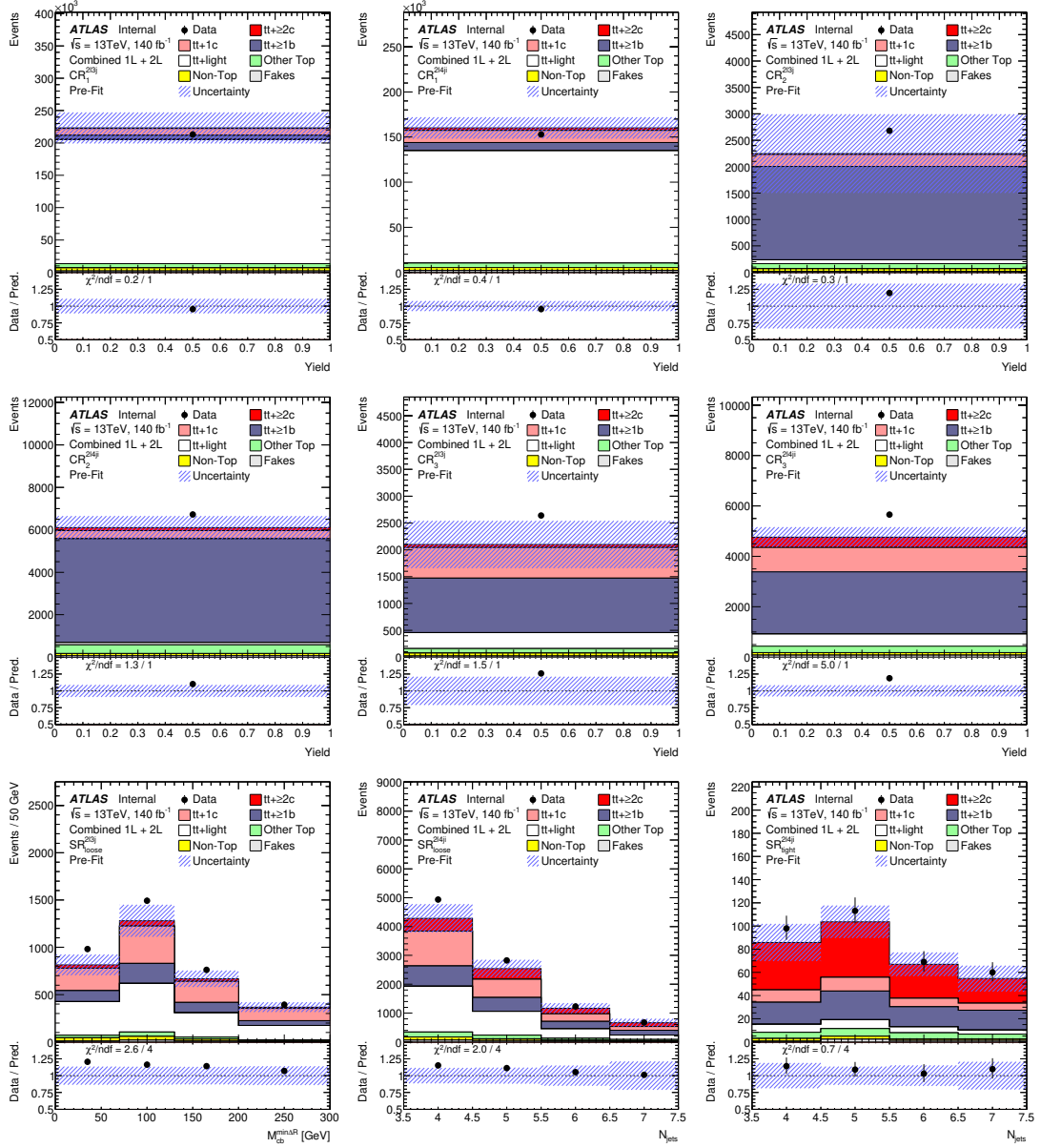


Figure D.22.: Pre-fit agreement between data and prediction for observables used in fitting in dilepton channel control and signal regions. The hashed band includes all prediction uncertainties. Overflow and underflow events are contained in the first and last bin respectively.

D.3. Post-fit plots - lepton + jets channel

D. Kinematics Control Plots

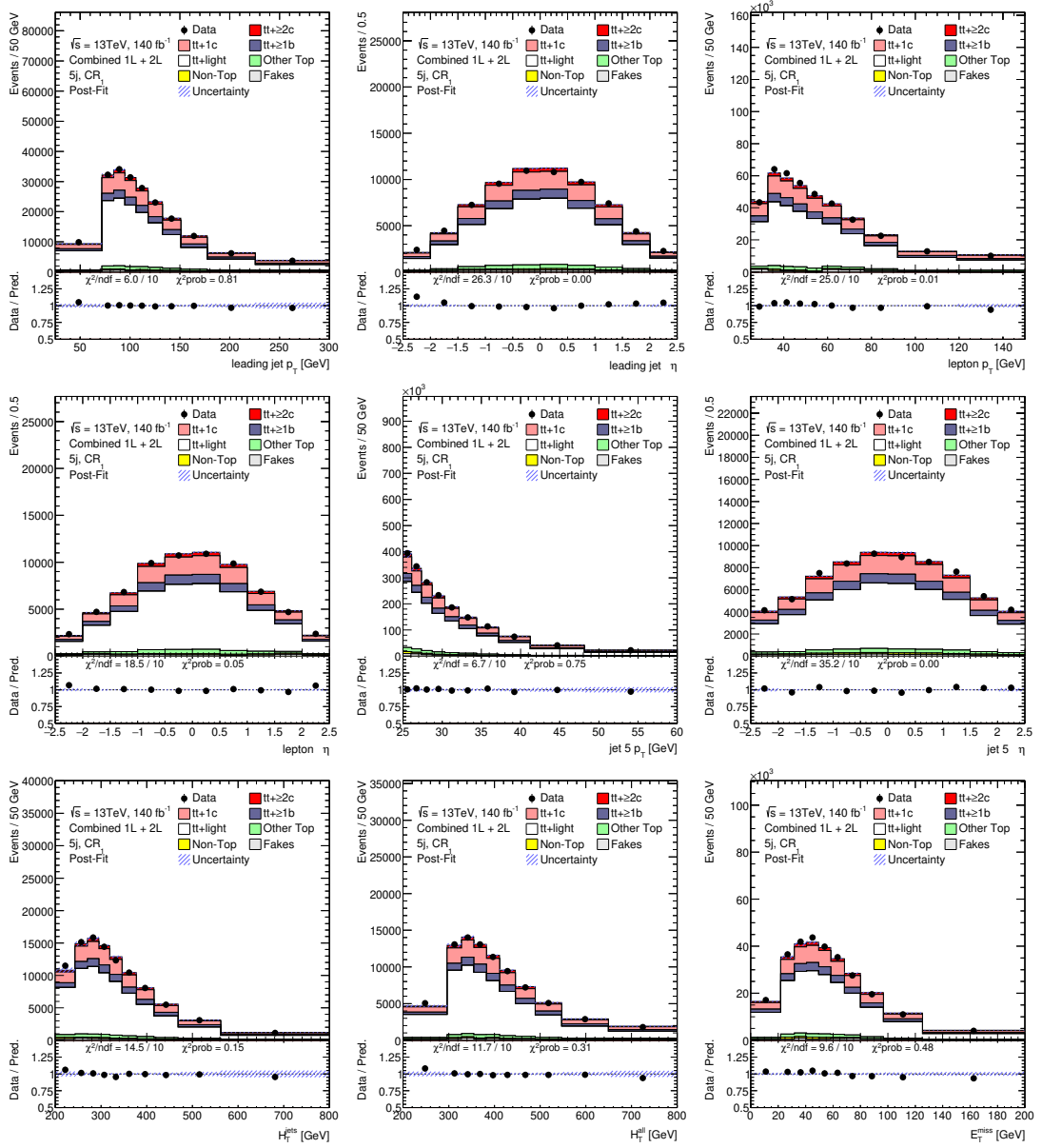


Figure D.23.: Post-fit agreement between data and prediction for basic kinematic variables in $\text{CR}_1^{1\ell5j}$. The hashed band includes all prediction uncertainties. Overflow and underflow events are contained in the first and last bin respectively.

D.3. Post-fit plots - lepton + jets channel

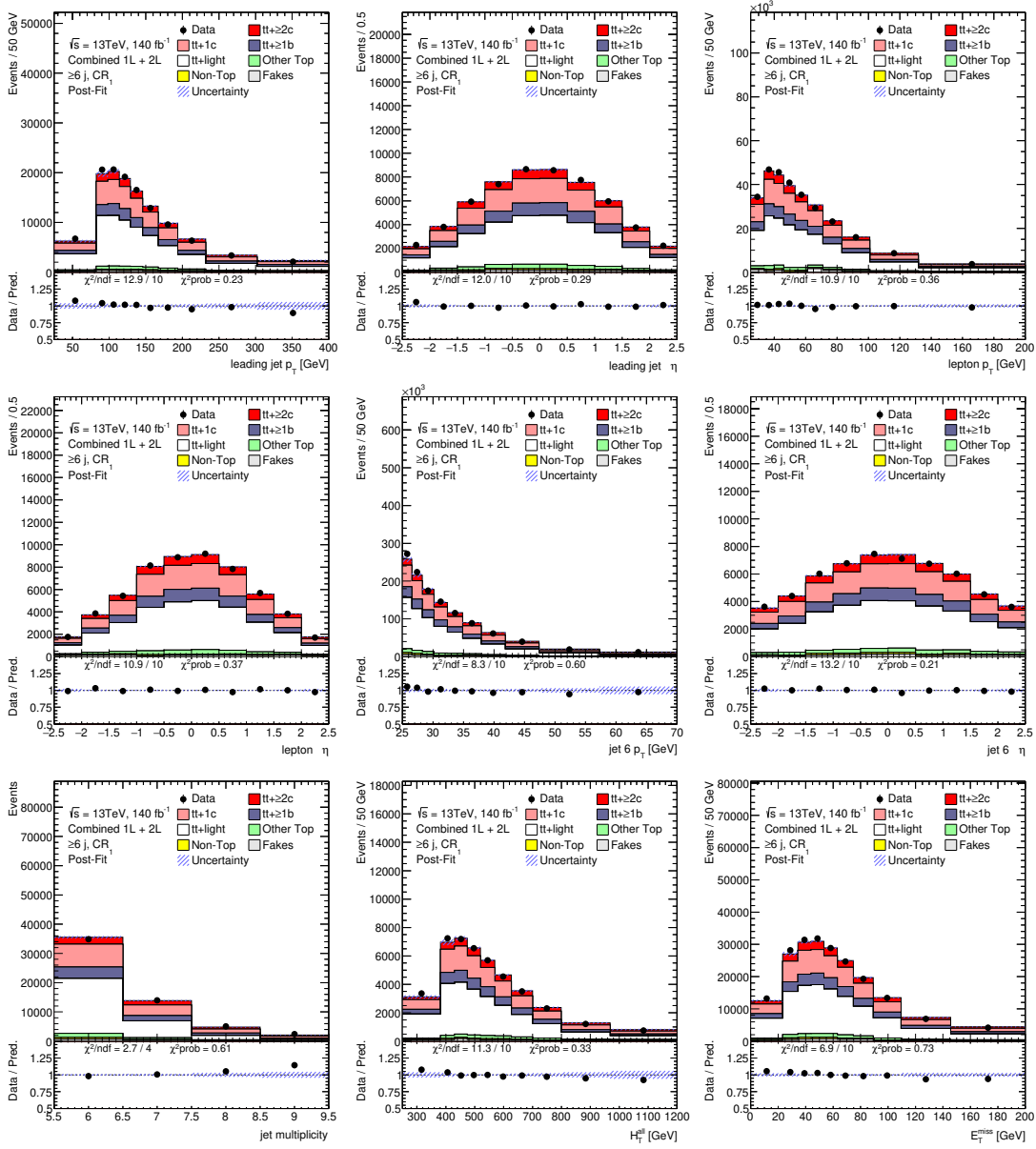


Figure D.24.: Post-fit agreement between data and prediction for basic kinematic variables in $CR_1^{l \geq 6j}$. The hashed band includes all prediction uncertainties. Overflow and underflow events are contained in the first and last bin respectively.

D. Kinematics Control Plots

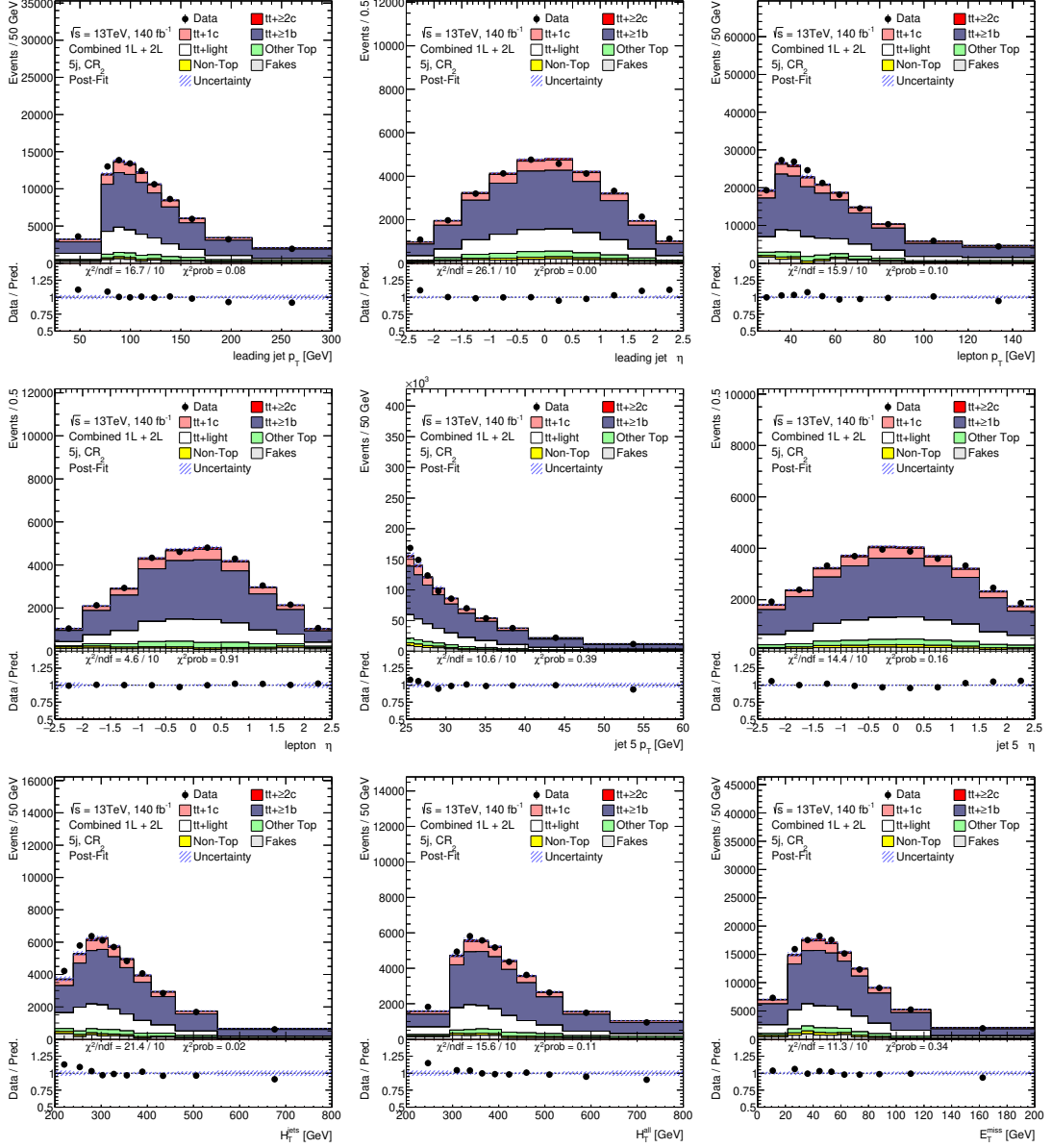


Figure D.25.: Post-fit agreement between data and prediction for basic kinematic variables in $\text{CR}_2^{1\ell5j}$. The hashed band includes all prediction uncertainties. Overflow and underflow events are contained in the first and last bin respectively.

D.3. Post-fit plots - lepton + jets channel

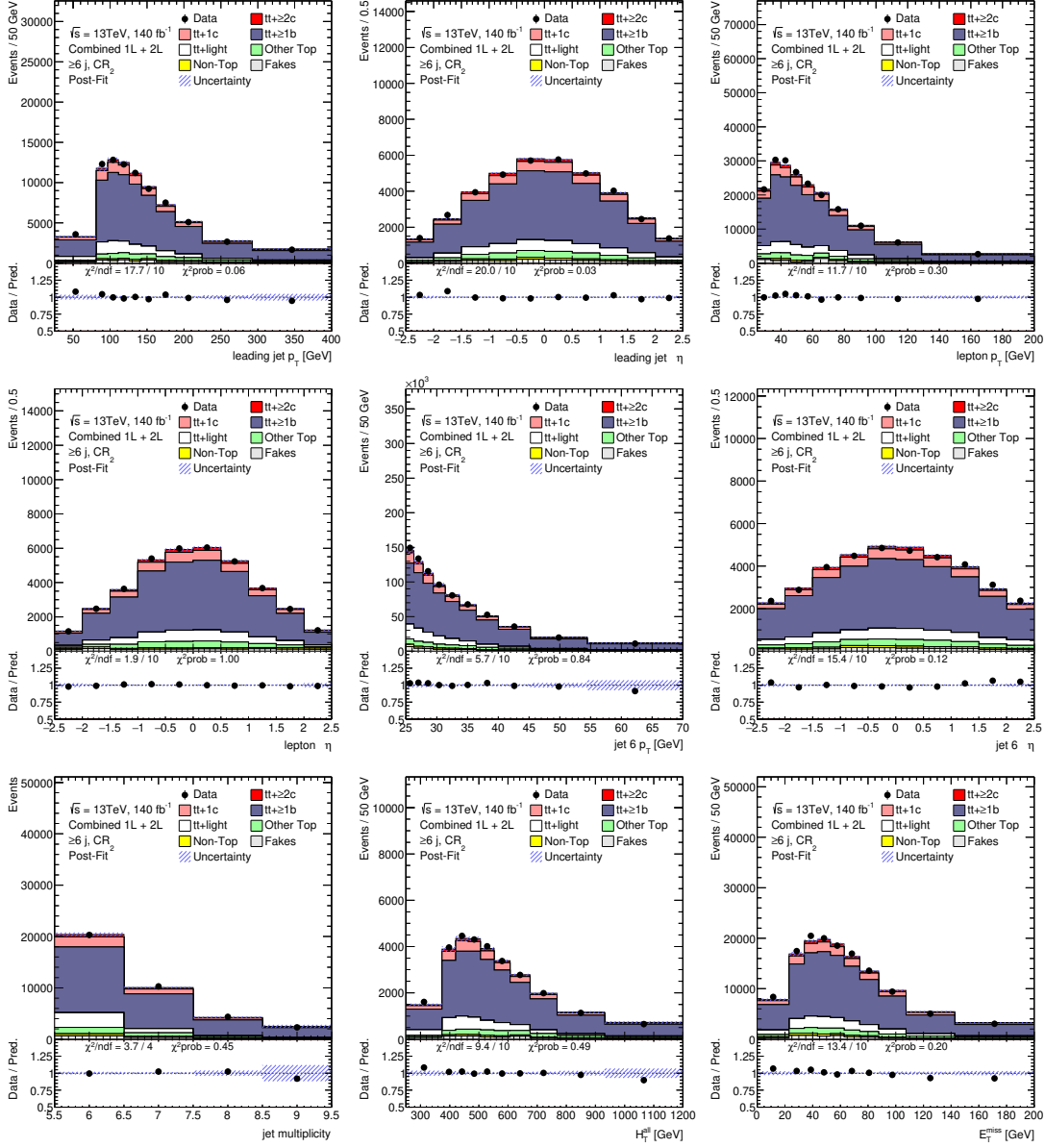


Figure D.26.: Post-fit agreement between data and prediction for basic kinematic variables in $\text{CR}_2^{1\ell\geq 6j}$. The hashed band includes all prediction uncertainties. Overflow and underflow events are contained in the first and last bin respectively.

D. Kinematics Control Plots

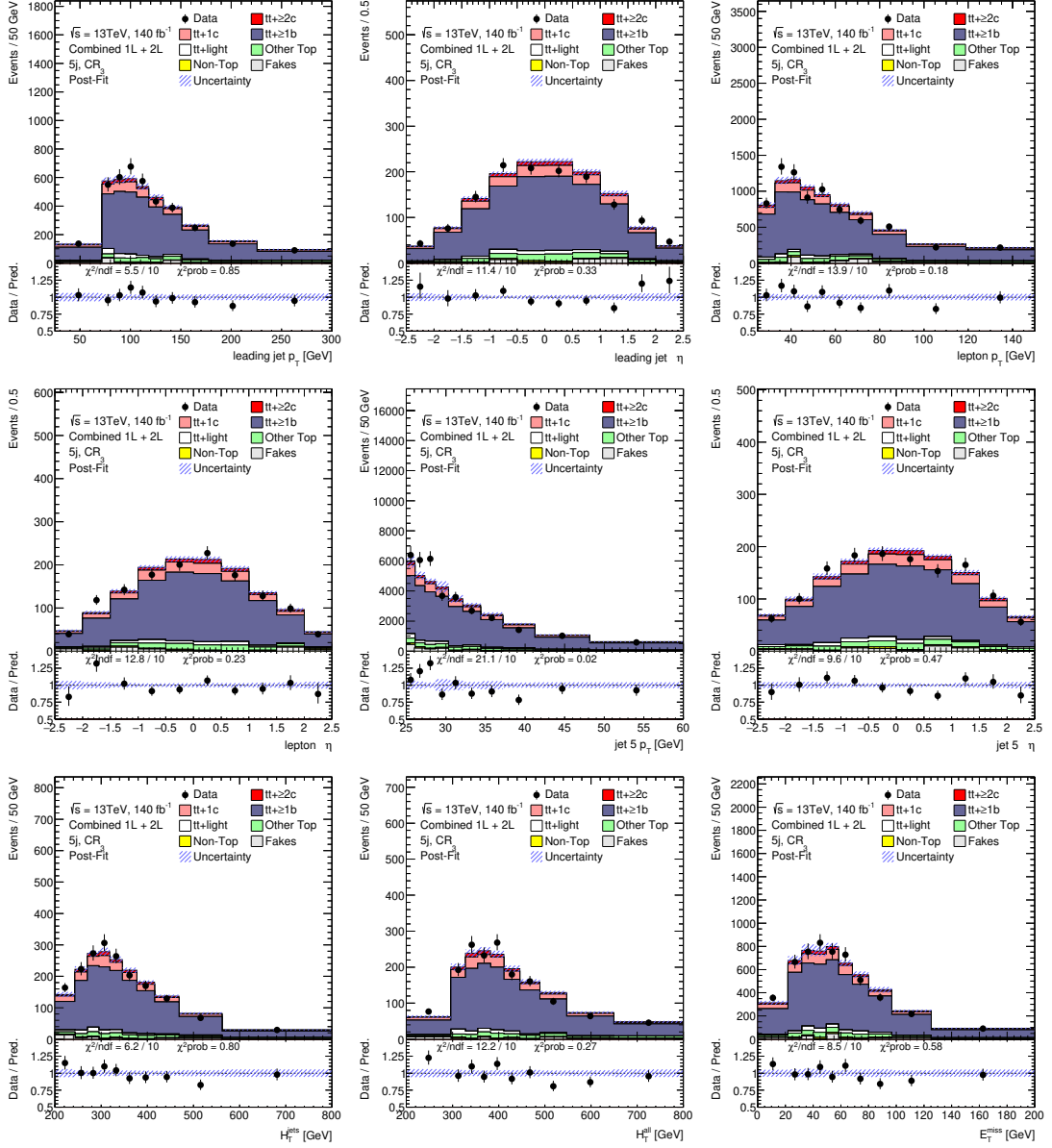


Figure D.27.: Post-fit agreement between data and prediction for basic kinematic variables in $CR_3^{1\ell5j}$. The hashed band includes all prediction uncertainties. Overflow and underflow events are contained in the first and last bin respectively.

D.3. Post-fit plots - lepton + jets channel

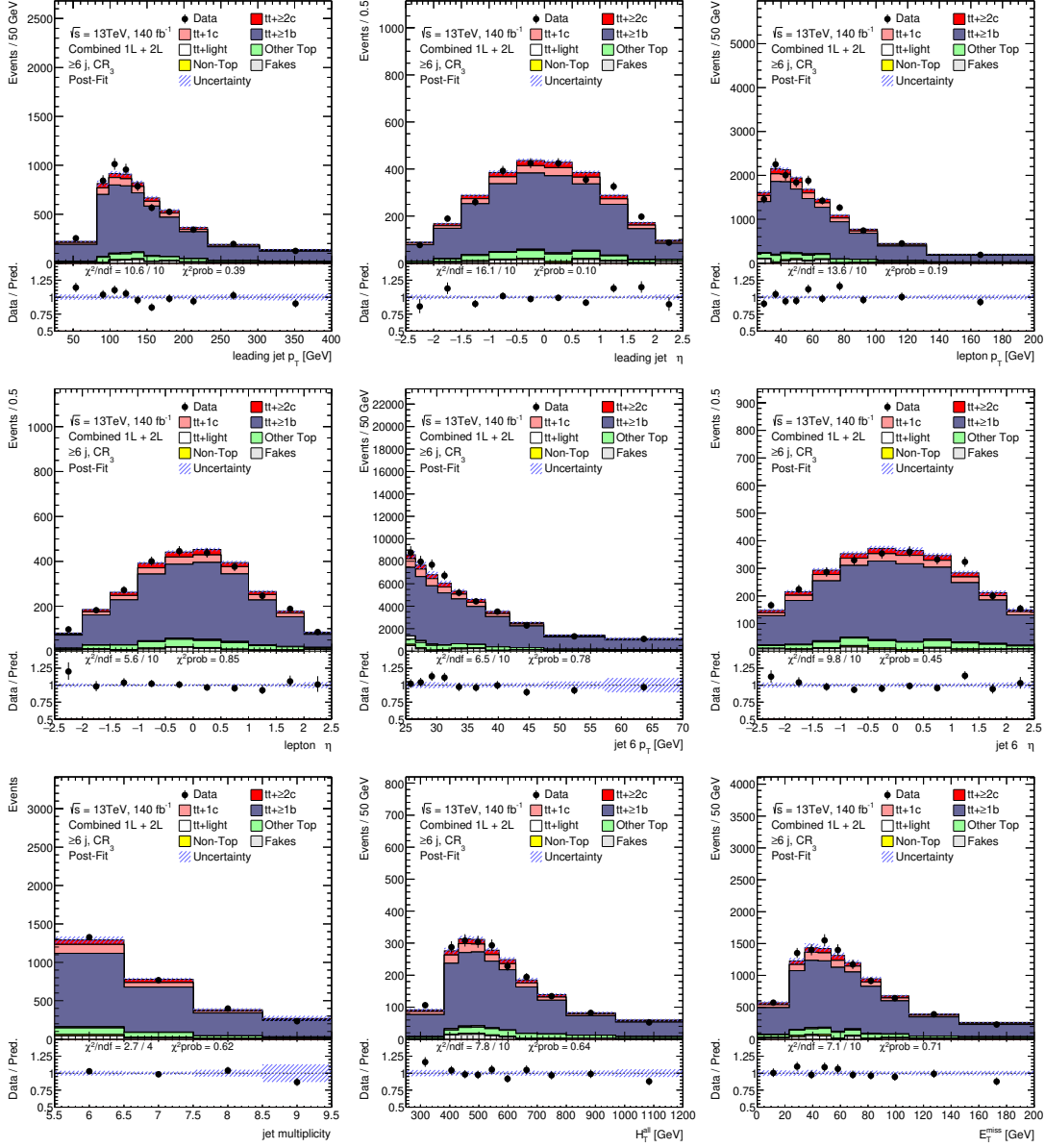


Figure D.28.: Post-fit agreement between data and prediction for basic kinematic variables in $CR_3^{1\ell \geq 6j}$. The hashed band includes all prediction uncertainties. Overflow and underflow events are contained in the first and last bin respectively.

D. Kinematics Control Plots

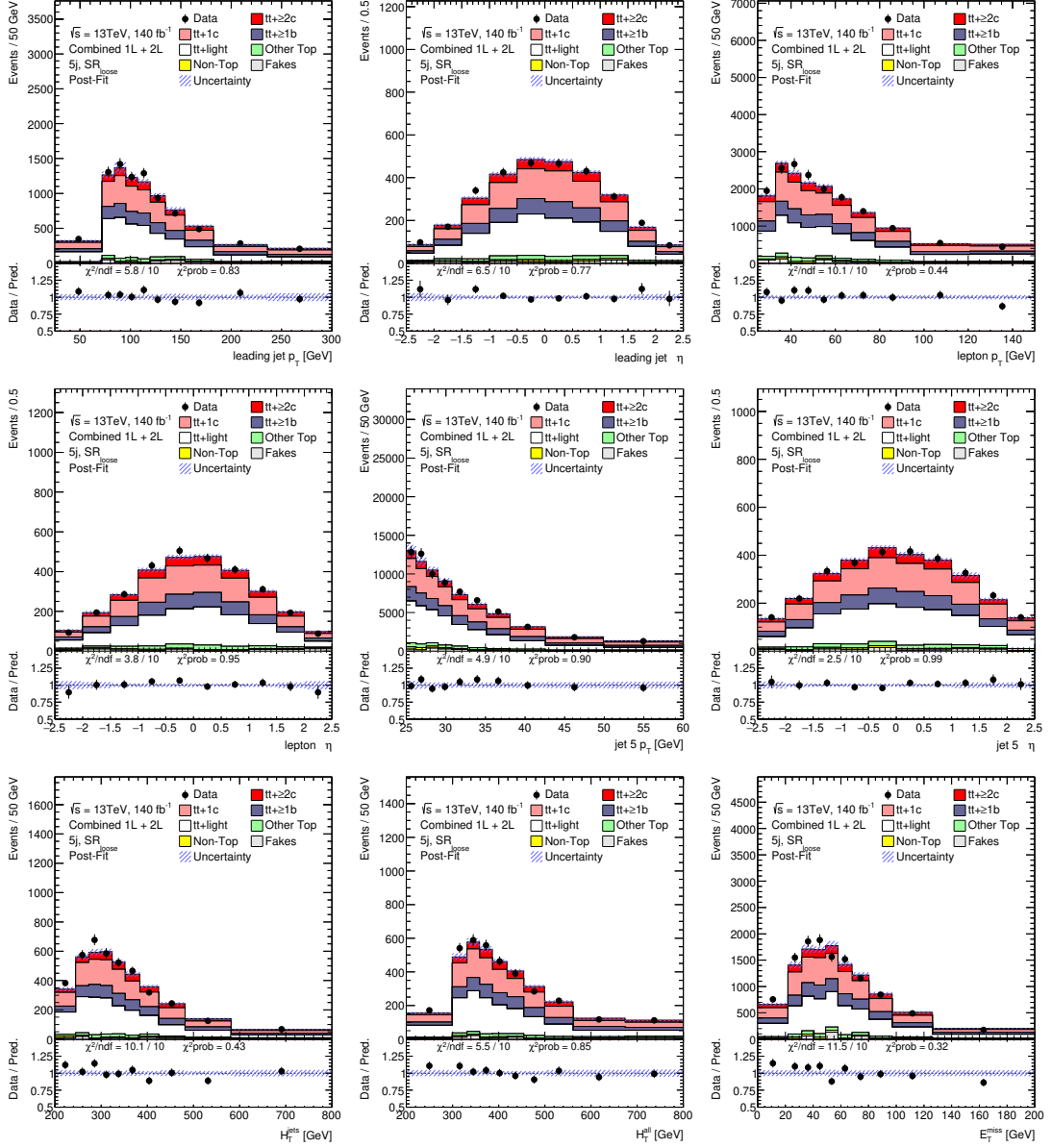


Figure D.29.: Post-fit agreement between data and prediction for basic kinematic variables in $\text{SR}_{\text{loose}}^{1\ell 5j}$. The hashed band includes all prediction uncertainties. Overflow and underflow events are contained in the first and last bin respectively.

D.3. Post-fit plots - lepton + jets channel

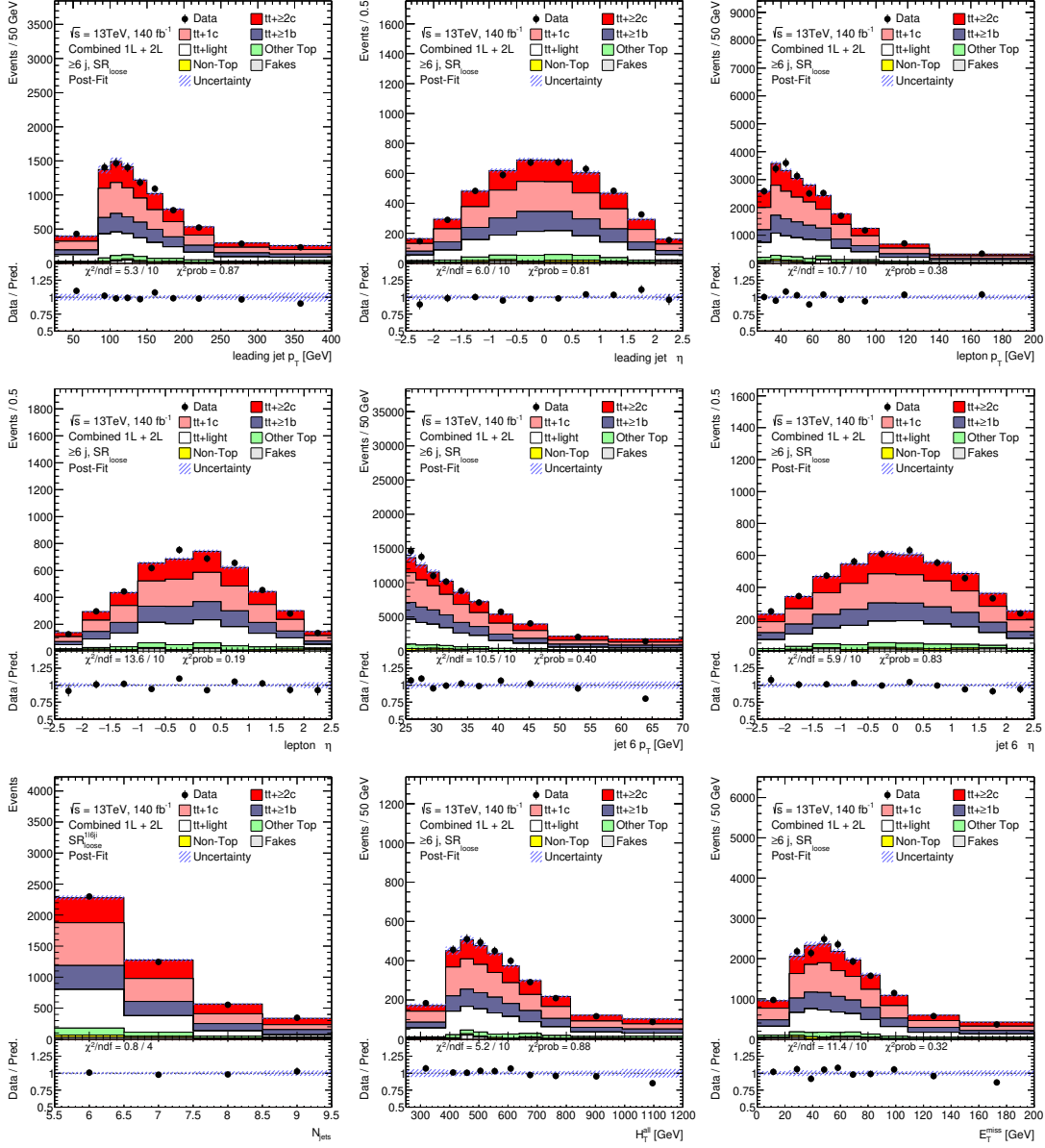


Figure D.30.: Post-fit agreement between data and prediction for basic kinematic variables in $\text{SR}_{\text{loose}}^{1\ell \geq 6j}$. The hashed band includes all prediction uncertainties. Overflow and underflow events are contained in the first and last bin respectively.

D. Kinematics Control Plots

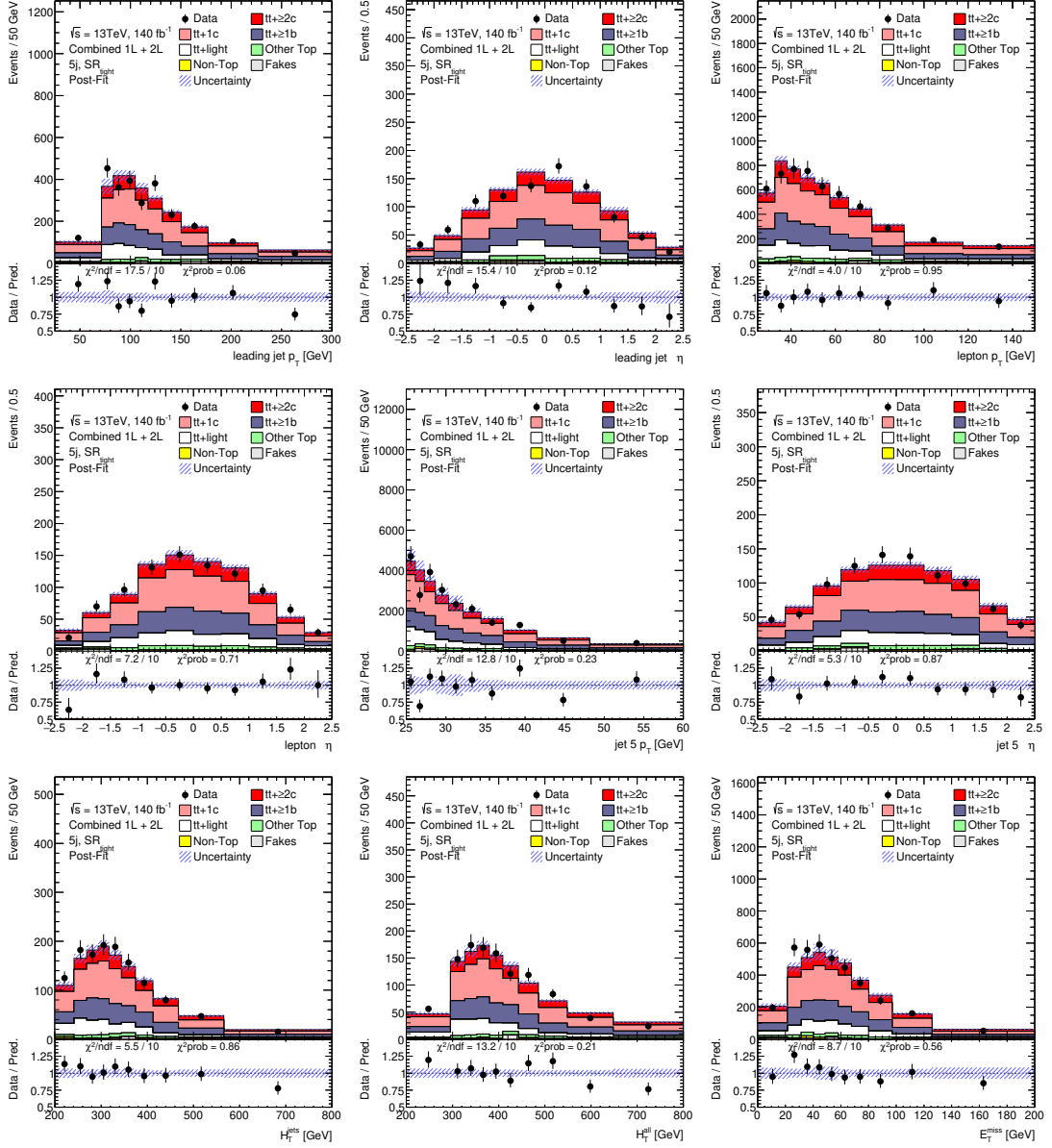


Figure D.31.: Post-fit agreement between data and prediction for basic kinematic variables in $SR_{tight}^{1\ell 5j}$. The hashed band includes all prediction uncertainties. Overflow and underflow events are contained in the first and last bin respectively.

D.3. Post-fit plots - lepton + jets channel

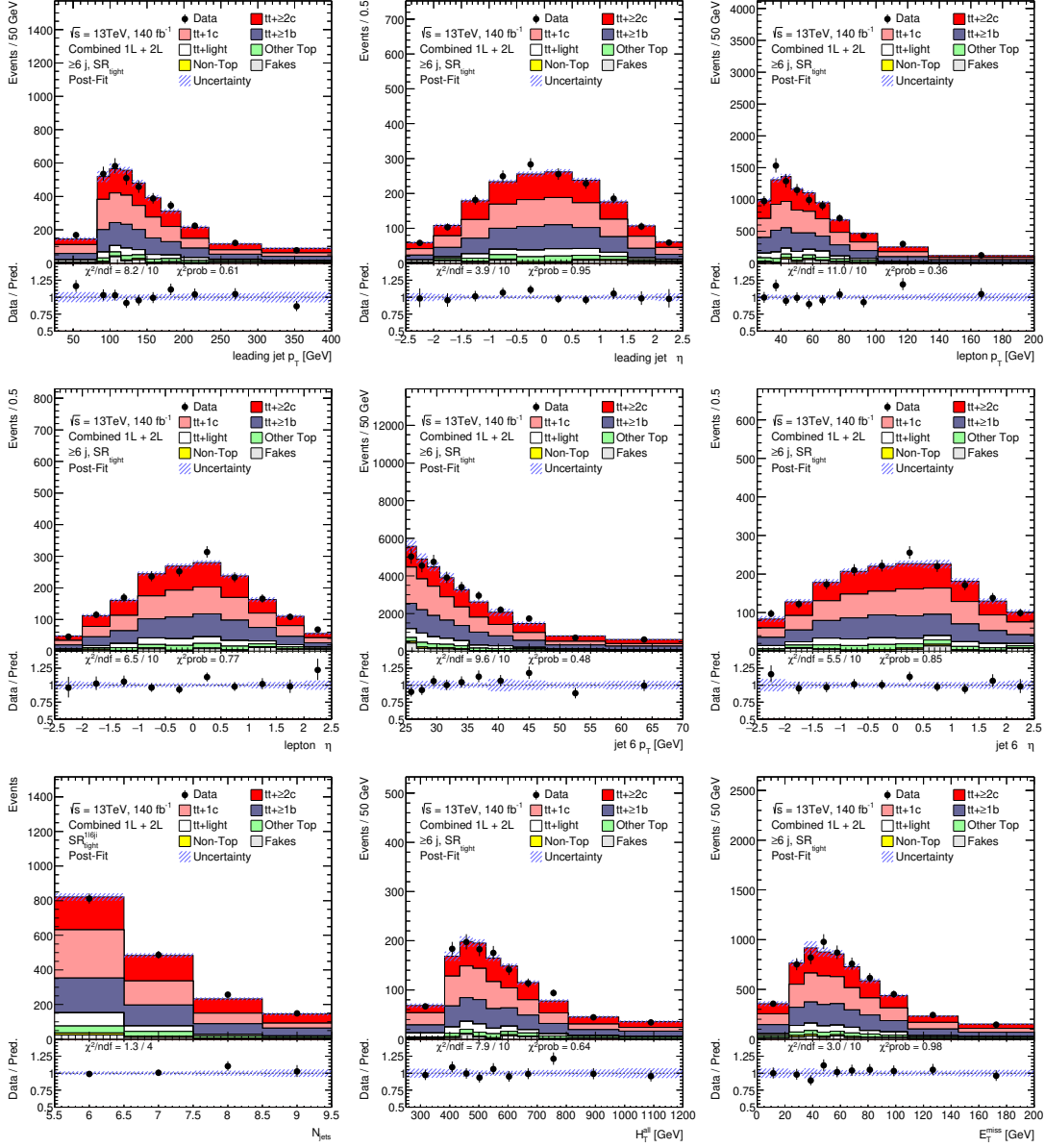


Figure D.32.: Post-fit agreement between data and prediction for basic kinematic variables in $SR_{tight}^{1\ell \ge 6j}$. The hashed band includes all prediction uncertainties. Overflow and underflow events are contained in the first and last bin respectively.

D. Kinematics Control Plots

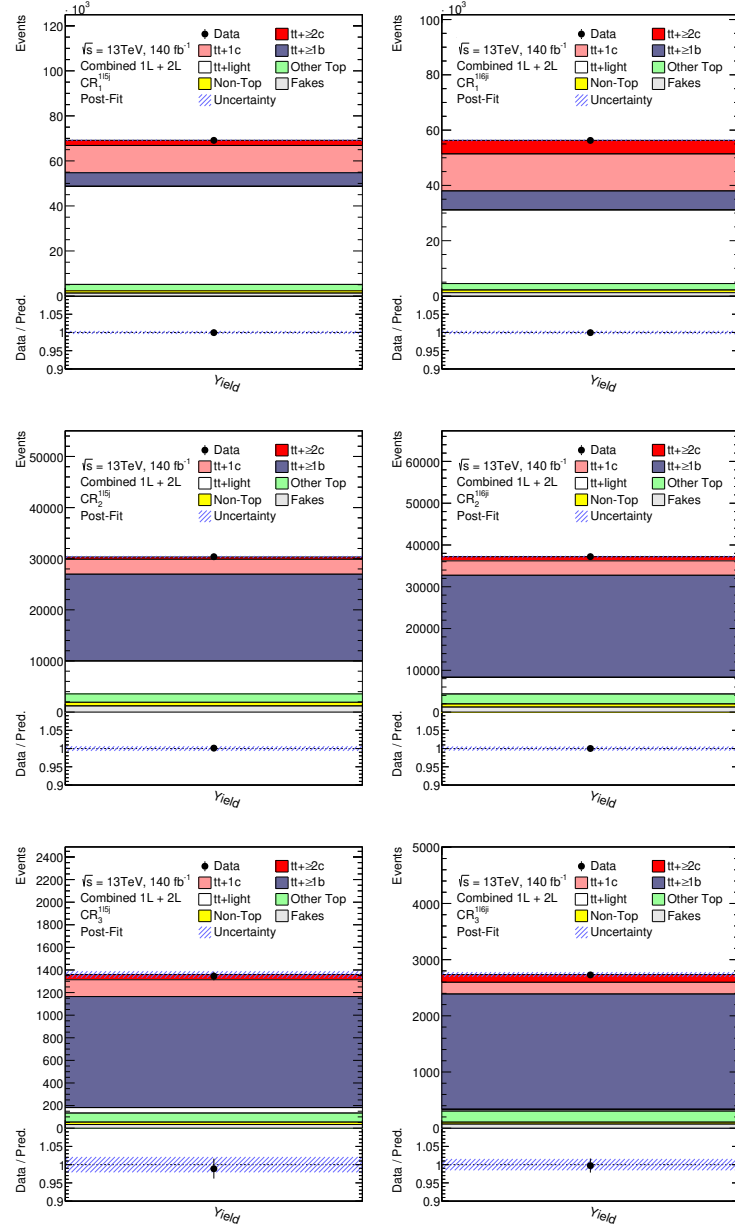


Figure D.33.: Post-fit agreement between data and prediction for observables used in fitting in lepton + jets channel control regions. The hashed band includes all prediction uncertainties.

D.3. Post-fit plots - lepton + jets channel

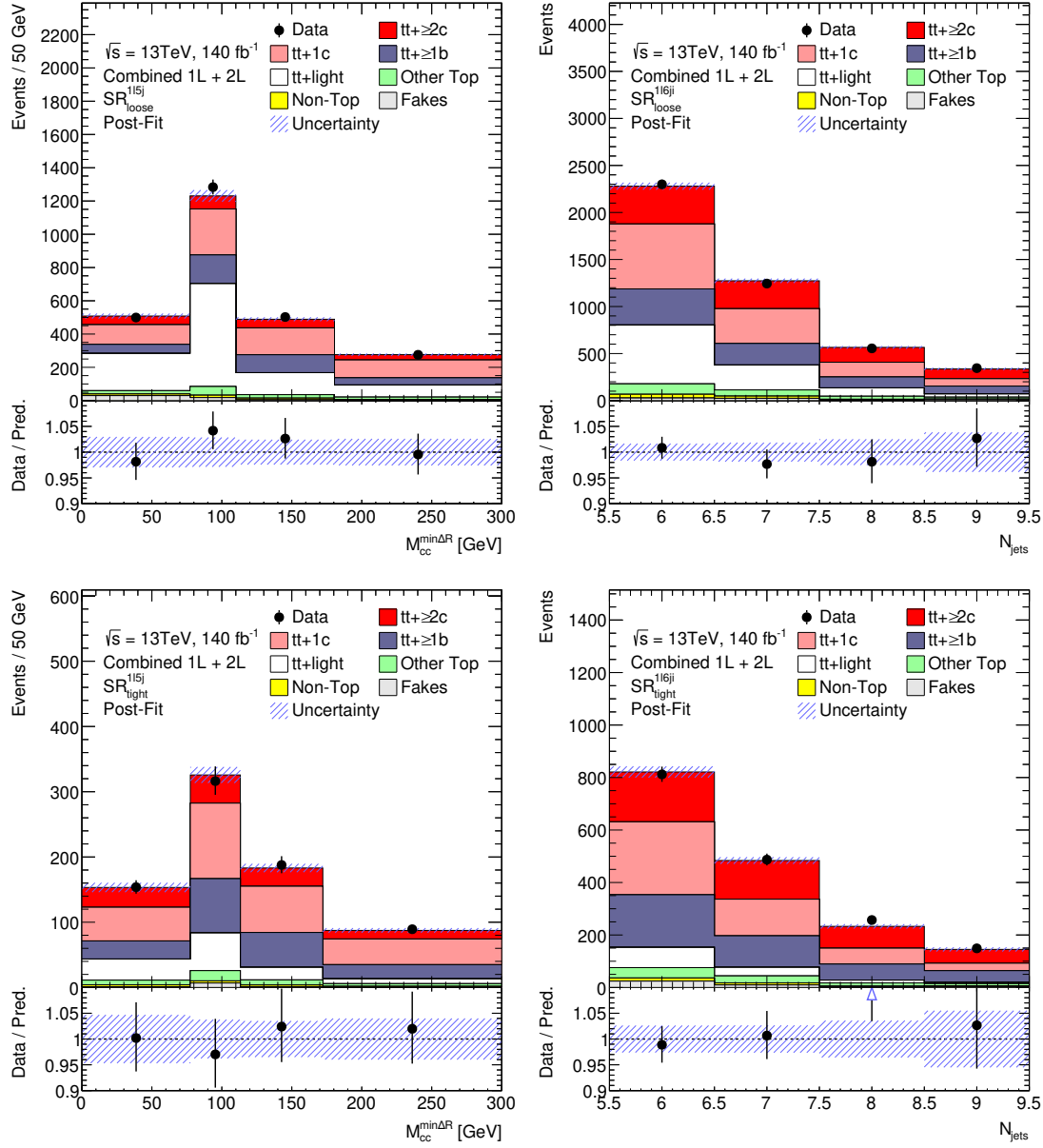


Figure D.34.: Post-fit agreement between data and prediction for observables used in fitting in lepton + jets channel signal regions. The hashed band includes all prediction uncertainties. Overflow and underflow events are contained in the first and last bin respectively.

D.4. Post-fit plots - dilepton channel

D.4. Post-fit plots - dilepton channel

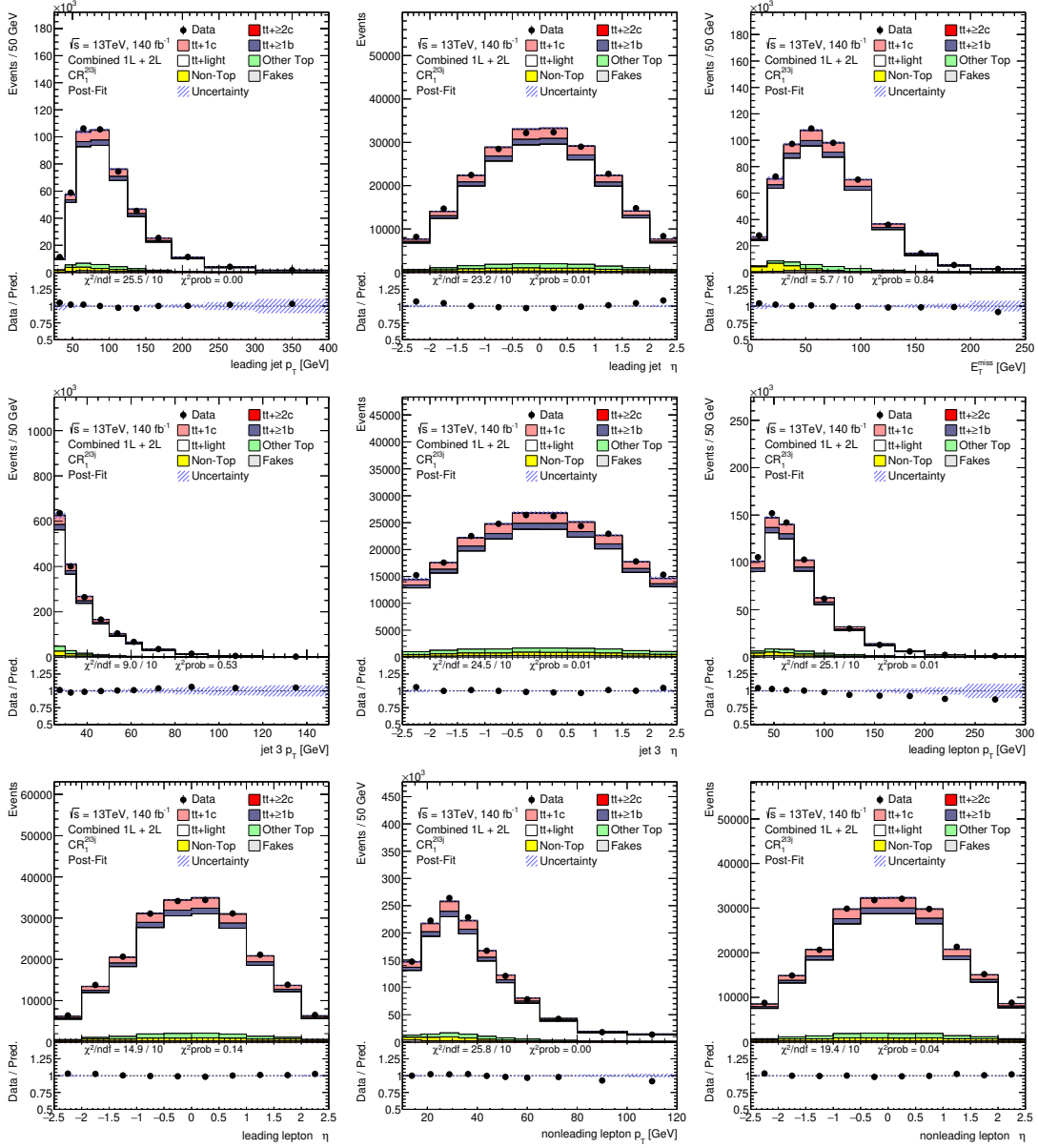


Figure D.35.: Post-fit agreement between data and prediction for basic kinematic variables in $CR_1^{2\ell 3j}$. The hashed band includes all prediction uncertainties. Overflow and underflow events are contained in the first and last bin respectively.

D. Kinematics Control Plots

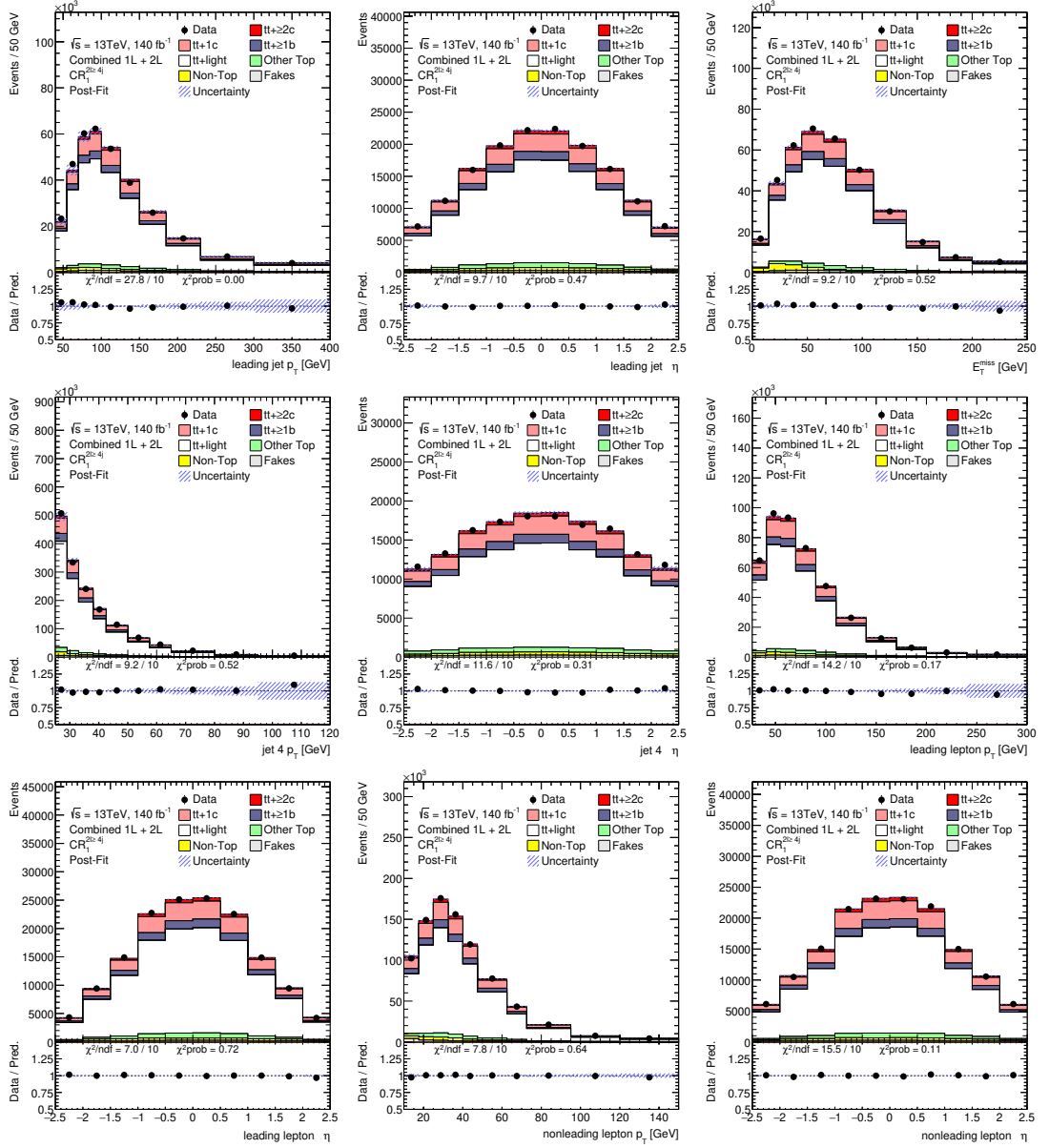


Figure D.36.: Post-fit agreement between data and prediction for basic kinematic variables in $CR_1^{2\ell\geq 4j}$. The hashed band includes all prediction uncertainties. Overflow and underflow events are contained in the first and last bin respectively.

D.4. Post-fit plots - dilepton channel

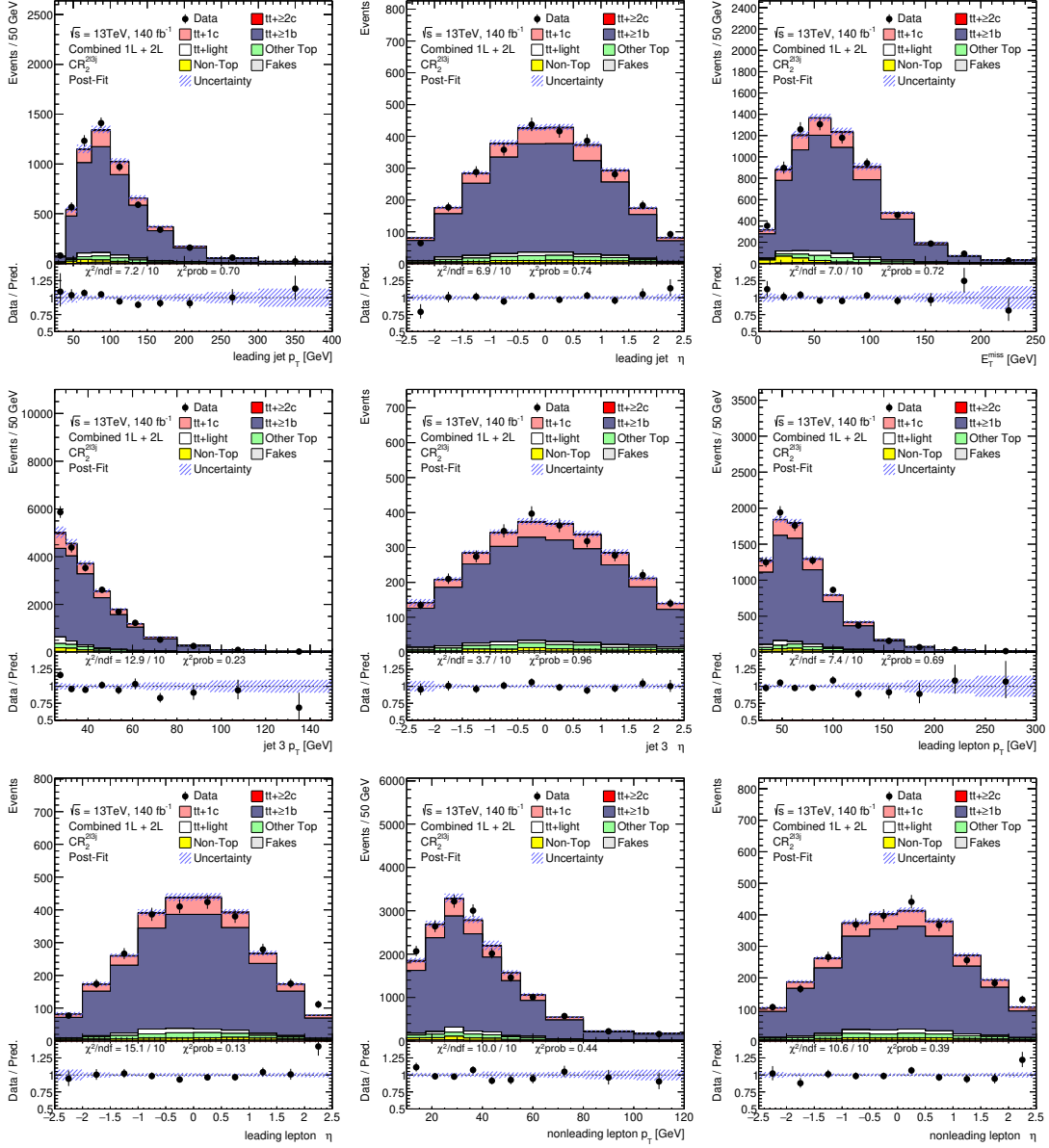


Figure D.37.: Post-fit agreement between data and prediction for basic kinematic variables in $CR_2^{2\ell 3j}$. The hashed band includes all prediction uncertainties. Overflow and underflow events are contained in the first and last bin respectively.

D. Kinematics Control Plots

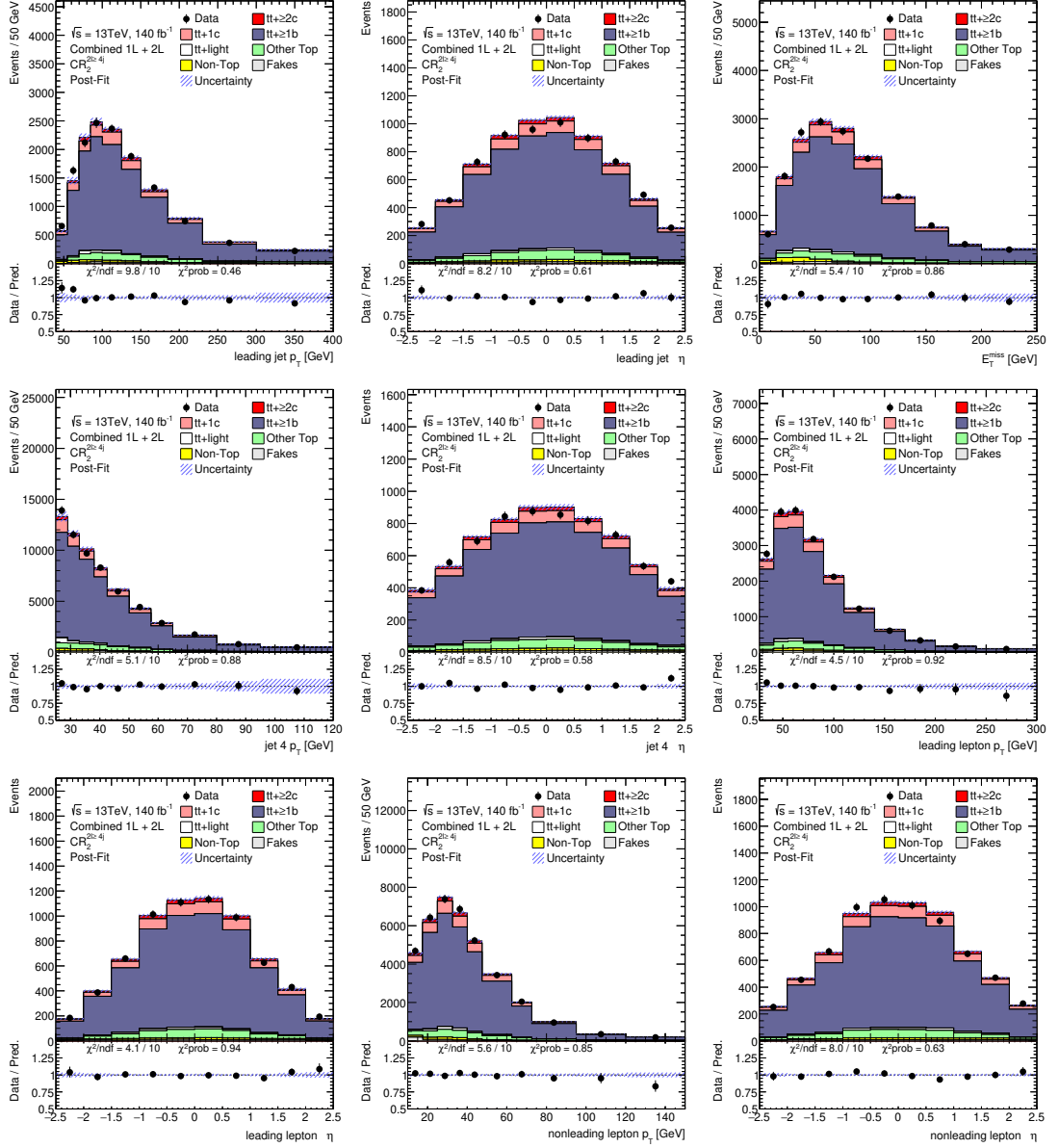


Figure D.38.: Post-fit agreement between data and prediction for basic kinematic variables in $CR_2^{2\ell\geq 4j}$. The hashed band includes all prediction uncertainties. Overflow and underflow events are contained in the first and last bin respectively.

D.4. Post-fit plots - dilepton channel

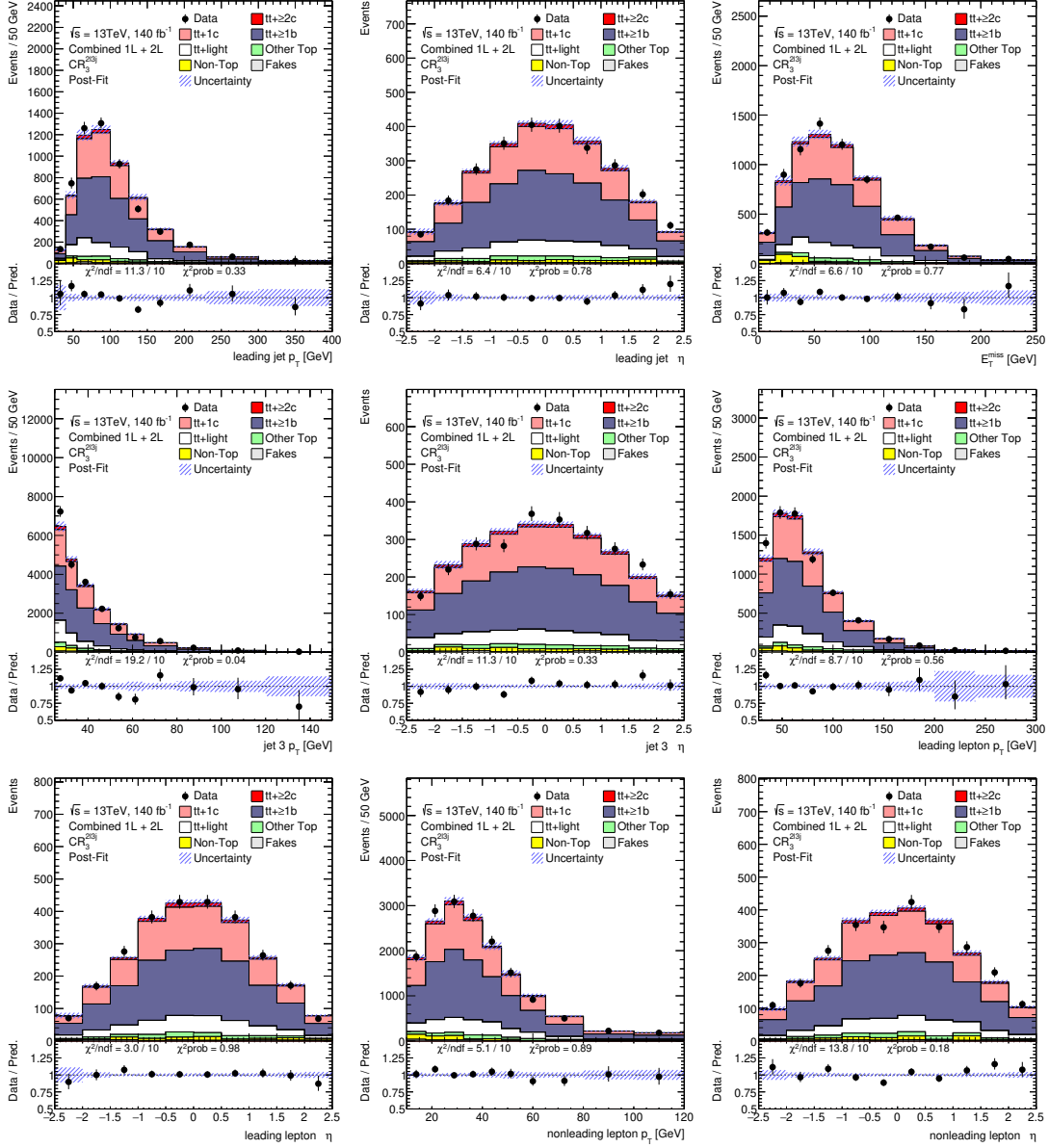


Figure D.39.: Post-fit agreement between data and prediction for basic kinematic variables in $CR_3^{2\ell 3j}$. The hashed band includes all prediction uncertainties. Overflow and underflow events are contained in the first and last bin respectively.

D. Kinematics Control Plots

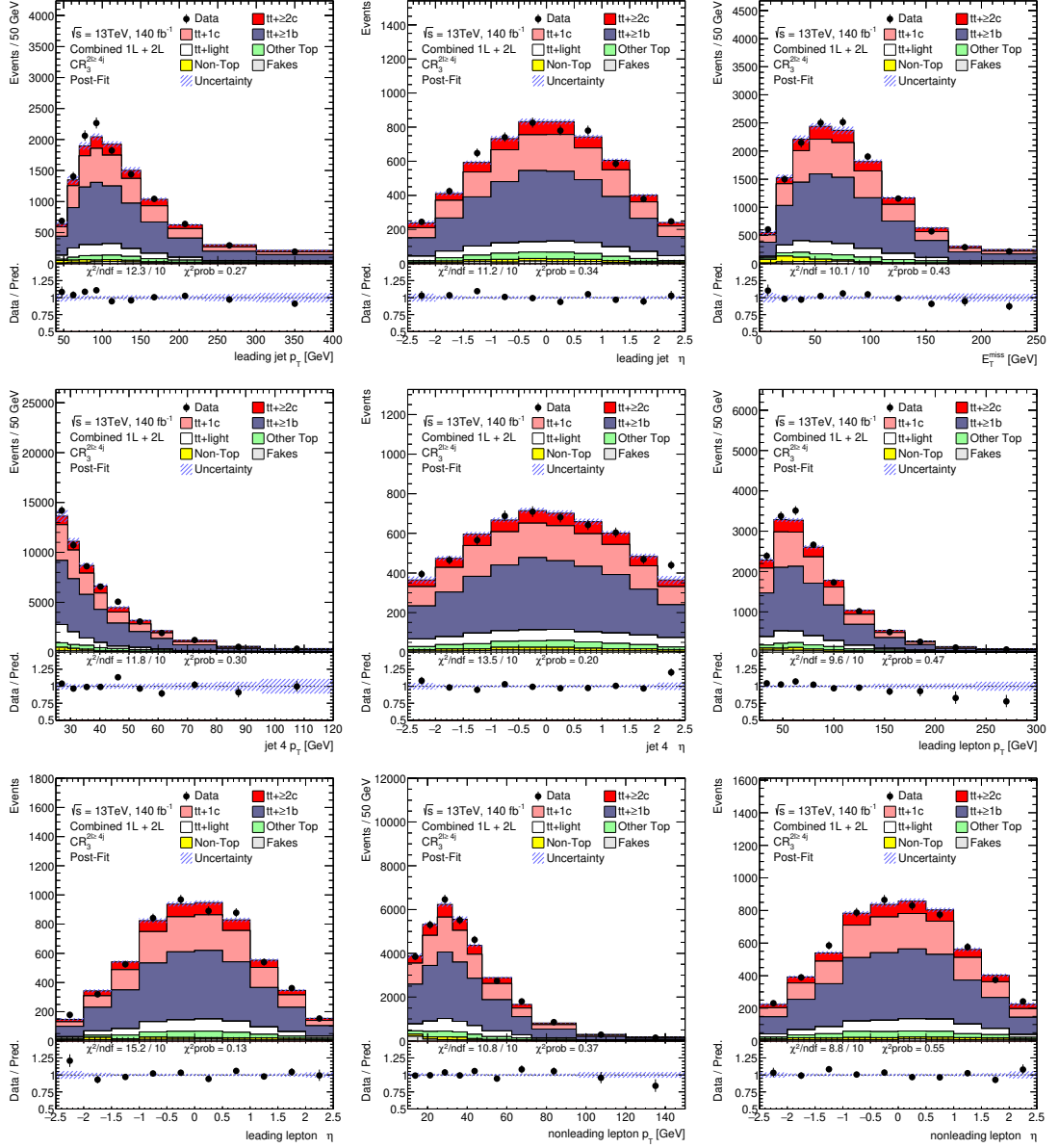


Figure D.40.: Post-fit agreement between data and prediction for basic kinematic variables in $CR_3^{2\ell\geq 4j}$. The hashed band includes all prediction uncertainties. Overflow and underflow events are contained in the first and last bin respectively.

D.4. Post-fit plots - dilepton channel

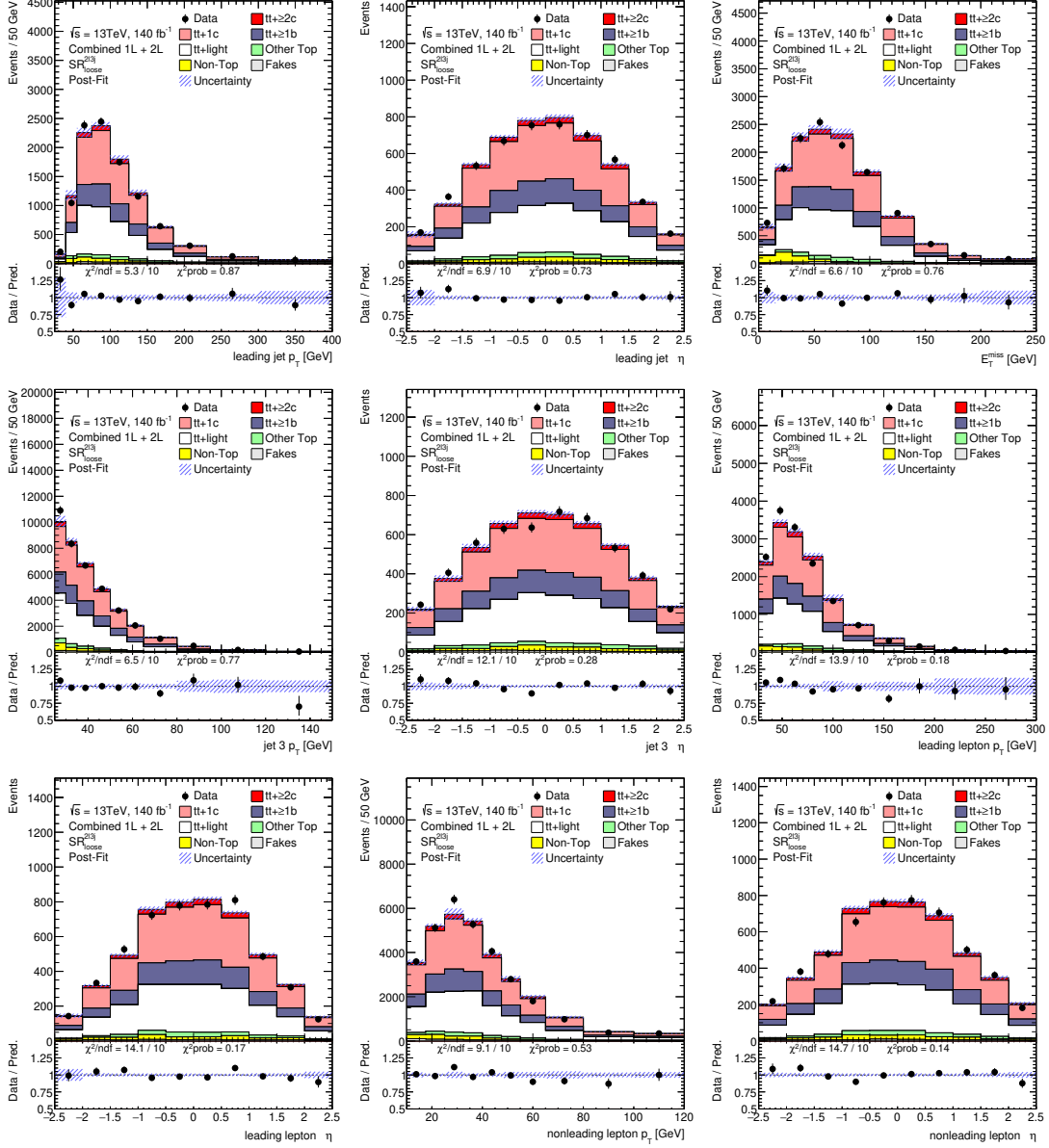


Figure D.41.: Post-fit agreement between data and prediction for basic kinematic variables in $SR_{loose}^{2\ell 3j}$. The hashed band includes all prediction uncertainties. Overflow and underflow events are contained in the first and last bin respectively.

D. Kinematics Control Plots

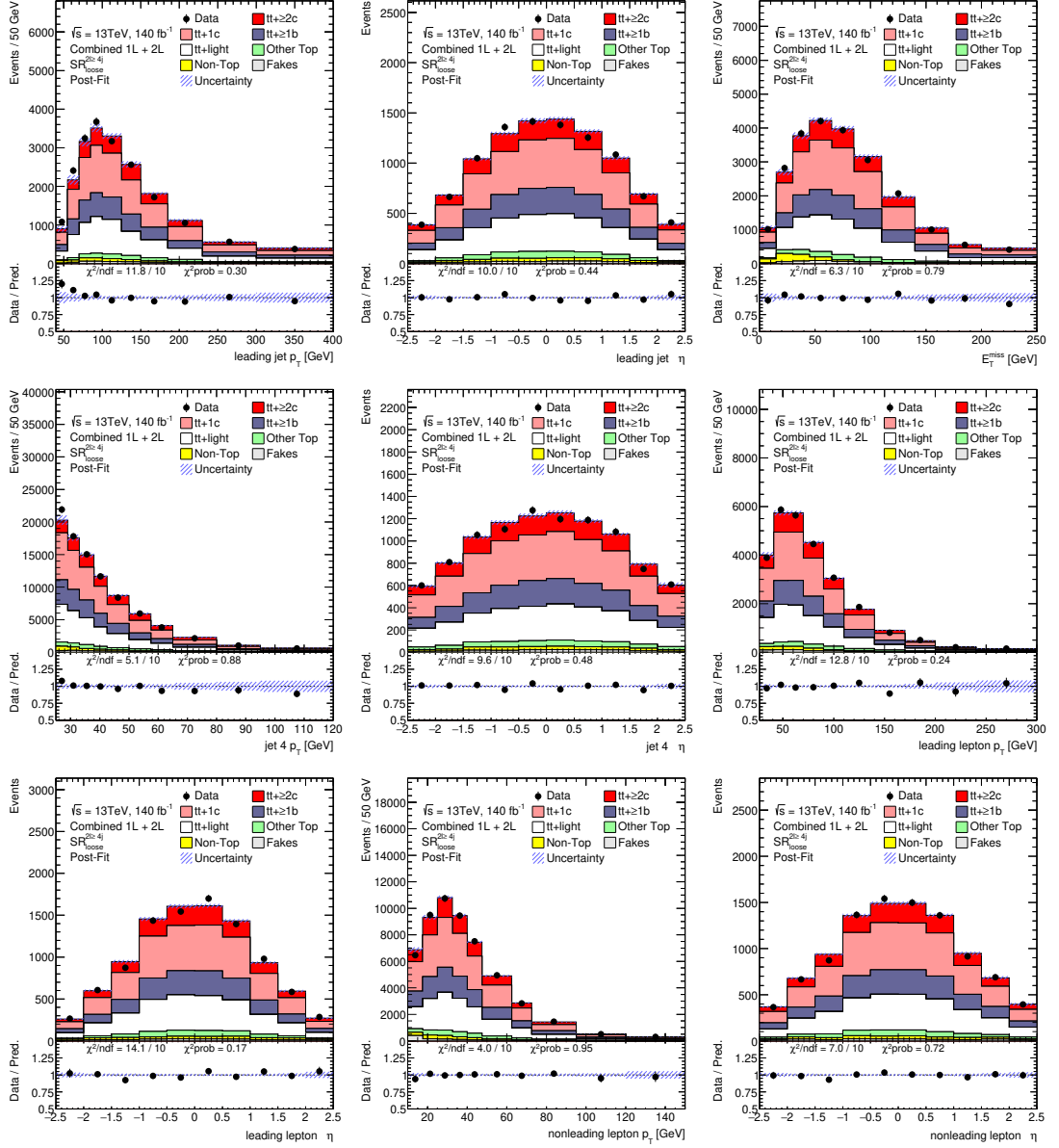


Figure D.42.: Post-fit agreement between data and prediction for basic kinematic variables in $SR_{loose}^{2\ell \ge 4j}$. The hashed band includes all prediction uncertainties. Overflow and underflow events are contained in the first and last bin respectively.

D.4. Post-fit plots - dilepton channel

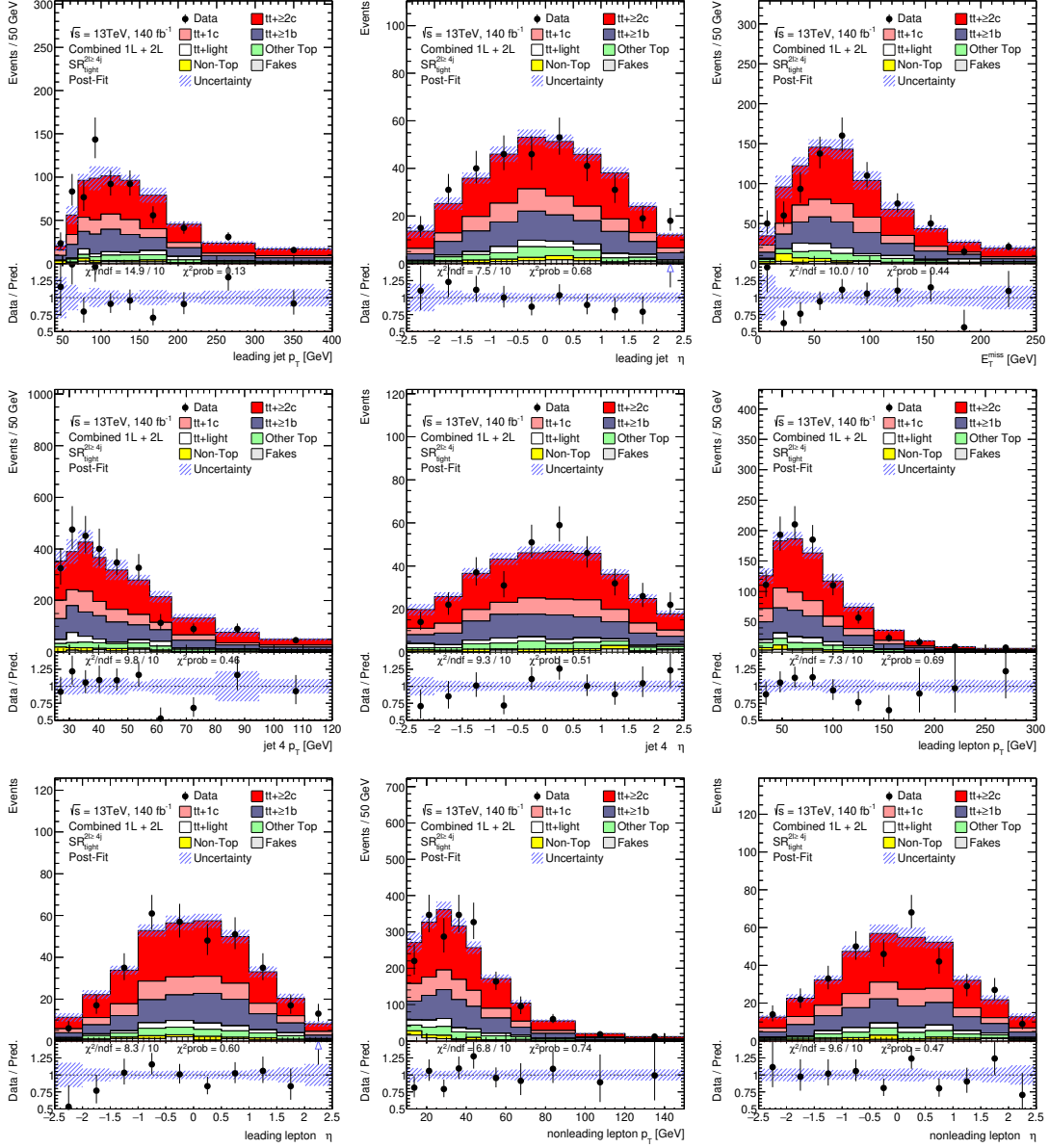


Figure D.43.: Post-fit agreement between data and prediction for basic kinematic variables in $\text{SR}_{\text{tight}}^{2\ell\geq 4j}$. The hashed band includes all prediction uncertainties. Overflow and underflow events are contained in the first and last bin respectively.

D. Kinematics Control Plots

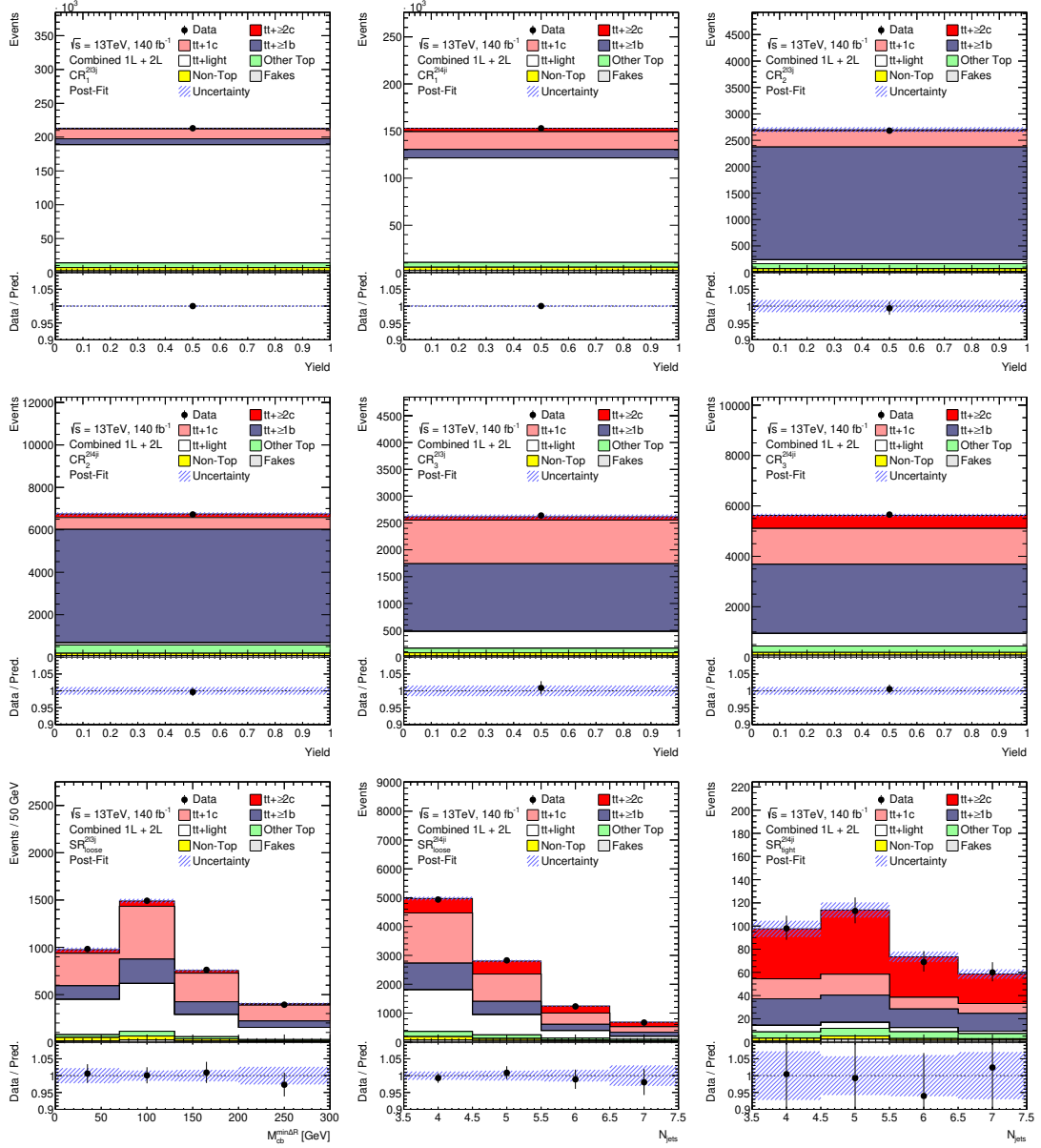


Figure D.44.: Post-fit agreement between data and prediction for observables used in fitting in dilepton channel control and signal regions. The hashed band includes all prediction uncertainties. Overflow and underflow events are contained in the first and last bin respectively.

APPENDIX E

Additional Figures - Results

E.1. Fiducial phase space fit to data

E. Additional Figures - Results

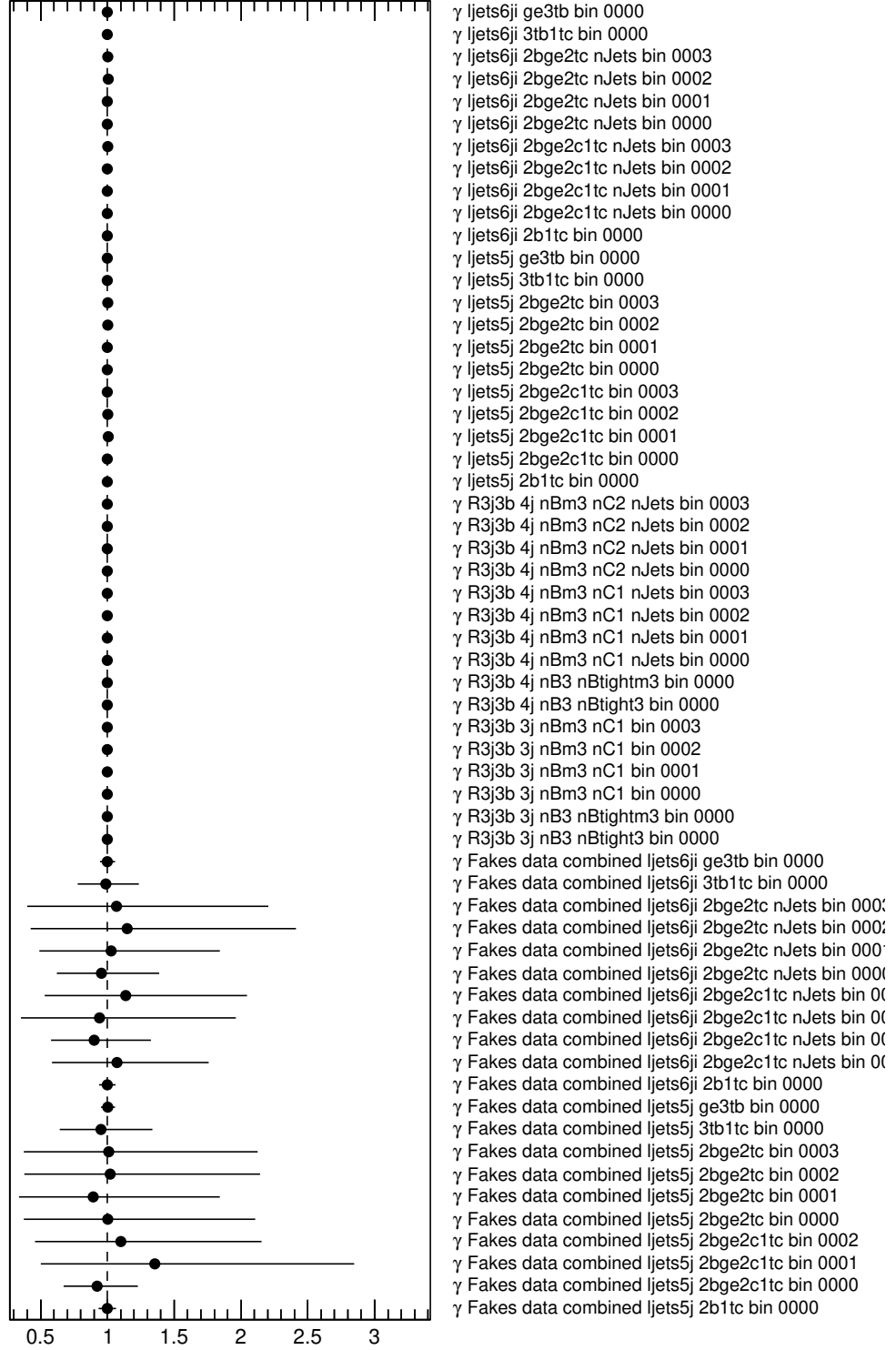


Figure E.1.: Post-fit pulls and constraints on nuisance parameters related to MC statistical uncertainty in each bin, in a fit to data in a fiducial phase space. Nuisance parameters denoted 'Fakes' are related to the fake lepton contribution in the lepton + jets channel. The rest are associated with the sum of all other processes.

E.1. Fiducial phase space fit to data

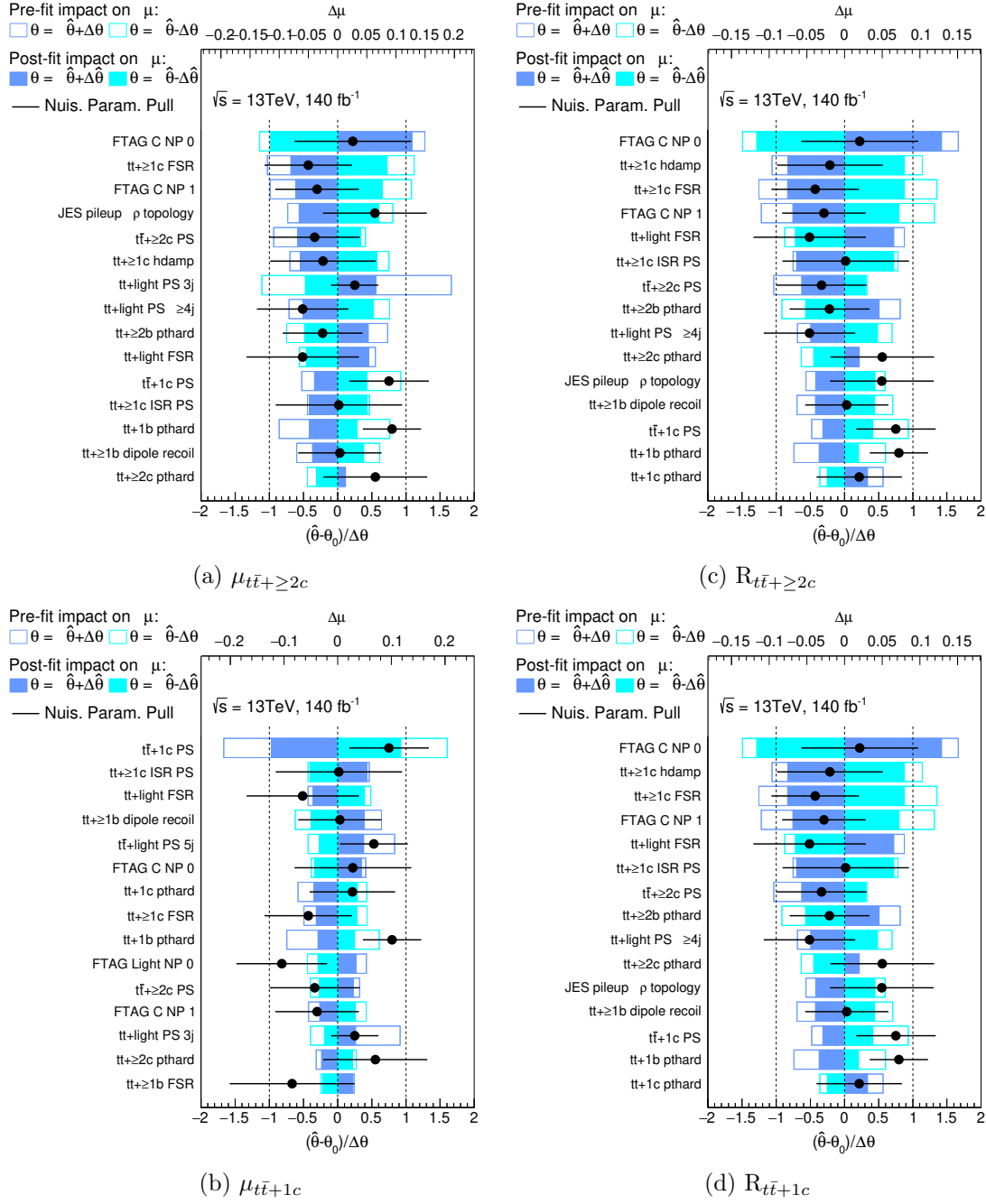


Figure E.2.: Ranking of the 15 most impactful systematic uncertainties, in fits to ATLAS data in a fiducial phase space, on a) $t\bar{t} + \geq 2c$ signal strength b) $t\bar{t} + 1c$ signal strength c) $R_{t\bar{t}+\geq 2c}$ d) $R_{t\bar{t}+1c}$. The latter two denote the fraction of events in that category relative to all $t\bar{t} + \text{jets}$ events. The (pre-) post-fit impact is calculated by measuring the change in POI when the nuisance parameter is fixed, shifted by its (pre-) post-fit uncertainty, and is shown in blue. The post-fit pulls and constraints of these nuisance parameters are also shown.

E. Additional Figures - Results

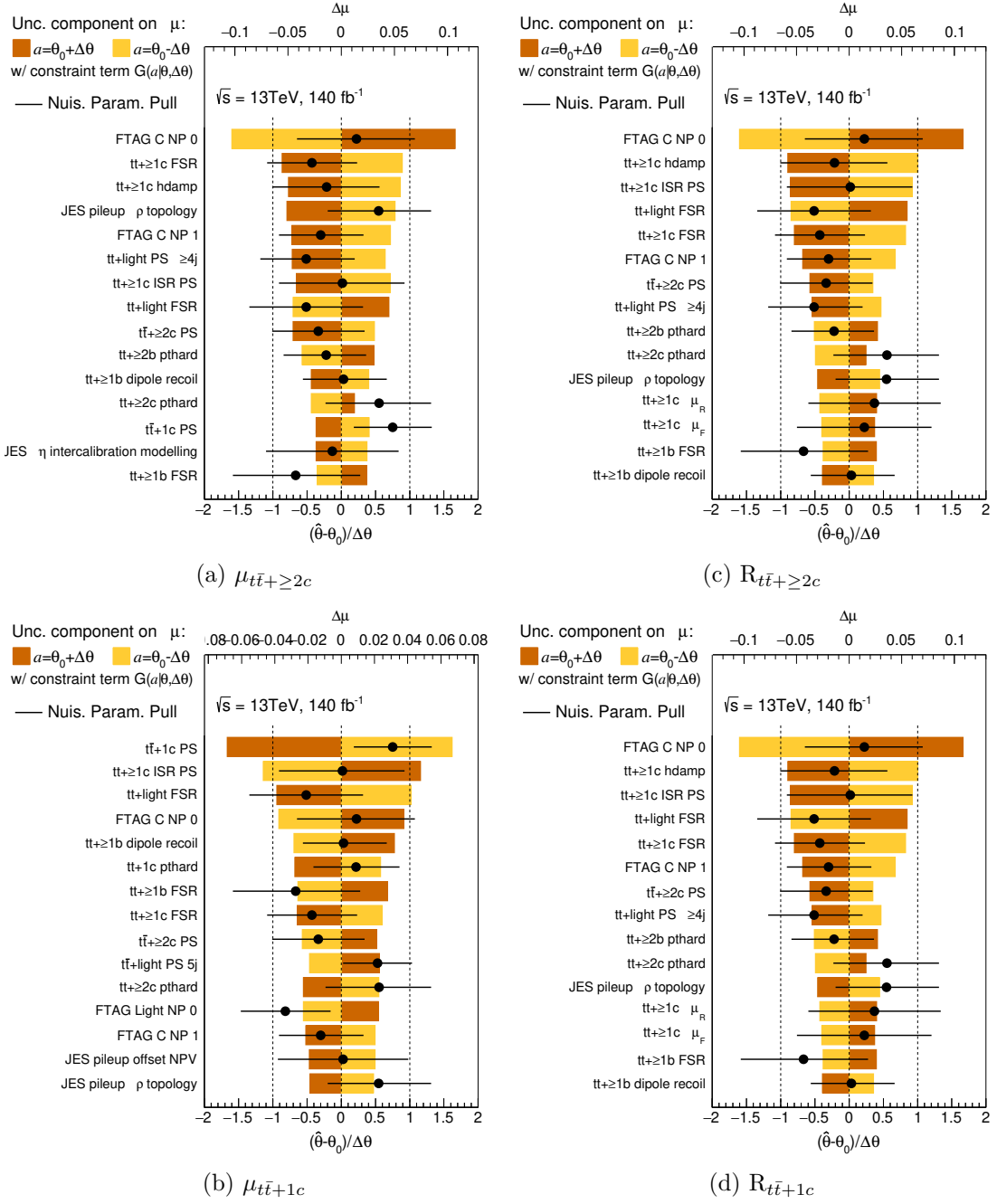


Figure E.3.: Ranking of the 15 most impactful systematic uncertainties, in fits to ATLAS data in a fiducial phase space, on a) $t\bar{t} + \geq 2c$ signal strength b) $t\bar{t} + 1c$ signal strength c) $R_{t\bar{t} + \geq 2c}$ d) $R_{t\bar{t} + 1c}$. The latter two denote the fraction of events in that category relative to all $t\bar{t} + \text{jets}$ events. The impact is calculated by shifting the point at which the NP's Gaussian constraint term is evaluated up or down one standard deviation, and is shown in yellow/brown. The post-fit pulls and constraints of these nuisance parameters are also shown.

E.1. Fiducial phase space fit to data

Table E.1.: Comparison of measured cross-section values with a range of predicted values from simulation, in a fiducial phase space. Uncertainties are symmetrised. Measurement uncertainties include all systematic and statistical components. Uncertainties in predicted values include simultaneous and independent variations of μ_R and μ_F , and uncertainties in the choice of PDF set. Data taken from Ref. [1].

	$t\bar{t} + \geq 2c$ [pb]	$t\bar{t} + 1c$ [pb]	$t\bar{t} + \geq 1b$ [pb]	$t\bar{t} + \text{light}$ [pb]	$t\bar{t} + \text{jets}$ [pb]
$t\bar{t}$ POWHEG+PYTHIA 8	1.04 ± 0.18	5.1 ± 0.8	3.2 ± 0.5	40 ± 6	50 ± 7
$t\bar{t}$ POWHEG+PYTHIA 8, $h_{\text{damp}} = 3 m_t$	1.12 ± 0.16	5.4 ± 0.7	3.3 ± 0.5	41 ± 5	51 ± 7
$t\bar{t}$ POWHEG+PYTHIA [8], $p_T^{\text{hard}} = 1$	1.05 ± 0.18	5.2 ± 0.8	3.1 ± 0.5	40 ± 6	50 ± 7
$t\bar{t}$ POWHEG+HERWIG 7	0.94 ± 0.16	4.2 ± 0.7	3.3 ± 0.5	43 ± 6	52 ± 8
$t\bar{t}$ MADGRAPH5_aMC@NLO +HERWIG 7	0.74 ± 0.19	4.0 ± 0.8	2.7 ± 0.6	46 ± 8	53 ± 10
$t\bar{t}b\bar{b}$ POWHEG+PYTHIA 8	—	—	3.2 ± 1.6	—	—
$t\bar{t}b\bar{b}$ POWHEG+PYTHIA 8, $p_T^{\text{hard}} = 1$	—	—	2.8 ± 1.3	—	—
$t\bar{t}b\bar{b}$ POWHEG+PYTHIA 8, $h_{\text{bzd}} = 2$	—	—	3.1 ± 1.5	—	—
$t\bar{t}b\bar{b}$ POWHEG+PYTHIA 8, dipole recoil	—	—	3.0 ± 1.4	—	—
$t\bar{t}b\bar{b}$ POWHEG+HERWIG 7	—	—	3.1 ± 1.6	—	—
$t\bar{t}b\bar{b}$ SHERPA 2.2.10	—	—	3.5 ± 1.0	—	—
Data	1.28 ± 0.25	6.4 ± 0.9	3.46 ± 0.24	36.0 ± 1.8	47.1 ± 2.3

E.2. Inclusive phase space fit to data

E.2. Inclusive phase space fit to data

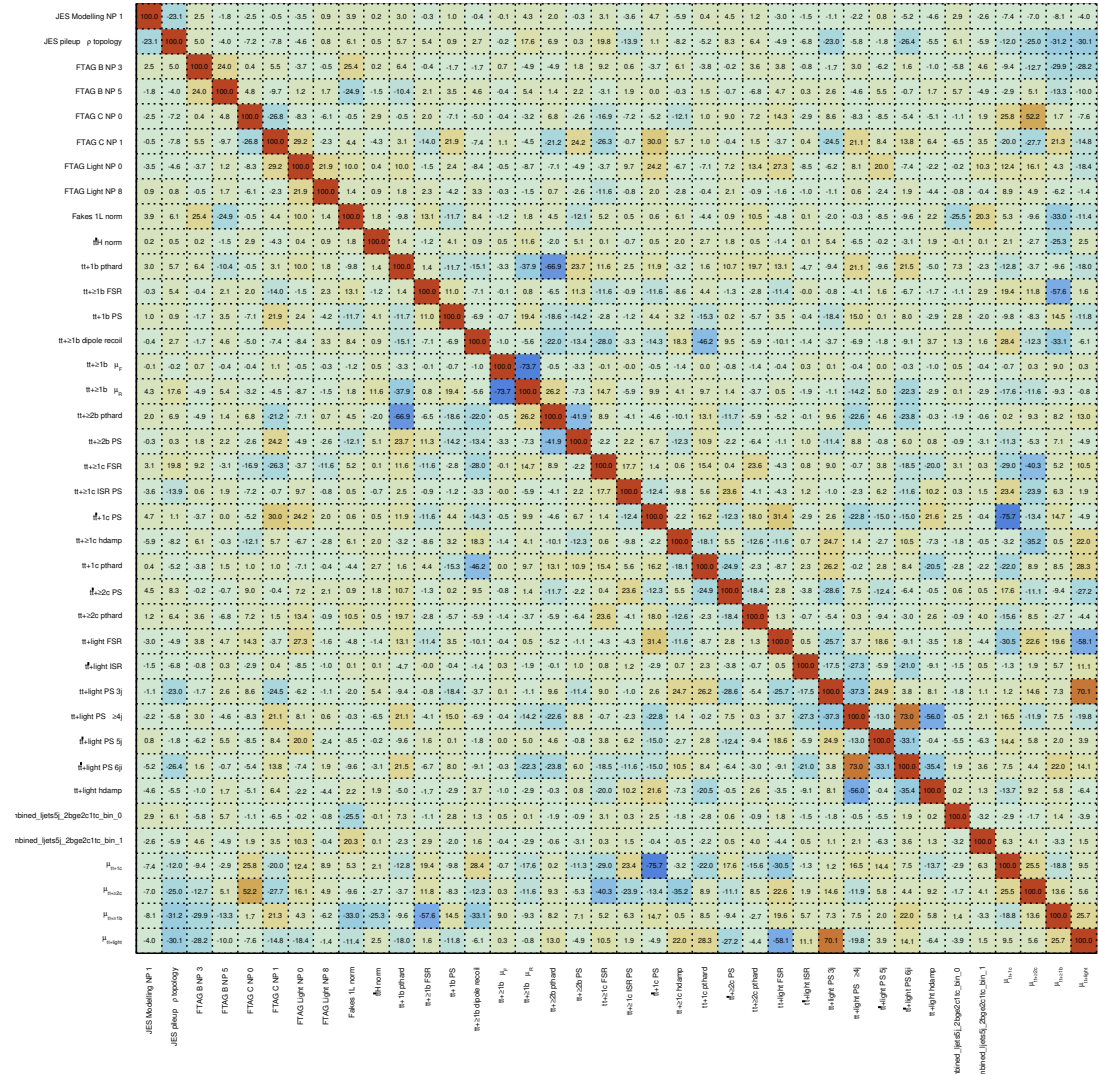


Figure E.4.: Matrix showing the percentage correlation between nuisance parameters and $t\bar{t}$ + jets signal strengths, in a fit to ATLAS data in an inclusive phase space. Only those nuisance parameters and signal strengths which have at least one correlation $\geq 20\%$ are shown.

E. Additional Figures - Results

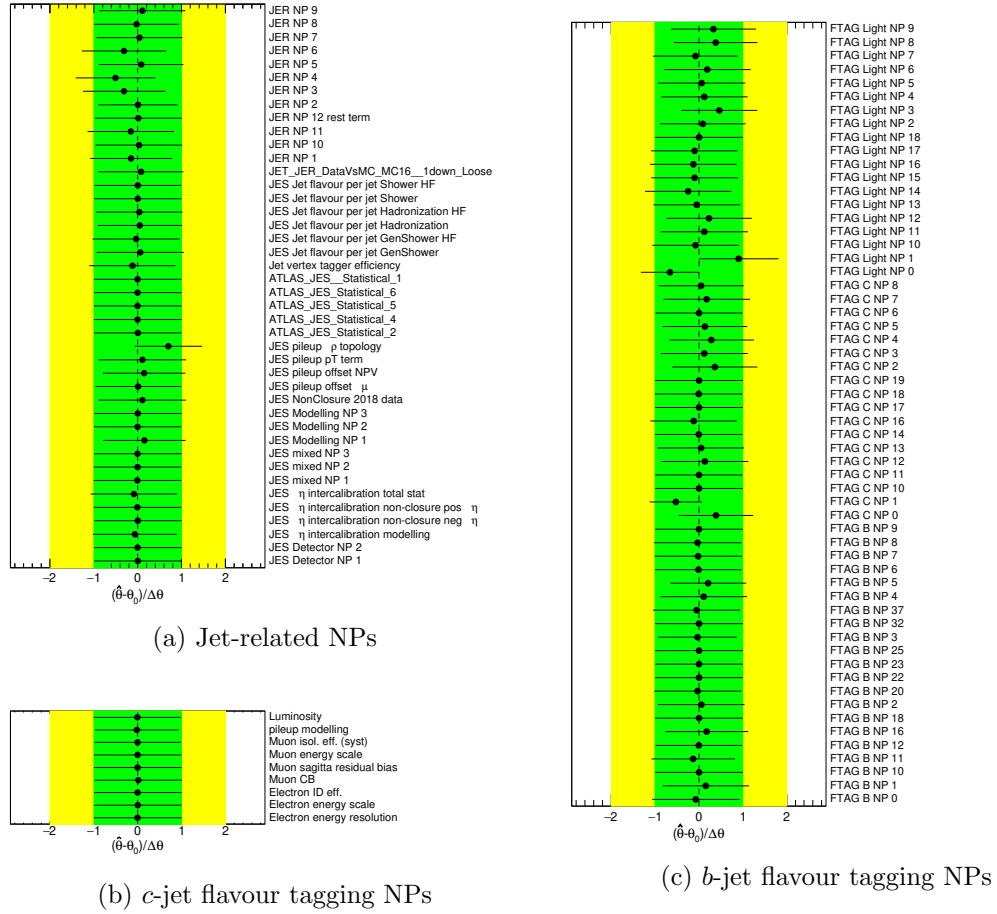


Figure E.5.: Pulls of instrumental NPs in a fit to data in an inclusive phase space, grouped into those related to a) jets b) c -jet flavour tagging c) b -jet flavour tagging d) light jet flavour tagging e) other experimental NPs.

E.2. Inclusive phase space fit to data

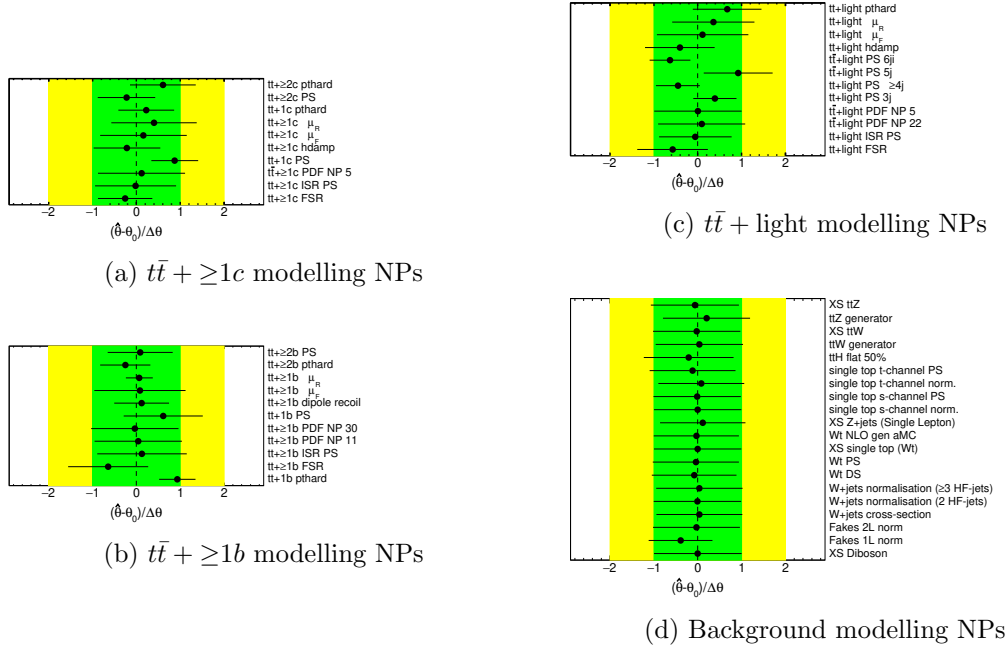


Figure E.6.: Pulls of modelling NPs in a fit to data in an inclusive phase space, grouped into those related to a) $t\bar{t} + \geq 1c$ b) $t\bar{t} + \geq 1b$ c) $t\bar{t} + \text{light}$ d) background processes.

E. Additional Figures - Results

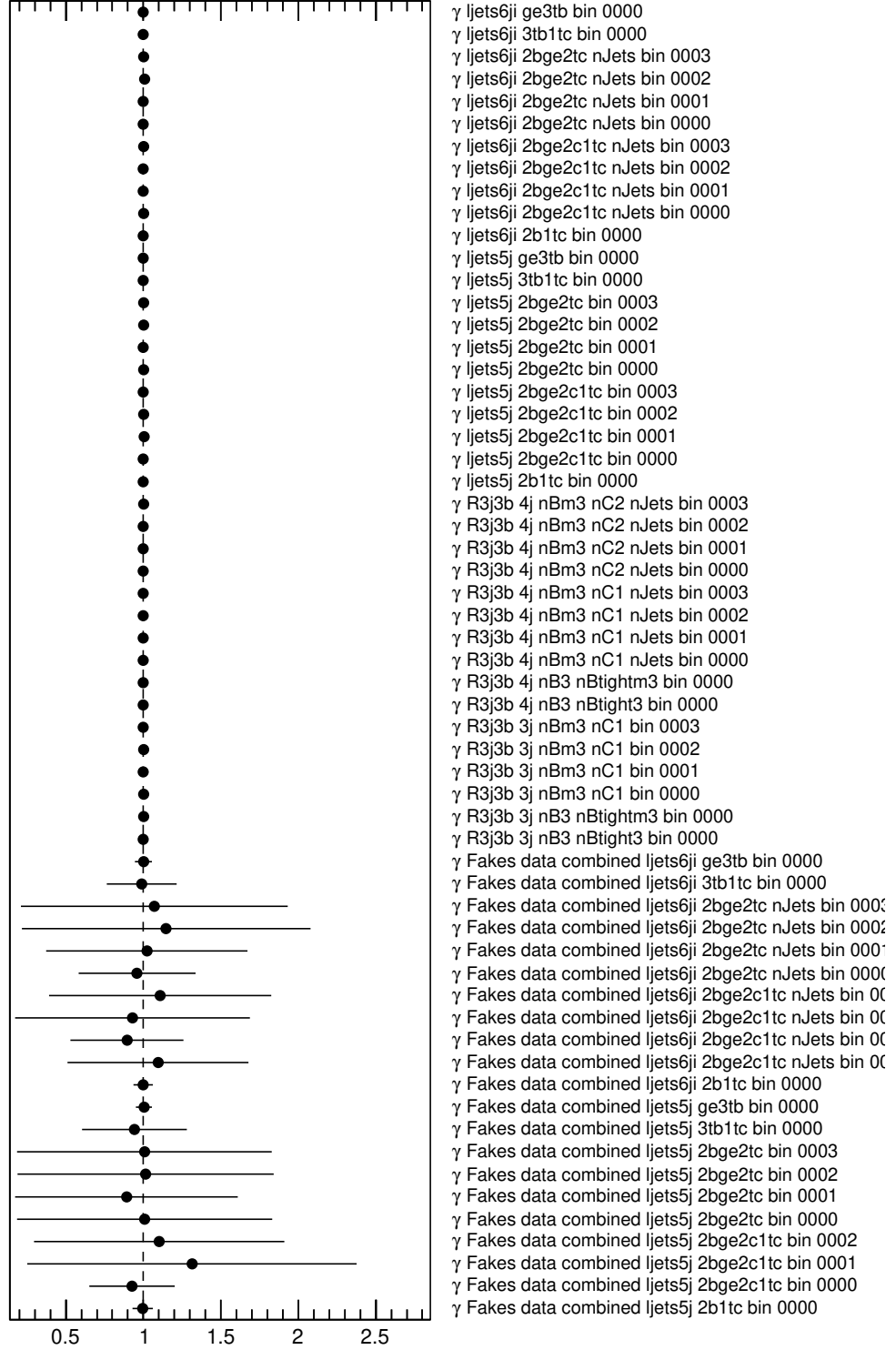


Figure E.7.: Post-fit pulls and constraints on nuisance parameters related to MC statistical uncertainty in each bin, in a fit to data in an inclusive phase space. Nuisance parameters denoted ‘Fakes’ are related to the fake lepton contribution in the lepton + jets channel. The rest are associated with the sum of all other processes.

E.2. Inclusive phase space fit to data

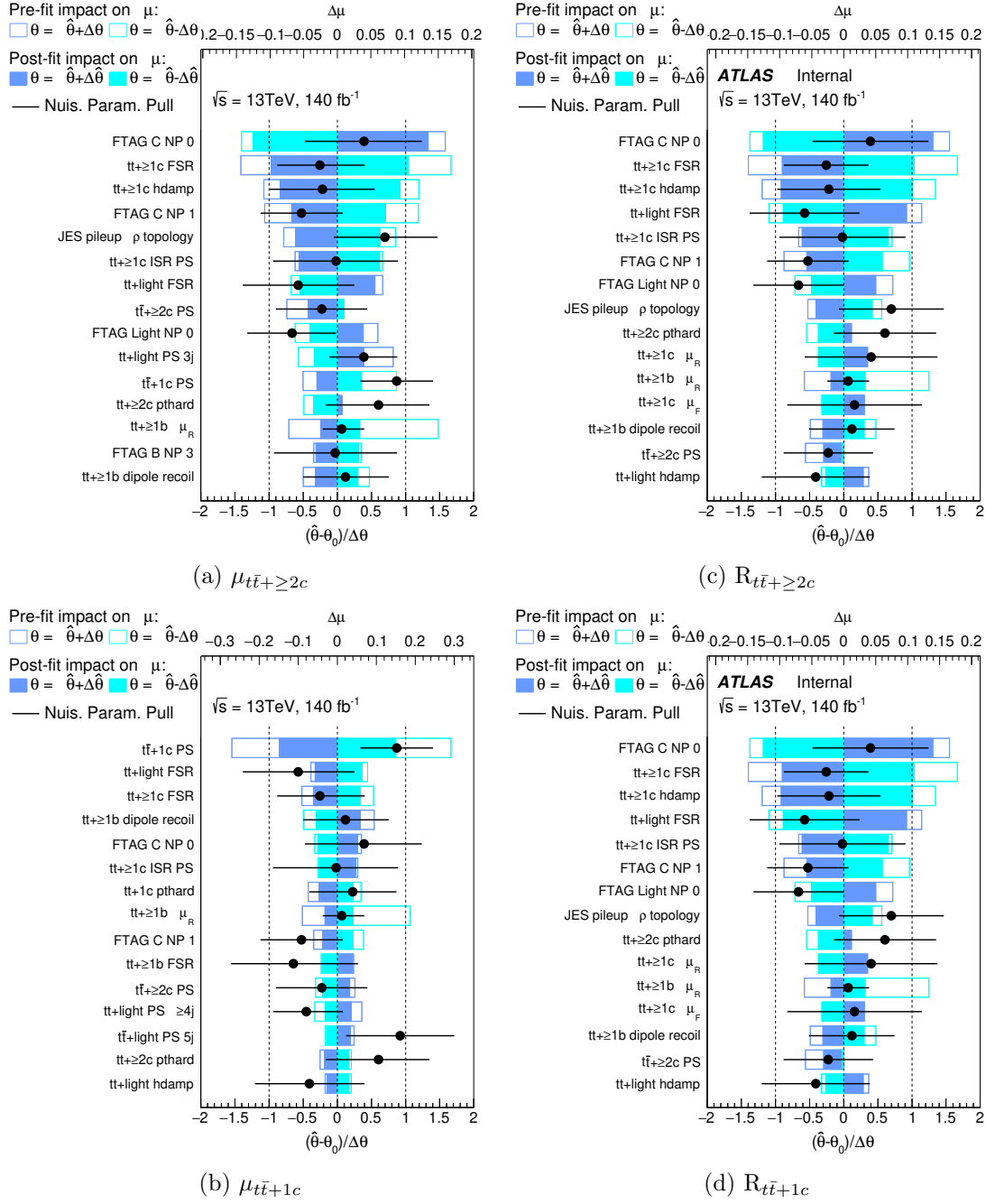


Figure E.8.: Ranking of the 15 most impactful systematic uncertainties, in fits to ATLAS data in an inclusive phase space, on a) $t\bar{t} + \geq 2c$ signal strength b) $t\bar{t} + 1c$ signal strength c) $R_{t\bar{t} + \geq 2c}$ d) $R_{t\bar{t} + 1c}$. The latter two denote the fraction of events in that category relative to all $t\bar{t}$ + jets events. The (pre-) post-fit impact is calculated by measuring the change in POI when the nuisance parameter is fixed, shifted by its (pre-) post-fit uncertainty, and is shown in blue. The post-fit pulls and constraints of these nuisance parameters are also shown.

E. Additional Figures - Results

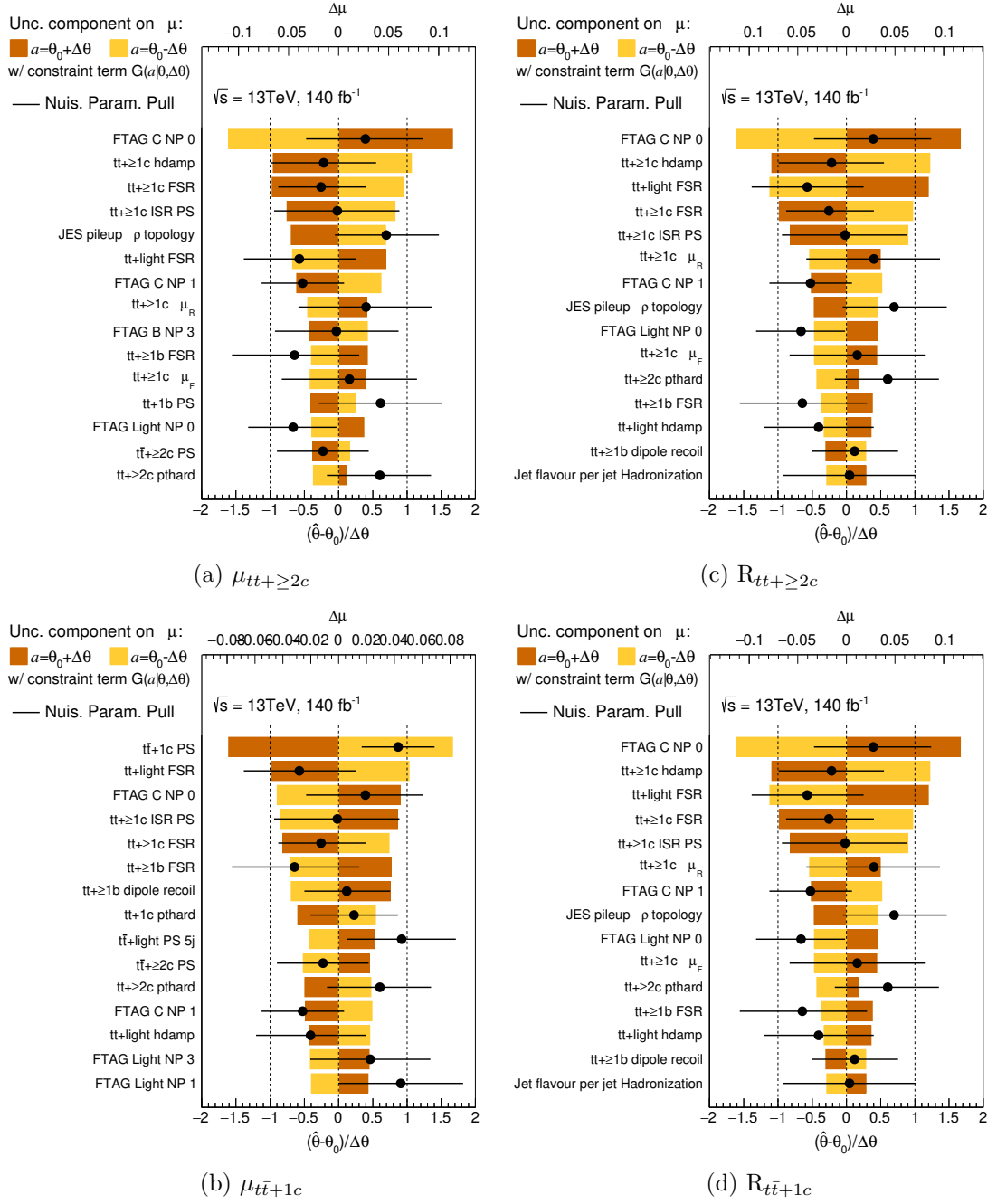


Figure E.9.: Ranking of the 15 most impactful systematic uncertainties, in fits to ATLAS data in an inclusive phase space, on a) $t\bar{t} + \geq 2c$ signal strength b) $t\bar{t} + 1c$ signal strength c) $R_{t\bar{t}+\geq 2c}$ d) $R_{t\bar{t}+1c}$. The latter two denote the fraction of events in that category relative to all $t\bar{t} + \text{jets}$ events. The impact is calculated by shifting the point at which the NP's Gaussian constraint term is evaluated up or down one standard deviation, and is shown in yellow/brown. The post-fit pulls and constraints of these nuisance parameters are also shown.